

A Holistic Approach to Structural Health Monitoring of
Composite Aerospace Structures using Lamb Waves: From
Manufacturing to Service

by

Gary Scott Bishop

A thesis submitted to the Faculty of Graduate and Postdoctoral
Affairs in partial fulfillment of the requirements for the degree of

Doctor of Philosophy

in

Aerospace Engineering

Carleton University
Ottawa, Ontario

© 2021, Gary Scott Bishop

Abstract

The successful application of a structural health monitoring (SHM) system for composite aerospace structures requires a holistic approach encompassing the full life cycle of the structure. Important capabilities of an SHM system include: 1) recognition, 2) identification, 3) severity, and 4) location of a defect. This was achieved, first, by designing a novel manufacturing method to co-cure piezoelectric sensors to the surface of carbon fibre reinforced polymer (CFRP) panels, allowing for *in-situ* cure monitoring, manufacturing inspection, and in-service monitoring. Second, numerical and experimental techniques used Lamb wave propagation to recognize and identify multiple types of manufacturing defects and determine the severity of a delamination defect.

A comparison of co-cured and bonded piezoelectric sensors showed similar waveform shape, Lamb wave propagation velocity, and signal amplitude for the anti-symmetric Lamb wave mode. Performing a time-frequency domain analysis using the continuous wavelet transform demonstrated the ability to recognize and identify delamination, porosity, and foreign object defects. To determine the severity of a delamination defect, five input signals were compared and it was determined the Mexican hat excitation provided the best average main lobe width resolution and signal-to-noise ratio over a range of frequencies, particularly at lower frequencies. Finally, a multiple level discrete wavelet transform decomposition was able to provide signal compression, up to 450 times, while still maintaining the important signal features to determine the severity of a delamination defect. This allowed both the length ratio and depth sequence of multiple delamination defects to be correctly identified. The practical approach of this research to

focus on the manufacturing process and manufacturing defects provided an important step towards a holistic SHM system for CFRP structures.

Acknowledgements

To my supervisor, mentor, and friend Dr. Jeremy Laliberte. This would not have been possible without your guidance, support, and encouragement – it was more than an academic undertaking, it was a journey in life. Thank-you.

I would like to thank the National Research Council of Canada, Aerospace Portfolio, for access to the facility, and more importantly, expertise. Specifically, Marc Genest – you set me on this path and helped me take the first steps; thank-you for all your guidance and understanding. I would also like to thank Dr. Min Liao for ensuring everything was in place for my success - I sincerely appreciate all your support to ensure my continuing success.

To all the faculty and staff in the Department of Mechanical and Aerospace Engineering at Carleton University, I could not have succeeded without you. Especially, Neil McFadyen for the countless hours setting up computer access to the cluster and ensuring my simulations ran successfully.

I would like to thank Mitacs, NSERC, and Comtek Advanced Structures for their financial support to complete this thesis. More importantly, I would like to thank Comtek Advanced Structures for access to their facility, donating materials, and providing help.

Finally, I would like to thank my friends and family, especially Helen, this took longer than expected and I am grateful for your encouragement and motivation. I am no longer a student. To my beautiful little girl, Ella:

*The more that you read, the more things you will know. The more that you learn,
the more places you'll go. – Dr. Seuss*

Table of Contents

Abstract	ii
Acknowledgements	iv
Table of Contents	v
List of Tables	x
List of Figures	xii
Nomenclature	xix
Acronyms	xix
Symbols	xxi
Chapter 1: Introduction	1
1.1 Non-Destructive Testing (NDT).....	2
1.2 Structural Health Monitoring (SHM)	4
1.3 Fundamental Principles of Lamb Waves.....	7
1.4 Research Objective	14
1.5 Research Limitations	14
1.6 Dissertation Overview	15
Chapter 2: Manufacturing Process to Integrate Sensors	17
2.1 Methods	21
2.1.1 Materials.....	21
2.1.2 Manufacturing Process.....	23
2.1.3 Experimental Procedure	28
2.1.4 Signal Processing	29
2.2 Experimental Results.....	30
2.3 Discussion.....	35

Chapter 3: Defect Identification	38
3.1 Analysis Technique	43
3.1.1 Continuous Wavelet Transform (CWT).....	44
3.1.1.1 Morlet Wavelet.....	44
3.1.1.2 Biorthogonal Wavelet.....	46
3.2 Finite Element Model	47
3.2.1 Implicit versus Explicit FEM for Lamb Wave Research	48
3.2.2 Finite Element Parameters for Lamb Wave Propagation	51
3.2.2.1 Element Type	51
3.2.2.2 Mesh Density.....	52
3.2.2.3 Load Application.....	55
3.2.2.4 FEM Absorbing Layers	57
3.2.2.5 Finite Element Modelling Defect Definition.....	60
3.2.2.5.1 Delamination Defect.....	61
3.2.2.5.2 Foreign Object Defect	64
3.2.2.5.3 Porosity.....	64
3.3 Experimental Setup	65
3.3.1 Composite panels	66
3.3.2 Defects	66
3.3.3 Experimental Absorbing Layer	67
3.3.4 Excitation and Measurement.....	68
3.4 Results	68
3.4.1 FE Model Validation: Piezoelectric Voltage versus Nodal Displacement.....	69
3.4.2 FE Model Validation: ABAQUS/Explicit versus Experimental Results	71
3.4.3 Continuous Wavelet Transform (CWT) Analysis.....	76
3.4.3.1 Reference Standard.....	77

3.4.3.2	Delamination Defect.....	81
3.4.3.3	Foreign Object.....	90
3.4.3.4	Porosity.....	94
3.4.3.5	Defect Comparison.....	97
3.5	Discussion.....	99
3.6	Conclusions	102
Chapter 4: Input Signal Comparison.....		104
4.1	Input Signal Theory.....	109
4.1.1	Narrowband Tone Burst Excitation.....	110
4.1.2	Mexican Hat Excitation.....	111
4.1.3	Broadband Chirp Excitation.....	112
4.1.4	Auto-Correlated Linear Chirp	114
4.1.5	Barker Code Sine Wave	115
4.2	Simulation Methodology	116
4.2.1	Material Properties	117
4.2.2	Finite Element Model.....	119
4.3	Results	120
4.3.1	Broadband Signal Reconstruction using a Chirp Signal	121
4.3.2	Frequency Range for Delamination Identification.....	123
4.3.3	Main Lobe Width Comparison.....	126
4.3.4	Signal-to-Noise Ratio.....	129
4.3.5	Effective Frequency Range	130
4.4	Discussion.....	132
4.5	Conclusions	134
Chapter 5: Delamination Defect Analysis.....		136
5.1	Analysis Technique	143

5.1.1	Discrete Wavelet Transform (DWT).....	144
5.1.2	Multiple Level Decomposition.....	145
5.1.3	Daubechies Wavelets	148
5.1.4	Delamination Length and Depth Calculations	152
5.2	2D Analysis of Delamination Length and Depth	153
5.2.1	2D ABAQUS Simulation Results	154
5.2.2	2D DWT Analysis.....	155
5.2.3	Theoretical Dispersion Curves.....	157
5.2.4	2D Delamination Length and Depth Results.....	158
5.3	3D Analysis of Delamination Length and Depth	159
5.3.1	3D ABAQUS Simulation Results	159
5.3.2	3D DWT Analysis.....	161
5.3.3	Dispersion Curves	163
5.3.4	3D Delamination Length and Depth Results.....	164
5.4	Experimental Results.....	165
5.4.1	Experimental DWT Analysis	167
5.4.2	Dispersion Curve.....	169
5.4.3	Experimental Delamination Length and Depth Results.....	170
5.5	2D Analysis of Delamination Length.....	170
5.5.1	2D DWT Analysis.....	172
5.5.2	Theoretical Dispersion Curve	173
5.5.3	2D Delamination Length Results	174
5.6	Discussion.....	174
5.7	Conclusions	178
	Chapter 6: Discussion	179
6.1	Manufacturing of CFRP Structures	179

6.2	Identification of Multiple Defect Types	181
6.3	Defect Severity	182
6.4	Summary.....	183
Chapter 7: Conclusions and Statement of Contributions		184
7.1	Manufacturing Process to Integrate Sensors (Chapter 2)	184
7.2	Defect Identification (Chapter 3).....	185
7.3	Input Signal Comparison (Chapter 4).....	185
7.4	Delamination Defect Analysis (Chapter 5)	186
7.5	Statement of Research Contributions	187
7.6	Future Recommendations	189
References		192

List of Tables

Table 1: Comparison of SHM techniques for CFRP structures.....	4
Table 2: Piezoelectric properties.....	22
Table 3: Finite element model parameters for an Implicit and Explicit model.	50
Table 4: Finite element parameters for the comparison of different element sizes.	53
Table 5: Finite element model parameters for the comparison of different applied loads.	55
Table 6: SRM boundary layer properties.....	60
Table 7: Finite element model parameters for the comparison of different delamination methods.	62
Table 8: Material properties for the CFRP, Teflon, and stainless steel materials.	66
Table 9: Finite element model parameters for the comparison of PZT voltage and nodal displacement.	69
Table 10: Finite element model parameters for the ABAQUS/Explicit model.	73
Table 11: Finite element model parameters for the comparison of different defect types.	77
Table 12: Defect type and signature feature.	98
Table 13: Defect type and associated CWT contour plot regions with changes in signal energy.....	99
Table 14: Finite element model parameters for the excitation signal models.	117
Table 15: Piezoelectric PZT material properties.	118
Table 16: The best main lobe width times for S_0 , A_0 , and A_θ reflection and corresponding frequency of the five compared signals.	127

Table 17: Signal-to-Noise ratio of the A_0 reflection for the five compared signals.....	130
Table 18: A_0 reflection MLW calculated for the 3-cycle sine wave, Mexican hat, and 13-bit Barker Code signals for a range of frequencies.	131
Table 19: A_0 reflection SNR calculated for the 3-cycle sine wave, Mexican hat, and 13-bit Barker code signals for a range of frequencies.	131
Table 20: Scaling coefficients for the db10 wavelet.....	151
Table 21: 2D finite element model parameters for delamination depth.	153
Table 22: Calculated length and depth for the 2D ABAQUS simulations.	158
Table 23: 3D finite element model parameters for delamination depth.	159
Table 24: Calculated length and depth for the 3D ABAQUS simulations.	165
Table 25: Calculated length and depth for experimental panels.....	170
Table 26: 2D finite element model parameters for delamination length.	171
Table 27: Calculated length and depth for a 25.4 mm and 50.8 mm delamination defect.	174

List of Figures

Figure 1: Common defects occurring in CFRP structures, taken from [8].	2
Figure 2: Longitudinal wave, taken from [20].	8
Figure 3: Shear wave, taken from [20].	8
Figure 4: Lamb wave in a thin plate depicting two different mode types: left - anti-symmetrical, and right – symmetrical, taken from [20].	8
Figure 5: Dispersion curves for a steel plate, a) Phase velocity, and b) Group velocity, taken from [25].	11
Figure 6: Piezoelectric sensor with wrap-around electrode pattern, taken from [48].	22
Figure 7: Schematic of CFRP panel with piezoelectric sensors (not to scale).	23
Figure 8: Manufacturing tool to co-cure piezoelectric sensors.	24
Figure 9: Isometric view of manufacturing tool with spring pins shown.	24
Figure 10: Electrical spring pins connectors (Mill-Max, model # 0973-0-15-20-77-14-11-0).	25
Figure 11: The layup sequence for a CFRP panel with co-cured piezoelectric sensors. Left: aluminum tool with piezoelectric inserted into machined positioning holes, Center: composite laminate layup, Right: connecting wires sealed with vacuum bagging tape.	26
Figure 12: CFRP panel vacuum bagged and placed inside an oven.	27
Figure 13: CFRP panel with bonded piezoelectric sensors.	28
Figure 14: Experimental setup to generate and collect Lamb wave signals.	29
Figure 15: Comparison of the signal response for co-cured (blue) and bonded (red) sensors, from 50 kHz (top) to 150 kHz (bottom).	31

Figure 16: Ultrasound c-scan image of CFRP panel with co-cured sensors (top) and bonded sensors (bottom).....	32
Figure 17: Signal amplitude for the S_0 and A_0 modes in CFRP panels with co-cured and bonded piezoelectric sensors.....	33
Figure 18: Experimental dispersion curve for the S_0 and A_0 modes for a frequency-thickness range from 60 - 600 kHz*mm.....	34
Figure 19: Representation of the Morlet wavelet	44
Figure 20: Biorthogonal decomposition and reconstruction wavelets ($m = 3$ and $n = 5$).	47
Figure 21: Implicit versus Explicit FEM for Lamb wave propagation in an aluminum plate.....	51
Figure 22: Comparison of element length for a 3-cycle sine wave with an excitation frequency of 300 kHz; 0.4 mm (top), 0.5 mm (middle), and 0.6 mm (bottom).	54
Figure 23: Concentrated forces to generate a 3-cycle sine wave with an excitation frequency of 300 kHz; balanced x and y forces (top), and force in the z direction (bottom).....	56
Figure 24: Comparison of three methods to create a delamination defect using ABAQUS.	63
Figure 25: Close-up of the A_0 and A_0 reflection of the three methods used to create a delamination defect using ABAQUS.....	63
Figure 26: Generalized porosity region modelled in ABAQUS.....	65
Figure 27: Experimental absorbing layers (top surface).....	68
Figure 28: Experimental absorbing layers (bottom surface).....	68

Figure 29: ABAQUS/Implicit FE model comparing the piezoelectric and displacement signal response.	70
Figure 30: ABAQUS/Implicit FE model comparing the piezoelectric and inverted displacement signal response to align the A_0 mode.	70
Figure 31: ABAQUS/Implicit FE model comparing the piezoelectric and inverted-shifted displacement signal response to align the S_0 mode.	71
Figure 32: Ultrasound c-scan image of a CFRP without any embedded defects.	72
Figure 33: Experimental and ABAQUS/Explicit results for a CFRP panel.	73
Figure 34: Experimental and ABAQUS/Explicit results for a CFRP panel with the ABAQUS results normalized with respect to the A_0 mode.	74
Figure 35: Experimental and ABAQUS/Explicit results for a CFRP panel with the ABAQUS results normalized and shifted to align the S_0 mode.	75
Figure 36: Experimental and ABAQUS/Explicit results for a CFRP panel with the ABAQUS results normalized and shifted to align the A_0 mode.	76
Figure 37: ABAQUS simulation of a reference standard specimen.	78
Figure 38: ABAQUS simulation signal for a reference standard specimen: time domain (top), CWT contour plot with logarithmic scale (bottom).	79
Figure 39: Experimental signal for a reference standard specimen: time domain (top), CWT contour plot with logarithmic scale (bottom).	79
Figure 40: Comparison of the CWT contour plot for a reference standard specimen with a linear scale: ABAQUS simulation (top), experimental simulation (bottom).	80
Figure 41: ABAQUS simulation of a CFRP specimen with a delamination defect located mid-thickness (ply 4).	83

Figure 42: Ultrasound c-scan image of a CFRP panel with a mid-thickness delamination defect.....	84
Figure 43: Comparison of the CWT contour plot for a CFRP specimen with a delamination defect (mid-thickness, ply 4): ABAQUS simulation (top), experimental simulation (bottom).....	86
Figure 44: ABAQUS simulation of a CFRP specimen with a near surface delamination defect (ply 2).....	87
Figure 45: Ultrasound c-scan image of a CFRP panel with a near surface delamination defect.....	88
Figure 46: Comparison of the CWT contour plot for a CFRP specimen with a near-surface delamination defect (ply 2): ABAQUS simulation (top), experimental simulation (bottom).....	89
Figure 47: ABAQUS simulation of a CFRP specimen with a mid-surface foreign object defect (ply 4).....	91
Figure 48: Ultrasound c-scan image of a CFRP panel with a foreign object defect.....	92
Figure 49: Comparison of the CWT contour plot for a CFRP specimen with a mid-surface foreign object defect (ply 4): ABAQUS simulation (top), experimental simulation (bottom).....	93
Figure 50: ABAQUS simulation of a CFRP specimen with a mid-surface porosity defect (ply 4).....	95
Figure 51: Ultrasound c-scan image of a CFRP panel with a porosity defect.....	96
Figure 52: Comparison of the CWT contour plot for a CFRP specimen with a mid-surface porosity defect (ply 4): ABAQUS simulation (top), experimental simulation (bottom)..	97

Figure 53: CWT contour plot divided into 16 regions.....	98
Figure 54: Predicted time-traces showing (a) two twenty-cycle wave-packets with centre frequency of 1 MHz completely separated in time. The effect of progressively reducing the separation between centres of the wave-packets is illustrated in time-traces (b), (c) and (d). Time-trace (e) shows the effect of reducing the number of cycles in the wave-packet to five while maintaining the same separation between the centres of the wave-packets as in time-trace (d), taken from [95].	105
Figure 55: Comparison of auto-correlation curves for different excitation waveforms. Here, A indicates the main lobe region, B indicates the sidelobe regions, and C indicates the background regions, taken from [96].	107
Figure 56: A 300 kHz narrowband tone burst signal, (a) 5-cycle sine wave, (b) FFT of 5-cycle sine wave, (c) 3-cycle sine wave, and (d) FFT of 3-cycle sine wave.....	111
Figure 57: Mexican hat input excitation, (a) waveform when the dilation factor is set to provide a peak frequency of 300 kHz, and (b) FFT of Mexican hat.	112
Figure 58: Broadband chirp excitation, (a) chirp signal from 50 - 500 kHz with a time duration of 200 μ s, and (b) FFT of chirp signal.....	113
Figure 59: Auto-correlation of a linear chirp signal with a frequency range from 50 - 500 kHz and time duration of 200 μ s.....	114
Figure 60: 13-bit Barker code 300 kHz sine wave.	116
Figure 61: 13-bit Barker code 300 kHz sine wave, (a) auto-correlation, and (b) FFT of auto-correlation.	116
Figure 62: Schematic of 2D aluminum plate with piezoelectric sensors (not to scale)..	117
Figure 63: Abaqus FEM interaction of the A_0 mode with a delamination.....	120

Figure 64: FEM response for the 5-cycle sine wave, 3-cycle sine wave, Mexican hat, 13-bit Barker code, and auto-correlation of the linear chirp excitations compared to the respective extracted response from the broadband chirp response.	122
Figure 65: 3-cycle sine wave extracted from a broadband chirp response over a range of frequencies, from 50 kHz (top left) to 500 kHz (bottom right).	124
Figure 66: Input signal extracted from a broadband chirp response over a range of frequencies from 100 kHz (top) to 500 kHz (bottom): 5-cycle sine wave (left), Mexican hat (center), and 13-bit Barker code (right).	125
Figure 67: Auto-Correlation of a linear chirp signal from 50 - 500 kHz (Left) and 200 - 500 kHz (Right).	126
Figure 68: Comparison of five input signals for identification of a delamination (normalized with respect to the A_0 reflection).	128
Figure 69: Close-up of Figure 68 to highlight the A_0 and A_0 delamination reflection....	129
Figure 70: Interaction of S_0 and A_0 modes with a delamination defect.	137
Figure 71: Multiple level decomposition tree (3 levels).	146
Figure 72: Signal decomposition to generate wavelet details (cD) and approximations (cA) [124].	147
Figure 73: db10 wavelet function and scaling function used to determine the wavelet details and approximations, respectively.	149
Figure 74: 2D simulation plots for a delamination defect at multiple depths.	154
Figure 75: 2D simulation plots for a delamination defect at multiple depths – a close-up of the A_0 arrival time.	155

Figure 76: DWT level 5 detail coefficients (2D analysis) for each delamination depth; baseline (top), and ply 1 (second from top) to ply 4 (bottom). 156

Figure 77: Theoretical dispersion curve for an aluminum plate with thickness of 2.06 mm. 157

Figure 78: 3D simulation plots for a delamination defect at multiple depths. 160

Figure 79: 3D simulation plots for a delamination defect at multiple depths - a close-up of the A_0 arrival times. 161

Figure 80: DWT level 9 detail coefficients (3D analysis) for each delamination depth; baseline (top), ply 1 (second from top) to ply 4 (bottom). 162

Figure 81: Model based dispersion curve for a CFRP composite plate with a thickness of 1.60 mm. 164

Figure 82: Experimental plots for a ply 2 and ply 4 delamination defect. 167

Figure 83: DWT level 9 detail coefficients (experimental analysis) for a ply 2 delamination (top) and a ply 4 delamination (bottom). 168

Figure 84: Model based dispersion curve for a CFRP composite plate and a shifted version to match the experimental panel. 169

Figure 85: 2D simulation plots for a 25.4 mm and 50.8 mm delamination defect. 171

Figure 86: DWT level 5 approximation coefficients for a 2D ABAQUS simulation; 25.4 mm delamination (top) and 50.8 mm delamination (bottom). 173

Nomenclature

Acronyms

AE	Acoustic Emission
ALID	Absorbing Layers of Increasing Damping
AoS	Area of Study
AU	Acousto-Ultrasonic
BC	Barker Code
BVID	Barley Visible Impact Damage
CCAA	Canadian Council for Aviation and Aerospace
CFRP	Carbon Fibre Reinforced Polymer
CGSB	Canadian General Standards Board
CWT	Continuous Wavelet Transform
DWT	Discrete Wavelet Transform
EMD	Empirical Mode Decomposition
FBG	Fiber Bragg Grating
FE	Finite Element
FEM	Finite Element Method
FFT	Fast Fourier Transform
FSDT	First-order Shear Deformation Theory
GCC	Golay Complementary Code
MLW	Main Lobe Width
MPD	Matching Pursuit Decomposition
NDT	Non-Destructive Testing
NRC	National Research Council
NRCan	Natural Resources Canada
OEM	Original Equipment Manufacturer
PML	Perfectly Matched Layers
prepreg	Expoy pre-impregnated fibre composite
PZT	Lead Zirconate Titanate

RTM	Resin Transfer Moulding
SHM	Structural Health Monitoring
SNR	Signal to Noise Ratio
SRM	Stiffness Reduction Method

Symbols

a	Dilation coefficient
A_0	Fundamental anti-symmetric Lamb wave mode
b	Translation parameter
B	Chirp bandwidth
c_d	Maximum wave speed in the material
c_k	Scaling coefficient at given translation, k
c_L	Longitudinal velocity
c_T	Transverse wave velocity
C_M	Rayleigh mass proportional damping term
d_{sen}	Distance between the actuator and sensor
d_{33}, d_{31}, d_{15}	Piezoelectric charge constants
E	Young's modulus
f	Frequency
f_0	Center frequency
f_{max}	Maximum frequency
G	Shear modulus
h	Plate half thickness
I	Internal element forces
k	Wavenumber
k_{11}, k_{22}, k_{33}	Relative dielectric constants
l	Length
L^e	Element length
m	Integers representing the order for the wavelet reconstruction
M	Mass matrix
n	Integers representing the order for the wavelet decomposition
N	Number of cycles
P	External applied forces
$S_{m,n}$	Approximation coefficients for the DWT
S_0	Fundamental symmetric Lamb wave mode

SH_0	Fundamental shear horizontal wave
t	Time
Δt	Change in time
T	Wavelet transform
t_{A_0}	A_0 time of arrival
$t_{A_0(Ref)}$	A_0 reflection time of arrival
u	Displacement
\dot{u}	Velocity
\ddot{u}	Accelerations
v	Wave velocity
$v_{A_0(base)}$	A_0 mode velocity of a baseline signal
v_{A_0}	A_0 mode velocity
v_{del}	A_0 velocity across the delamination
α	Attenuation factor
λ	Wavelength
ν	Poisson ratio
ρ	Density
τ	Time shift
ϕ	Scaling function for discrete wavelet transform
ψ	Wavelet function
ψ^*	Complex conjugate of the wavelet function
$\tilde{\psi}$	Reconstructed wavelet function
ω	Angular frequency
ω_c	Cutoff frequency

Chapter 1: Introduction

The use of advanced carbon fibre reinforced polymer (CFRP) composite structures has become widespread in the aerospace industry. The Boeing 787 and the Airbus A350 are composed of 50% and 53% composite materials (by weight), respectively [1], [2]. However, the failure modes for CFRP composites are unique and require new testing and inspection methods when compared to traditional metallic structures. To ensure safe operation, aircraft must be periodically taken out of service and undergo a costly and onerous non-destructive testing (NDT) schedule to detect hidden damage. This often still fails to address damage occurring or growing to potentially dangerous sizes between scheduled inspection intervals. An important step in safely detecting damage or degradation in CFRP materials is to develop technologies that provide real-time structural health monitoring (SHM) to be used on in-service aircraft.

The manufacturing process for composite structures is heavily dependent on the skill of human technicians and is sensitive to environmental conditions at all phases of the process; if any step is incorrectly executed defects will result. Following the human layup process, three important factors in manufacturing include: consolidation pressure (i.e. autoclave pressure, hot-press, or vacuum bag), energy input (i.e. thermal, chemical, or microwave), and time [3], [4]. The proper sequence and application of these factors is critical to ensure a defect-free structure. Figure 1 shows common defects that can occur in CFRP materials. Of the defect types shown in Figure 1, delamination, cracks, and voids are the most concerning because they are prone to in-service growth that can reduce the life of the structure. This type of damage could have contributed to the near-disastrous Air Transat rudder loss [5]. An analysis of the Air Transat rudder loss [5] indicated disbond

and delaminations in the CFRP material of the rudder rapidly propagated in-flight causing failure. Further, the inspection program did not adequately detect the rudder defects that may have been present prior to the actual failure flight. The existence of an SHM system on the fatal American Airlines 587 flight [6] that experienced a vertical stabilizer separation could have made the accident investigation more efficient and cost effective by eliminating initial focus on CFRP damage and failure. It was concluded the failure was the result of unnecessary and excessive rudder pedal inputs that caused loads to exceed the ultimate design strength. From a business perspective, 27% of operating costs are related to maintenance and inspection [7]. Reducing the time an aircraft must be grounded for routine maintenance and inspections will greatly reduce the costs for an airline. Therefore, both increased safety and decreased operating costs are driving factors for an effective SHM system.

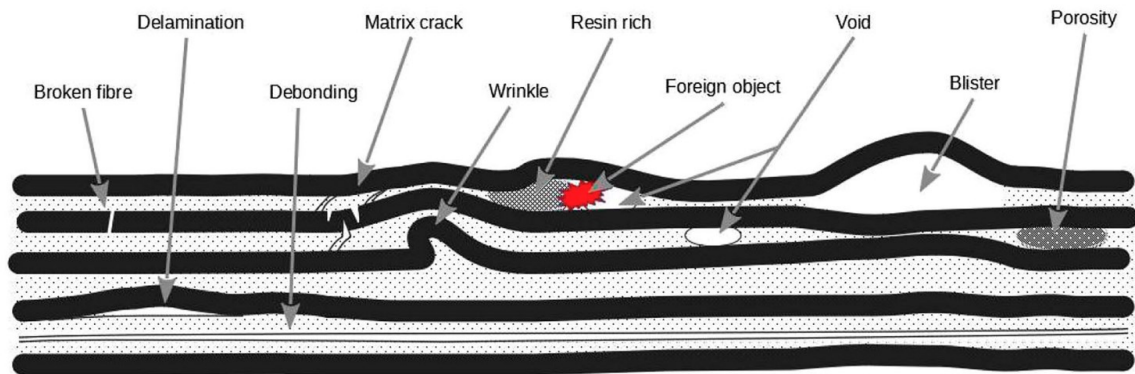


Figure 1: Common defects occurring in CFRP structures, taken from [8].

1.1 Non-Destructive Testing (NDT)

Non-destructive testing plays a vital role for the detection of damage, including visible and hidden defects. NDT is a well-established method to ensure the safety of

aircraft using certified testing methods and technicians. In Canada, Natural Resources Canada (NRCan) is the certification body and technicians are certified as per the Canadian General Standards Board (CGSB-48-9712). Technicians can also become certified with the Canadian Council for Aviation and Aerospace (CCAA) if they meet the CGSG Level II certification requirements. Current NDT methods that are certified by NRCan include: radiographic testing, ultrasonic testing, penetrant testing, magnetic testing, and eddy current testing. Magnetic and eddy current testing are not relevant for CFRP structures because they require a magnetic field be produced within the structure. Penetrant testing is rarely used for CFRP structures because the penetrant acts as a contaminant as it is absorbed into surface cracks or voids. Additional NDT methods are often used in the aerospace industry and certified by international standards or specific manufacturers. These additional methods include: visual inspection, sonic or tap testing, thermography, and laser shearography.

Despite the requirement of NDT to be used for regular inspections, it has many disadvantages that make it onerous and costly, these include: specific ground-based inspection intervals, removal of parts for inspection, labour intensive, and no information about the health of the structure between inspection intervals. As the process to ensure the structural integrity and safety of the aircraft changes from an inspection based process to continuous health monitoring, first, a complimentary approach between NDT and SHM is required. This would involve the traditional and certified NDT inspections coupled with SHM to recognize any damage occurring between scheduled inspections and helping technicians quickly identify the location of defects. As a specific SHM method becomes

proven, it can then be used to transition from inspection based maintenance to condition based maintenance.

1.2 Structural Health Monitoring (SHM)

SHM extends traditional NDT techniques to an on-board, in-service condition monitoring technique. This requires a shift from the labour intensive and bulky setup required for NDT to continuous or semi-continuous monitoring with small, lightweight equipment that can operate in a noisy service environment. An important component of SHM are the sensors and how they are incorporated into the structure. To date, research has focused on the following SHM techniques: fiber optics, acoustic emission, acousto-ultrasonic, comparative vacuum monitoring, laser Doppler vibrometry, and strain gauges. Table 1 was created to provide a comparative overview of the different SHM techniques.

Table 1: Comparison of SHM techniques for CFRP structures.

SHM Method	Passive / Active	Inspection Area	Relative Weight	Installation Features	Relative Cost	Limitations
Fiber Optics	Active	Large	Light	Fragile	\$\$\$	Fragile & expensive
Acoustic Emission	Passive	Large	Light	Durable	\$	Passive 'listening' – potential to miss damage event
Acousto-Ultrasonic	Active	Large	Light	Durable	\$	Signal processing
Comparative Vacuum Monitoring	Passive	Localized	Light	Durable	\$\$	Localized area & surface defects only
Laser Doppler Vibrometry	Active	Point-by-point	Heavy	Fragile	\$\$\$	Heavy, expensive, equipment set up, ground based
Strain Gauges	Passive	Localized	Light	Durable	\$	Localized area, no classification of defects

Fiber optic sensors for sensing strain, temperature, and certain types of damage has shown promising results [9][10][11]. The Fiber Bragg Grating (FBG) sensor has been one of the most widely used fiber optic sensors for composite structures [12]. Changes in strain or temperature cause the spacing of the Fiber Bragg Grating to change, thus altering the peak reflected wavelength. Despite the promising results for optic sensor, the major drawback preventing widespread use, include: 1) installing or embedding the fragile optical sensors into the CFRP structures, and 2) expense of both the optical fibers and supporting equipment.

Acoustic emission (AE) refers to the elastic stress waves created in the material because of static or dynamic stress. Operational damage or damage growth (e.g., delamination growth, fiber breakage, or matrix cracking) causes a rapid release of energy generating transient AE waves [13][14]. The stress waves generated are commonly detected with piezoelectric sensors. The main disadvantages associated with the AE method, include: 1) it is a passive ‘listening’ technique so if an AE event is missed it will go undetected, and 2) noisy operational environment have the potential to mask AE events.

Acousto-ultrasonic (AU) sends acoustic waves through the structure using an actuator and detects the signal with sensors. The ability to generate a signal creates an active technique that can inspect the structure at any point in time. Lamb wave propagation is a common wave type for AU inspections. The difficulties associated with Lamb wave propagation is the multiple wave modes generated and the associated signal processing – this will be discussed later in the chapter.

Comparative vacuum monitoring sensors are bonded to the surface of the structure and contain fine channels of alternating galleries under vacuum and at atmospheric

pressure [15][16]. If a crack or other damage is initiated in the region, air will flow from the atmospheric galleries to the vacuum galleries; this pressure change is monitored in real time. The limitations of this method include a highly localized inspection region and it may only detect defects that are close to the surface.

Laser Doppler vibrometry measures the Doppler shift of the reflected laser beam resulting from vibrations generated in the structure. Displacement amplitude and frequency measurement are collected and used for analysis. This method has been frequently researched for CFRP aerospace structures using Lamb waves generated with a piezoelectric actuator and measurements made with the laser Doppler vibrometry [17][18][19]. This technique allows for non-contact inspection, however, the bulky equipment, precision setup, and point-by-point inspection area limit this technique to ground based inspections.

Strain gauges have been widely used in SHM with a range of applications [10]. The resistance of the strain gauge changes in response to strain in the structure. This provides insight in structure loading, fatigue, and localized damage. However, the ability to inspect large areas and distinguish between a range of damage types is limited.

For an SHM system to effectively monitor aerospace structures it must meet the following criteria:

- Large inspection area,
- Low power requirements,
- Lightweight,
- Securely attach to aerospace structures,
- Automatic,
- High probability of detection,
- Inspection of areas that are typically inaccessible,

- Meet civil aviation airworthiness requirements, and
- Withstand rapid changes in environmental and loading conditions.

A Lamb wave based SHM system was selected for further research in this thesis because Lamb waves have the potential to achieve the above criteria.

Further, there are four important objectives of an SHM system: 1) recognition, 2) identification, 3) severity, and 4) location. First and most importantly, the system must be able to recognize the presence of a defect. Next, identifying the type of defect (e.g., porosity versus delamination) and the severity provides important information about necessary action that must be taken. Finally, knowing the location of the defect allows maintenance personnel to quickly find, assess, and repair the defect or replace the structure.

Finally, a holistic approach to SHM would provide a complete understanding of the health of the structure, improving safety, reducing traditional NDT inspection costs, and reducing maintenance costs. A holistic approach covers the full life cycle of a part; for CFRP structures this includes three key components: *in-situ* cure monitoring, manufacturing inspection, and in-service monitoring.

1.3 Fundamental Principles of Lamb Waves

Lamb waves have demonstrated great potential for SHM applications because of their long-range propagation characteristics, even in materials with high attenuation such as CFRP. This allows fast inspection of large structural areas. Lamb waves are composed by the superposition of two types of bulk waves: longitudinal and shear waves (Figure 2 and Figure 3) and propagate in thin plates along the upper and lower surfaces. Two types of Lamb wave modes exist: symmetric (S_n), and anti-symmetric (A_n), as seen in Figure 4.

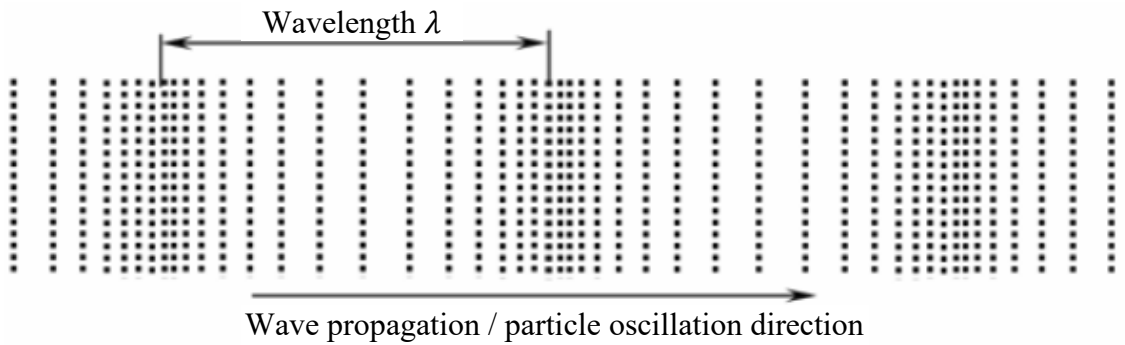


Figure 2: Longitudinal wave, taken from [20].

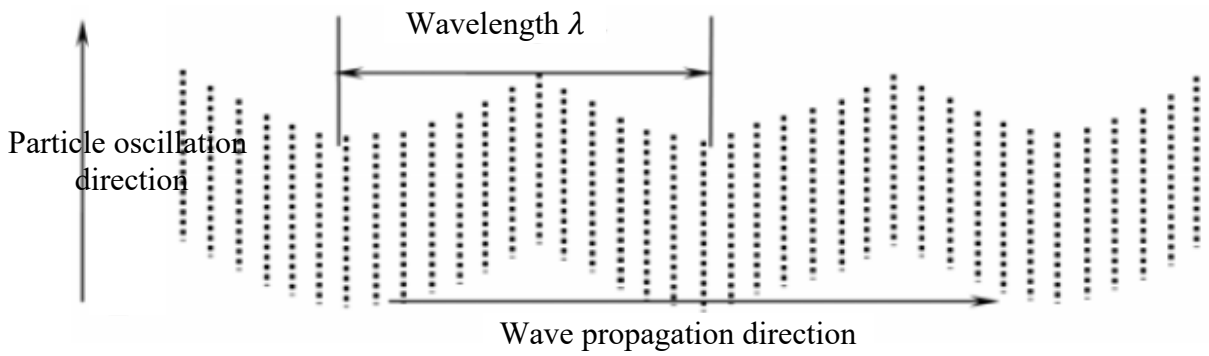


Figure 3: Shear wave, taken from [20].

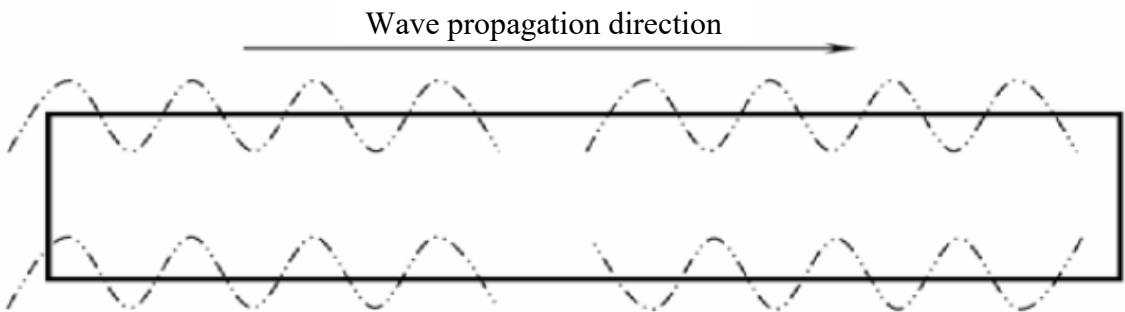


Figure 4: Lamb wave in a thin plate depicting two different mode types: left - anti-symmetrical, and right - symmetrical, taken from [20].

The characteristic Lamb wave equations for an isotropic medium are described by the following two equations:

Symmetric Lamb wave:

$$\frac{\tan(qh)}{\tan(ph)} = \frac{-4k^2pq}{(q^2 - k^2)^2} \quad (1)$$

Anti-symmetric Lamb wave:

$$\frac{\tan(qh)}{\tan(ph)} = \frac{-(q^2 - k^2)^2}{4k^2pq} \quad (2)$$

where,

$$p^2 = \left(\frac{\omega^2}{c_L^2} - k^2 \right) \quad q^2 = \left(\frac{\omega^2}{c_T^2} - k^2 \right) \quad k = \frac{\omega}{c_{phase}}$$

h is the plate half thickness, ω is the angular frequency, k is the wave number, c_T is the transverse wave velocity, and c_L is the longitudinal velocity. The velocities can be further described as:

$$c_T^2 = \frac{\mu}{\rho} \quad c_L^2 = \frac{(\lambda + 2\mu)}{\rho} \quad (3)$$

where, ρ is density, and μ and λ are the Lamé's constants defined as:

$$\mu = \frac{E}{2(1 + \nu)} \quad (4)$$

$$\lambda = \frac{E\nu}{(1 - 2\nu)(1 + \nu)} \quad (5)$$

where, μ is known as the shear modulus, E is Young's modulus, and ν is Poisson ratio.

Given a certain frequency-thickness product the phase velocity (c_{phase}) can be solved for in Equations (1) and (2) producing the dispersion curves seen in Figure 5. For a given material the Young's modulus, Poisson ratio, and density are known. However, for an n-layered anisotropic composite material the solution is much more complex and is solved using the partial wave technique by implementing the 3-D linear elasticity theory using a Global Matrix or Transfer Matrix method. This was the focus of Pant's PhD thesis [21] and works described in [22][23][24].

Each mode type (symmetric and anti-symmetric) has an infinite number of mode orders ($n = 0, 1, 2, \dots$) where the order represents the number of inflection points across the plate thickness. Each mode and mode order offers unique benefits for damage detection including the size of area that can be inspected and sensitivity. Three important factors that affect the selection of the optimal wave mode, mode order, and frequency include: 1) dispersion, 2) attenuation, and 3) defect characteristics (i.e., size, location, and type).

Wave dispersion is when the velocity of propagation is dependent on frequency – waves with different wavelengths travel at different velocities. Two problems associated with wave dispersion are a reduction in amplitude and loss of resolution. To reduce these

effects an understanding of the dispersion characteristics of Lamb waves can be obtained from dispersion curves for the material of interest (Figure 5). From the dispersion curves in Figure 5, it can be seen that the fundamental modes (S_0 and A_0) are almost non-dispersive for lower frequency-thickness values. In addition, selecting the signal frequency below the first cutoff frequency ensures only two wave modes will be present in the received signal, making the results easier to interpret and simplifying feature extraction.

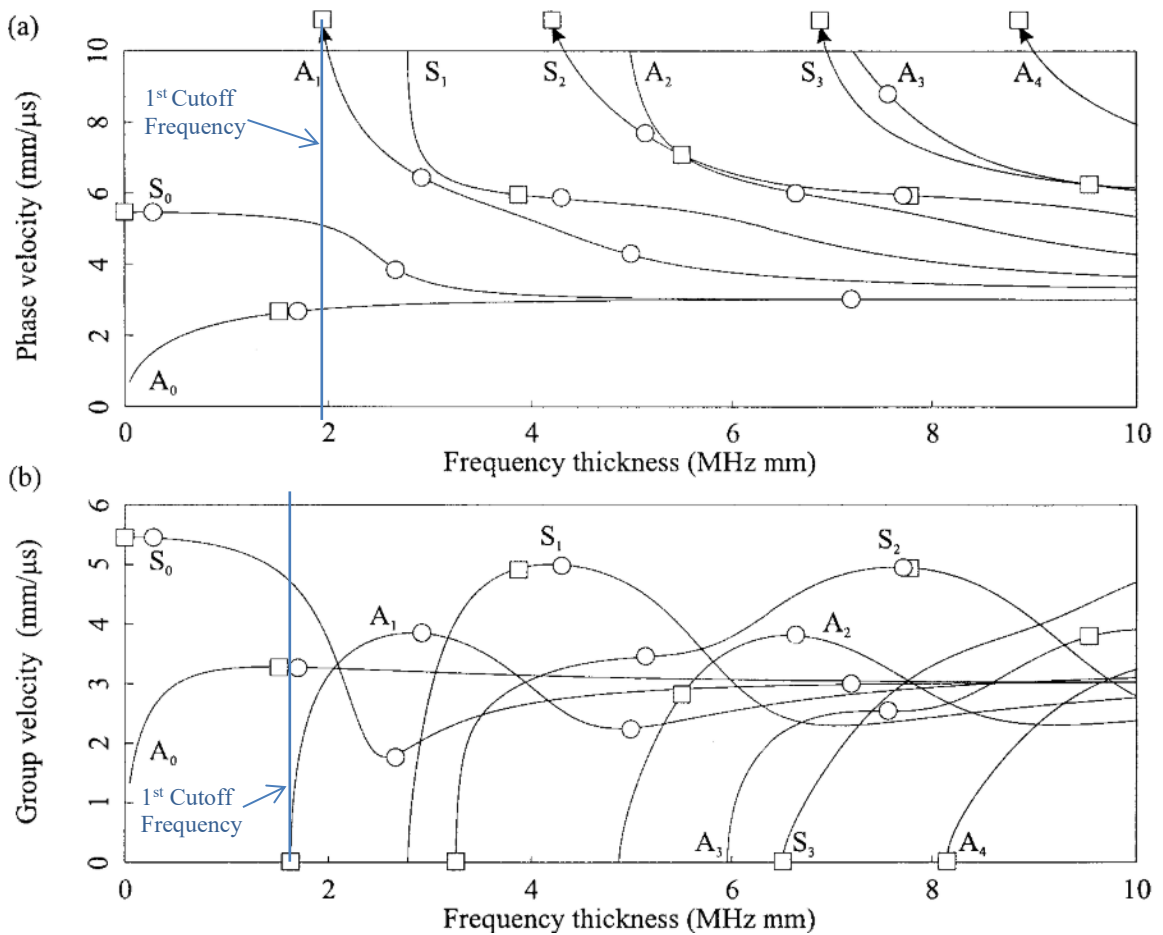


Figure 5: Dispersion curves for a steel plate, a) Phase velocity, and b) Group velocity, taken from [25].

Attenuation is the decrease in signal amplitude with propagation distance. A low level of attenuation is necessary for long range SHM using Lamb waves. Willcox *et al.*

[25] had identified five mechanisms that contribute to Lamb wave attenuation: 1) dispersion (as discussed above), 2) beam divergence, 3) material damping, 4) scattering, and 5) leakage into surrounding media. Lamb waves have been demonstrated to have a low level of attenuation in an 8-ply CFRP composite structure as indicated by the propagation distance of 1700 mm and 85 mm for the S_0 and A_0 mode, respectively, before a 10% decrease in signal amplitude is experienced [20]. The anti-symmetric mode is more susceptible to attenuation because of the out-of-plane particle displacement, which causes energy leakage into the surrounding media.

The selection of wave mode, mode order, and frequency can increase the likelihood of identifying potential defects or damage of interest. For example, the anti-symmetric mode has been found to be most effective at identifying surface defects because of the out-of-plane displacement and the resulting loss of energy when a surface defect is present [26] [27]. Specific types of defects are also easier to detect with certain wave modes, for example the A_0 mode is able to detect delamination and transverse ply cracks better than the S_0 mode [28]. Further, to ensure good resolution a wavelength of half the acceptable defect size should be selected. Higher resolution is easier to achieve with the anti-symmetric mode because it has a smaller wavelength when compared to the symmetric mode at a given frequency or mode order.

Selecting and activating a single desired wave mode is very difficult. Each mode type has an infinite number of mode orders - even at a single activation frequency multiple modes and mode orders can be activated as shown in the dispersion curves (Figure 5). The solution in most cases is to operate in a frequency-thickness range below the first cut-off frequency, which ensures that only the S_0 and A_0 modes are activated.

The proposed research will use piezoelectric lead zirconate titanate (PZT) transducers to activate Lamb waves. The size and the driving frequency of the PZT transducer will be selected to improve the tuning of the Lamb mode being activated [29]. Research has shown that specially designed PZT transducers can activate a single Lamb mode, but the proposed research will use off-the-shelf actuators and sensors. Other methods to suppress unwanted mode activation includes a dual PZT actuator arrangement with PZTs bonded directly above and below each other on the part [30] or bonded at a specific distance (multiple of the mode wavelength) from each other [31] with a circuit coordinating the activation of each PZT.

Lamb waves have the potential to be a key part of an effective, practical SHM system; however, the selection of the optimal Lamb wave properties including mode type, mode order, and frequency is very complex. This is further complicated by the many variables associated with composite aerospace structures, including:

- Ply orientation
- Number of plies or thickness
- Resin type
- Fibre type (carbon, glass, aramid)
- Fibre orientation and/or weave (unidirectional, plain weave, twill weave, etc.)
- Manufacturing process

These variables in addition to dispersion, attenuation, and defect characteristics must be consider before Lamb waves can be used effectively. The current field of Lamb wave research has been limited mostly to in-service damage of composite panels with simple geometries. This fails to address the full life cycle of the CFRP structure and the ability to recognize and identify different defect types, especially manufacturing related defect types.

1.4 Research Objective

To utilize the long distance propagation characteristics of Lamb waves, this research will develop a Lamb wave based SHM system capable of monitoring a CFRP structure from manufacturing to end-of-life. This will extend the existing SHM research focusing on in-service defects to a holistic approach, including: cure monitoring, manufacturing inspection, and in-service monitoring. This holistic approach will improve the quality and safety of CFRP aerospace structures by fully integrating sensors during the curing process. By focusing on manufacturing inspection and manufacturing specific defects, the author's prior industry experience in composite manufacturing will be utilized, while extending the limited body of knowledge in this research area. This will be achieved by focusing on the following research objectives:

1. Design a manufacturing process that incorporates piezoelectric sensors into the CFRP structure during the curing process.
2. Identifying unique features associated with three types of manufacturing defects: delaminations, porosity, and foreign objects.
3. Quantifying the severity of a defect by determining the length and depth of a delamination defect. This will also include identifying the optimal excitation signal to interrogate a delamination defect.

1.5 Research Limitations

The proposed research will be limited to an active ground based SHM system. The concept of this type of SHM system is to generate Lamb waves to interrogate the structure between flights, on the ground, when environmental and loading conditions are controlled.

This is the necessary first step in applying SHM to aerospace structures to gain acceptance from the industry, OEMs, and regulatory bodies.

1.6 Dissertation Overview

This thesis research utilizes both numerical and experimental results to determine the interaction of Lamb waves with CFRP defects.

Chapter 2 provides a unique manufacturing method to co-cure piezoelectric sensors to the surface of CFRP structures. This was achieved using an oven cured manufacturing process with prepreg CFRP material. Finally, an experimental comparison of co-cured and bonded piezoelectric sensors was completed.

In Chapter 3, a finite element model was created to identify the unique features associated with a delamination, porosity, and foreign object defects. A comparison of the finite element model and experiment results was performed using a continuous wavelet analysis.

Chapter 4 compares five different excitation signals to determine the optimal signal to quantify a delamination defect. The five signals analyzed included: 5-cycle sine wave, 3-cycle sine wave, Mexican hat, 13-bit Barker coded sine wave, and an auto-correlated linear chirp.

Chapter 5 quantifies the severity of a delamination defect by calculating the length and depth. This is performed using a Mexican hat excitation signal with a multiple level discrete wavelet decomposition analysis. Results were presented for 2D and 3D finite element models, and experimental tests.

Finally, Chapter 6 and 7 present a general discussion and overall conclusions, respectively. In addition, a statement of research contributions and future recommendations are provided.

Chapter 2: Manufacturing Process to Integrate Sensors

The successful development of SHM for composite structures includes three important areas: 1) sensor development, 2) signal processing and software development, and 3) manufacturing structures with integrated sensors. The first two areas have been widely researched [28]; however, the method to integrate sensors into CFRP structures has seen less research activity. The two primary methods for sensor integration are: 1) bonding the sensor to the surface of the CFRP structure after it is cured, or 2) embedding the sensor into the material layers prior to curing. The objective of this thesis is to investigate an additional and unique manufacturing process that is a hybrid between embedding and bonding. The proposed method integrates the piezoelectric sensor onto the surface of the CFRP structure with a co-curing method. This will help provide a holistic approach to SHM, which includes: *in-situ* cure monitoring, manufacturing inspection, and in-service monitoring. Additional advantages that could potentially be realized with a co-curing method, include: precise and repeatable sensor placement, easy wire management during manufacturing, elimination of bonding adhesive layers and the associated extra manufacturing step, prevention of short circuiting the electrodes, and elimination of any negative mechanical performance effects on the host structure.

Sensors embedded between material layers are more sensitive to damage detection [32] [33], protect the sensor from environmental factors, and provide a holistic approach to SHM. However, the primary concern with embedded sensors is the potential negative effects on the strength of the CFRP structure. The current literature has conflicting results regarding the effects of embedded sensors on the strength of CFRP structures. Lin and Chang [34] did a comprehensive study on embedding piezoelectric sensors using a

SMART Layer and did not find any strength reductions. The SMART layer is a sheet of polyimide film with piezoelectric sensors embedded in the sheet using a printed circuit technology and is designed to be inserted into the CFRP laminate as an extra individual ply. The testing performed by Lin and Chang [34] included: flatwise tension, double lap shear, short beam shear, quasi-static impact, and plate compression. Similarly, Mall [35] and Arellano *et al.* [36] did not find a reduction in ultimate strength or Young's modulus while performing tensile tests with specimens with embedded sensors.

Alternatively, small reductions in strength were found in several studies. Masmoudi *et al.* [37] reported a 8% reduction in flexural strength during a three-point bend test when a piezoelectric sensor was embedded in a cross-ply laminate, but did not find a reduction in strength when the same test was performed on a unidirectional laminate. Chilles *et al.* [38] performed a four-point bend test on specimens that had been produced with two different methods for embedding the piezoelectric sensor: 1) a formed method, which inserts the sensor directly between plies, and 2) a ply cutout method, which cuts three plies to accommodate the sensor. Chilles *et al.* [38] reported a 4% reduction in strength for the formed method and no reduction for the ply cutout method. Xiao *et al.* [39] embedded a thin film lithium energy cell (40mm x 25mm x 0.1mm) into a carbon fiber 8-ply laminate and found a 5.2-6.4% reduction in tensile strength. However, Xiao *et al.* [39] observed a delamination was initiated at only 40% of the failure load. Ghezzi *et al.* [40] also noted that damage was initiated at the embedded sensor interface location resulting in a 25-33% lower stress level when compared to a specimen without an embedded sensor.

The size of the embedded sensor can significantly affect the strength of the composite structure. Masmoudi *et al.* [33] demonstrated a 4% reduction in strength for a 5mm diameter piezoelectric sensor and a 13% reduction in strength for a 10mm piezoelectric sensor when performing a three-point bending test. Javdanitehran *et al.* [41] embedded 10 x 10 x 0.5 mm and 25 x 25 x 0.5 mm printed circuit board in a glass fibre composite panel and found that sensor size, laminate thickness, and ply orientation angle at the interface with the sensor affected tensile and three-point bend test results. Warkentin *et al.* [42] found a 15% decrease in ultimate strength when a 9.5 x 12.7 x 0.5 mm electronic chip was embedded in graphite/epoxy laminate. Duffy *et al.* [43] reported the largest decrease in strength as the result of an embedded piezoelectric sensor, including: 31-47% reduction for four-point bending tests, 19-29% reduction for short beam shear tests, and a 83-85% reduction in flatwise tensile tests.

In addition to identifying the effects of piezoelectric sensors on the strength of the CFRP structure, the manufacturing method to embed piezoelectric sensors needs to be easy and repeatable to gain industry-wide acceptance. The SMART layer, manufactured by Acellent Technologies Inc., is one of the most promising techniques and is currently being tested on actual aerospace structures. The SMART layer has also been demonstrated to work for resin transfer moulding (RTM) and filament winding manufacturing processes [44]. However, the addition of a full ply of material (polyimide film with piezoelectric sensors) could add significant weight to the structure. In addition, electrical connection for parts that need to be trimmed must be solved because currently the wires exit the edge of the structure. Chilles *et al.* [45] designed a piezoelectric sensor with an inductance coil, which allows for the sensor to be controlled without any connecting wires. This is a good

solution for manufacturing; however, the embedded sensor and coil is very large with a diameter of 50mm. To embed sensors with connecting wires, Ghasemi-Nejhad *et al.* [46] proposed three different methods: cutout holes, molded-in holes, and embedded wires, and suggested the embedded method is superior when considering six different factors. Finally, Shukla and Vizzini [47] created an “interlacing” manufacturing method to reduce the negative strength effects from embedding sensor. The “interlacing” stacks plies above and below the sensor with staggered cutouts to limit the resin rich areas surrounding the sensor edges.

The wide range of results related to embedded sensors indicates changes in strength are highly dependent on many variables, including: the size of the sensor, the size of resin rich areas, type of embedding method, embedding location, and the design of the composite structure. The next generation of aircraft should have sensors designed into the CFRP structures from the beginning to ensure an effective and safe SHM solution. However, for current aircrafts and replacement parts being built the proposed co-cured manufacturing technique does not modify the design of the structure or have the potential to affect the material properties. The objective of this chapter is to establish a method to co-cure piezoelectric sensors to the surface of CFRP flat panels. The generated waveform shape, signal amplitude, and wave velocity of a co-cured sensor will be compared to a bonded piezoelectric sensor.

2.1 Methods

This section describes the materials, manufacturing process, and experimental procedure used for testing CFRP panels with co-cured and bonded piezoelectric sensors.

2.1.1 Materials

The CFRP panels were manufactured with an out-of-autoclave carbon fibre and epoxy prepreg material (AX-6111-C), manufactured by Axiom Materials Incorporated. The AX-6111-C material is made with unidirectional carbon fibre (150 g/m^2) embedded in a toughened epoxy resin system. The CFRP panels for this experiment were $500 \times 200 \times 1.2 \text{ mm}$ and consisted of 8-ply in a symmetric and quasi-isotropic layup, $[0/90/+45/-45]_s$. Initially, the panels were manufactured slightly larger and trimmed to the final dimensions using a tile saw with a diamond cutting blade.

The piezoelectric sensors were made with a lead zirconate titanate ceramic material, by APC International Limited, model number 70-3000, as shown in Figure 6. Model number 70-3000 was selected because it was the smallest, ‘off the shelf’ PZT available from APC International Limited. With a diameter of 6.35 mm and thickness of 0.254 mm, the resonance frequency was 2.0 MHz and 312 kHz in the thickness and radial directions, respectively. Further, this piezoelectric sensor was previously used in Pant’s PhD thesis research with acceptable results [21].



Figure 6: Piezoelectric sensor with wrap-around electrode pattern, taken from [48].

The PZT material was an 850 Navy type II equivalent with a wrap-around electrode pattern. The piezoelectric properties are shown in Table 2, where the charge constants are represented by d_{33} , d_{31} , and d_{15} , and the relative dielectric constant are given by k_{11} , k_{22} , and k_{33} .

Table 2: Piezoelectric properties.

Property	Value
Diameter	6.35 mm
Thickness	0.254 mm
Material Type	850 Navy II
Capacitance	2000 pF
Curie Temperature	360°C
$E_{11} = E_{22}$	63 GPa
E_{33}	54 GPa
$G_{13} = G_{23}$	24 GPa
G_{12}	29 GPa
$\nu_{12} = \nu_{31} = \nu_{32}$	0.31
d_{33}	400×10^{-12} C/N
d_{31}	-175×10^{-12} C/N
d_{15}	590×10^{-12} C/N
$k_{11} = k_{22}$	1900
k_{33}	1320
ρ	7600 kg/m ³

Two sensors were placed 400 mm apart on the surface of the CFRP panel in a ‘pitch-catch’ configuration, as shown in Figure 7. The ‘pitch-catch’ configuration has one piezoelectric acting as an actuator and a second piezoelectric acting as a sensor – this maximized the inspection area of each piezoelectric sensor pair. This thesis uses the term “sensor” for both the piezoelectric sensor and piezoelectric actuator to indicate it is the same device, which can perform both the sensing and actuating functions.

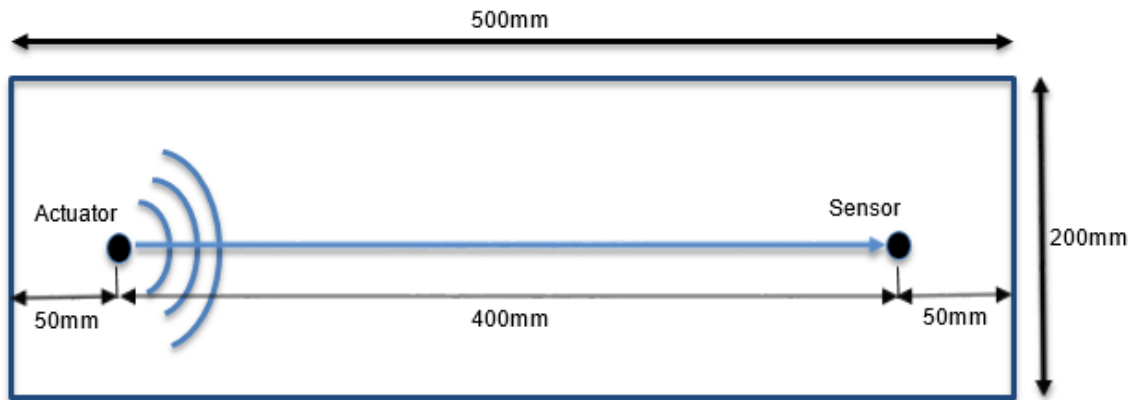


Figure 7: Schematic of CFRP panel with piezoelectric sensors (not to scale).

2.1.2 Manufacturing Process

To manufacture the CFRP panel with co-cured piezoelectric sensors on the surface, a flat aluminum tool was customized with two flat bottom holes designed to hold the sensors during the layup and curing steps. The flat bottom holes were machined to create a transition fit with the sensors to securely hold the sensors in place. The holes were drilled 400 mm apart resulting in the exact placement of the piezoelectric sensors, see Figure 8. Two additional small through holes were drilled between the flat bottom hole and the back of the aluminum tool to install spring pins, see Figure 9.

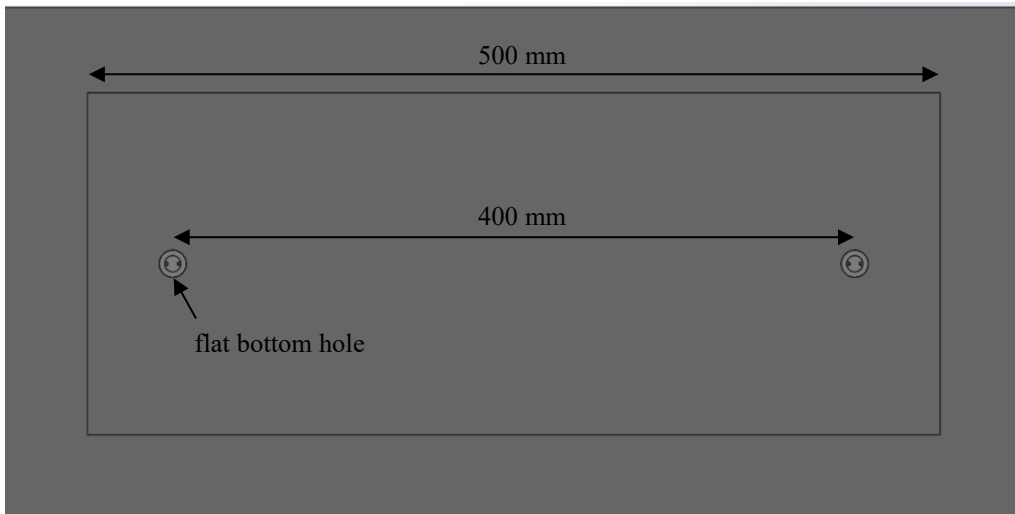


Figure 8: Manufacturing tool to co-cure piezoelectric sensors.

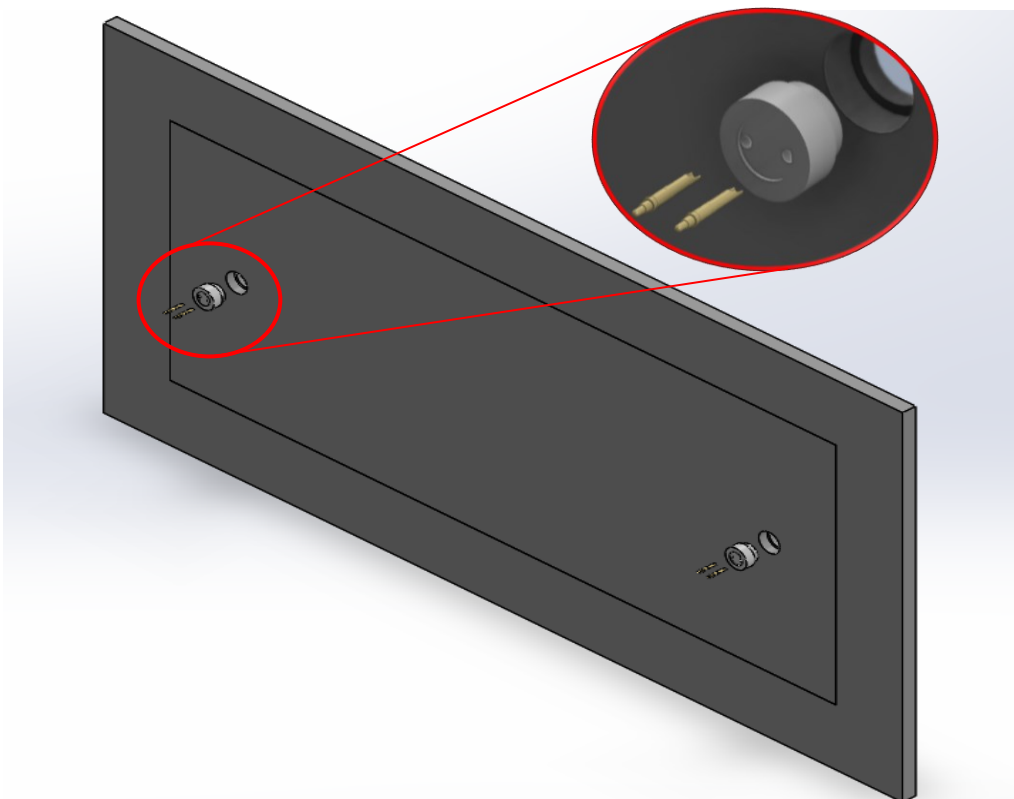


Figure 9: Isometric view of manufacturing tool with spring pins shown.

The spring pins were manufactured by Mill-Max Manufacturing Corporation (Mill-Max model number 0973-0-15-20-77-14-11-0) with a height of 14.6 mm and diameter of 1.8 mm, see Figure 10. These spring pins provided a temporary electrical connection with the piezoelectric sensor to allow for *in-situ* cure monitoring, without the burden of wires being attached to the sensor/structure during the curing process or for the remainder of the manufacturing processes (e.g., trimming, inspection, assembly, and finishing).



Figure 10: Electrical spring pins connectors (Mill-Max, model # 0973-0-15-20-77-14-11-0).

To perform the material layup step, the piezoelectric sensors were placed into the flat bottom hole in contact with the spring pins to create an electrical connection. After the sensors were in place, the CFRP plies were placed, by hand, in the desired sequence $[0/90/+45/-45]_s$, followed by an aluminum caul plate to ensure a good surface finish on both the top and bottom surfaces of the structure. Finally, the connecting wires were sealed to the backside of the aluminum tool using vacuum bagging tape (Figure 11).

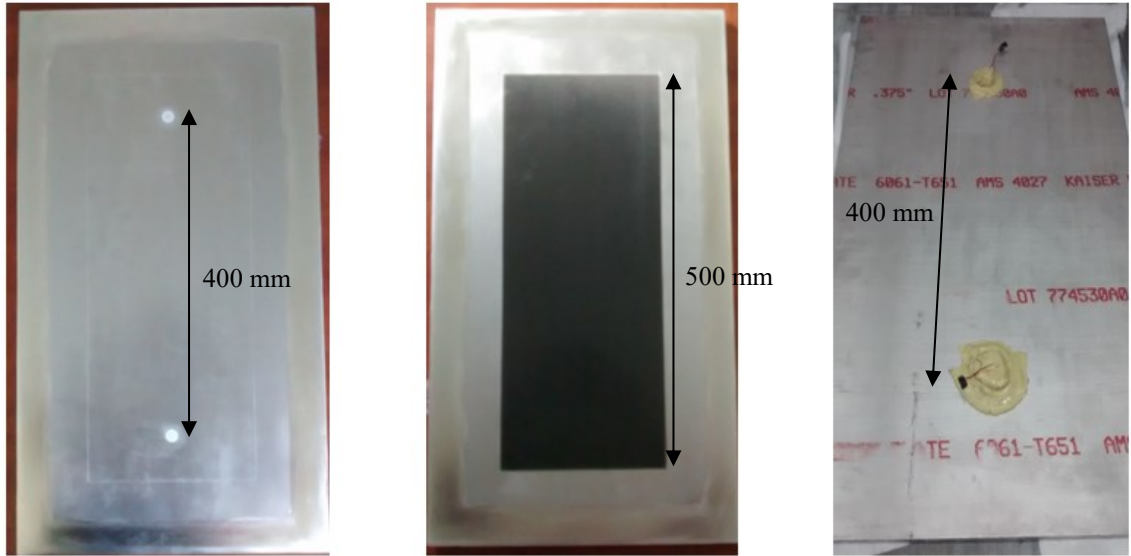


Figure 11: The layup sequence for a CFRP panel with co-cured piezoelectric sensors. Left: aluminum tool with piezoelectric inserted into machined positioning holes, Center: composite laminate layup, Right: connecting wires sealed with vacuum bagging tape.

After the layup step was completed, the part was vacuum bagged and tested to ensure a good seal. A vacuum gauge pressure of 28.0 inHg (94.8 kPa) was applied, and the panel was debulked for 1 hour under vacuum (Figure 12). The panel was cured in an oven under vacuum pressure, according to the manufacturer's instructions, at 121°C for 60 minutes with a ramp rate of 1°C/minute. The curing temperature was much lower than the Curie temperature of the piezoelectric sensor (360°C), avoiding any potential depolarizing effects of the sensors.

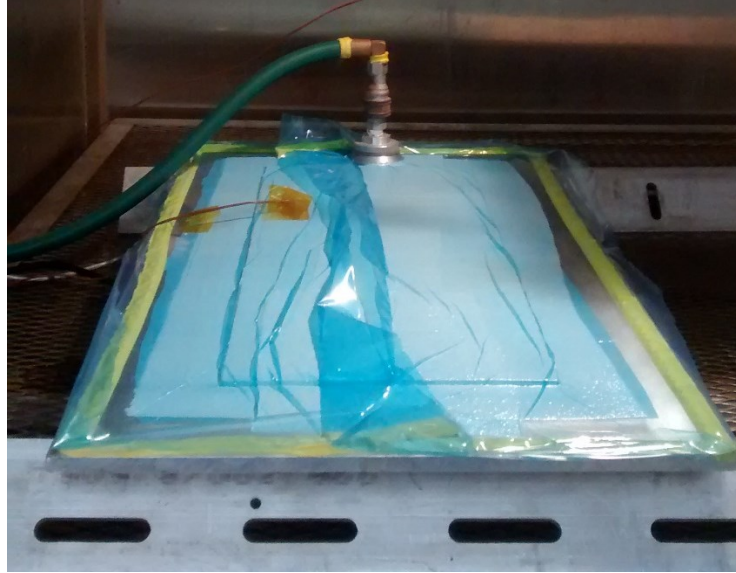


Figure 12: CFRP panel vacuum bagged and placed inside an oven.

The panel with bonded piezoelectric sensors was manufactured using the same process as described above, except a standard aluminum tooling plate was used instead of one with flat bottom holes. After the CFRP panel was cured and allowed to cool, the sensors were bonded using a Loctite super glue (Ultra Gel Control), as recommended by Mustapha and Ye [49]. To ensure precision placement of the sensors, the co-cured CFRP layup tool with flat bottom holes was used as an alignment template. The sensors were placed into the flat bottom holes, a small amount of Loctite super glue (cyanoacrylate) was applied to cover the entire surface of the sensors, then the cured CFRP panel was aligned and pressed onto the piezoelectric sensors. The cyanoacrylate glue was cured at room temperature for 24 hours, as per the manufacturer's instruction, before testing was completed. Figure 13 shows a finished CFRP panel with bonded sensors.

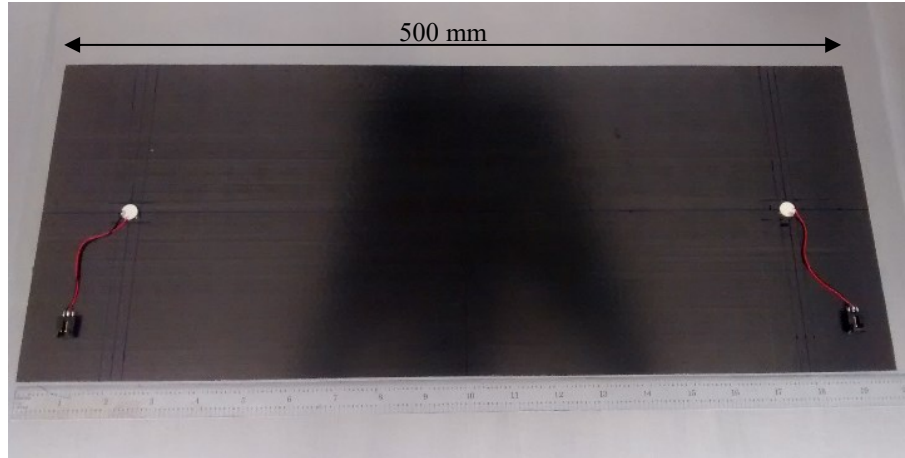


Figure 13: CFRP panel with bonded piezoelectric sensors.

2.1.3 Experimental Procedure

The experimental setup (Figure 14) generated a Lamb wave signal using a Picoscope function generator (model 3403D). The Lamb waves were activated using a 3-cycle sine wave with a hanning window that was generated using Matlab and uploaded to the Picoscope. A Krohn-Hite wideband power amplifier (model 7602) was used to amplify the signal to +/- 30 volts for activation of the piezoelectric sensors. Signal acquisition was achieved using the Picoscope portable oscilloscope (model 3403D) and the Picoscope software (Picoscope6). Additional signal processing was completed using the Matlab Signal Processing toolbox.

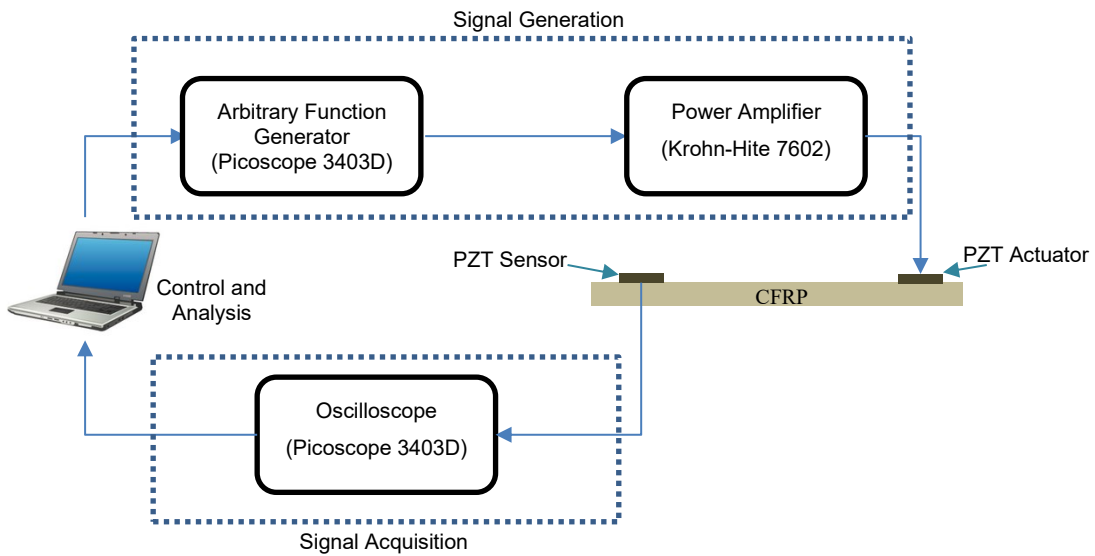
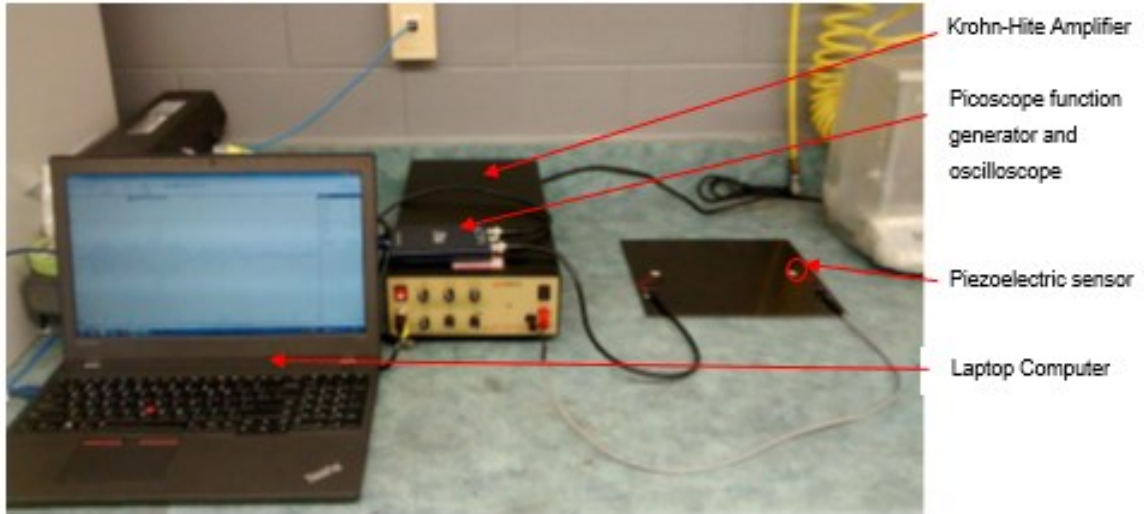


Figure 14: Experimental setup to generate and collect Lamb wave signals.

2.1.4 Signal Processing

The raw signal was filtered in Matlab using a lowpass Butterworth filter with an amplitude response defined by:

$$|H(j\omega)| = \frac{1}{\sqrt{1 + \left(\frac{\omega}{\omega_c}\right)^{2n}}} \quad (2)$$

where ω is the frequency, ω_c is the cutoff frequency, and n is the filter order.

Further analysis was completed by obtaining the analytic signal:

$$z(t) = x(t) + jH[x(t)] \quad (3)$$

where $z(t)$ is the analytic signal, $x(t)$ is the filtered signal, and $H[x(t)]$ denotes the Hilbert transform, defined by:

$$H[x(t)] = \frac{1}{\pi} \int_{-\infty}^{\infty} \frac{x(\tau)}{t - \tau} d\tau \quad (4)$$

The peak values and threshold levels of the analytic signal were used to compare the co-cured and bonded waveforms.

2.2 Experimental Results

The objective of the research described in this chapter is to demonstrate a co-curing manufacturing method capable of a holistic approach to SHM, while still providing similar results to the traditional method of bonding piezoelectric sensors to a CFRP structure. In this regard, a comparison of waveform shape, signal amplitude, and wave velocity for the co-cure and bonded piezoelectric sensors was completed.

Figure 15 shows the signal response for CFRP panels with co-cured and bonded piezoelectric sensors to a 50, 75, 100, and 150 kHz 3-cycle sine wave with a hanning window.

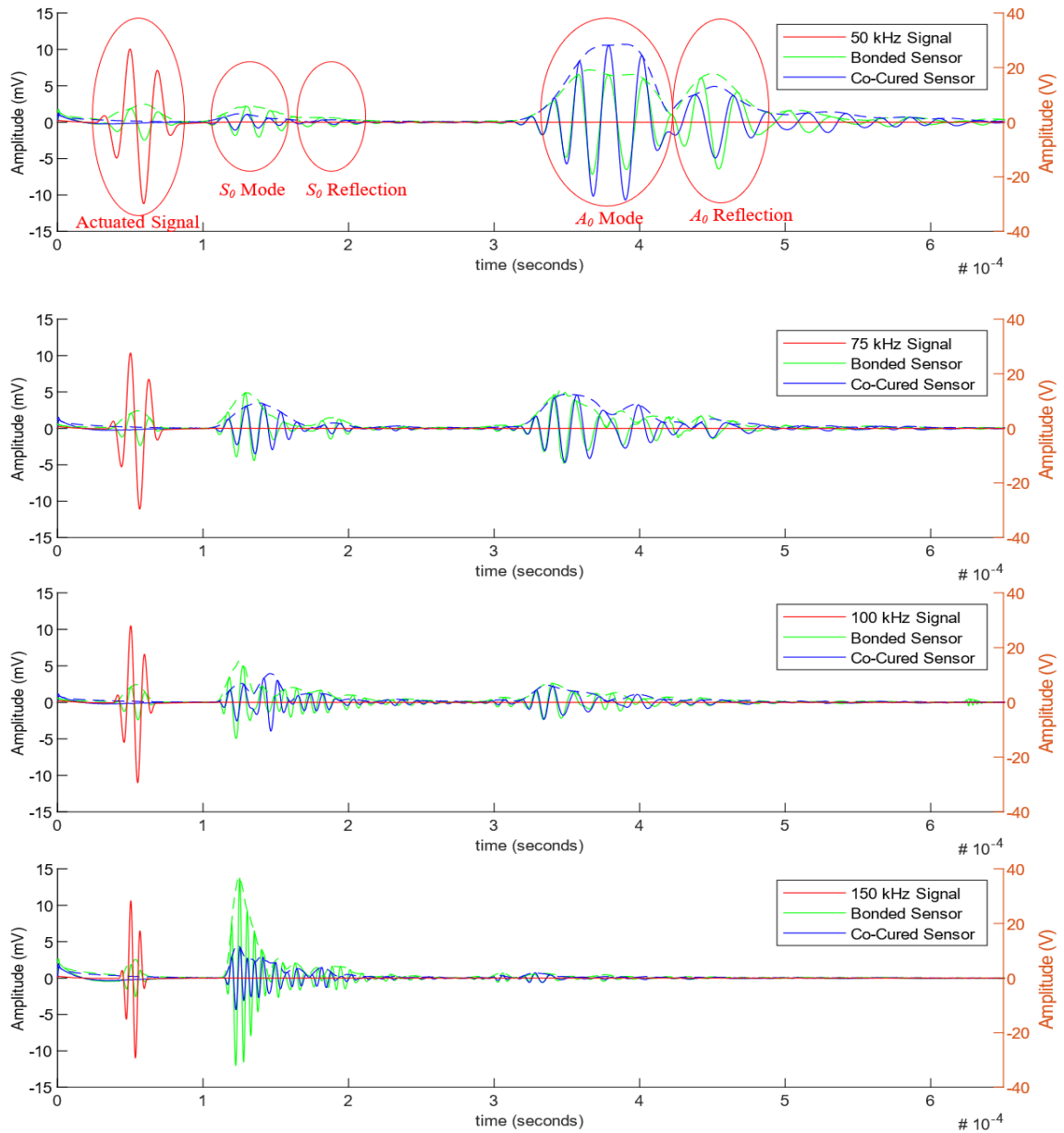


Figure 15: Comparison of the signal response for co-cured (blue) and bonded (red) sensors, from 50 kHz (top) to 150 kHz (bottom).

The fundamental symmetric mode (S_0) and fundamental anti-symmetric mode (A_0), as shown in Figure 15, have a similar waveform shape for the co-cured and bonded sensors; however, the amplitude of the S_0 wave is larger for the bonded sensor. In addition, the reflected S_0 and A_0 signals display discrepancies between the bonded and co-cured sensors;

this is explained after further examination using an ultrasound c-scan analysis, performed by the National Research Council (NRC), Ottawa, Canada, see Figure 16. These reflections can overlap with part of the original S_0 and A_0 signals creating a shift in peaks or the generation of new peaks.

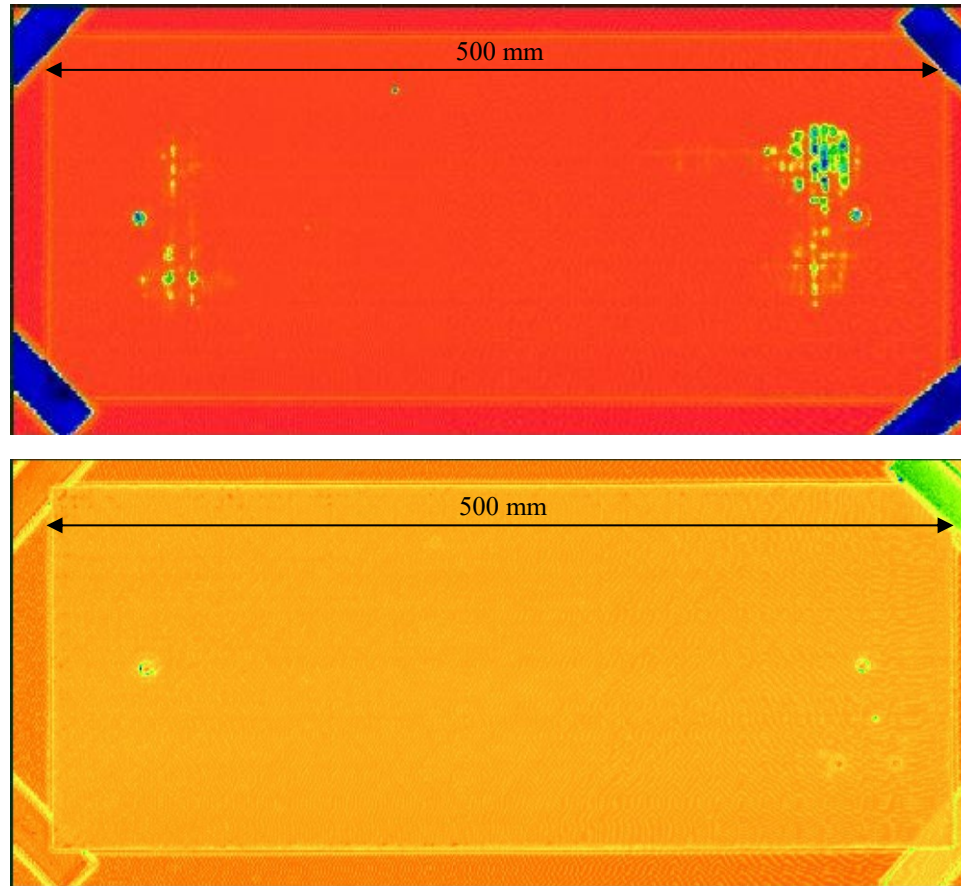


Figure 16: Ultrasound c-scan image of CFRP panel with co-cured sensors (top) and bonded sensors (bottom).

The ultrasound c-scan images in Figure 16 were not taken on the same day with the same experimental settings; therefore, the images only provide a qualitative analysis of the CFRP panels. However, from these c-scan images it can be seen that the panel with co-

cured sensors has regions of poor quality or defects around the sensors. The defects were not examined further to determine the cause; however, from the author's experience it is believed to be trapped air. It is believed the trapped air was initially contained in the housing of the spring pins and pulled into the CFRP panel when the vacuum was applied. These regions of poor quality will affect both the amplitude of the received signals and create additional S_0 and A_0 reflections as a result of the excited Lamb wave scattering as it interacts with the region of poor quality.

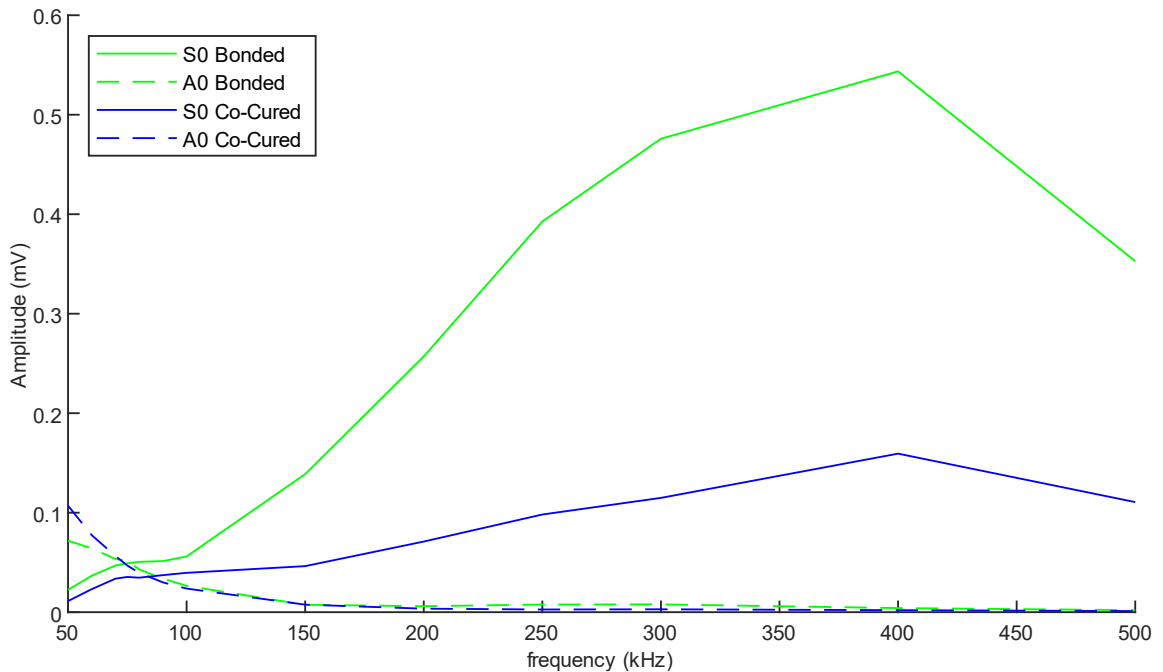


Figure 17: Signal amplitude for the S_0 and A_0 modes in CFRP panels with co-cured and bonded piezoelectric sensors.

Figure 17 shows the S_0 mode signal amplitude was larger for the bonded piezoelectric sensor when compared to the co-cured sensor; however, the A_0 mode signal amplitude was similar for both the bonded and co-cured sensors. In addition, it was found

that the A_0 mode is dominant at low frequencies between 50 – 75 kHz for the bonded sensor and 50 – 80 kHz for the co-cure sensor; above these frequencies the S_0 mode is dominant. The Lamb wave mode with the larger signal amplitude is identified as the dominant mode. At higher frequencies, when the S_0 mode is dominant and wavelength is smaller, the effects of poor quality regions have a greater impact on the S_0 signal amplitude.

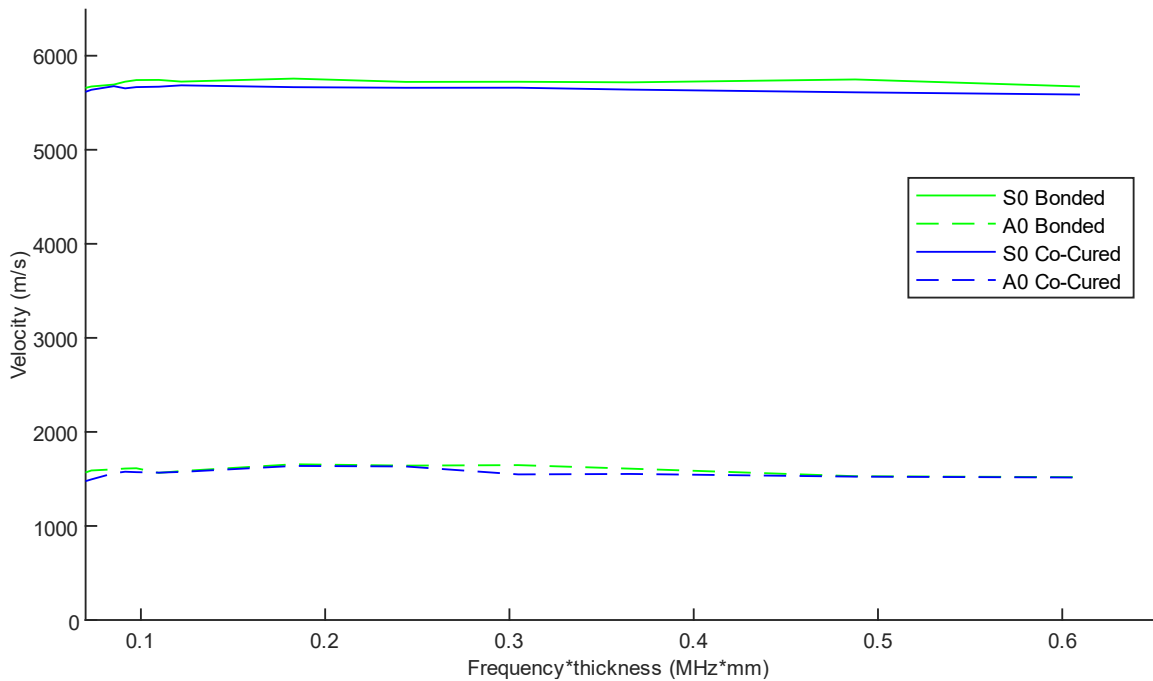


Figure 18: Experimental dispersion curve for the S_0 and A_0 modes for a frequency-thickness range from 60 - 600 kHz*mm.

The experimental dispersion curves for the S_0 and A_0 modes (Figure 18) are similar for both the bonded and co-cured piezoelectric sensors. The average experimental phase velocity, for a frequency range from 50 – 500 kHz, was found to be 5675 and 5515 m/s for the S_0 mode bonded and co-cured sensors, respectively, and 1479 and 1456 for the A_0 mode bonded and co-cured sensors, respectively. This indicates the CFRP panel with the bonded

sensor had a slightly faster velocity. In addition, the S_0 and A_0 are relatively non-dispersive in the tested frequency range.

2.3 Discussion

The primary objective of the research described above was to develop a manufacturing method to co-cure piezoelectric sensors to the surface of CFRP structures. Co-curing the sensors with the structure during the curing process allows for a holistic approach to SHM, which can include: *in-situ* cure monitoring, manufacturing defect identification, and in-service monitoring. The co-curing method solves some of the problems associated with embedding and bonding sensors to CFRP structures. Benefits associated with the co-curing method, include:

1. Precise and repeatable piezoelectric sensor placement: sensors are placed into flat bottom holes drilled into the manufacturing tool during the layup step, thus ensuring the precise location.
2. Wire management during manufacturing: the electrode wires are connected to the piezoelectric sensor through the tool during the curing process using spring pins, allowing the wires to be disconnected from the piezoelectric sensor before the CFRP part is demoulded from the tool and further processed.
3. Elimination of the bonding adhesive layers and the additional bonding step: the piezoelectric sensors are co-cured with the CFRP material when the resin begins to flow during the curing process.
4. Elimination of any negative effects on the mechanical performance of the host structure caused by an embedded sensor: the piezoelectric sensors are located on

the surface of the CFRP structure and do not alter the material fibers or create resin rich areas inside the structure.

5. Prevention of short circuiting the sensor electrodes: sensors embedded directly within a carbon fibre structure will short circuit when carbon fibres arc across the sensor electrodes.

However, the co-curing method proposed in this research must be improved to eliminate the regions of poor quality. The co-curing technique has to ensure repeatable and high quality structures before a manufacturer will modify the layup tooling with flat bottom holes for the piezoelectric sensors.

The results comparing the co-cured and bonded piezoelectric sensors demonstrated that the received waveform shape was similar, in a general sense, with respect to alignment and arrival time of the S_0 and A_0 modes (Figure 15). Differences in the S_0 and A_0 reflections were evident at higher frequencies (75 kHz and above), resulting from the regions of poor quality or defects shown on the c-scan images (Figure 16). The S_0 signal amplitude (Figure 17) was much larger for the bonded sensors, especially at frequencies above 100 kHz. Higher frequencies are more susceptible to defects or damage due to the smaller wavelength; therefore, it is believed the poor quality regions identified on the c-scan images (Figure 16) impacted the signal amplitude of the co-cured panel. Initially, it was hypothesized that eliminating the bonding adhesive layer would result in a higher signal amplitude for the co-cured panels because signal energy would not be lost from wave reflections associated with the additional adhesive material interface; however, the influence of the poor quality regions had a larger influence on the received signal.

Finally, the bonded and co-cured sensors had similar wave velocities for both the S_0 and A_0 modes (Figure 18). The wave velocity of the bonded sensors was slightly faster when a close-up of the zero crossing for individual wave cycles was compared. As previously mentioned, it is believed the quality of the CRFP panels would have caused this difference in velocity, as opposed to the difference between the bonded and co-cure sensors.

The unique approach to co-cure sensors to CFRP panels has demonstrated to be very promising. The benefits of the co-cured sensors on the manufacturing process and the potential for a holistic approach to SHM has the ability to advance Lamb wave research to actual aircraft structures. Minor adjustments to the tooling and fixtures used to co-cure the piezoelectric sensors to the CRFP panels will eliminate the regions of poor quality, as shown in the c-scan images, therefore, eliminating the differences between the bonded and co-cured results.

Chapter 3: Defect Identification

A holistic approach to structural health monitoring must cover the full life cycle of a part; for CFRP structures this includes three key components: *in-situ* cure monitoring, manufacturing inspection, and in-service monitoring. Incorporating and co-curing sensors into the composite structure was discussed in Chapter 2 and *in-situ* cure monitoring has been previously studied [50]–[54]. In-service monitoring has been the focus for SHM techniques and is widely researched [55], [56]. This chapter focuses on defects that can occur during the manufacturing process, which are traditionally identified using nondestructive testing methods for flight critical components.

Manufacturing inspection requires identification of a unique set of defects, including: porosity, delamination, foreign object or inclusions, resin rich areas, wrinkle, fiber waviness, gaps and overlaps, and ply orientation error. Careful quality control of the manufacturing process can help eliminate many of these defects, however, porosity and delamination remain difficult to control. From the author's prior industry experience in composites manufacturing, including working on the development and qualification of an ultrasonic NDT system for a Boeing supplier of 787 components; the ultrasonics inspection system was specifically required to identify porosity, delamination, and foreign objects or inclusions. A review of the current body of knowledge indicates a lack of research on the use of Lamb waves to inspect CFRP aerospace structures. Therefore, this is the motivation of the research described in this chapter to ensure Lamb wave inspection can effectively identify these same defect types and address this lack of knowledge.

Porosity is the result of many microvoids accumulating during the manufacturing process and can result in reduced mechanical properties. The microvoids are a result of

volatiles (air, volatile gasses, and moisture) created during the manufacturing process. Microvoids and porosity are both difficult to identify and control because they can be introduced into the process from a number of factors and sources, including: material storage and handling, material life, material tack or dryness, improper thawing and freezing procedures, humidity and environmental conditions, layup process and ply debulk, bagging procedure (both materials and physical conditions such as bag bridging), and cure process factors including resin flow, vacuum, pressure, cure profile, and bleeder systems. Porosity is one of the more difficult types of defects to identify, especially if only a small concentration of microvoids are present.

Bar-Cohen and Chimenti [57] provided promising results in 1985, indicating Lamb waves were more sensitive at identifying porosity than a conventional bulk ultrasonic. Despite this promising finding, no additional research had been done on detection of porosity using Lamb waves until Hudson *et al.* [58] found Lamb wave group velocity decreased with increasing levels of porosity. Inspection was performed using a pitch-catch configuration of piezoelectric PZT sensors on a twenty-four ply CFRP panels with porosity levels created by removing the panels from the oven, at different stages of the cure cycle, prior to the cure cycle being completed. Hudson *et al.* [18] extended this research and was able to identify small concentrations of porosity (diameter varying from 1.59 – 6.35 mm) using an air-coupled transducer and laser doppler vibrometer experimental setup. Post processing of the signal was performed using wavelet transforms. Given this limited research and the importance of identifying porosity in composite structures, reinforces the need for additional research in this area.

Porosity and foreign objects are the two most prevalent defects found in solid composite structures [59]. This author has seen, first-hand, backing material and OLFA™ utility knife blade fragments in cured CFRP structures. However, no research related to Lamb wave inspection and foreign objects or inclusions in composite structures was found during the literature search.

Delamination damage is one of the most widely researched defect types in Lamb wave SHM research; not necessarily from a manufacturing perspective but more commonly from an in-service SHM perspective. This is for two reasons, first, in-service delamination do occur, but secondly, impact damage is one of the most common types of in-service defects and produces delaminations through the thickness. Therefore, identifying delamination damage can be an indicator of the ability to detect impact damage. Kessler *et al.* [60] studied a variety of defect types (delamination, crack, fiber fracture, and hole) and concluded a Teflon induced delamination resulted in a 55 μs signal delay with the phase and frequency remaining the same. Kessler *et al.* [60] warned that variability between samples makes it difficult to establish a specific damage signature. Feng *et al.* [61] used a 2D finite element model to define the specific behavior of Lamb waves as they interact with delaminations, showing mode conversion of the S_0 mode to an A_0 mode. In addition to mode conversion, Feng *et al.* [61] demonstrated that as a Lamb waves travel across a delamination there are changes in the velocity and amplitude - these can be used to further define and locate the delaminations. Liu *et al.* [62] also utilized mode conversion of the S_0 mode to identify a 5 x 5 mm² delamination. To improve the ability to identify the delamination a time-frequency analysis was performed with the Matching Pursuit Decomposition. Carboni *et al.* [63] applied a Design of Experiment statistical approach to

highlight the differences between an 8 mm and 24 mm delamination at depths of 0.124 mm and 2 mm when using a 45 - 60 kHz A_0 mode excitation.

Birt [64] used the attenuation of the S_0 mode to identify delamination defects at different depths. Birt [64] found the ability to detect the delamination was depended on the location of the delamination through the thickness because stress distributions change through the thickness of the part. It was also noted that square delaminations were easier to detect than circular delaminations. Kudela and Ostachowicz [65] applied a 3D finite element model to identify a delamination with a length of 5 mm using a 5-cycle 30 kHz excitation in a pulse-echo configuration. Kudela and Ostachowicz [65] also found the Lamb wave response to a delamination was dependent on the through thickness depth. A delamination was detectable in a curved structure [66] using a 3-cycle 150 kHz piezoelectric excitation and measured with a laser doppler vibrometer. Mei *et al.* [67] used an angle beam transducer to generate a 500 kHz shear horizontal (SH_0) wave to identify a delamination by observing changes in the signal amplitude. In addition, Mei *et al.* [67] generated a 500 kHz S_0 Lamb wave to identify a wrinkle defect. However, it should be noted that an angle beam transducer is more applicable to NDT versus SHM due to its large size.

Impact damage can result from numerous causes, some potential causes include: bird strike, hail, runway debris, baggage cart contact, and drop tools. As mentioned above, impact damage can result in delaminations, fiber breakage, and matrix cracking. Dafydd and Khodaei [68] quantified the through thickness severity of barely visible impact damage using the A_0 mode. The A_0 mode was generated with a piezoelectric actuator and the response measured with a laser doppler vibrometer. A damage index compared the damage

signal to a baseline signal. Yeum *et al.* [69] also used the A_0 mode to identify impact damage; the A_0 mode was found to have a lower velocity as it travels across the damaged region. Using a network of piezoelectric sensors, the velocity of each path was calculated and compared to the other paths. An amplitude reduction of the S_0 mode was used by Santos *et al.* [70] to identify impact damage, however, fiber breakage needed to occur for this to be effective. In addition, Santos *et al.* [70] used a cross-correlation time shift between the damage signal and a baseline signal to accurately predict impact damage. Guy *et al.* [71] created a damage index using the frequency spectrum, this damage index was applied to a selected time window based on predicted signal arrival times. Matrix cracking was studied by Liu *et al.* [72] using a recursive plot and a variety of nonlinear time series characteristics.

Most current defect analysis techniques require a baseline signal compared with a damage signal. This could cause issues if environmental conditions vary during use. Yeum *et al.* [69] used the different effects of the S_0 mode and A_0 mode interacting with a delamination to create a baseline free analysis approach; the S_0 mode has a constant velocity as it travels across impact damage, however, the A_0 experiences a reduction in velocity. The delay of the A_0 mode relative to the S_0 mode was used to eliminate the need for a baseline signal. In addition, Yeum *et al.* [69] studied the ability of a dual ring piezoelectric PZT to extract the A_0 mode. Mode conversion has been applied by both Jia *et al.* [73] and Feng *et al.* [61] to eliminate the need for a baseline signal. Jia *et al.* [73] utilized the failed principle of reciprocity when a defect is present – unfortunately, if the defect is symmetric to both the actuator and sensor this method does not work; however, a network of sensors was applied to prevent this from occurring.

Important objectives of any holistic SHM or NDT systems should identify: 1) presence of a defect, 2) type of defect, 3) severity, and 4) location. The first objective has been widely researched, however, the ability for an SHM system to identify the type of damage has seen less attention, specifically for manufacturing defects. A ‘cradle to grave’ approach requires manufacturing inspection to be considered. Therefore, the focus of this research is to replicate the Boeing requirements for the qualification of an ultrasonic NDT system approach to an SHM system. Identifying the different type of manufacturing defects not only improves the final part quality but improves the manufacturing process making it more reliable and efficient – an ultimate goal for any manufacturer.

3.1 Analysis Technique

Lamb wave analysis is difficult due to the different mode types (symmetric and antisymmetric), mode numbers, mode conversions, dispersion, propagation distance, noise, reflections, and nonstationary defect signals. Signal amplitude, time-of-flight, and frequency analysis are useful analysis techniques, but can be limited due to the complex nature of the signal. Analysis performed in the time-frequency domain identifies the nonstationary characteristics of damage and cases where mode conversion occurs. The wavelet analysis is a common time-frequency tool and has been applied for Lamb wave analysis [18], [58], [63], [74]. Liu *et al.* [75] extended the wavelet analysis to include two statistical indexes of the wavelet coefficients: skewness and variance, this allowed the detection of multiple types of nonstationary bearing defects to be identified. The Matching Pursuit Decomposition (MPD) and Empirical Mode Decomposition (EMD) have also been applied for time-frequency analysis of Lamb wave signals. Yeum *et al.* [69] extracted the A_0 mode using the MPD to identify impact damage. Liu *et al.* [62] identified delamination

defects by extracting mode converted aspects of a signal using the MPD. Esmaeel and Taheri [76] applied the EMD method to identify delamination defects.

3.1.1 Continuous Wavelet Transform (CWT)

This research applies the CWT analysis technique to help identify the unique signature associated each defect type. The wavelet transform is a convolution of the selected wavelet function with the output signal. The Morlet and Biorthogonal wavelets were selected for the ABAQUS and experimental analysis, respectively. To select the best wavelet type, a qualitative analysis was performed on all the wavelet types available in Matlab – examining the resolution of the important signal features. The wavelet is dilated and translated along the signal to determine how well the wavelet correlates with the signal.

3.1.1.1 Morlet Wavelet

The Morlet wavelet [77] is a complex wavelet and is modulated with a Gaussian envelope, see Figure 19.

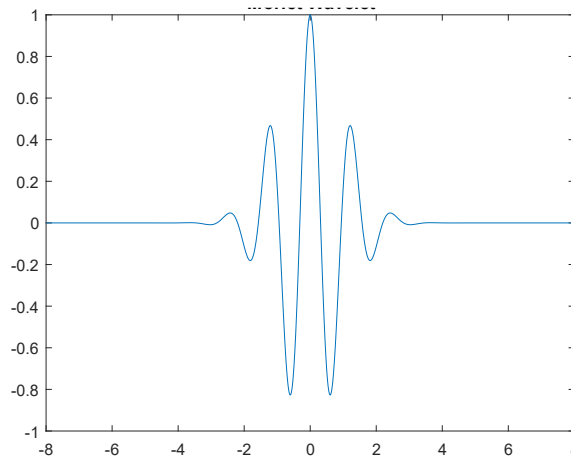


Figure 19: Representation of the Morlet wavelet

The Morlet wavelet is defined by the following equation:

$$\psi(t) = \frac{1}{\pi^{1/4}} e^{i2\pi f_0 t} e^{-t^2/2} \quad (5)$$

where f_0 is the wavelet center frequency and $\pi^{1/4}$ is a normalization factor to ensure the wavelet has unit energy. To define the dilated and translated wavelet, t is replaced with $(t - b) / a$ as shown below:

$$\psi\left(\frac{t-b}{a}\right) = \frac{1}{\pi^{1/4}} e^{i2\pi f_0 \left[\frac{t-b}{a}\right]} e^{-\frac{1}{2}\left[\frac{t-b}{a}\right]^2} \quad (6)$$

where a is the dilation coefficient and b is the translation parameter. Finally, the wavelet transform is defined by:

$$T(a, b) = w(a) \int_{-\infty}^{\infty} x(t) \psi^*\left(\frac{t-b}{a}\right) dt \quad (7)$$

where $w(a)$ is a weighting function and set to $1 / \sqrt{a}$ so every scale has the same energy, and ψ^* is the complex conjugate of the wavelet function.

3.1.1.2 Biorthogonal Wavelet

The biorthogonal wavelet [77] is a real, symmetric wavelet with two sets of wavelets; one set to decompose the signal, $\psi_{m,n}$, and one set to reconstruct the signal, $\tilde{\psi}_{m,n}$.

The wavelet transform can be defined as follows:

$$T_{m,n} = \int_{-\infty}^{\infty} x(t)\psi_{m,n}(t) dt \quad (8)$$

where, m and n are integers representing the order for the reconstruction and decomposition, respectively. The inverse transform is performed using $\tilde{\psi}_{m,n}$:

$$x(t) = \sum_{m=-\infty}^{\infty} \sum_{n=-\infty}^{\infty} T_{m,n}\tilde{\psi}_{m,n}(t) \quad (9)$$

The two wavelets satisfy the biorthogonality condition:

$$\int_{-\infty}^{\infty} \psi_{m,n}(t)\tilde{\psi}_{m',n'}(t) dt = \begin{cases} 1 & \text{if } m = m' \text{ and } n = n' \\ 0 & \text{otherwise} \end{cases} \quad (10)$$

The biorthogonal wavelet allows desirable signal properties to be identified by modifying the m and n integers. For example, if the reconstruction is performed with a lower order it results in a smoother output. The biorthogonal wavelets ($m = 3$ and $n = 5$) are shown in Figure 20 with the decomposition wavelet (left) and the reconstruction wavelet (right):

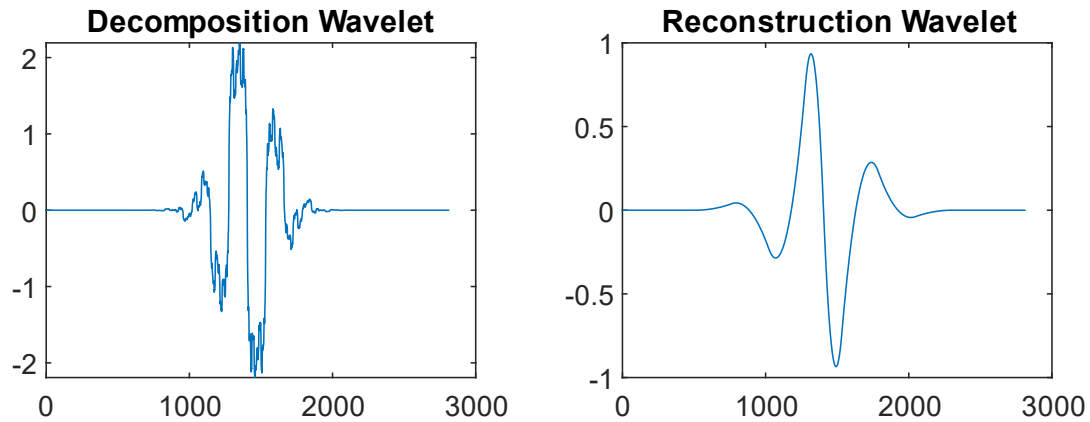


Figure 20: Biorthogonal decomposition and reconstruction wavelets ($m = 3$ and $n = 5$).

3.2 Finite Element Model

The choice of finite element method (FEM) software is an important consideration to ensure simulation results can be related to experimental and real-world applications. The study of ultrasonic Lamb waves propagating in composite CFRP structures has many important considerations to ensure accurate results, including ply orientation, wave excitation, propagation, and interaction with defects and boundaries. Three commercially available software packages capable of meeting these requirements are ABAQUS, ANSYS, and COMSOL. Each of these tools has been frequently cited in the literature and Leckey *et al.* [78] provided a direct comparison of the three software packages for both a baseline and delamination case. It was reported that each FEM software provide adequate results, however, some minor discrepancies were reported with group velocities and wavenumber. This was most notable between the experimental results and the FEM simulations, which was caused by differences between the material properties of manufacture parts versus data sheets. Computational demand was difficult to compare

directly because simulations were executed on different computer hardware with variables optimized for the specific software package being used. However, a generalization would indicate COMSOL was the fastest (when the time step is manually controlled) followed by ABAQUS. Ultimately, the decision for which FEM software package to use is typically based on availability; at Carleton University ABAQUS is available and has been previously used within the research group for Lamb wave related studies [21].

3.2.1 Implicit versus Explicit FEM for Lamb Wave Research

The choice between Implicit (ABAQUS/Standard) and Explicit (ABAQUS/Explicit) is sometimes very clear; Implicit is widely used to solve smooth nonlinear problems and Explicit is designed to solve dynamic problems, such as wave propagation analysis [79]. Both methods solve the problem with the same general equation:

$$M\ddot{u} = P - I \quad (11)$$

where M is the mass matrix, \ddot{u} are the nodal accelerations, P are the external applied forces, and I are the internal element forces. The Explicit method solves the nodal accelerations using a diagonal mass matrix. The accelerations are integrated with respect to time using the central difference rule to obtain the velocities and displacements:

$$\dot{u}|_{(t+\frac{\Delta t}{2})} = \dot{u}|_{(t-\frac{\Delta t}{2})} + \frac{\Delta t|_{(t+\Delta t)} + \Delta t|_{(\Delta t)}}{2} \cdot \ddot{u}|_{(t)} \quad (12)$$

$$u|_{(t+\Delta t)} = u|_{(t)} + \Delta t|_{(t+\Delta t)} \cdot \dot{u}|_{(t+\frac{\Delta t}{2})} \quad (13)$$

where \dot{u} is the velocity, u is displacement, and Δt is the change in time. This method assumes constant accelerations, therefore, the time increments must be small to ensure the accelerations are nearly constant. However, the overall computational time is reduced because each time step is inexpensive. To ensure the time increment is small enough and the solution does not diverge and become unstable, the following equation is used to define the stability limit:

$$\Delta t_{stable} = \frac{L^e}{c_d} \quad (14)$$

where L^e is the element length and c_d is the maximum wave speed in the materials, in our case we use the S_0 velocity.

The Implicit method solves Equation (11) using the Newton-Raphson method, which performs successive iterations until an approximation converges on a solution for each time step. Each iteration to improve the approximation (also called correction) requires the Jacobian matrix to be inverted, this can be computationally expensive and require substantial disk space and memory. Solution convergence means at every node the force and moment equilibrium and contact conditions are satisfied. The benefit is a larger time step, Δt , can be used because the method is unconditionally stable.

The recommended time step for finite element modelling of Lamb waves [80] is given by:

$$\Delta t = \frac{1}{20f_{max}} \quad (15)$$

where Δt is the integration time step and f_{max} is the highest frequency of interest. This time step is comparable to the requirement for the Explicit method, however, when used with the Implicit method computational cost are high.

A key advantage of the Implicit model is the availability of a larger selection of element types, including piezoelectric elements (CPE4E). This allows the piezoelectric actuators and sensors to be include in the model, whereas, in the Explicit model the excitation must be created using a load or displacement boundary condition. Figure 21 shows displacement at the sensor location for Lamb wave propagation in an aluminum plate for an Implicit and Explicit model. The 3-cycle sine was generated with a piezoelectric actuator in the Implicit model and concentrated forces in the Explicit model. The time step for the Explicit model was five times smaller than the Implicit model, however, the Implicit simulation took 4 days, 15 hours, and 7 minutes, compared to 2 hours and 7 minutes for the Explicit solution – both simulations were run on an AMD server with 24 cores and 128 GB of RAM. A summary of the model parameters used to compare the Implicit and Explicit models is shown in Table 3.

Table 3: Finite element model parameters for an Implicit and Explicit model.

Model Type	Geometry (m)	Element Size (m)	Element Number	Element Type	Time Step (s)	Force Input
Implicit	0.554 x 0.254 x 0.002	0.0005	3106640	C3D8R	5E-8 (max)	Voltage
Explicit	0.554 x 0.254 x 0.002	0.0005	3051288	C3D8R	5R-8 (max)	Point Force (F1 & F2)

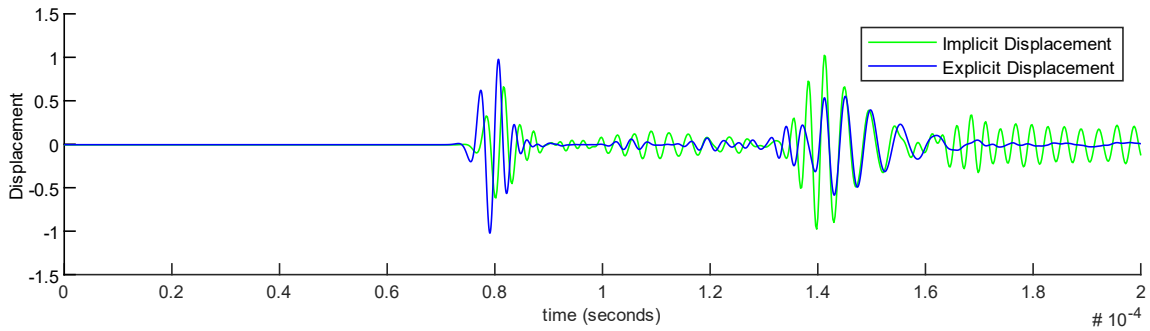


Figure 21: Implicit versus Explicit FEM for Lamb wave propagation in an aluminum plate.

Figure 21 shows differences between the Implicit and Explicit solutions, specifically: 1) the S_0 wave velocity is faster in the Explicit model, 2) the A_0 wave has a larger initial amplitude in the Implicit model, and 3) better resolution of the mode converted wave packets that occur between the arrival of the S_0 and A_0 wave in the Explicit model. Ultimately, the Explicit model was also selected due the drastic reduction in simulation time.

3.2.2 Finite Element Parameters for Lamb Wave Propagation

The finite element modelling of lamb wave propagation in composites materials needs to consider many of the same parameters as other types of structural modelling of composite materials, including element type, mesh density, load applications, and boundary conditions. This section will discuss these parameters with special consideration given to the propagation of Lamb waves.

3.2.2.1 Element Type

Continuum shell elements are similar to 3D solid elements; however, they are computationally less expensive and do not have the same aspect ratio restriction as solid

elements. Compared to conventional shell elements, continuum shell elements provide more accurate results for the transverse shear deformation. Further, continuum shell elements can be stacked to represent each laminate layer, thus providing a better representation of the shear stresses through the thickness. The continuum shell elements enforce the first-order shear deformation theory (FSDT), which is the most common shell theory for composite structures. The FSDT assumes that: 1) a line through the thickness of the shell can rotate but remains straight, and 2) changes in the shell thickness are negligible. The FSDT is enforced using the element interpolation functions. For this research, initial simulations were completed using both continuum shell elements (SC8R) and solid elements (C3D8R), however the continuum elements were select because of the reduced computational costs. The SC8R elements only have displacement degrees of freedom, and the notation indicates the element is a shell (S), continuum (C), has eight nodes (8), and reduced integration (R).

3.2.2.2 Mesh Density

Mesh density is an important parameter to ensure accurate results for Lamb wave propagation, but computational cost must also be taken into consideration. For Lamb wave propagation 10 – 20 elements per wavelength is recommended [80]–[82]. The A_0 mode is used to calculate the element length because it has a smaller wavelength. For this research, it was determined the optimal frequency for analysis occurred when the A_0 mode was dominant, this occurs at lower frequencies. Therefore, an excitation frequency of 90 kHz was used; however, to be able to measure and analyze higher frequencies, potentially created from interactions with defects, a frequency of 300 kHz was used for element length

calculation. Applying the below Equations (16) and (17) for the A_0 mode results in an A_0 wavelength of 4 mm and an element length between 0.2 to 0.4 mm.

$$\lambda = \frac{v}{f} \quad (16)$$

where λ is wavelength, v is wave velocity, and f is frequency.

$$L_e = \frac{\lambda_{min}}{10 \text{ to } 20} \quad (17)$$

where L_e is element length.

Implementing the above guidelines and considering the size of the composite panel being modelled, with eight laminate layers, creates a very large finite element (FE) model with approximately four million elements, see Table 4 for a summary of the FE model parameters. Therefore, an attempt was made to increase the element length to 0.5 or 0.6 millimeters, see Figure 22.

Table 4: Finite element parameters for the comparison of different element sizes.

Model Type	Geometry (m)	Element Size (m)	Element Number	Element Type	Time Step (s)	Force Input
Explicit	0.572 x 0.272 x 0.00163	0.0004	4062300	SC8R	1.25E-7 (max)	Point Force (F1 & F2)
Explicit	0.572 x 0.272 x 0.00163	0.0005	2615912	SC8R	1.25E-7 (max)	Point Force (F1 & F2)
Explicit	0.572 x 0.272 x 0.00163	0.0006	1783208	SC8R	1.25E-7 (max)	Point Force (F1 & F2)

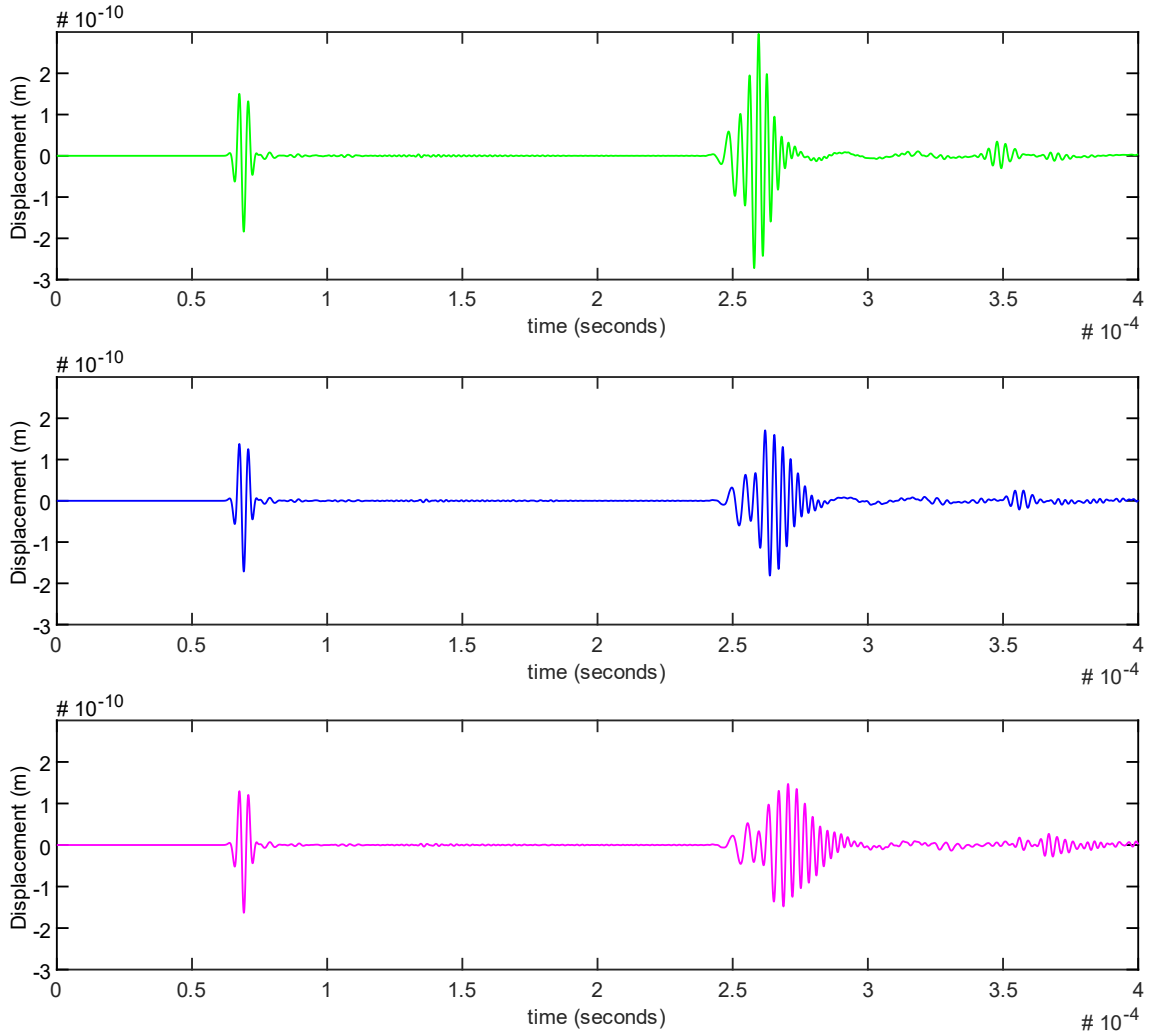


Figure 22: Comparison of element length for a 3-cycle sine wave with an excitation frequency of 300 kHz; 0.4 mm (top), 0.5 mm (middle), and 0.6 mm (bottom).

Figure 22 shows that attempting to increase the element length above the recommended 0.4 mm does cause changes in the A_0 mode – the amplitude of the signal is reduced, and the wave packet shape is modified. Therefore, an element length of 0.4 mm was selected for further FE modelling.

3.2.2.3 Load Application

Section 3.2.1 compared implicit and explicit FE modelling, concluding explicit modelling would be used for the current research. As indicated in Section 3.2.1, piezoelectric elements are not available in ABAQUS explicit modelling, therefore, an alternative method has to be used to generate the Lamb wave. Gresil *et al.* [82] provided guidelines for using ABAQUS explicit for modelling Lamb waves and indicated a series of concentrated forces provided similar results to experimental results where Lamb waves were generated using piezoelectric actuators. The orientation of the applied concentrated forces has varied in the literature, therefore, a comparison of in-plane (forces in the x and y directions) and normal (z direction) is provided in Figure 23. A summary of the model parameters used to compare the different load applications is shown in Table 5.

Table 5: Finite element model parameters for the comparison of different applied loads.

Model Type	Geometry (m)	Element Size (m)	Element Number	Element Type	Time Step (s)	Force Input
Explicit	0.572 x 0.272 x 0.00163	0.0004	8109460	SC8R	1.25E-7 (max)	Point Force (F1 & F2)
Explicit	0.572 x 0.272 x 0.00163	0.0004	8109460	SC8R	1.25E-7 (max)	Point Force (F3)

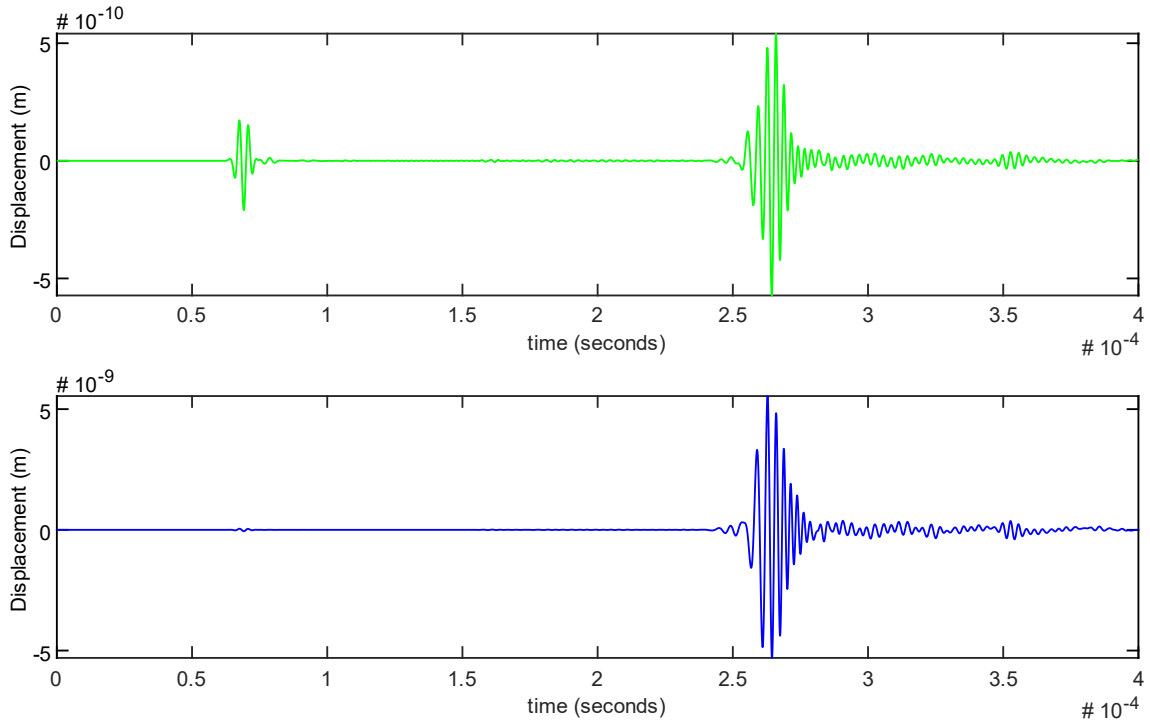


Figure 23: Concentrated forces to generate a 3-cycle sine wave with an excitation frequency of 300 kHz; balanced x and y forces (top), and force in the z direction (bottom).

In Figure 23, the in-plane forces are balanced in the x and y directions, whereas the normal force is applied in the negative z direction (applied on the top surface towards the bottom surface). Figure 23 shows similar results for the A_0 mode, however, the S_0 mode has a small amplitude and is difficult to recognize when applying a concentrated force in the z direction. This indicates the importance of using balanced forces to create the S_0 mode. Based on the results in Figure 23, it was decided to apply balanced concentrated forces in the x and y directions to excite Lamb waves.

3.2.2.4 FEM Absorbing Layers

To eliminate unwanted reflected waves from the FE model boundary edges, absorbing layers can be implemented around the model edges. This helps identify unique damage signatures that result when Lamb waves interact with defects. These damage signatures, and techniques to identify them, can then be applied to experimental results to help recognize defects in actual composite structures. Absorbing or reducing these unwanted reflections can be achieved by: 1) increasing the geometric size of the FE model, 2) perfectly matched layers (PMLs), 3) absorbing layers of increasing damping (ALID), and 4) infinite elements. Increasing the geometric size of the FE model is computationally expensive and not practical given the current size of the model. PMLs are effective at damping reflection and are computationally efficient [83]; however, they require precise parameter calculations to ensure the impedance of the PML elements match that of the area of study. In addition, PMLs often require user subroutines to be programmed. Alternatively, ALID are easily implemented with commercial FE software, including ABAQUS. Finally, ABAQUS has an infinite element type (CIN3D8) that create a boundary condition to absorb wave energy; these infinite elements are most effective when waves are propagating perpendicular to the boundary edges [84] and are only available with ABAQUS implicit modelling. Based on these considerations, ALID were implemented for the FE model in this research.

Pettit *et al.* [85] created ALID with a technique they refer to as the stiffness reduction method (SRM). This method requires additional layers be added to the model edges with each successive layer having gradually changing material properties to absorb the wave energy without causing reflections resulting from impedance mismatch. The

SRM increases the Rayleigh mass proportional damping term, C_M , while decreasing the Young's modulus, thus providing a unique advantage over other ALID methods. Pettit *et al.* [85] outlined a seven step approach to implementing the SRM, which was followed for the current research:

1. Create an SRM boundary region equal to 1.5 the wavelength (λ).
2. Assign multiple layers, x , to the SRM boundary region each consisting of one finite element length. The research for this thesis used 20 layers, $x = 20$.
3. Set the maximum Rayleigh mass proportional damping term (C_{Mmax}) equal to the angular frequency of the incident wave.
4. Apply the below Equation (18) to change C_M for each layer x :

$$C_M(x) = C_{Mmax}X(x)^p \quad (18)$$

where, $X(x)$ is 0 for the area of study (AoS) and increases linearly to 1 at the final boundary layer, and p represents the power law set to a value of three for this thesis research.

5. Calculate the maximum attenuation factor, α_{max} , using the following Equation (19):

$$\alpha_{max} = \frac{\ln\left(\frac{E(x)}{E_0}\right)}{k_{inc}x} \quad (19)$$

where, k_{inc} is the wavenumber of the incident wave, x is the boundary region layer number, and $\frac{E(20)}{E_0} = 0.01$.

6. Calculate the attenuation factor, $\alpha(x)$, for each layer using the following Equation (20):

$$\alpha(x) = \alpha_{max}X(x)^p \quad (20)$$

where, α_{max} is calculated in Step 5, $X(x)$ is 0 for the AoS and increases linearly to 1 at the final boundary layer, and p represents the power law set to a value of three for this thesis research.

7. Calculate the Young's modules, $E(x)$, for each layer using the following Equation (21):

$$E(x) = E_0e^{-\alpha(x)k_{inc}x} \quad (21)$$

where, E_0 is the Young's modulus for the AoS, $\alpha(x)$ is defined in Step 6, k_{inc} is the wavenumber of the incident wave, and x is the boundary region layer number.

Implementing the above SRM steps gives the material properties for each boundary region layer, see Table 6.

Table 6: SRM boundary layer properties.

Material Region	E_x (GPa)	E_y (GPa)	E_z (GPa)	C_M
Area of Study	7.9600E+10	5.1000E+09	5.1000E+09	0
Layer 1	7.9598E+10	5.0999E+09	5.0999E+09	5.8905E+01
Layer 2	7.9563E+10	5.0977E+09	5.0977E+09	4.7124E+02
Layer 3	7.9415E+10	5.0881E+09	5.0881E+09	1.5904E+03
Layer 4	7.9016E+10	5.0626E+09	5.0626E+09	3.7699E+03
Layer 5	7.8181E+10	5.0091E+09	5.0091E+09	7.3631E+03
Layer 6	7.6685E+10	4.9133E+09	4.9133E+09	1.2723E+04
Layer 7	7.4285E+10	4.7595E+09	4.7595E+09	2.0204E+04
Layer 8	7.0748E+10	4.5328E+09	4.5328E+09	3.0159E+04
Layer 9	6.5902E+10	4.2224E+09	4.2224E+09	4.2942E+04
Layer 10	5.9692E+10	3.8245E+09	3.8245E+09	5.8905E+04
Layer 11	5.2228E+10	3.3462E+09	3.3462E+09	7.8402E+04
Layer 12	4.3824E+10	2.8078E+09	2.8078E+09	1.0179E+05
Layer 13	3.4987E+10	2.2416E+09	2.2416E+09	1.2941E+05
Layer 14	2.6346E+10	1.6880E+09	1.6880E+09	1.6163E+05
Layer 15	1.8540E+10	1.1878E+09	1.1878E+09	1.9880E+05
Layer 16	1.2070E+10	7.7334E+08	7.7334E+08	2.4127E+05
Layer 17	7.1928E+09	4.6085E+08	4.6085E+08	2.8940E+05
Layer 18	3.8789E+09	2.4853E+08	2.4853E+08	3.4353E+05
Layer 19	1.8703E+09	1.1983E+08	1.1983E+08	4.0403E+05
Layer 20	7.9600E+08	5.1000E+07	5.1000E+07	4.7124E+05

3.2.2.5 Finite Element Modelling Defect Definition

The focus of this chapters is to define and identify different types of defects that occur in CFRP structures, specifically those that occur during the manufacturing process. There are numerous types of manufacturing defects, however, delamination, foreign object, and porosity were selected for further analysis because of the detrimental effect these defects have on the integrity and strength of the structure.

3.2.2.5.1 Delamination Defect

To correctly model the unique signal features associated with delamination damage careful consideration is required to ensure the FE model closely simulates an actual delamination. ABAQUS/CAE can model a delamination using cohesive elements, cohesive surface behaviour, or separated nodes. The cohesive elements and cohesive surface behaviour provide detailed modelling of the adhesive interface and are typically applied for progressive separation of two initially bonded surfaces.

The goal of SHM is to identify damage, not study the real-time damage progression, therefore, separating the nodes in the FE model is the most relevant method. Node separation is also a simpler method to implement for a delamination because it does not require defining specific elements. However, the delamination thickness must be negligibly small to simulate accurate results.

To model an existing delamination the top and bottom contact surfaces must be able to move independent of each other. This can be achieved by duplicating the nodes [86][87][88][89], separating the nodes by a small distance [90], or rigidly connecting the top and bottom part sections using tie constraints - except in the delamination region [78]. To ensure an accurate representation of an actual delamination, the FE model should not remove significant mass from the original part and aim to achieve a zero volume delamination [90]. The experimental CFRP specimens for this research replicated a delamination using a 25.4 x 25.4 mm piece of Teflon tape, with a thickness of 10 μm ; therefore, this was considered for the FE modelling of the delamination.

To create a delamination using the FE model, this research compared three methods: Method 1) a small amount of CFRP material (thickness of 10 μm) was removed

to separate the nodes, Method 2) a small amount of CFRP material (thickness of 10 μm) was replaced with a Teflon material connected with TIE constraints on all surfaces except the top surface, and Method 3) similar to Method 2 but with the top and bottom sections of the CFRP plate defined separately and rigidly connected using TIE constraints except along the top surface of the Teflon. A summary of the model parameters used to compare the different methods to implement a delamination defect is shown in Table 7.

Table 7: Finite element model parameters for the comparison of different delamination methods.

Model Type	Geometry (m)	Element Size (m)	Element Number	Element Type	Time Step (s)	Force Input
Implicit (Method 1)	1.0 x 0.00206	0.00024	125380	CPE4R	5E-8 (max)	Voltage
Implicit (Method 2)	1.0 x 0.00206	0.00024	122711	CPE4R	5E-8 (max)	Voltage
Implicit (Method 3)	1.0 x 0.00206	0.00024	124911	CPE4R	5E-8 (max)	Voltage

A qualitative comparison of the three methods, shown in Figure 24, demonstrates the small gap between nodes versus the Teflon material behave in a similar manner. A close-up of Figure 24 shows a very good agreement between the three delamination conditions, see Figure 25. However, it can be noted that the Teflon insert causes a slight time delay of the A_0 reflection response. The A_0 reflection wave pulse travels across the delamination area three times - forward, reverse, and forward directions. This time delay is more pronounced when the top and bottom sections of the CFRP plate are defined separately and joined using TIE constraints (Method 3).

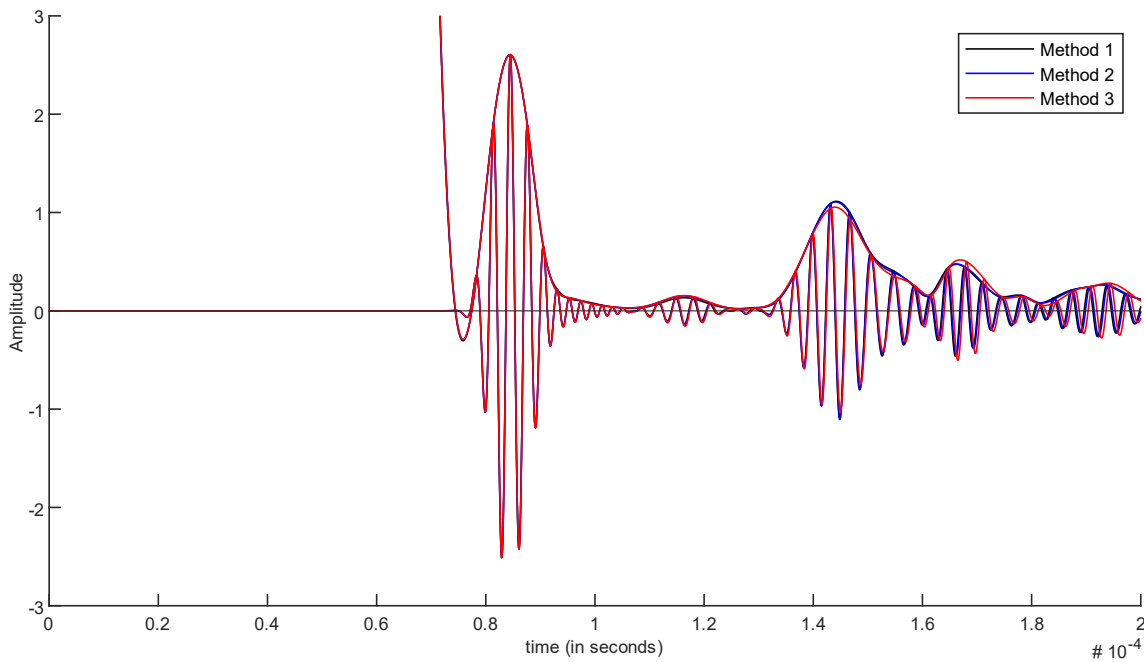


Figure 24: Comparison of three methods to create a delamination defect using ABAQUS.

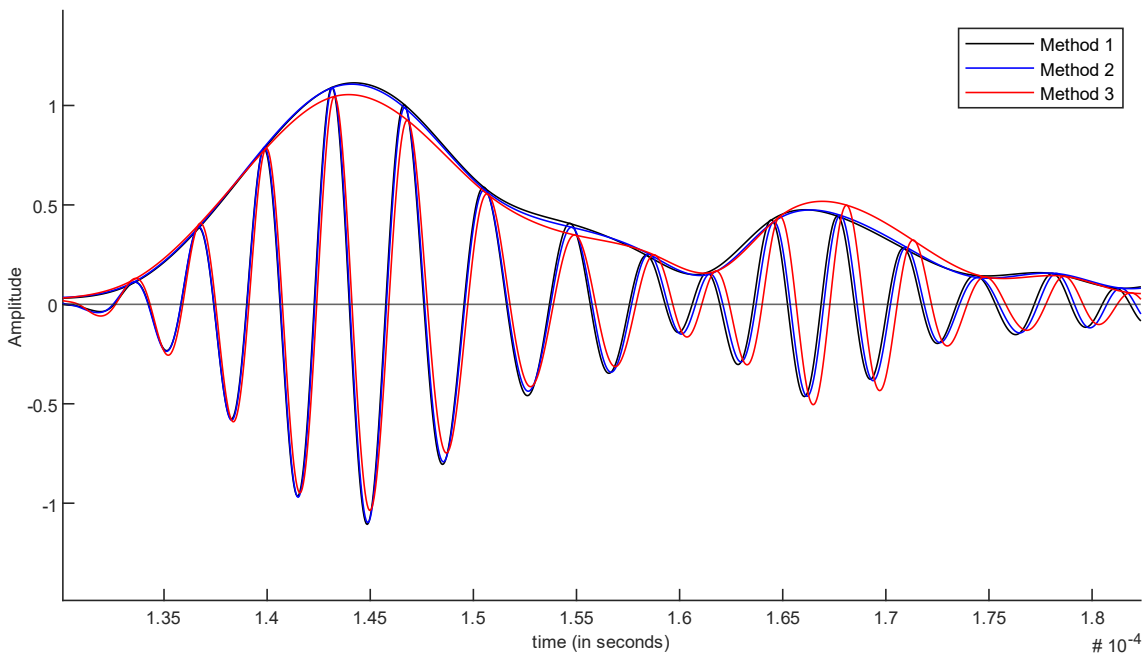


Figure 25: Close-up of the A_0 and A_0 reflection of the three methods used to create a delamination defect using ABAQUS.

The close agreement between the FE model delamination using Method 1 and Method 2 indicates using a Teflon insert for experimental testing provides a good representation of a delamination. Therefore, going forward this research will model a delamination using a Teflon insert, as described in Method 2, to replicate the experimental work in CFRP panels.

3.2.2.5.2 Foreign Object Defect

Foreign objects are one of the more prevalent manufacturing defects found in solid composite structures [59], however, no research has been completed in this area using Lamb wave propagation – this will be the first. The author’s first-hand experience and discussions with experienced NDT technicians has identified OLFA™ utility knife blade fragments (or similar), rulers, and backing material as the most common foreign object defects left inside parts during fabrication. For the qualification of an NDT bulk ultrasonic c-scan machine, Boeing required brass shim stock be inserted into reference standard parts for identification. This research used the same concept, however, a 25.4 x 25.4 mm stainless steel shim stock with a thickness of 25.4 μm was used. This was modelled using the same method (Method 2) described in Section 3.2.2.5.1, except the Teflon material properties was replace with stainless steel and the insert was connected with TIE constraints on all surfaces.

3.2.2.5.3 Porosity

Porosity and microvoids are a widespread problem in composite structures with a common industry goal of reducing them to less than two percent of the inspected area.

There are many potential causes of porosity [91], unfortunately, the ability to easily detect and quantify porosity remains challenging. Regardless of the importance of being able to identify and control porosity, only two authors have completed research in this area using Lamb waves since 1985 [18], [57]. Both these studies applied NDT techniques to excite and detect Lamb waves, which are not easily transferable to SHM inspection techniques. To further study and model porosity using ABAQUS, a similar approach was applied as Method 2 in Section 3.2.2.5.1; however, the Teflon material was replaced with the CFRP material properties defined in the AoS with 1 mm radius holes. The size of the porosity region was 25.4 x 25.4 mm with 36 holes representing a concentrated area of 17.5% porosity, see Figure 26.

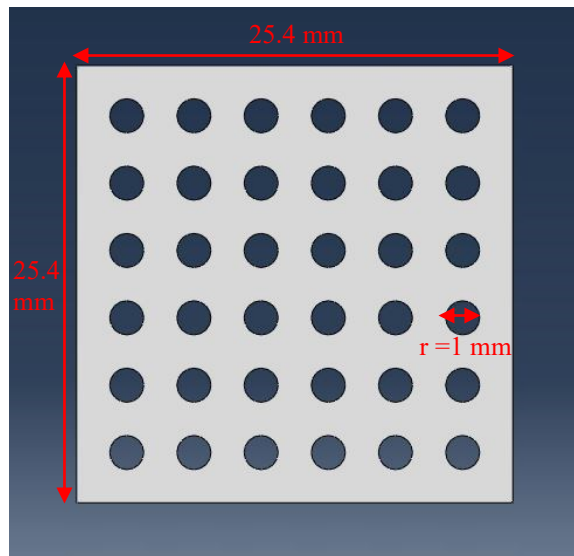


Figure 26: Generalized porosity region modelled in ABAQUS.

3.3 Experimental Setup

The experimental setup is similar to that outlined in Chapter 2, Section 2.1.3, with modification for the embedded defects described in the following sections.

3.3.1 Composite panels

The CFRP panels were manufactured using an oven cure with a vacuum of 28.0 inHg (94.8 kPa) (out-of-autoclave). The layup consisted of eight plies of material with a material orientation of $[0/90/+45/-45]_s$. The material properties, as provided by the material manufacturer, are listed in Table 8. The cured panels were trimmed to a final size of 500 x 200 mm with a thickness of 1.6 mm. Following the cure, the piezoelectric sensors (APC International Limited, model number 70-3000) were bonded 400 mm apart on the surface of the CFRP panel using a cyanoacrylate Loctite super glue (Ultra Gel Control).

Table 8: Material properties for the CFRP, Teflon, and stainless steel materials.

Material	E_1 (GPa)	$E_2 = E_3$ (GPa)	$\nu_{12} = \nu_{13}$	ν_{23}	$G_{12} = G_{13}$ (GPa)	G_{23} (GPa)	ρ (kg/m ³)
CFRP	79.6	5.1	0.318	0.396	7.6	7.6	1610
Teflon	0.5	0.5	0.46	0.46	-	-	2200
Stainless Steel	195	195	0.29	0.29	-	-	8000

3.3.2 Defects

The manufacturing defects that were the focus of this research include delamination, foreign object, and porosity. The objective was to replicate the defects used to qualify a traditional bulk ultrasonic c-scan inspection system in a similar approach required by Boeing. A delamination defect was created by inserting a piece of Teflon 25.4 x 25.4 mm with a thickness of 10 μm . The foreign object was replicated using a 25.4 x 25.4 mm piece of 304 stainless steel shim stock with a thickness of 25.4 μm . Finally, the porosity was replicated using a 25.4 x 25.4 mm piece of nylon peel ply. The defects were located at the midplane of the panel at a depth between the fourth and fifth layer. An

additional test specimen was manufactured with a near surface delamination, located between the second and third layer.

3.3.3 Experimental Absorbing Layer

To reduce unwanted Lamb wave reflections from the part edges an absorbing layer was introduced. Little research has been completed on the optimal edge damping material for experimental testing; however, Haider *et al.* [92] applied modelling clay around the plate edges with varying thickness, starting with a zero thickness and increasing to 12 mm. A similar approach was applied for the current research, however, a combination of modelling clay and bagging sealant tape (tacky tape) was applied in distinct layers. Three absorbing layers were applied: 1) outer layer consisting of bagging sealant tape applied directly on the part edge and folded over to the top and bottom part surfaces, 2) middle layer consisting of 8 grams and 21 grams of modelling clay rolled out and placed along the short and long surfaces, respectively, and 3) inner layer consisting of 2 grams and 5 grams of modelling clay rolled out and placed along the short and long surfaces, respectively. The modelling clay was applied to both the top and bottom surface of the plate, see Figure 27 and Figure 28. The best damping results were found when the modelling clay was rolled into the appropriate length and pressed lightly onto the part surface.

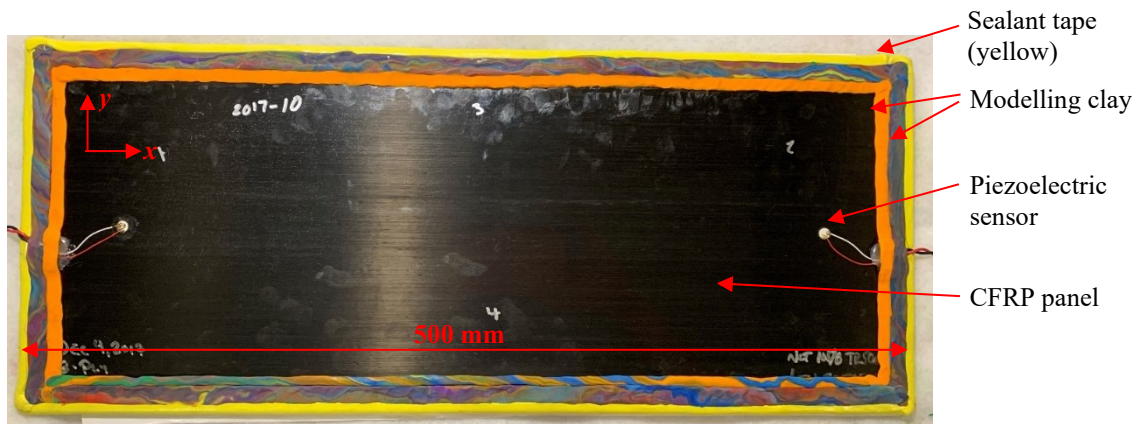


Figure 27: Experimental absorbing layers (top surface).

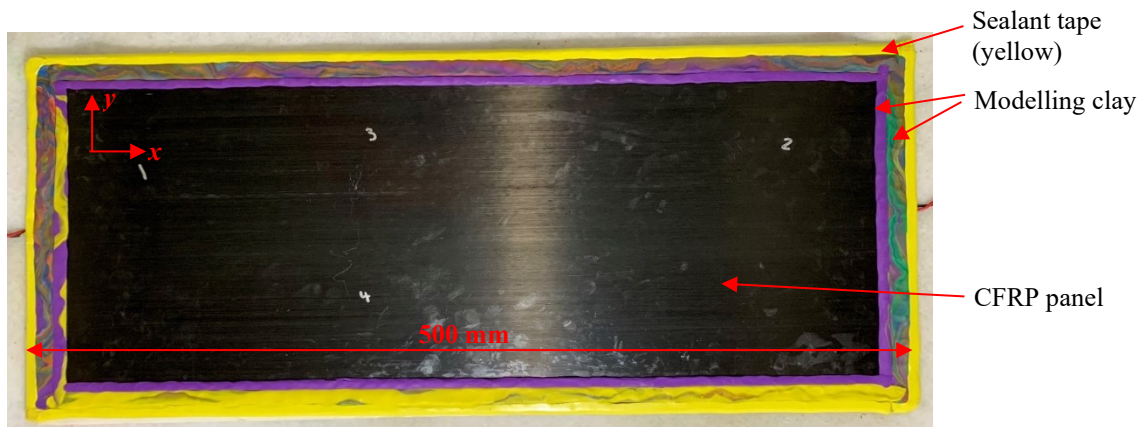


Figure 28: Experimental absorbing layers (bottom surface).

3.3.4 Excitation and Measurement

The experimental testing was the same as that described in Chapter 2, Section 2.1.3, with a 90 kHz 3-cycle sine wave excitation.

3.4 Results

The objective of this chapter was to identify delamination, foreign object, and porosity in CFRP panels. To complete this objective, the FE model response to each defect was identified and used to help identify each defect in the experimental panel. These steps were achieved in both the time domain and time-frequency domain.

3.4.1 FE Model Validation: Piezoelectric Voltage versus Nodal Displacement

To validate the ABAQUS/Explicit model with experimental results, first, an understanding about the limitations of the Explicit model, as discussed Section 3.2.1, was examined. Specifically, the changes associated with the concentrated force input and a displacement output versus the piezoelectric actuator and sensor. To make this comparison an ABAQUS/Implicit model was created that had the ability to model the piezoelectric sensor using piezoelectric elements (CPE4E). To simplify the ABAQUS simulation, the test specimen was model as an aluminum plate. Figure 29 compares the ABAQUS/Implicit total displacement (x , y , z directions) of a point on the aluminum plate located at the center of the piezoelectric sensor (equivalent output location of the ABAQUS/Explicit model) and the ABAQUS/Implicit voltage output of the piezoelectric sensor. A summary of the model parameters used to compare the output voltage and the nodal displacement is shown in Table 9.

Table 9: Finite element model parameters for the comparison of PZT voltage and nodal displacement.

Model Type	Geometry (m)	Element Size (m)	Element Number	Element Type	Time Step (s)	Sensor Output
Implicit	0.554 x 0.254 x 0.002	0.0005	3106640	C3D8R	5E-8 (max)	PZT Voltage
Implicit	0.554 x 0.254 x 0.002	0.0005	3106640	C3D8R	5E-8 (max)	Nodal Displacement

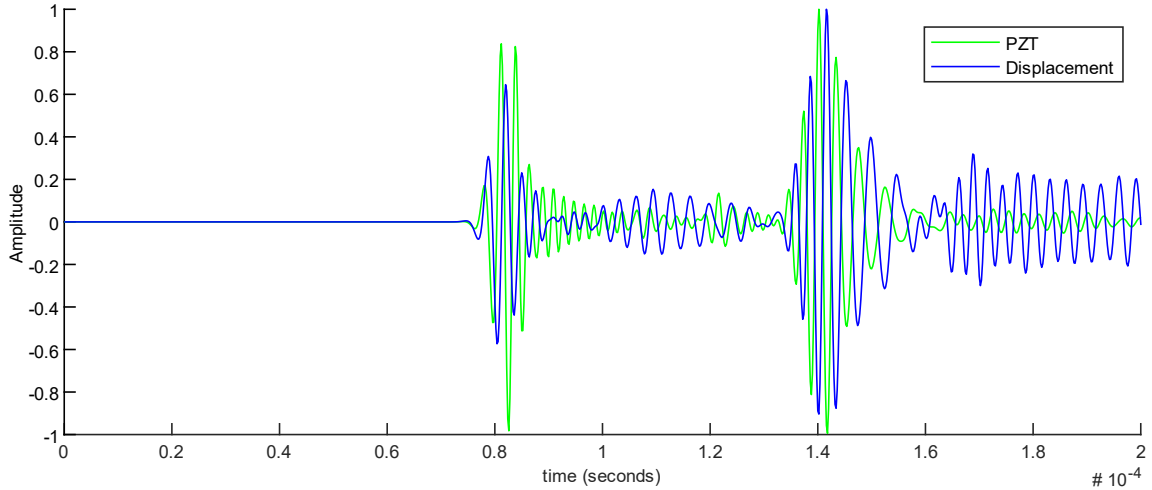


Figure 29: ABAQUS/Implicit FE model comparing the piezoelectric and displacement signal response.

The amplitude of both signal responses has been normalized with respect to the A_0 mode in Figure 29. Regardless, the piezoelectric and displacement signals do not align. However, if the displacement response is inverted the A_0 mode aligns well, see Figure 30. The S_0 mode still displays a slight mismatch between the piezoelectric and displacement signals. This is improved with a shift in the time domain, see Figure 31 (normalized with respect to the S_0 mode).

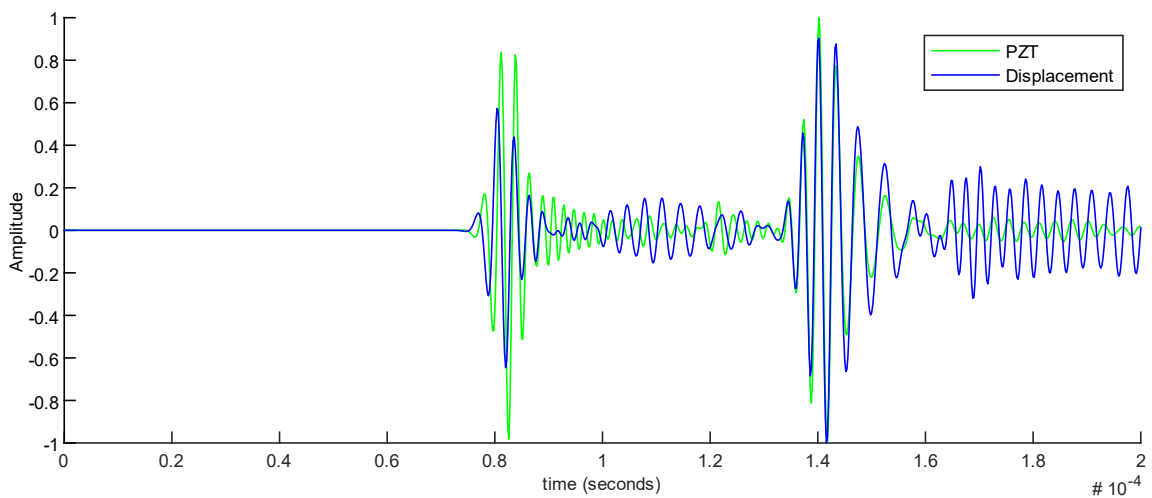


Figure 30: ABAQUS/Implicit FE model comparing the piezoelectric and inverted displacement signal response to align the A_0 mode.

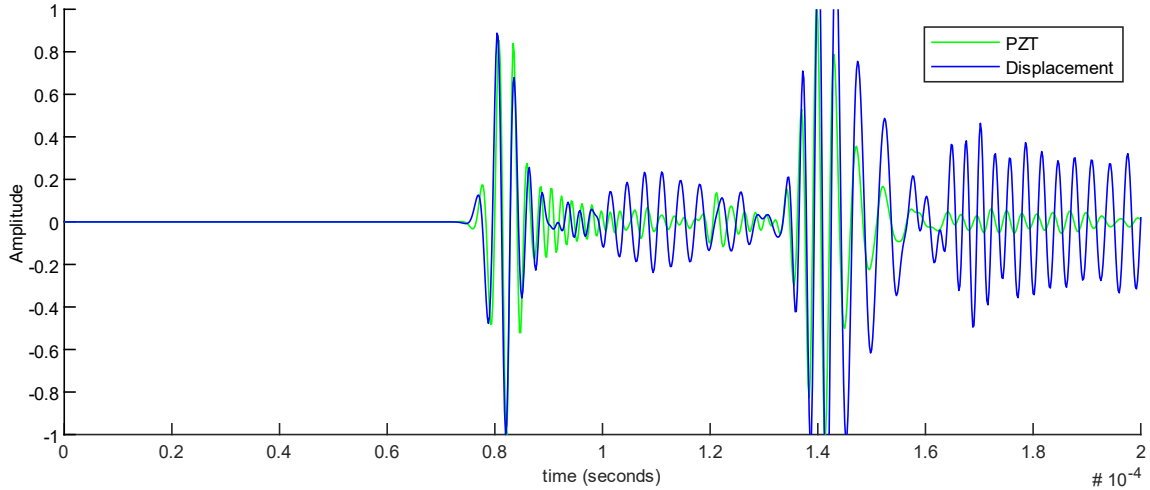


Figure 31: ABAQUS/Implicit FE model comparing the piezoelectric and inverted-shifted displacement signal response to align the S_0 mode.

The comparison of the piezoelectric voltage output and nodal displacement output indicates the displacement signal needs to be inverted and will have a small misalignment of the S_0 mode in the time domain. This needs to be considered when comparing experimental results with the ABAQUS/Explicit FE model which uses nodal displacement as an output.

3.4.2 FE Model Validation: ABAQUS/Explicit versus Experimental Results

The ABAQUS/Explicit model was validated against a CFRP experimental panel with material properties listed in Table 8. The CFRP panel was manufactured as outlined in Section 3.3.1 and an ultrasonic c-scan inspection performed by the National Research Council (NRC), Ottawa, Canada, as shown in Figure 32. The c-scan image displays minor inconsistencies as indicated by the colour discrepancy; however, the output signal still provided an acceptable baseline signal without any significant S_0 or A_0 reflections that would be associated with defects. This was confirmed by the similarities between the

experimental and ABAQUS/Explicit results. Further, Pant [21] indicated Lamb waves propagation lacked sensitivity to minor changes in CFRP material properties.

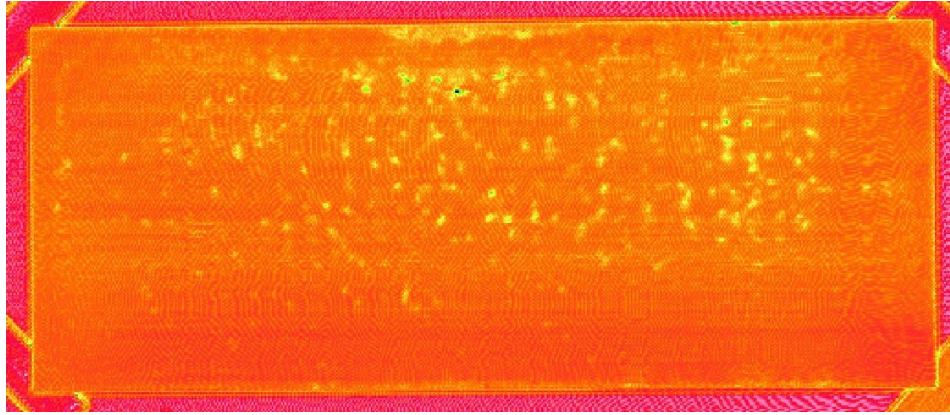


Figure 32: Ultrasound c-scan image of a CFRP without any embedded defects.

Two important considerations when comparing the ABAQUS/Explicit model and the experimental results include, first, the ABAQUS/Explicit model does not have piezoelectric elements available. Instead, concentrated forces are used to generate an input excitation and the nodal displacement are used as the output response to mimic the actuation and sensing behaviour of piezoelectric materials. The nodal displacement is the total displacement (x , y , z directions) of a point on the CFRP plate located at the center of the piezoelectric sensor. Second, the final material properties of a cured CFRP component are not the same as the published material properties provided by the material supplier (Table 8), which are used in the FE model. These two factors cause differences between the ABAQUS/Explicit model and the experimental results, see Figure 33 and Figure 34. A summary of the ABAQUS/Explicit model parameters is shown in Table 10.

Table 10: Finite element model parameters for the ABAQUS/Explicit model.

Model Type	Geometry (m)	Element Size (m)	Element Number	Element Type	Time Step (s)	Force Input
Explicit	0.572 x 0.272 x 0.00163	0.0004	8109908	SC8R	1.25E-7 (max)	Point Force (F1 & F2)

In Figure 33, the signals were normalized with respect to the input signals. The output signals are difficult to compare because the amplitude of the ABAQUS/Explicit output is small. Figure 34 normalizes the ABAQUS/Explicit signal with respect to the A_0 mode.

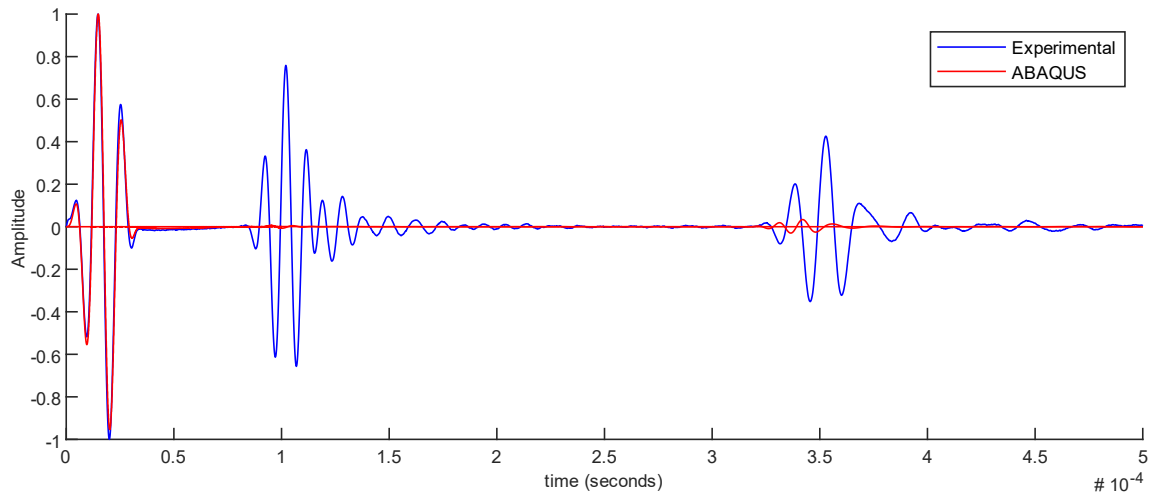


Figure 33: Experimental and ABAQUS/Explicit results for a CFRP panel.

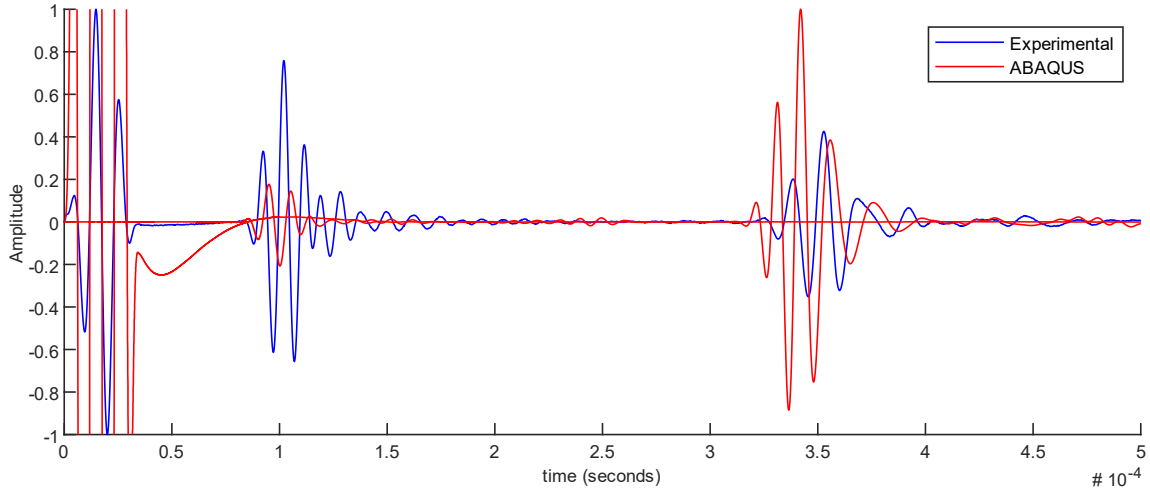


Figure 34: Experimental and ABAQUS/Explicit results for a CFRP panel with the ABAQUS results normalized with respect to the A_0 mode.

Figure 34 shows two main differences between the experimental and ABAQUS/Explicit response; first, the experimental results for the A_0 mode has a delayed response in the time domain. This delay is the result of the minor imperfections shown in c-scan image (Figure 32) and the cured CFRP specimen being different than the material properties listed in the manufacturer’s data sheet. The second difference highlighted in Figure 34 is the ratio of the S_0 and A_0 amplitude; the experimental results have a dominant S_0 mode whereas the ABAQUS/Explicit results have a dominant A_0 mode. This trend was identified in Figure 29 with the displacement output displaying a more dominant A_0 mode, indicating a limitation of the ABAQUS simulation when using nodal displacement as an output, not piezoelectric voltage. Further, any changes of the material properties of the cured CFRP specimen and the minor imperfections (Figure 32) could have also contributed to the reduced A_0 amplitude of the experimental panel.

The methods described in this thesis did not include the alteration (e.g., “tuning”) of the material properties used in the ABAQUS/Explicit model to match the experimental

results. The cured CFRP properties not only have variations from the manufacturer's data sheets, but also vary between specimens. Therefore, rather than alter the FE model to match a single cured CFRP specimen, this research focuses on understanding the changes caused by defects regardless of minor variations in material properties, which will always be present in real-world CFRP structures.

Figure 35 and Figure 36 compare the experimental and ABAQUS/Explicit results when the output is normalized and aligned to the S_0 and A_0 , respectively.

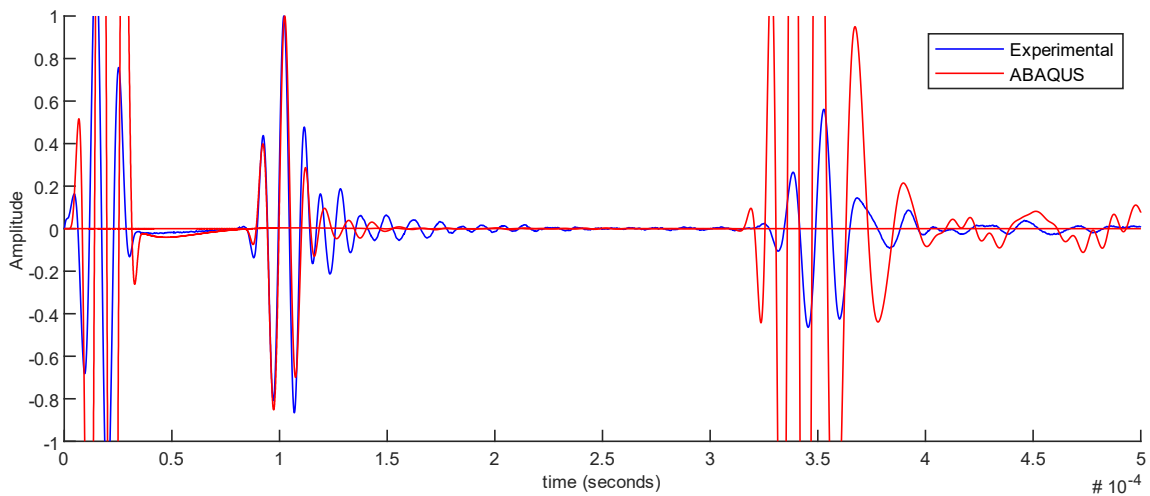


Figure 35: Experimental and ABAQUS/Explicit results for a CFRP panel with the ABAQUS results normalized and shifted to align the S_0 mode.

The alignment of the S_0 mode, in Figure 35, required the ABAQUS/Explicit signal to be inverted and shifted to the right by $2.12 \mu\text{s}$ (positive shift).

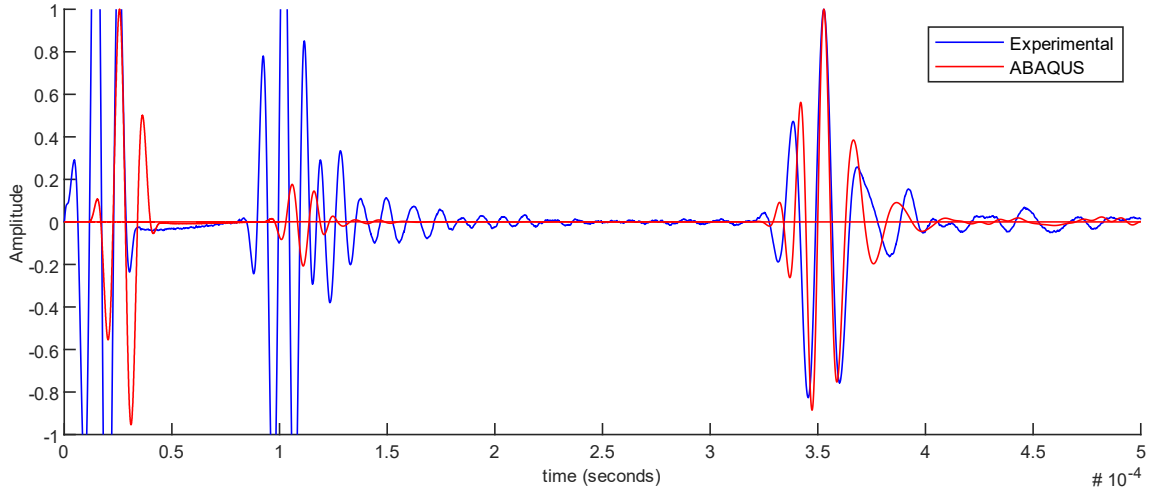


Figure 36: Experimental and ABAQUS/Explicit results for a CFRP panel with the ABAQUS results normalized and shifted to align the A_0 mode.

The alignment of the A_0 mode, in Figure 36, required the ABAQUS/Explicit signal to be shifted to the right by $10.7 \mu s$ (positive shift). The experimental A_0 signal appears more dispersive.

3.4.3 Continuous Wavelet Transform (CWT) Analysis

The time-frequency analysis provided by the CWT allows separate analysis of the S_0 and A_0 modes to identify how each mode is uniquely affected by the presence of a defect. The CWT plot, available in Matlab, provides an effective analysis to identify signal changes. A trained and skilled inspector could use the CWT plot to identify defects. However, additional analysis techniques are necessary for automated identification and detailed analysis of defect size, severity, and location. The CWT analysis is used to examine both ABAQUS simulations and experimental results to gain an understanding of the effects of different defect types. A summary of the ABAQUS model parameters used for each defect type is shown in Table 11.

Table 11: Finite element model parameters for the comparison of different defect types.

Model Type	Geometry (m)	Element Size (m)	Element Number	Element Type	Time Step (s)	Force Input
Explicit	0.572 x 0.272 x 0.00163	0.0004	8109908	SC8R	1.25E-7 (max)	Point Force (F1 & F2)

3.4.3.1 Reference Standard

The reference standard specimen is used to establish a defect-free baseline signal for comparison to specimens with an embedded defect. This allows for the specific changes resulting from different defect types to be identified. Figure 37 shows the A_0 mode wave propagating along the flat plate specimen ($t = 2.64 \times 10^{-4}$ s) with the corresponding edge reflections. The edge reflections amplitude has been significantly reduced due to the SRM layer, but not completely eliminated – this is beneficial when comparing the ABAQUS simulation to experimental results because the experimental results always contain edge reflections. At the time interval shown in Figure 37, the S_0 mode has already propagated across the plate surface and is absorbed by the SRM layer on the far (right) end of the plate specimen. The amplitude of the S_0 mode is smaller than the A_0 mode and difficult to see in the ABAQUS simulation plot without an increase in the amplitude scale.

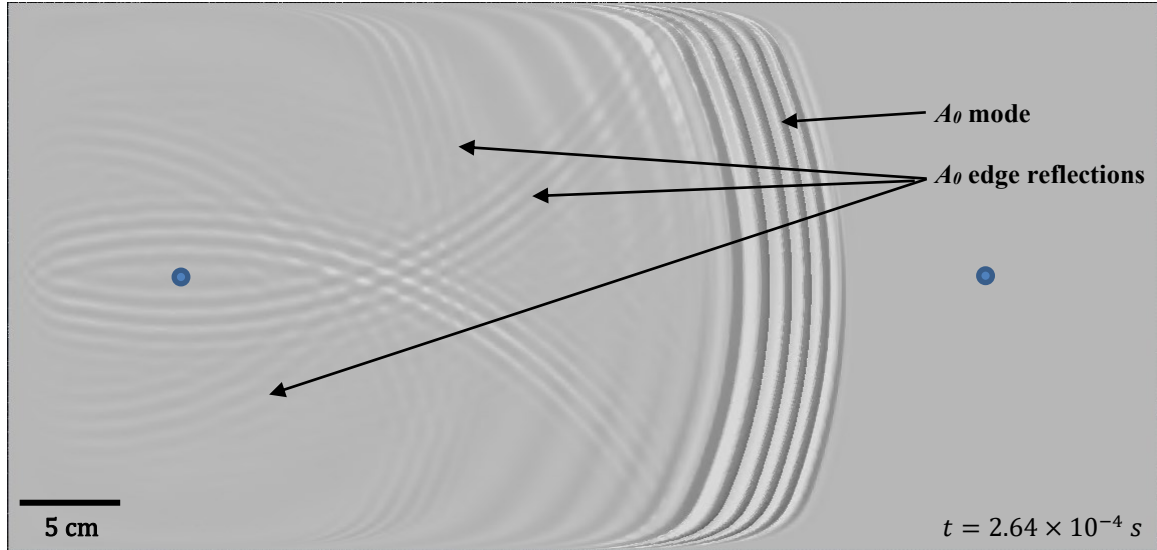


Figure 37: ABAQUS simulation of a reference standard specimen.

Figure 38 and Figure 39 show the signal response in the time domain and the corresponding CWT contour plot for the ABAQUS/Explicit simulation and experimental results, respectively. The CWT contour plot is constructed using the Morlet wavelet and the y-axis uses a logarithmic scale to allow a larger frequency spectrum. The input signal, S_0 mode, and A_0 mode are clearly distinct using the time-frequency domain of the CWT analysis. The experimental signal (Figure 39) displays additional wave cycles following the S_0 and A_0 modes that correspond to edge reflections. Additionally, the experimental A_0 mode is delayed in the time domain, which was identified to be a result of the differences between the ABAQUS model and experimental results, see Section 3.4.2.

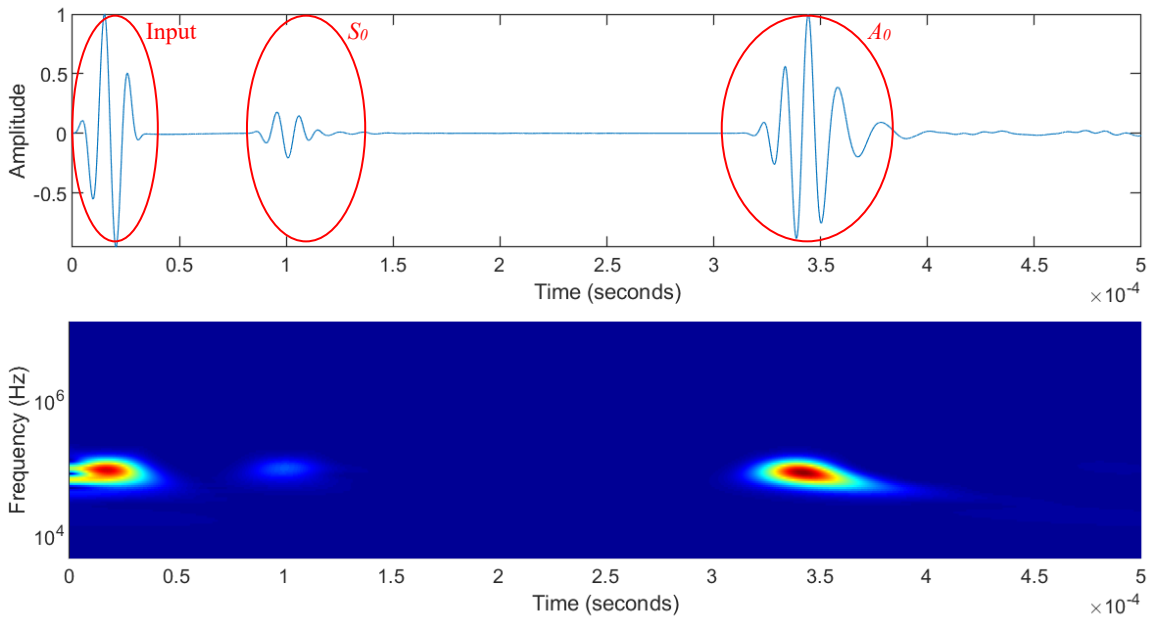


Figure 38: ABAQUS simulation signal for a reference standard specimen: time domain (top), CWT contour plot with logarithmic scale (bottom).

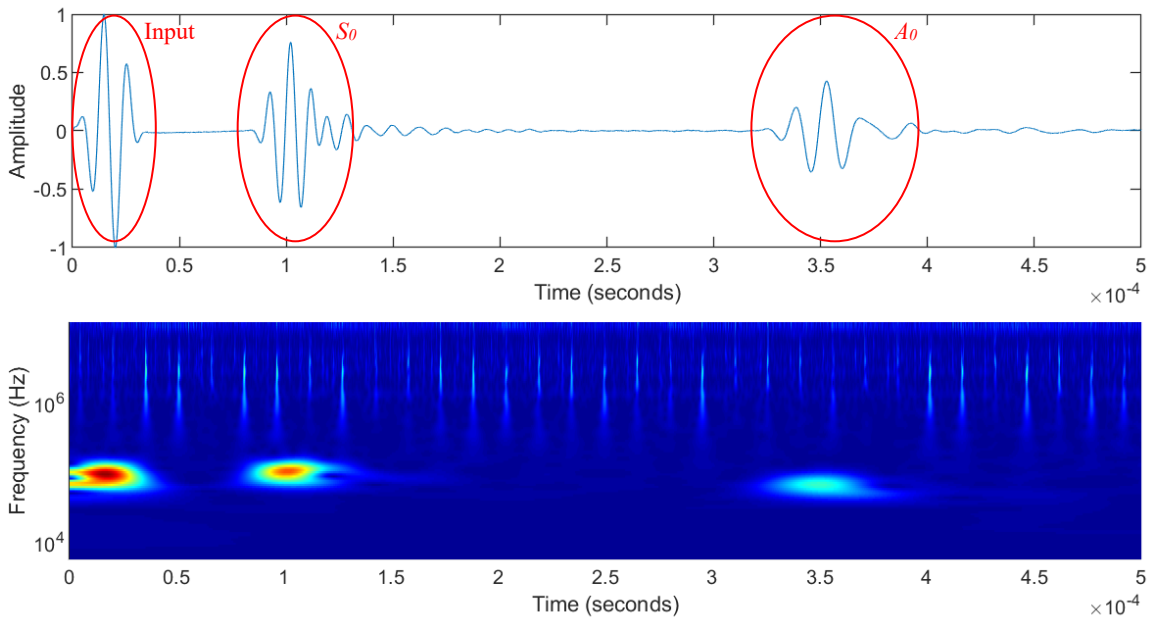


Figure 39: Experimental signal for a reference standard specimen: time domain (top), CWT contour plot with logarithmic scale (bottom).

Figure 40 compares the CWT contour plot for the ABAQUS simulation and experimental results using the Morlet wavelet and Biorthogonal 3.5 wavelet, respectively. These wavelets were selected to provide the best detailed analysis for each respective data set. In addition, the plot colour (ABAQUS – pink and experimental – jet) was used to best highlight important details for each data set. To provide additional detail, Figure 40 uses a frequency analysis in the range from 25 - 500 kHz.

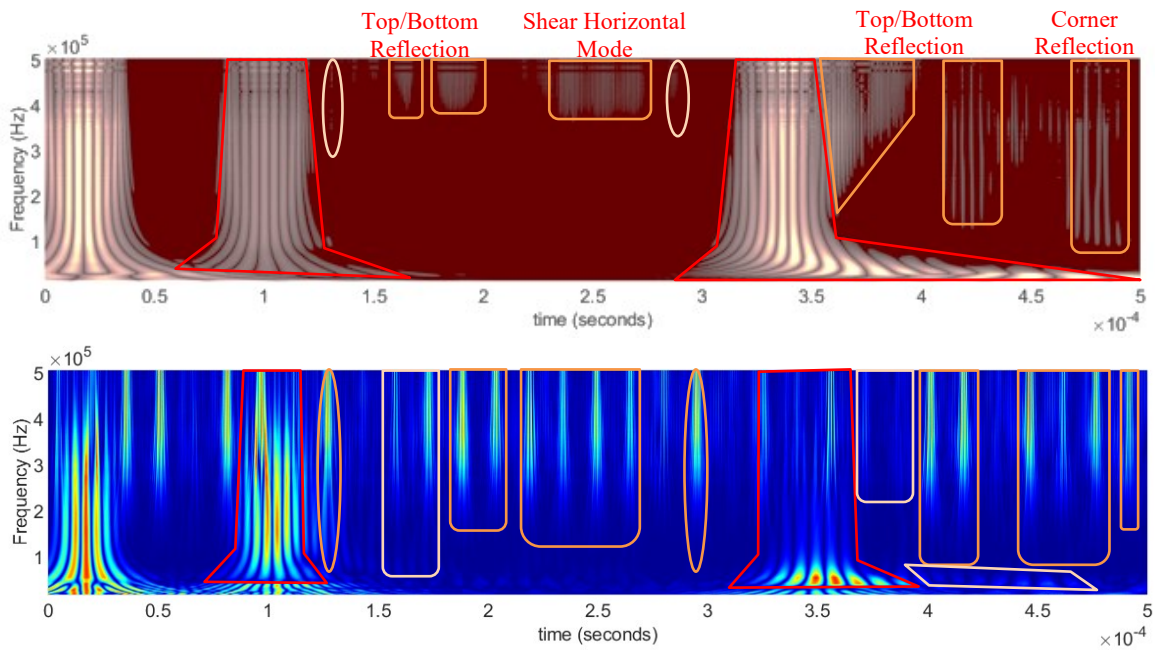


Figure 40: Comparison of the CWT contour plot for a reference standard specimen with a linear scale: ABAQUS simulation (top), experimental simulation (bottom).

Figure 40 identifies many similarities and corresponding features between the ABAQUS simulation and experimental results. For example, the reflections associated with the S_0 and A_0 mode in the ABAQUS simulation (oval and rectangular highlighted

regions) can be identified in the experimental results; a key difference is the frequency range of the reflections. The difference in the frequency can be attributed to the damping boundary region; the ABAQUS model applies the SRM boundary elements, as described in Section 3.2.2.4, whereas the experimental panel has modelling clay and tacky tape applied around the outside edge, as described in Section 3.3.3. This discrepancy in damping boundary layers affects which frequencies are absorbed and which frequencies are allowed to reflect back into the area of study (AoS). The important point is the ability to relate and compare these reflections between the ABAQUS simulation and the experimental results.

Further, Figure 40 highlights the findings from Section 3.4.2 (Finite element model validation), which indicated a delayed arrival time for the experimental S_0 and A_0 modes, and dominant mode reversal (S_0 versus A_0). Further, it can be seen the S_0 mode is non-dispersive while the A_0 mode is dispersive in the frequency range shown, with the low frequency waves travelling slower.

Although there are differences between the ABAQUS simulation and the experimental results, it is important to note the unique features identified in the ABAQUS simulation are present and identifiable in the experimental results – this will help identify and confirm different defect types.

3.4.3.2 Delamination Defect

Lamb waves travel along the top and bottom sub-laminates of a delamination defect generating reflections from the delamination edges. These reflections can also result in mode conversion. Figure 41 shows multiple time sequences of an ABAQUS simulation for a CFRP specimen with a 25.4 x 25.4 mm delamination defect located at the mid-

thickness layer (4 plies below the surface). When compared to Figure 37 (reference standard specimen) the reflections of the A_0 mode resulting from the delamination are clearly visible as they propagate in concentric circles away from the delamination. The instabilities associated with the delamination region are the result contact surface interactions defined in ABAQUS. These instabilities are increased when the contact surface interactions are altered (e.g., Normal = Hard or Tangential = Rough). The large scaling factor used in the simulation images, Figure 41, amplify these instabilities. However, they are confined to the delamination region and are numerical instabilities not physical instabilities.

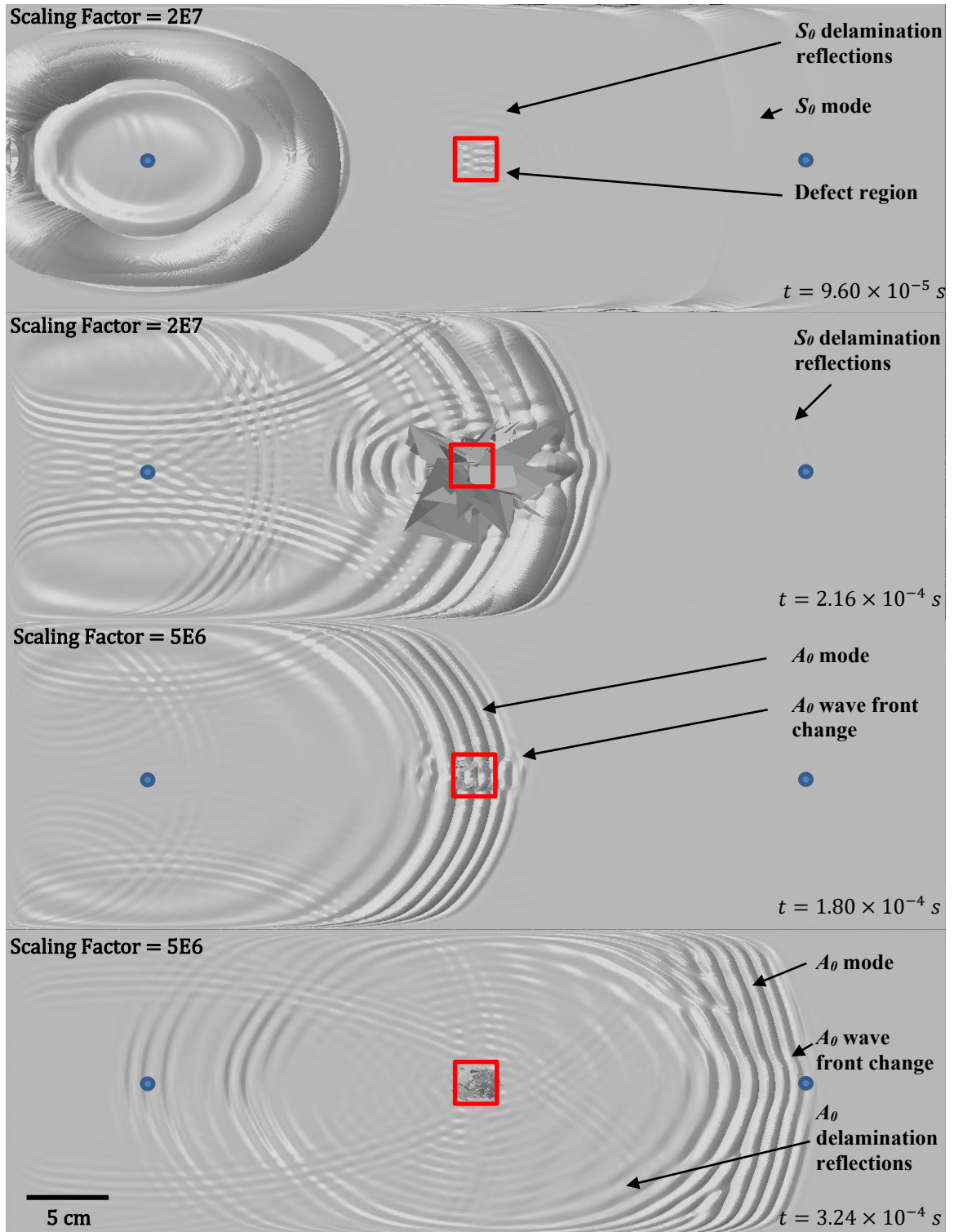


Figure 41: ABAQUS simulation of a CFRP specimen with a delamination defect located mid-thickness (ply 4).

Figure 42 shows a c-scan image of the experimentally manufactured panel. The delamination defect is clearly visible in the middle of the panel. The consistent colour in the surrounding areas of the panel indicates a high quality CFRP panel.

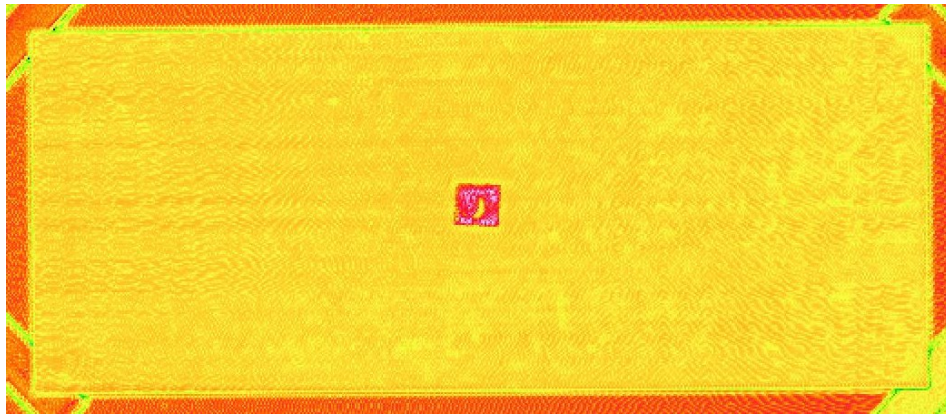


Figure 42: Ultrasound c-scan image of a CFRP panel with a mid-thickness delamination defect.

Figure 43 compares the CWT contour plot of the ABAQUS simulation and experimental results for the CFRP specimen with a mid-thickness delamination defect. The ABAQUS simulation when compared to the baseline ABAQUS simulation (Figure 40) has a slight time delay, which is associated with a lower velocity as the Lamb wave travels across the two delamination sub-laminate layers with smaller thicknesses. However, the experimental results when compared to the experimental reference standard signal, show the opposite effect – the A_0 mode arrives earlier when the delamination is present. This is the result of the material properties difference between the manufactured parts and highlights the need for a more robust defect signature than time of flight alone. Figure 32 and Figure 42 show the c-scan images of the baseline and mid-thickness delamination CFRP panels, respectively, and indicates the quality of the mid-thickness delamination panels is better.

Additional changes between the baseline simulation and the mid-thickness delamination are highlighted in Figure 43 by superimposing the important features of the baseline signals (dashed areas) and highlighting new features using solid green regions. The ABAQUS simulation highlights three main regions that are the result of the delamination defect: 1) shift in the S_0 reflections located between 2.5 to 2.7×10^{-4} s, 2) wave cycle preceding the A_0 mode wave, and 3) A_0 reflections. These three regions are also visible with the experimental results; however, they are located at a lower frequency.

The experimental results show a distinct A_0 reflection caused by the delamination defect, this can be seen as two wave packets – the initial A_0 mode and the A_0 delamination reflection separated with a region of low energy at 3.5×10^{-4} s. Finally, an important feature to highlight is the frequency range, from 41 – 55 kHz, for the region highlighted between 3.7 to 4.6×10^{-4} s and labeled “increased energy”. The frequency range of this region changes with the different defect types.

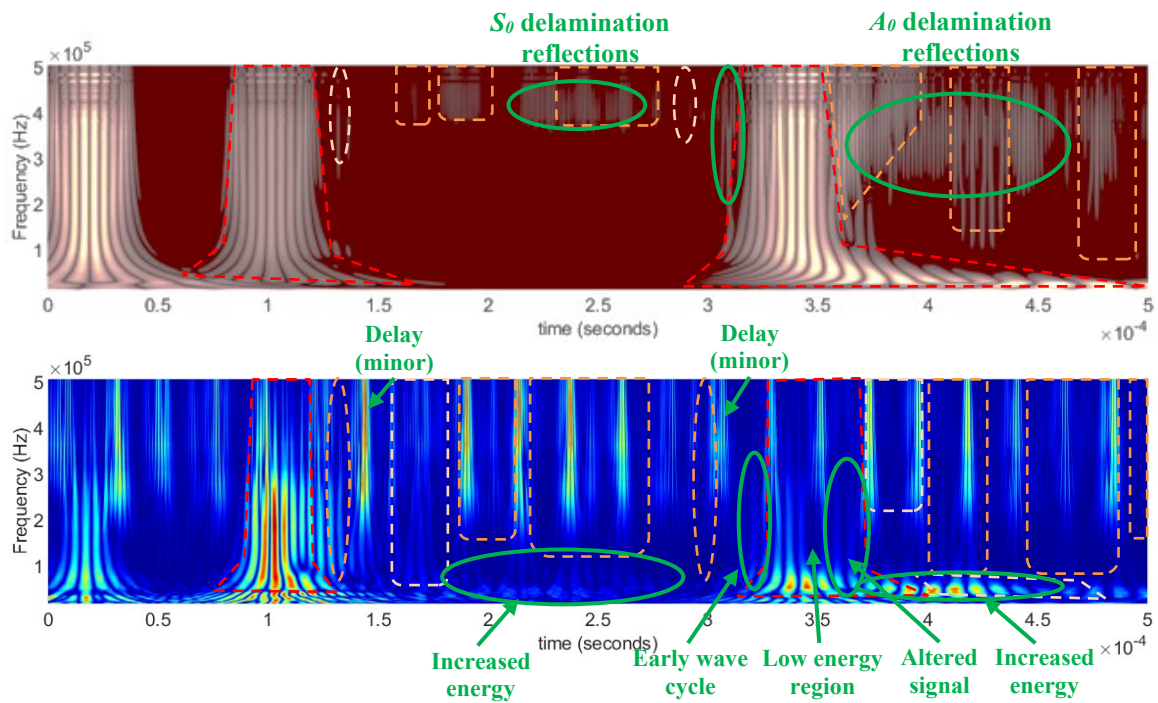


Figure 43: Comparison of the CWT contour plot for a CFRP specimen with a delamination defect (mid-thickness, ply 4): ABAQUS simulation (top), experimental simulation (bottom).

Additional analysis of a delamination defect was performed with a near surface delamination, located two plies below the surface. An ABAQUS simulation for a CFRP specimen with a near surface delamination is shown in Figure 44 with four different time steps. When compared to the mid-thickness delamination (Figure 41), the near-surface delamination is easier to identify; the amplitude of the delamination reflections are larger, particularly in the forward propagating direction, and the A_0 mode wave front is clearly altered after propagating across the delamination. For a near-surface delamination defect, when the top and bottom sub-laminates have different thickness values, the A_0 mode travels at different velocities across each sub-laminate. This causes changes to the wave front because they are not in phase when arriving on the far side of the delamination.

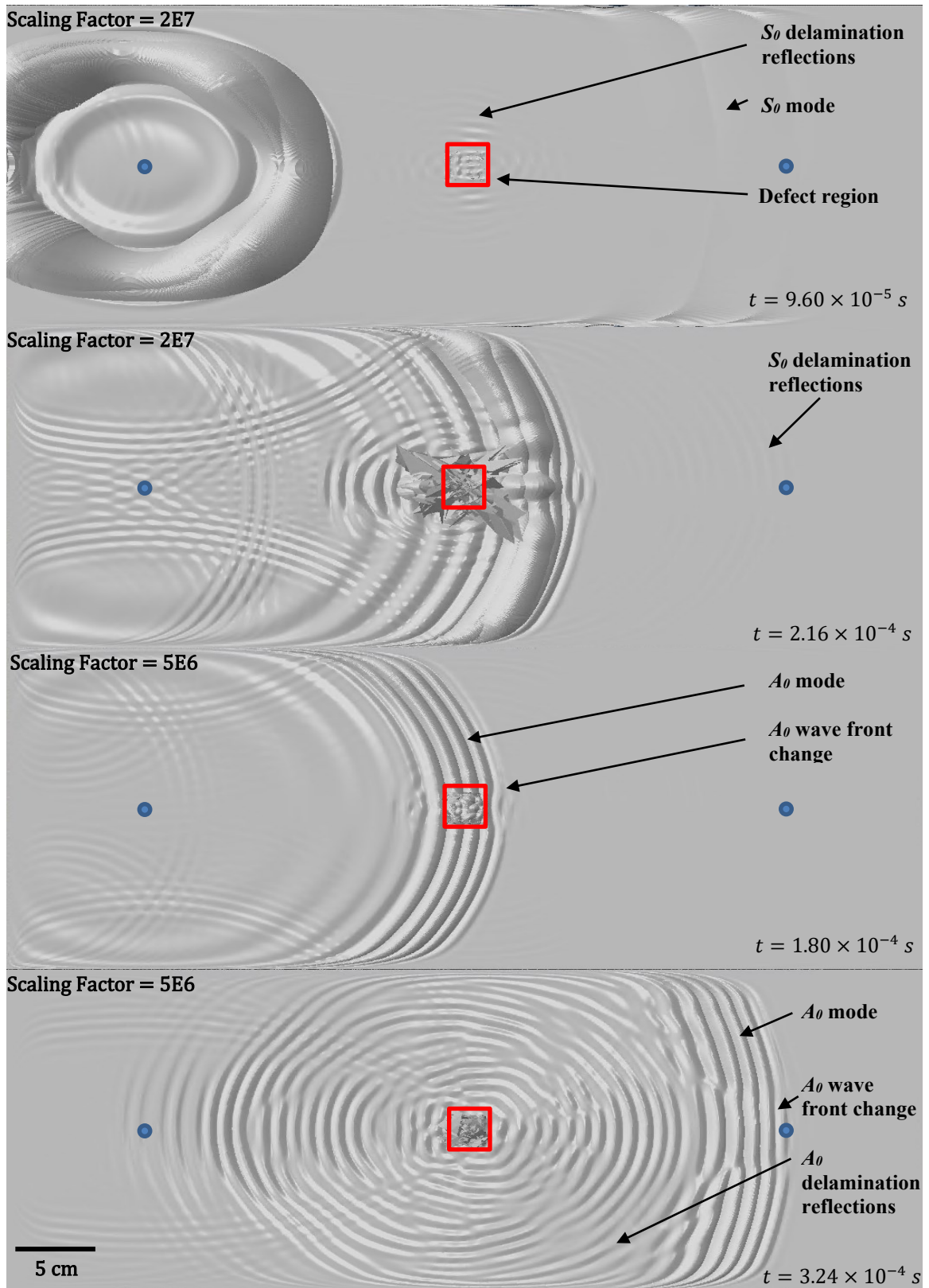


Figure 44: ABAQUS simulation of a CFRP specimen with a near surface delamination defect (ply 2).

Figure 45 shows a c-scan image of the experimentally manufactured panel with a near surface delamination defect. The delamination defect is clearly visible in the middle of the panel; however, it can be seen the quality of the panel is only average with areas of porosity or resin starvation. This increase in porosity and resin starvation increases the signal attenuation, thus reducing the amplitude of the output signal.

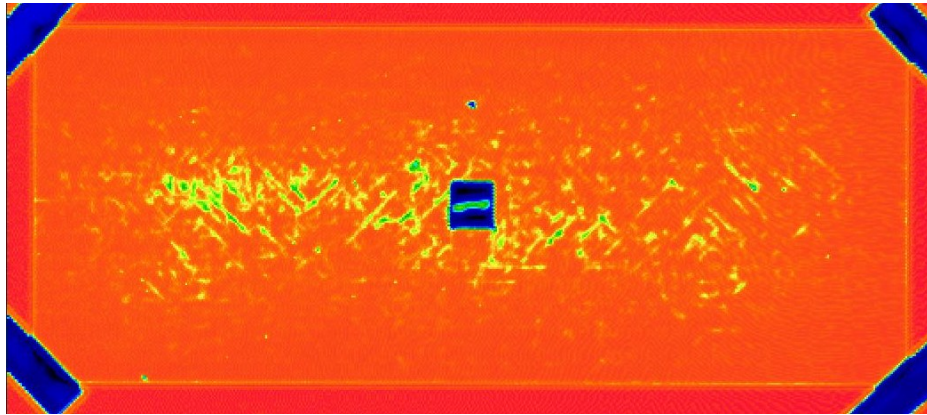


Figure 45: Ultrasound c-scan image of a CFRP panel with a near surface delamination defect.

The CWT contour plot for the near-surface delamination (Figure 46) shows the reflections from the delamination are easier to identify when compared to the mid-surface delamination, particularly for the A_0 mode. The CWT contour plot for the ABAQUS simulation confirms what can be seen in Figure 44 – continuous reflections from the delamination with additional periodicity of the wave group associated with A_0 mode travelling back and forth across the delamination. Similar to the mid-surface delamination, the ABAQUS simulation for the near surface delamination creates a slight time delay for the arrival of the Lamb waves. In addition, both the mid-surface and near surface delamination defects create similar signatures in the ABAQUS simulation, including: 1) shift in the S_0 reflections located between 2.5 to 2.7×10^{-4} s, 2) a small wave cycle

preceding the A_0 mode wave, and 3) A_0 reflections. The primary difference between the mid-surface and near surface delamination is the continuous and prominent A_0 reflections, as noted in Figure 44.

For the experimental results, the A_0 reflections show a distinct reflection at 3.6×10^{-4} s following a region of low energy at 3.5×10^{-4} s, similar to the mid-surface delamination. The experimental results also show a wave cycle preceding the A_0 mode wave. Overall, the experimental results display a lower peak amplitude of the S_0 and A_0 modes and their reflections, this is explained by the poorer quality of the manufactured CFRP panel as shown in Figure 45. Finally, as noted with the mid-surface delamination, the frequency range of the A_0 reflection between 3.7 to 4.6×10^{-4} s is 41 – 59 kHz. This frequency range is similar to the mid-surface delamination.

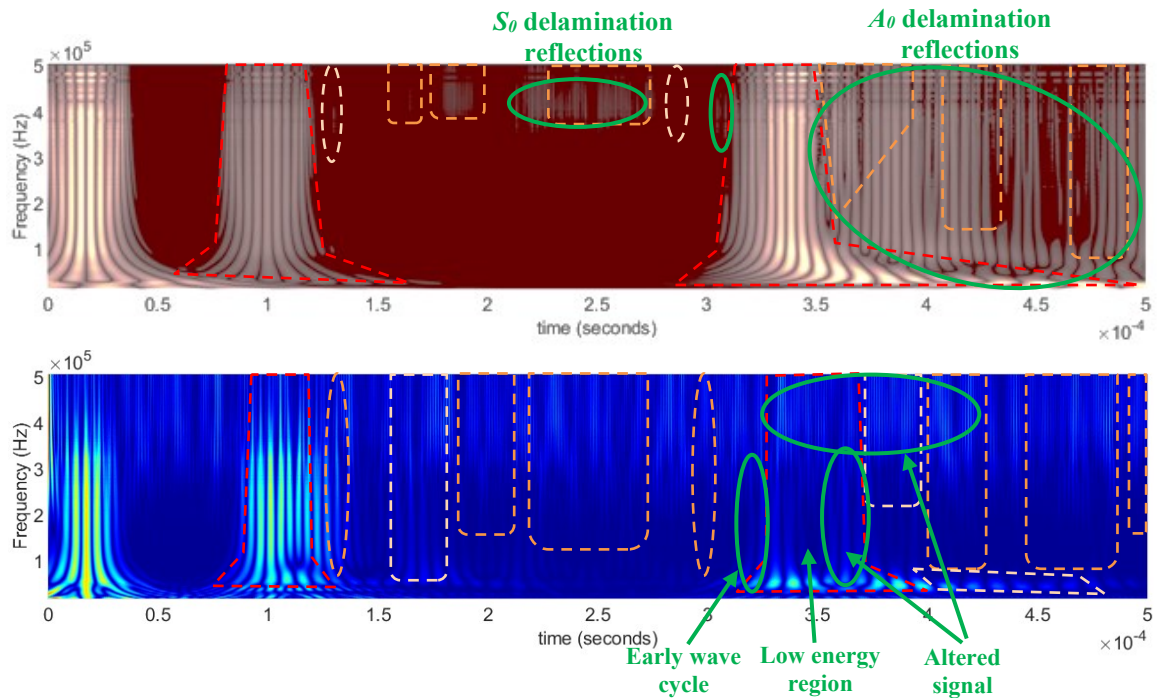


Figure 46: Comparison of the CWT contour plot for a CFRP specimen with a near-surface delamination defect (ply 2): ABAQUS simulation (top), experimental simulation (bottom).

3.4.3.3 Foreign Object

Foreign objects defects are bonded in the composite panel on all surfaces; however, they have a distinct difference in material properties. Unlike a delamination, the composite specimen remains solid through the thickness – it does not create top and bottom sub laminates. Figure 47 shows an ABAQUS simulation time sequence that highlight both the S_0 and A_0 mode as they interact with a foreign object defect. The reflections from the foreign object are clearly visible. When compared to a delamination defect the continuous nature of the reflections are missing. In addition, the S_0 and A_0 mode create distinct reflections when they reflect from the foreign object defect, unlike the delamination defect that creates continuous reflections as the Lamb wave travels back-and-forth across the delamination defect.

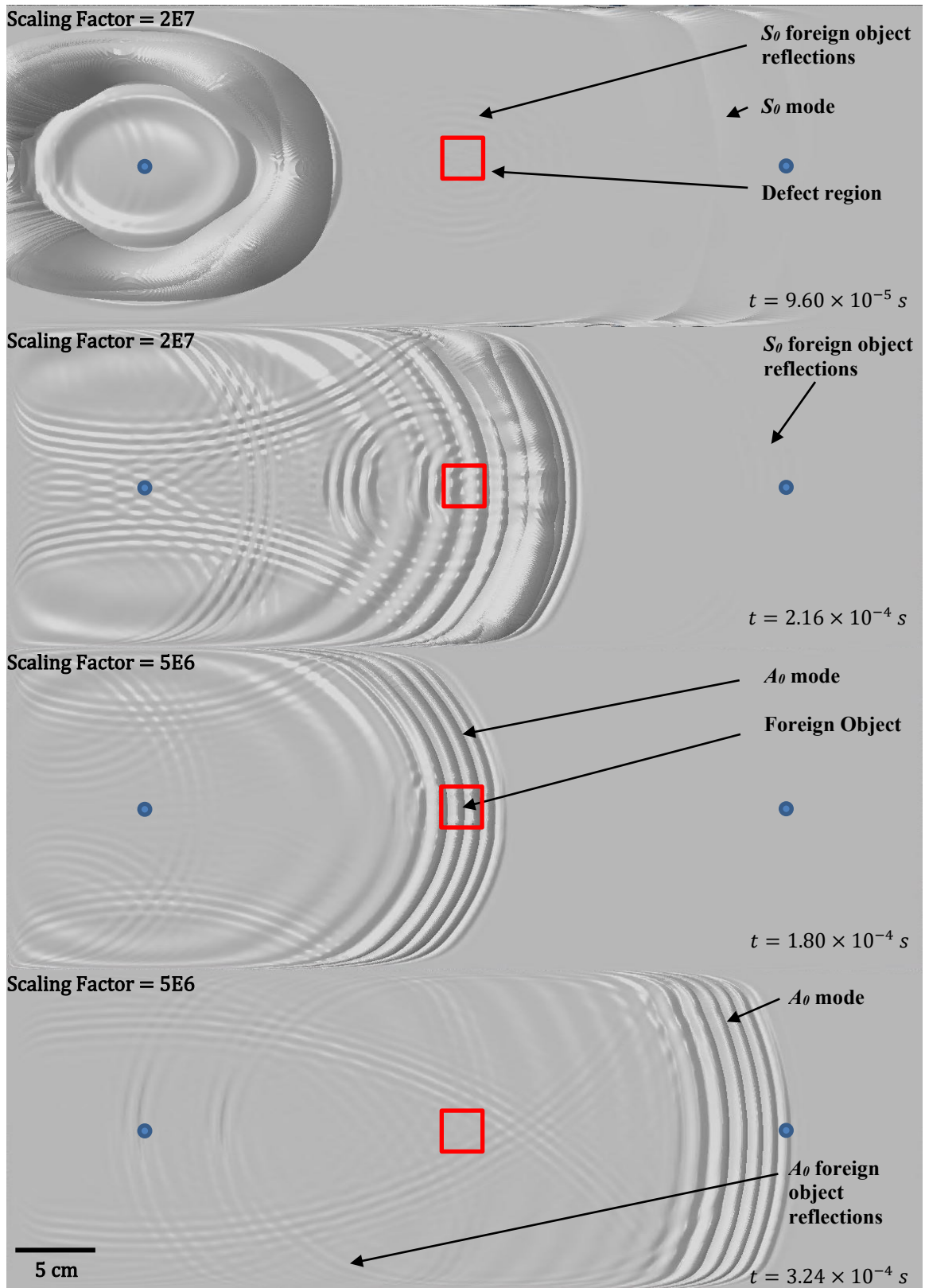


Figure 47: ABAQUS simulation of a CFRP specimen with a mid-surface foreign object defect (ply 4).

Figure 48 shows an ultrasonics c-scan image of a CFRP panel with a foreign object defect. The foreign object is clearly visible in the middle of the panel. The c-scan image shows the CFRP panels is of good quality, but it has some poorly compacted regions with minor voiding.

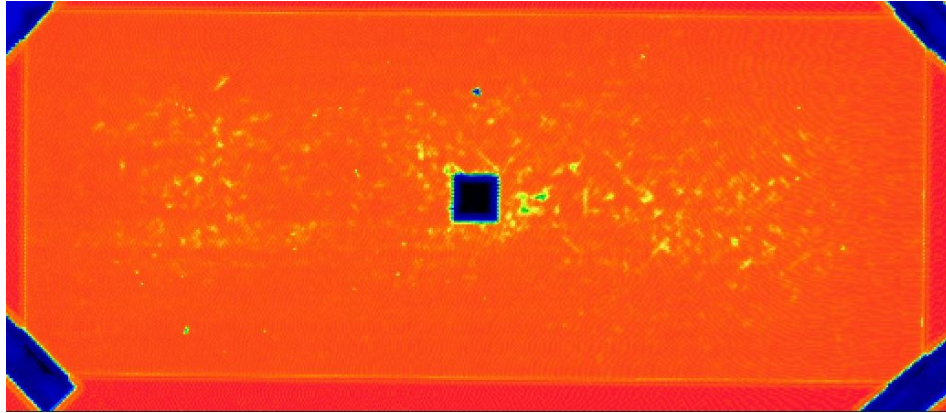


Figure 48: Ultrasound c-scan image of a CFRP panel with a foreign object defect.

The CWT contour plot for the ABAQUS simulation with a foreign object defect, Figure 49, indicates the foreign object defect is difficult to detect. Only small changes are evident when comparing it to the ABAQUS simulation for the reference standard (Figure 40). This agrees with the visual simulation results, in Figure 47, where the reflection in the forward propagating direction is difficult to identify. The important features of the reference standard are superimposed on Figure 49 with dashed lines and the green regions indicate unique features associated with the foreign object defect. The ABAQUS simulation shows the foreign object defect has a small increase in signal energy for the A_0 reflection at approximately $4.0 \times 10^{-4} s$.

The CWT contour plot for the experimental results show a distinct difference between the foreign object and baseline signals. The S_0 reflection has a significant increase

in signal energy and the A_0 mode has two distinct wave packets – the initial A_0 waveform ($t = 3.3 \times 10^{-4}$ s) and an A_0 reflection ($t = 3.8 \times 10^{-4}$ s). The experimental results also show the A_0 mode has significantly less energy than other defect types, with the initial A_0 waveform having less signal energy than the A_0 reflection. Finally, as noted with the delamination defects, the frequency range of the A_0 reflection wave packet is between 43 – 54 kHz. This frequency range is slightly smaller than the delamination defects.

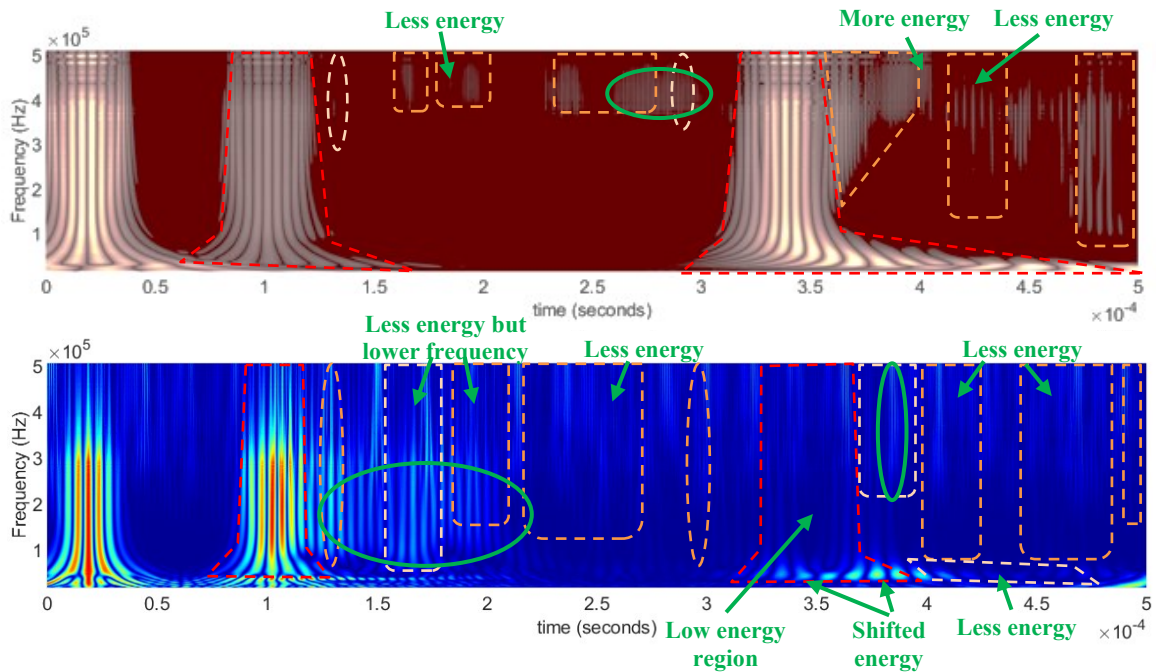


Figure 49: Comparison of the CWT contour plot for a CFRP specimen with a mid-surface foreign object defect (ply 4): ABAQUS simulation (top), experimental simulation (bottom).

3.4.3.4 Porosity

As noted previously, porosity is the accumulation of a large number of microvoids during the manufacturing process. The microvoids can be created from air, gas volatiles, or moisture. These microvoids are difficult to identify with bulk ultrasonic NDT methods, especially in low concentrations. Figure 50 shows multiple ABAQUS time sequences that highlight both the S_0 and A_0 mode as they interact with a concentrated porosity region. The S_0 reflection has a larger amplitude and is easier to identify when compared to the other defect types. However, it is still difficult to uniquely identify in the CWT contour plot in Figure 52. The S_0 and A_0 reflections have continuous concentric circles propagating outwards from the porosity region.

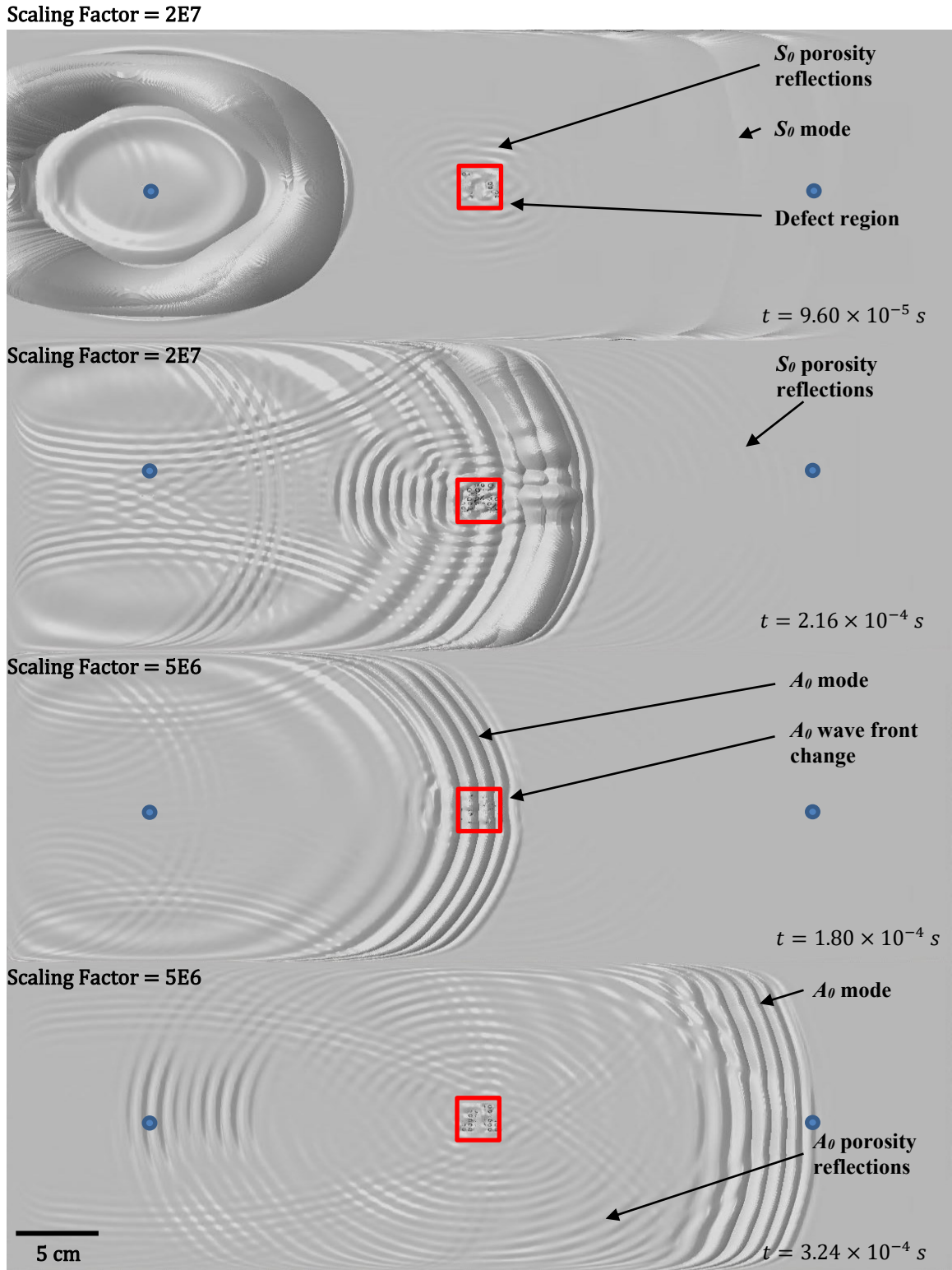


Figure 50: ABAQUS simulation of a CFRP specimen with a mid-surface porosity defect (ply 4).

Figure 51 is a c-scan image of the CFRP panel manufactured with a porosity defect. The 25.4 x 25.4 mm porosity defect is clearly visible in the middle of the panel. The consistent colour of the panel indicates a good quality CFRP panel with only minor voiding.

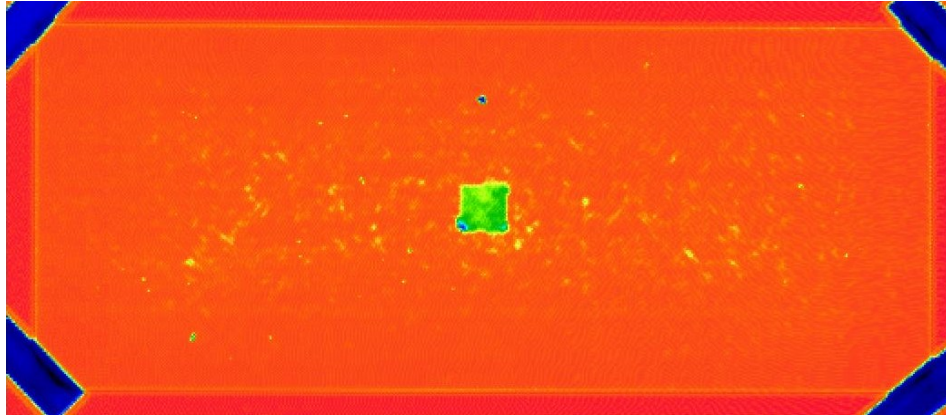


Figure 51: Ultrasound c-scan image of a CFRP panel with a porosity defect.

Figure 52 shows the CWT contour plots for a CFRP specimen with an area of high porosity. The ABAQUS simulation (top plot) highlights the changes created by the porosity defect when compared to important regions of the reference standard plot (dashed regions). The ABAQUS simulation comparison highlights the arrival time of the A_0 mode has a slight time delay, while the arrival time of the S_0 mode remains unchanged. Further, there is an increase in the S_0 reflections, which was not seen with other defect types. This increase in S_0 reflections is also identified in the ABAQUS time sequence images shown in Figure 50. Similarly, there is also an increase in the A_0 reflections.

The experimental results show the A_0 mode arrives early. As previously stated, the experimental arrival times of the S_0 and A_0 modes are highly dependent on the manufactured material properties and are not a good signature for the different types of

defects, on their own. The experiment results do show an increase in both the S_0 and A_0 reflections, as shown in the ABAQUS simulations. Finally, as noted with the other defect types, the frequency range of the A_0 reflection wave packet is between 35 – 63 kHz. This frequency range is larger than the other defect types and indicates a concentrated porosity defect creates reflections over a wide frequency band.

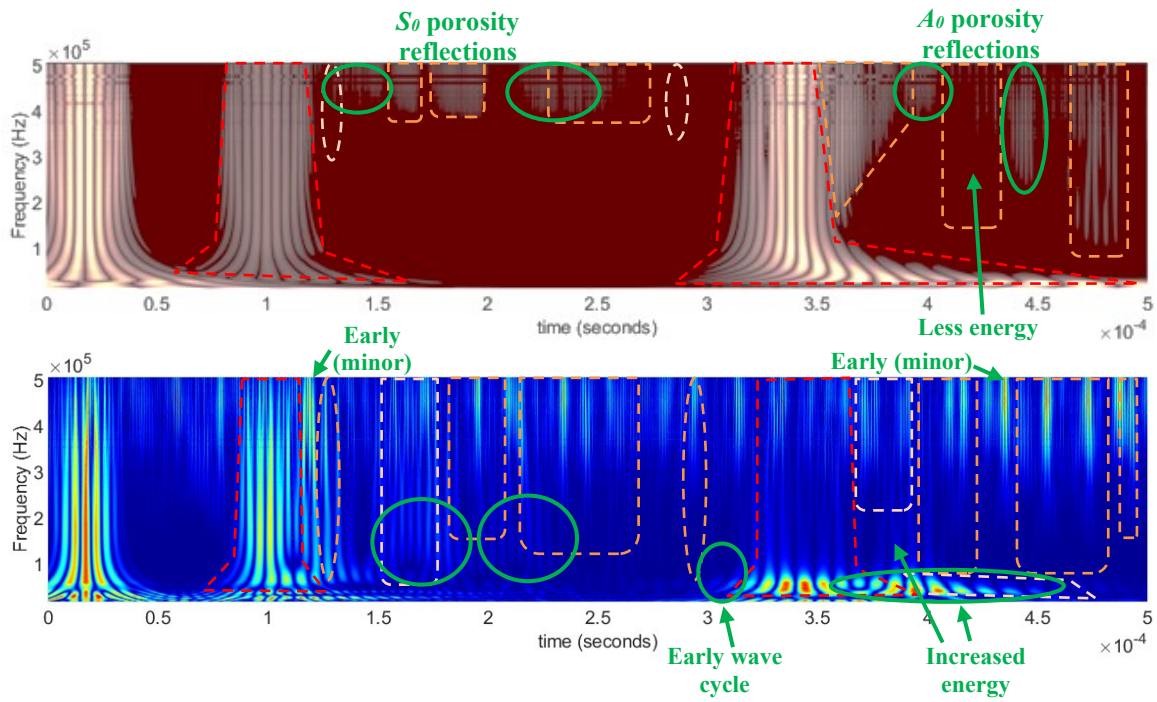


Figure 52: Comparison of the CWT contour plot for a CFRP specimen with a mid-surface porosity defect (ply 4): ABAQUS simulation (top), experimental simulation (bottom).

3.4.3.5 Defect Comparison

Gaining a better understanding of the influence of different defect types and their unique signatures will help develop a baseline free SHM system. This is important because the baseline signal varies with environmental conditions and changes in the CFRP material properties as the result of manufacturing. This chapter focused on defects that can occur

during the manufacturing process, including: delamination, porosity, and foreign objects. Each defect type had unique features that were identified using both an ABAQUS simulation and experimental results. These defect signatures are highlighted in Table 12.

Table 12: Defect type and signature feature.

Defect Type	Signature Feature				
	S_0 Reflections	A_0 Reflections	Early A_0 Wave Cycle	A_0 and $A_0^{(ref)}$ peaks	$A_0^{(ref)}$ Frequency Range
Delamination (mid-surface)	Minor	Yes	Yes	Similar	41 – 55 kHz
Delamination (near surface)	ABAQUS Only	Major	Yes	Similar	41 – 59 kHz
Foreign Object	Minor	Minor	No	$A_0^{(ref)}$ dominant	43 – 54 kHz
Porosity	Major	Yes	Minor	Similar	35 – 63 kHz

A further analysis of the experimental CWT contour plot divides the plot into 16 regions (Figure 53) to identify which areas have increased energy due to a specific defect type. This allows for direct comparison of the different defect types.

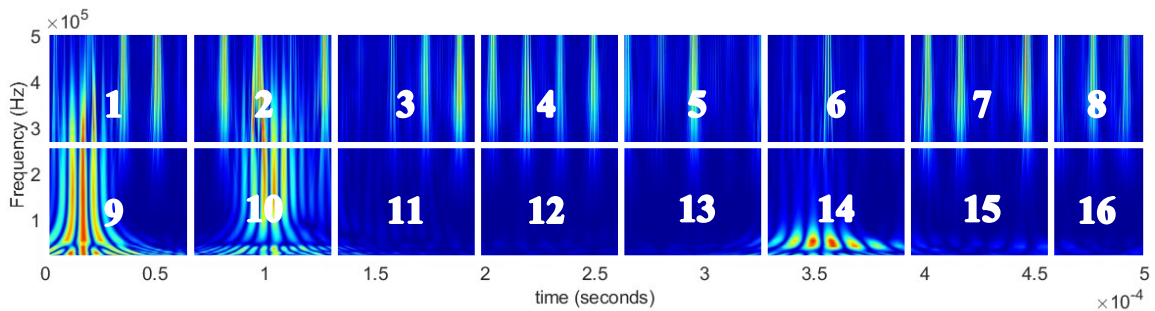


Figure 53: CWT contour plot divided into 16 regions.

Table 13 provides a summary of the regions with increased energy for each defect type. Table 13 highlights the similarity between the mid-surface and near surface

delamination because both regions 13 and 14 are affected. Porosity creates a unique signature with regions 11 – 12, 13, and 15 affected. The Foreign Object defect is the most difficult to detect with only regions 11 – 12 being affected.

Table 13: Defect type and associated CWT contour plot regions with changes in signal energy.

Defect Type	Regions with Increased Energy	Regions with Decreased Energy
Delamination (mid-surface)	12, 13, 14, 14 - 15	14 (mid)
Delamination (near surface)	13, 14	14 (mid)
Foreign Object	11 - 12	3, 4, 5, 7, 8 14 (mid), 15
Porosity	11 - 12, 13, 15	14 (mid)

All defects were clearly identifiable when compared to the baseline signal. This was evident from the A_0 mode being divided into two distinct wave packets separated by a region of low energy. The two distinct A_0 wave packets included the initial A_0 mode wave and the A_0 reflection.

3.5 Discussion

A holistic approach to SHM must include three important components: *in-situ* cure monitoring, manufacturing inspection, and in-service monitoring. This chapter focused on manufacturing inspection using Lamb waves, an area that has seen very little research. Three types of defects were studied: delamination (mid-surface and near surface), foreign object, and porosity. The goal of the research was to identify both the existence of a defect and determine the type of defect. This was completed using an ABAQUS finite element model and experimental testing.

The ABAQUS finite element analysis was performed using an Explicit method to reduce computational time; this came at the expense of the availability of piezoelectric elements for the actuator and sensor. Therefore, a 90 kHz 3-cycle sine wave was generated using balanced point loads in the x and y directions. The ABAQUS model was developed with continuum shell elements (SC8R) with one element per CFRP layer (8 layers) and an elements length of 0.4 mm (10 elements per wavelength). An absorbing boundary layer around the model edges was applied to reduce reflected waves.

The ABAQUS simulation results were validated against an experimental reference standard specimen, showing good agreement. Minor discrepancies with the arrival time of the S_0 and A_0 waves were the result of changes in the cured CFRP material properties, minor quality issues associated with the manufacturing process, and the lack of piezoelectric elements in the ABAQUS/Explicit model, as explained in Section 3.4.2.

The ABAQUS simulation provided visual time sequence images as shown in Figure 37 (reference standard), Figure 41 (mid-surface delamination), Figure 44 (near surface delamination), Figure 47 (foreign object), and Figure 50 (porosity). These visualizations clearly show the distinct response of the S_0 and A_0 modes when they interact with different defect types. A further time-frequency analysis was performed using CWT contour plots to differentiate the S_0 and A_0 modes and their corresponding defect responses. The CWT contour plots for the ABAQUS simulations displayed unique signatures for each defect type.

The delamination defect, Figure 43 and Figure 46, creates the following signatures: 1) S_0 reflections, 2) a wave cycle preceding the A_0 mode associated with a change in the A_0 wave front, and 3) continuous A_0 reflections. These features applied to both the mid-

surface and near surface delamination, with the near surface delamination experiencing more significant A_0 reflections. The foreign object defect, Figure 49, was the most difficult to identify. The signal response signature was limited to a minor increase in energy for the initial A_0 reflection. The porosity defect, Figure 52, created additional S_0 and A_0 reflections. The ABAQUS time sequence visualization (Figure 50) shows the porosity S_0 reflections are the easiest to identify when comparing all the defect types.

The experimental results captured similar features as the ABAQUS simulation, however, in some cases the frequency range was shifted. One potential explanation for this frequency shift is the different edge damping layers used for the ABAQUS simulation and experimental panels. These edge damping layers absorbed different frequency ranges, thus allowing different frequencies to be reflected back into the area of study, which could then superimpose with the S_0 and A_0 reflections.

The experimental results for the mid-surface delamination demonstrate that the S_0 reflections, between 2.5 to 2.7×10^{-4} s, occur at a lower frequency when compared to the ABAQUS simulation. These S_0 reflections were not clearly visible with near surface delamination, however, this is explained by the poorer quality of the CFRP panel as shown in the c-scan image (Figure 45). The experimental results for the delamination defect are similar to the ABAQUS simulation. The best approach to recognizing the delamination defect would focus on identifying the following signatures: two distinct wave packets for the A_0 mode and the A_0 reflection, followed by the continuous A_0 reflections with a lower frequency, and a wave cycle preceding the A_0 mode that indicates a change to the A_0 wave front.

The signal for the foreign object defect has significant changes when compared to the reference standard, however, unique signatures to distinguish it from other defect types are harder to identify. The best strategy is to identify the increased energy of the A_0 reflection, which creates two distinct wave packets - the A_0 wave and the A_0 reflection. The foreign object defect generates an A_0 reflection with a larger peak amplitude than the A_0 mode. Second, recognize that the A_0 wave and remaining S_0 and A_0 reflections contain less signal energy. Figure 49 shows an increased signal energy for the S_0 reflection at the mid-frequency range, however, it is believed that these reflections are the result of the minor voiding shown on the c-scan images (Figure 48) because this replicates the unique porosity signature.

The experimental results for the porosity defect display an increase in both the S_0 and A_0 reflections, see Figure 52. However, the two distinct signatures associated with porosity, include: 1) the S_0 reflections, and 2) the large frequency range, from 35 – 63 kHz of the A_0 reflections. As the A_0 mode interacts with a concentrated porosity region it increases the dispersion experienced by the A_0 mode. These two features help establish the unique signature associated with porosity.

3.6 Conclusions

This chapter identified the existence and type of three manufacturing defects: delamination, foreign object, and porosity. The unique defect signatures were identified using both an ABAQUS finite element model and experimental results. The analysis was performed using a CWT contour plot and showed:

1. All defect types created significant changes to the Lamb wave signal and were detectable.

2. The different defect types could be distinguished from each other.
3. The ABAQUS visualization images indicate a pulse-echo configuration would be useful to help identify the specific defect signature and to determine the defect location. Particularly, for the foreign object defect.

Overall, the results indicate a holistic SHM system based on Lamb waves can be used to identify and categorize common manufacturing defect types. The defect types selected for study; delamination, foreign object, and porosity, have been used to qualify a traditional ultrasonic NDT inspection system, such as the Boeing 787. This research used only a single actuator-sensor piezoelectric pair, proving a holistic SHM system is possible. This is an improvement over traditional bulk ultrasonic systems or Lamb wave research that requires a laser doppler vibrometer. Additional research must be completed to quantify the defect severity and location. The next two chapters will further examine a delamination defect to quantify the delamination size and depth. Future research will examine and quantify the foreign object and porosity defects. Finally, this research was limited to defects located in the center of a CFRP panel between a piezoelectric actuator and sensor. Therefore, future research will be required to determine the effects of defect position relative to the actuator and sensor and if additional actuator-sensor pairs are required. The ABAQUS visualization provided encouraging results that limiting the number of actuator-sensor pairs is possible due to the concentric waves propagating away from the defects in all directions.

Chapter 4: Input Signal Comparison

The dispersive and multi-mode nature of Lamb wave propagation makes it difficult to identify defects or unique features of a received signal. Therefore, an important first step in the detection of defects in CFRP composite structures is the selection of an input signal to limit dispersion and attenuation while being sensitive to a variety of defect types. This is achieved by selecting an input signal with an optimal frequency, wave type and shape, and number of wave cycles.

Much research has focused on optimizing the input signal to decrease dispersion and increase propagation distance [93][94][95]. Dispersion causes the wave packet to spread out, reducing the signal resolution and making it difficult to separate features associate with defects. The propagation distance of a wave packet determines the size of area that can be inspected. These two variables can be optimized using a narrowband tone burst input signal, which is commonly used in NDT and SHM applications. In Figure 54, Wilcox *et al.* [95] demonstrated the importance of selecting a narrowband tone burst input signal that provides good resolution by limiting the signal duration and reducing the amount of spreading out of the signal through dispersion. To easily identify a reflection or mode conversion from a defect, ideally the received signal would have narrow and distinct wave packets. Wilcox *et al.* [95] identified the best characteristics for a tone burst signal by calculating a “minimum resolvable distance” and concluded a 1-cycle sine and 7-cycle sine wave with a Hann window are optimal for the S_0 and A_0 modes, respectively. As a compromise, it has become common practice to use a 5-cycle sine wave with a Hann window for Lamb wave inspection.

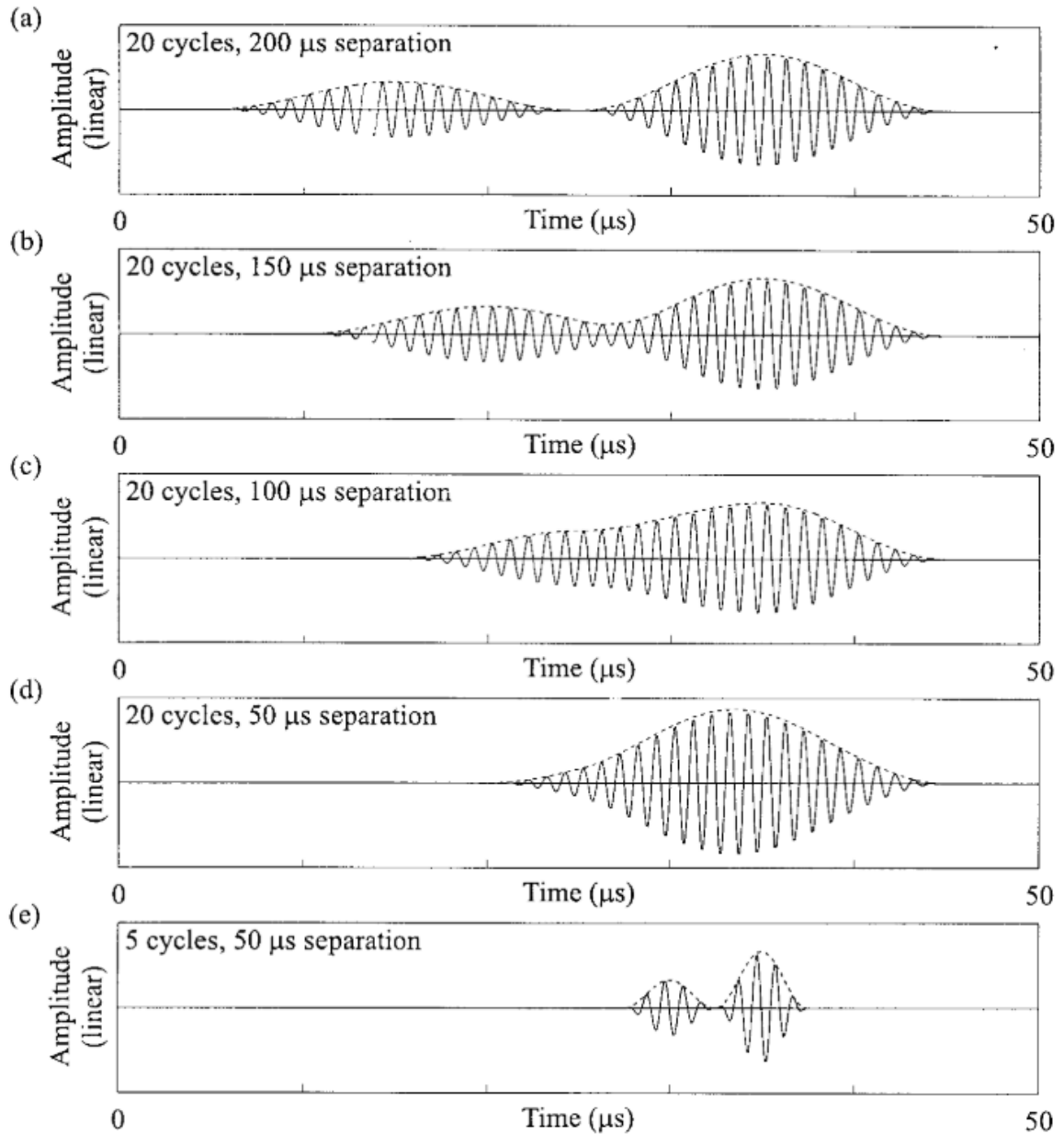


Figure 54: Predicted time-traces showing (a) two twenty-cycle wave-packets with centre frequency of 1 MHz completely separated in time. The effect of progressively reducing the separation between centres of the wave-packets is illustrated in time-traces (b), (c) and (d). Time-trace (e) shows the effect of reducing the number of cycles in the wave-packet to five while maintaining the same separation between the centres of the wave-packets as in time-trace (d), taken from [95].

A larger number of cycles narrows the frequency spectrum, reducing dispersion, but also increases the signal duration in the time domain, thus limiting the resolution. To overcome this problem, wave pulse compression techniques have been implemented to produce a Dirac delta type input signal. Lin *et al.* [96] compared four different signals that produce a Dirac delta type input signal when auto-correlation is applied, the signals include: linear chirp, nonlinear chirp, Barker code (BC) sine wave, and Golay complementary code (GCC) sine wave, see Figure 55. Lin *et al.* [96] found the linear chirp auto-correlation, with a frequency range of 0-150 kHz, had the narrowest main lobe width and thus the best resolution. However, the linear chirp had the largest sidelobes and the GCC had the smallest sidelobes. When compared to a 3-cycle sine wave with Hann window, the resolution of the linear chirp auto-correlation was 1.6-1.8 times better.

Hua *et al.* [97] applied the wave pulse compression technique with an additional time windowing function to improve signal resolution. Typically, narrowing the main-lobe width increases the side-lobe amplitude; therefore, Hua *et al.* [97] applied a pulse compression synthesis method to balance between optimal main-lobe and side-lobe characteristics. This included exciting a series of linear chirp waveforms with different windowing techniques, processing each response using pulse compression, and adding the resulting series of pulse compressed signals. Experimental testing of an aluminum plate with a through thickness cutout revealed promising results to increase resolution and establish distinct wave packets for defect reflections. Malo *et al.* [98] compared the wave pulse compression technique of a Barker coded sine wave and broadband linear chirp to a 10-cycle Hann window tone burst. The linear chirp autocorrelation excitation was found to have the best time-of-arrival, temporal-spatial resolution and the 10-cycle Hann window

had the worst. Zhou *et al.* [99] compared Barker code sine waves of different bit length (5,7, 11, and 13 bit) with different mother wavelet filters types (Daubechies, Symlet, and Coiflet) at different decomposition levels (4-8) and found a 13-bit Barker code sequence filtered using a Daubechies 7 discrete wavelet improved signal-to-noise ratio and peak amplitude of the received signal for air-coupled ultrasonic testing. Quaegebeur *et al.* [100] applied a sub-band decomposition method to a broadband chirp excitation. By decomposing the broadband excitation over several sub-band frequencies; improvements in time-of-flight measurements were achieved.

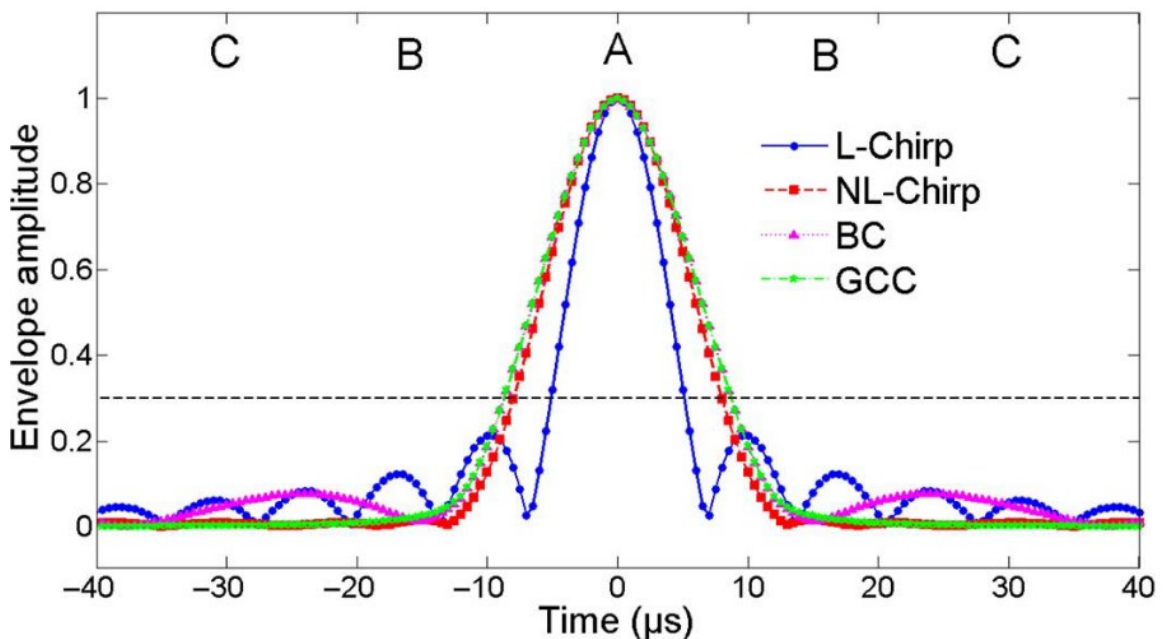


Figure 55: Comparison of auto-correlation curves for different excitation waveforms. Here, A indicates the main lobe region, B indicates the sidelobe regions, and C indicates the background regions, taken from [96].

A broadband chirp excitation signal can be used to extract multiple narrowband signal responses during post-processing if the frequency range of the narrowband signal is

within the frequency range of the broadband chirp excitation signal, thus saving the number of experiments that need to be performed. Michaels *et al.* [101] applied this technique to identify the optimal frequency to identify a specific defect. They applied a 50-500 kHz broadband chirp signal and the response to a variety of narrowband tone burst signals were extracted by deconvolution of the chirp response. Michaels *et al.* [101] found that a 3-cycle 100 kHz and 7-cycle 400 kHz tone burst signals provided the narrowest time and overall best response for the A_0 and S_0 wave, respectively. Michaels *et al.* [102] used this technique to locate weights glued to an aluminum plate to simulate potential defects. Dafydd and Khodaei [103] extracted multiple narrowband tone burst signals at a range of frequencies from a broadband chirp excitation, but focused on 75 kHz and 300 kHz to identify and characterize delamination and barely visible impact damage (BVID) using a laser doppler vibrometer. It was concluded the A_0 waveform was more sensitive at identifying damage severity, although the S_0 wave was still able to identify the damage through mode conversion.

Liu *et al.* [104] extended the concept of extracting narrowband signals from a broadband chirp by using PZT sensors on the top and bottom surfaces to provide mode purification. The received signals from the top and bottom PZT sensor were added and subtracted to obtain only the S_0 and A_0 , respectively. Although, it was not demonstrated in the research by Liu *et al.* [104], mode purification has the potential to effectively identify damage - if the actual structure can accommodate sensor on the top and bottom surface.

Feng *et al.* [86] applied a broadband chirp excitation to identify and size a delamination defect. It was proposed that as the delamination length increased, lower frequencies in the chirp signal would be disturbed. The analysis was limited to the S_0 wave

because it arrived first and only frequencies between 150 – 300 kHz due to amplitude problems. The S_0 mode wavelength is larger than the A_0 mode, thus increasing the minimum detectable defect. The results demonstrated the ability to differentiate between a 5 mm, 20 mm, and 40 mm delamination, however, specific defect sizing was not achieved.

The focus of the reviewed research has been to identify an optimal input signal that increases resolution and makes it easier to separate and identify the symmetric and antisymmetric modes. This present thesis research aims to extend these findings by determining if a specific input signal is more effective at identifying a specific type of defect, in this case a delamination. Each input signals acts as a forcing function when it interacts with a defect; therefore, different forcing functions could excite a different response from the defect of interest. This research will compare how a 5-cycle sine wave, 3-cycle sine wave, Mexican hat signal, 13-bit Barker code sine, an auto-correlated linear chirp, and a broadband chirp signal from 50 – 500 kHz interact with a delamination. This will contribute to the ability of an SHM system to effectively determine the severity of a defect.

This chapter is organized as follows: Section 4.1 provides the theory for each input excitation, Section 4.2 details the experimental methods and describes the finite element model used, Section 4.3 presents the results and highlights the input signal with the best signal resolution and signal-to-noise ratio for delamination damage, Section 4.4 discusses the results, and Section 4.5 provides a conclusion for the study.

4.1 Input Signal Theory

This section describes the six different input signals used to excite a Lamb wave in a flat aluminum plate using a lead zirconate titanate (PZT) piezoelectric actuator/sensor.

As mentioned in the previous section, the 5-cycle sine narrowband tone burst is the most widely used excitation signal for Lamb wave propagation, however, the benefits of the Dirac delta type pulse compressed signal of the Barker code sine wave and auto-correlated linear chirp have been used increasingly for Lamb wave excitation.

4.1.1 Narrowband Tone Burst Excitation

The narrowband tone burst signal contains a sine wave with a given number of cycles and a Hann window. The sine wave excitation signal is given by:

$$y(t) = \sin(2\pi ft), \quad 0 \leq t \leq N/f \quad (22)$$

where f is the frequency of the sine wave and N is the number of cycles (e.g. 3 or 5). The Hann window is defined by:

$$w(t) = \frac{1}{2} \left(1 - \cos\left(2\pi \frac{t}{T}\right)\right), \quad 0 \leq t \leq T \quad (23)$$

where the length of the window is $T = N/f$. Multiplying the sine wave function, $y(t)$, and the Hann window, $w(t)$, provides the desired input signal, as shown in Figure 56.

$$s_d(t) = w(t)y(t) \quad (24)$$

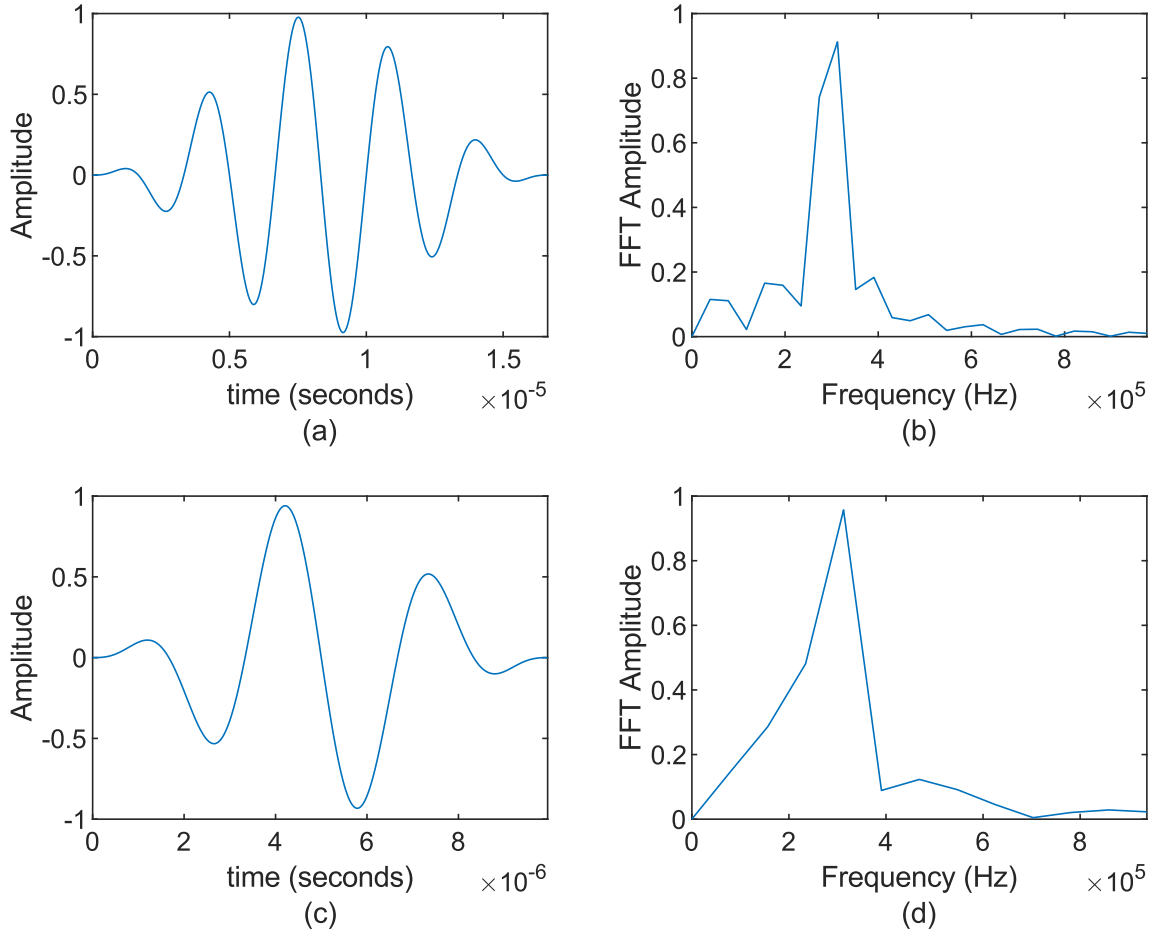


Figure 56: A 300 kHz narrowband tone burst signal, (a) 5-cycle sine wave, (b) FFT of 5-cycle sine wave, (c) 3-cycle sine wave, and (d) FFT of 3-cycle sine wave.

4.1.2 Mexican Hat Excitation

The Mexican hat narrowband tone burst excitation is defined by the Mexican hat wavelet, also called the Ricker wavelet, which is based on the second derivative of a Gaussian function. The Mexican hat excitation is defined as:

$$s_d(t) = \left(1 - \left(\frac{t}{a}\right)^2\right) e^{-(t/a)^2/2} \quad (25)$$

where a is the dilation parameter and can be used to modify the frequency of the excitation signal. Setting a equal to $\sqrt{2}/(2\pi) \times 300,000$ gives a peak frequency of 300 kHz, as shown in Figure 57.

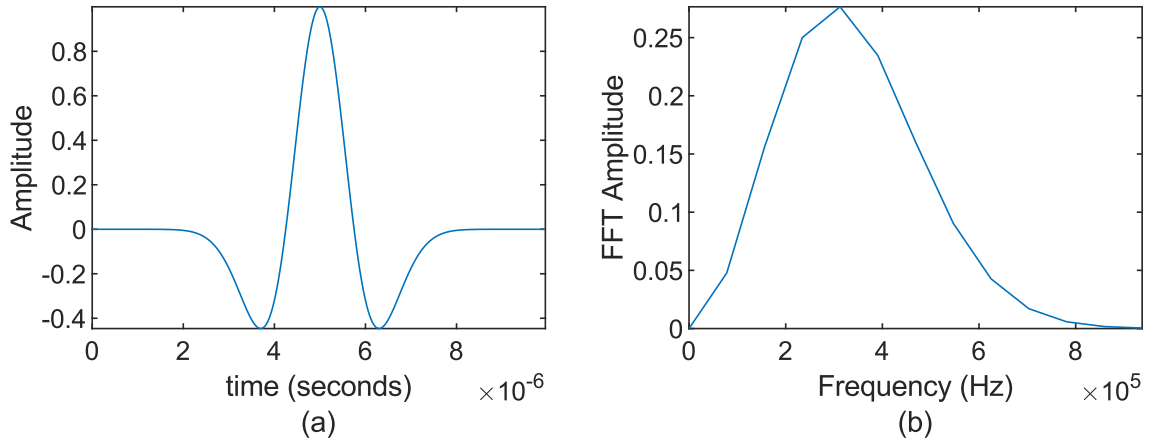


Figure 57: Mexican hat input excitation, (a) waveform when the dilation factor is set to provide a peak frequency of 300 kHz, and (b) FFT of Mexican hat.

4.1.3 Broadband Chirp Excitation

The broadband chirp signal is a sine wave that sweeps a linear range of frequencies, starting at a low frequency and extending to a high frequency. For this research, a constant amplitude sine wave from 50 to 500 kHz over a 200 μ s window will be implemented (see Figure 58), so the results can be compared to Michaels *et al.* [101]. The chirp excitation is defined as:

$$s_c(t) = w(t) \sin\left(2\pi f_0 t + \frac{\pi B t^2}{T}\right),$$

$$\text{where } w(t) = \begin{cases} 1, & \text{for } 0 \leq t \leq T \\ 0, & \text{for } t \geq T \end{cases} \quad (26)$$

where f_0 is the starting frequency (50 kHz), B is the chirp bandwidth (450 kHz), and T is the chirp duration (200 μ s).

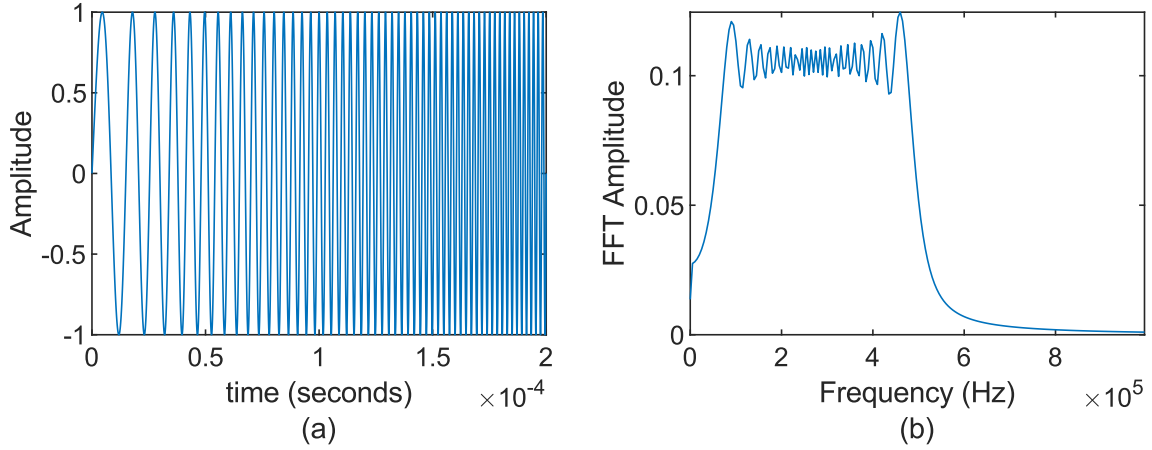


Figure 58: Broadband chirp excitation, (a) chirp signal from 50 - 500 kHz with a time duration of 200 μ s, and (b) FFT of chirp signal.

The desired response, $r_d(t)$, of the desired excitation signal, $s_d(t)$ – in this case a tone burst as defined in (24) or (25), is extracted from the chirp response, $r_c(t)$, in the frequency domain:

$$R_d(\omega) = R_c(\omega) \frac{S_d(\omega)}{S_c(\omega)} \quad (27)$$

where $R_d(\omega)$ is the desired tone burst response in the frequency domain, $R_c(\omega)$ is the measured response to the chirp signal in the frequency domain, $S_d(\omega)$ is the desired tone burst excitation (see (24) or (25)) in the frequency domain, and $S_c(\omega)$ is the chirp excitation (see (26)) in the frequency domain. $S_d(\omega)$ and $S_c(\omega)$ are both signals constructed using

Matlab not measured signals. Finally, $R_d(\omega)$ is converted to the time domain using an inverse Fast Fourier transform to obtain the desired response, $r_d(t)$.

$$r_d(t) = IFFT(R_d(\omega)) \quad (28)$$

4.1.4 Auto-Correlated Linear Chirp

The auto-correlation of a linear chirp signal produces a Dirac delta type input signal with a narrow main lobe and good resolution. The auto-correlation, R_{XX} , of a broadband linear chirp signal, as defined in (26), is given by:

$$R_{XX}(t_1, t_2) = E[X_{t_1} X_{t_2}^*] \quad (29)$$

where E is the expected value and $X_{t_2}^*$ is the complex conjugation of the linear chirp signal at t_2 . The auto-correlation of a linear broadband chirp excitation is shown in Figure 59.

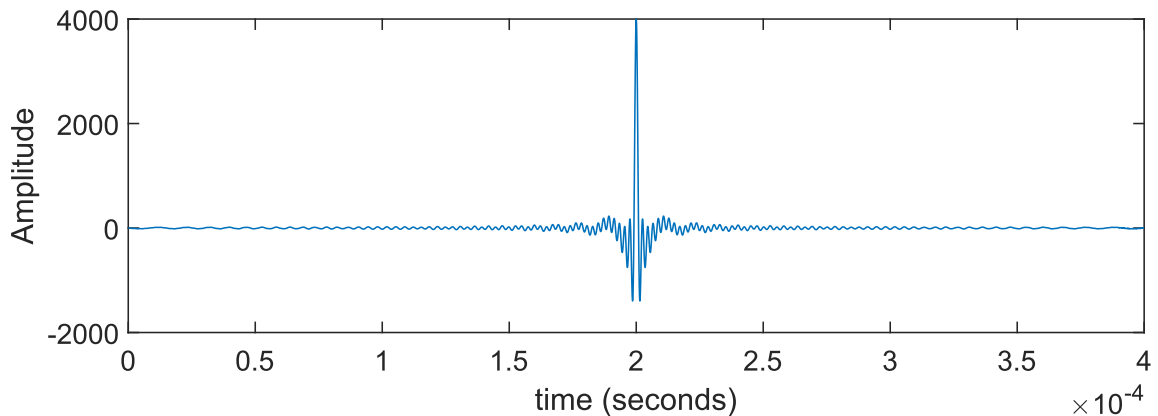


Figure 59: Auto-correlation of a linear chirp signal with a frequency range from 50 - 500 kHz and time duration of 200 μ s.

4.1.5 Barker Code Sine Wave

The Barker code (BC) sine wave also creates a Dirac delta type input signal, but with reduced sidelobes and slightly wider main lobe when compared to the auto-correlated linear chirp excitation. The BC consists of several +1 and -1 bits selected to create a Dirac delta type input signal. The BC can consist of 2, 3, 4, 5, 7, 11, and 13 bits. The greater the number of bits the larger the main lobe to side lobe ratio. Therefore, the present study implements a 13-bit BC. The BC N-bit sequence is defined as:

$$A[N] = [a_0, a_1, \dots, a_{N-1}], \text{ where } a_i \in \{-1, +1\} \quad (30)$$

The 13-bit BC is defined by:

$$13\text{bit BC} = [1, 1, 1, 1, 1, -1, -1, 1, 1, -1, 1, -1, 1] \quad (31)$$

The auto-correlation of a BC sequence creates a peak height of N (number of bits) and a side lobe peak of 0, +1, or -1, defined by:

$$R_{XX}(n) = \begin{cases} N, & n = 0 \\ 0 \text{ or } \pm 1, & n \neq 0 \end{cases} \quad (32)$$

To create a BC sine wave, when the BC bit is +1 or -1 that corresponds to a 0° or 180° phase shift of a single-frequency sine wave, respectively (see Figure 60).

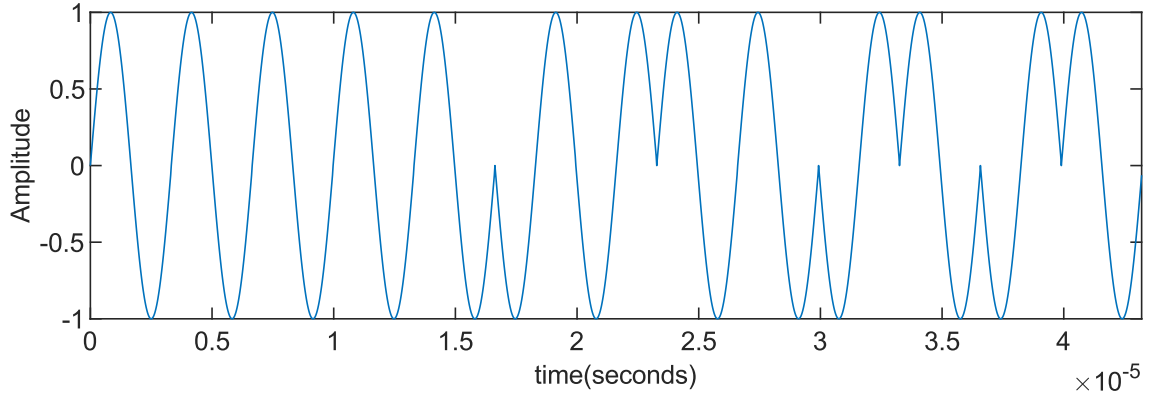


Figure 60: 13-bit Barker code 300 kHz sine wave.

The auto-correlation of a 13-bit Barker code 300 kHz sine wave and frequency plot are shown in Figure 61.

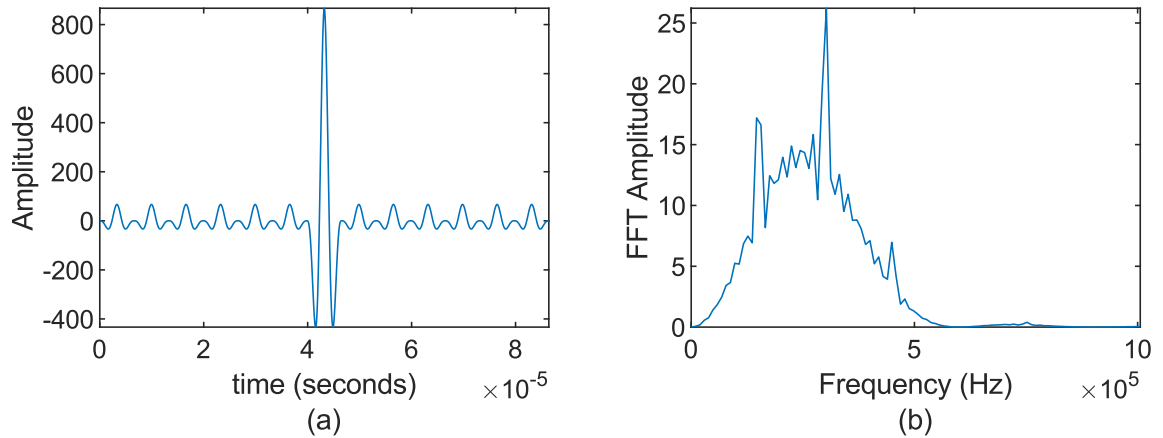


Figure 61: 13-bit Barker code 300 kHz sine wave, (a) auto-correlation, and (b) FFT of auto-correlation.

4.2 Simulation Methodology

Comparison of the input signals was completed using a 2D ABAQUS/CAE finite element (FE) model. The model was comprised of: an aluminum 5052 plate, a lead zirconate titanate (PZT) piezoelectric actuator and sensor with a pitch-catch configuration,

and a cohesive layer between the aluminum plate and piezoelectric sensors using Loctite Ultra™ contact adhesive. A summary of the model parameters used to compare the excitation signal is shown in Table 14.

Table 14: Finite element model parameters for the excitation signal models.

Model Type	Geometry (m)	Element Size (m)	Element Number	Element Type	Time Step (s)	Force Input
Implicit	1.0 x 0.00206	0.00024	125380	CPE4R	5E-8 (max)	Voltage

The focus of this chapter is to compare the changes associated with each signal type; the aluminum plate will demonstrate this while providing a significant reduction in the ABAQUS computational time by reducing the number of elements through the thickness (i.e., CFRP panels are modelled with one element per lamina layer).

4.2.1 Material Properties

The 5052-aluminum plate had a Young's modulus of 69.6 GPa, a Poisson's ratio of 0.33, a density of 2684 kg/m³ [105], and dimensions of 2.5 m x 0.002 m, see Figure 62. A delamination was introduced by separating the FEM nodes in the region of interest. A 0.0254 m long delamination was created at a depth of 0.0005 m below the surface.

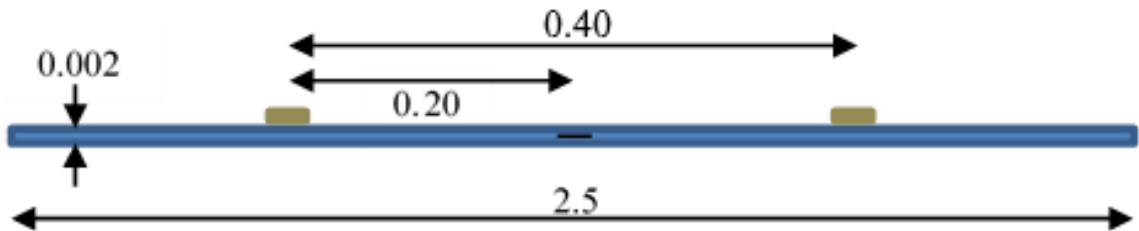


Figure 62: Schematic of 2D aluminum plate with piezoelectric sensors (not to scale).

The Loctite Ultra™ contact adhesive had a Young’s modulus of 1.5 GPa, a Poisson’s ratio of 0.35, a density of 1050 kg/m³, and dimensions of 0.00635 m x 0.00002 m.

The PZT properties were based on an APC International Ltd. sensor, model number 70-3000, which has a diameter of 0.00635 m and thickness of 0.000254 m. The PZT material was an 850 Navy type II equivalent with the material properties shown in Table 15. The piezoelectric charge constants are represented by d_{33} , d_{31} , and d_{15} , and the relative dielectric constant are given by k_{11} , k_{22} , and k_{33} . This thesis uses the term “sensor” for both the piezoelectric sensor and piezoelectric actuator to indicate it is the same device, which can perform either function.

Table 15: Piezoelectric PZT material properties.

Property	Value
$E_{11} = E_{22}$	63 GPa
E_{33}	54 GPa
$G_{13} = G_{23}$	24 GPa
G_{12}	29 GPa
$\nu_{12} = \nu_{31} = \nu_{32}$	0.31
d_{33}	$400 \times 10^{-12} \text{ C/N}$
d_{31}	$-175 \times 10^{-12} \text{ C/N}$
d_{15}	$590 \times 10^{-12} \text{ C/N}$
$k_{11} = k_{22}$	1900
k_{33}	1320
ρ	7600 kg/m ³

4.2.2 Finite Element Model

The model was executed using ABAQUS implicit so that piezoelectric elements could be implemented; piezoelectric elements are not available in ABAQUS explicit. The recommended number of elements per wavelength is between 10 – 20 [81][80][82].

$$L_e = \frac{\lambda_{min}}{20} \quad (33)$$

where, L_e is the element size and λ_{min} is the smallest wavelength to be modelled. With a maximum frequency of 500 kHz, this study implemented an element size of 0.00024 m, giving approximately 25 elements per wavelength for the A_0 mode. The elements were 4-node plain strain quadrilateral, CPE4R.

The recommended time step to ensure numerical stability is given by [80]:

$$\Delta t = \frac{1}{20f_{max}} \quad (34)$$

where Δt is the integration time step and f_{max} is the highest frequency of interest. Therefore, with a maximum frequency of 500 kHz, the recommended time step is 1×10^{-7} . This study used a time step of 5×10^{-8} .

4.3 Results

Previous research has shown that as an A_0 Lamb wave mode encounters a delamination it travels independently along the top and bottom sub-laminates, reflecting from both ends of the delamination [61][106][107], see Figure 63.

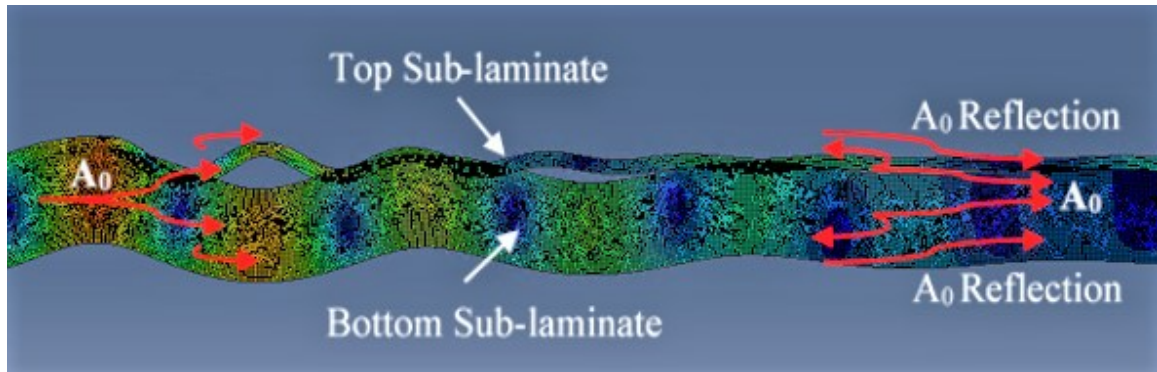


Figure 63: Abaqus FEM interaction of the A_0 mode with a delamination.

The objective of the present research is to identify an input signal and frequency that will improve the resolution and signal-to-noise ratio of the A_0 reflection associated with delamination damage. The following steps were completed to accomplish the above objective: 1) confirm the broadband chirp signal, defined in Section 4.1.3, is accurate for the extraction of the desired input signal response, 2) find the frequency range capable of identifying delamination damage for each of the five input signals, 3) determine the resolution of the S_0 , A_0 , and A_0 reflection wave packets by calculating the main lobe width (MLW), 4) calculate the signal-to-noise ratio (SNR) of the A_0 reflection wave packet, and 5) identify which input signal has the broadest frequency range for identifying delamination damage.

4.3.1 Broadband Signal Reconstruction using a Chirp Signal

The broadband chirp signal, defined in Section 4.1.3, can be used to extract the desired input signal response from the broadband chirp response. This reduces the number of FE simulations that need to be performed – only a single simulation is required for the broadband chirp signal; all other signal responses are extracted from the broadband chirp results, thus saving considerable time. To validate the broadband chirp extraction method, Figure 64 compares the signal response extracted from the broadband chirp signal versus an actual FE simulation signal response. It can be seen the extracted signals compare very well with the FE excitation signals in the regions of interest. Therefore, the broadband signal reconstruction technique will be used in the next section to analyze the input signal response over a range of frequencies from 50-500 kHz.

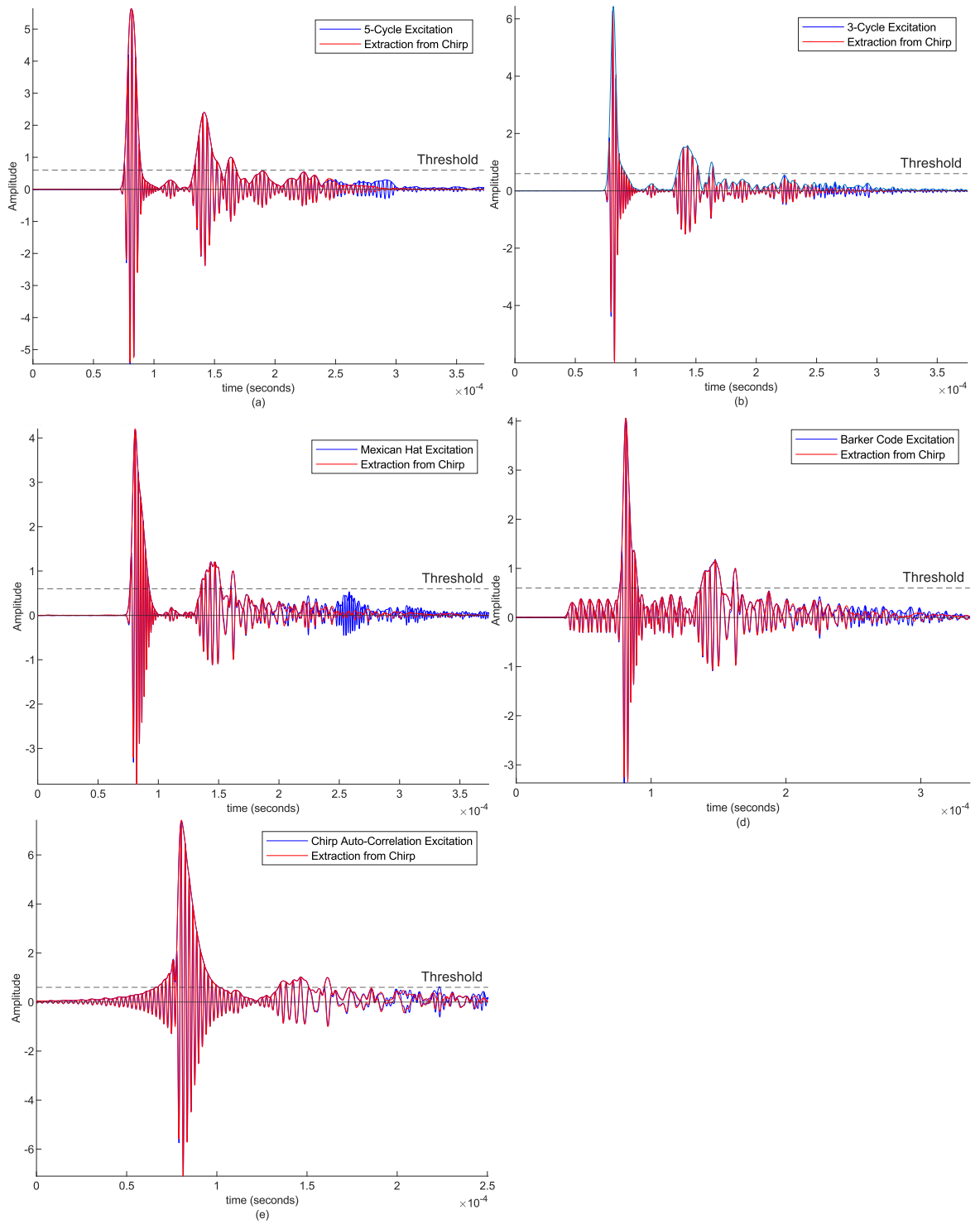


Figure 64: FEM response for the 5-cycle sine wave, 3-cycle sine wave, Mexican hat, 13-bit Barker code, and auto-correlation of the linear chimp excitations compared to the respective extracted response from the broadband chimp response.

4.3.2 Frequency Range for Delamination Identification

To find the optimal excitation frequency for identifying delamination damage, each input signal was extracted from the broadband chirp response over a range of frequencies from 50 – 500 kHz at 50 kHz increments. Figure 65 shows the 3-cycle sine wave has a distinct A_0 reflection wave packet from 250 – 400 kHz. This distinct wave packet clearly identifies the delamination damage and will be used in the next chapter to size and locate the damage. Figure 65 also highlights that the S_0 mode generates an A_0 mode conversion signal when it contacts the delamination at frequencies above 200 kHz.

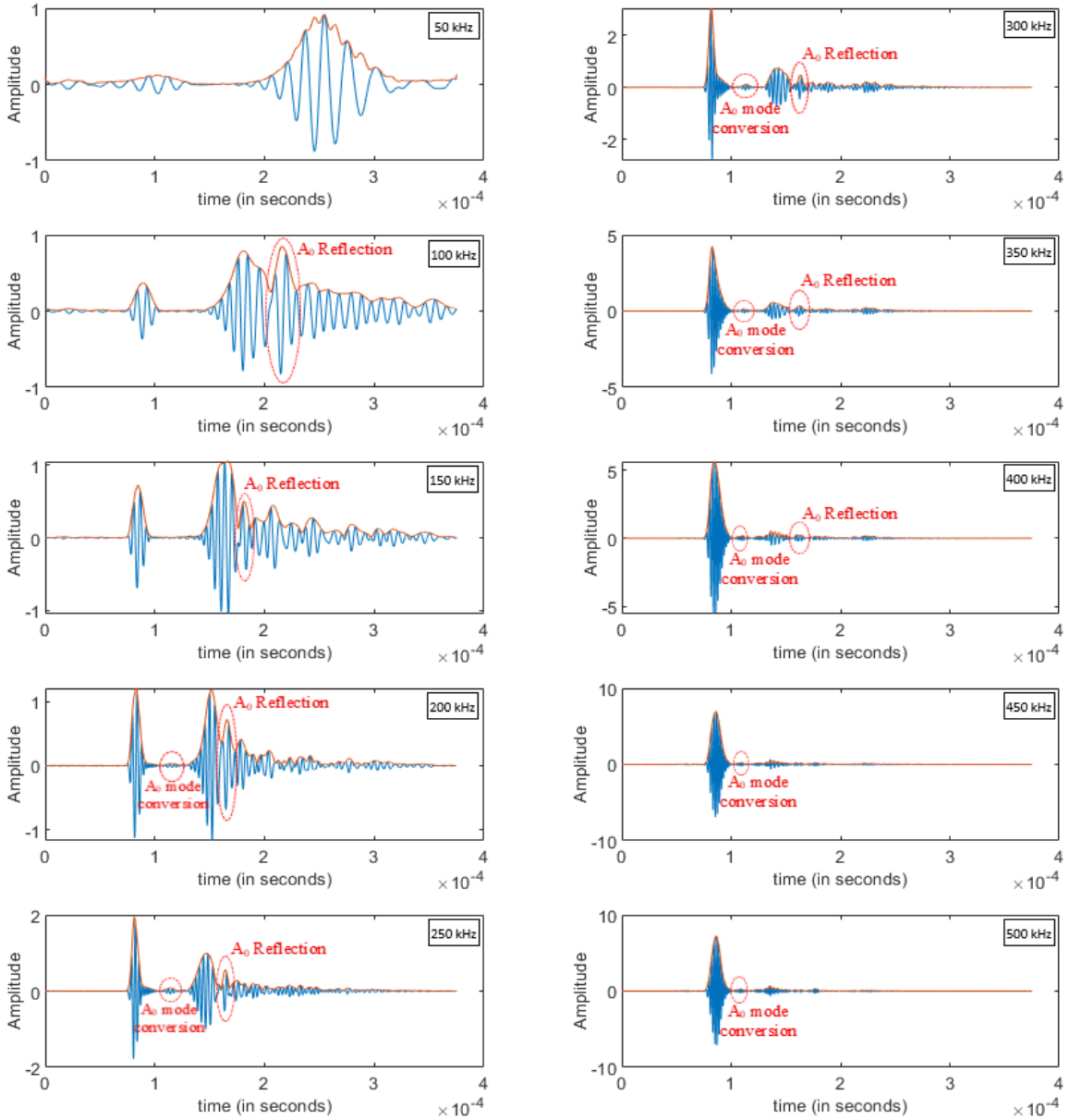


Figure 65: 3-cycle sine wave extracted from a broadband chirp response over a range of frequencies, from 50 kHz (top left) to 500 kHz (bottom right).

Figure 66 shows the response of the 5-cycle sine wave, Mexican hat, and 13-bit Barker code input signals over the frequency range from 100 – 500 kHz at 100 kHz increments. Figure 67 plots the response of an auto-correlation linear chirp signal from 50 – 500 kHz (275 kHz center frequency) and 200 – 500 kHz (350 kHz center frequency).

Figure 66 and Figure 67 are used to identify the frequencies that show a distinct wave packet associated with the A_0 reflection, similar to Figure 65. These frequencies will be analyzed further in the following sections.

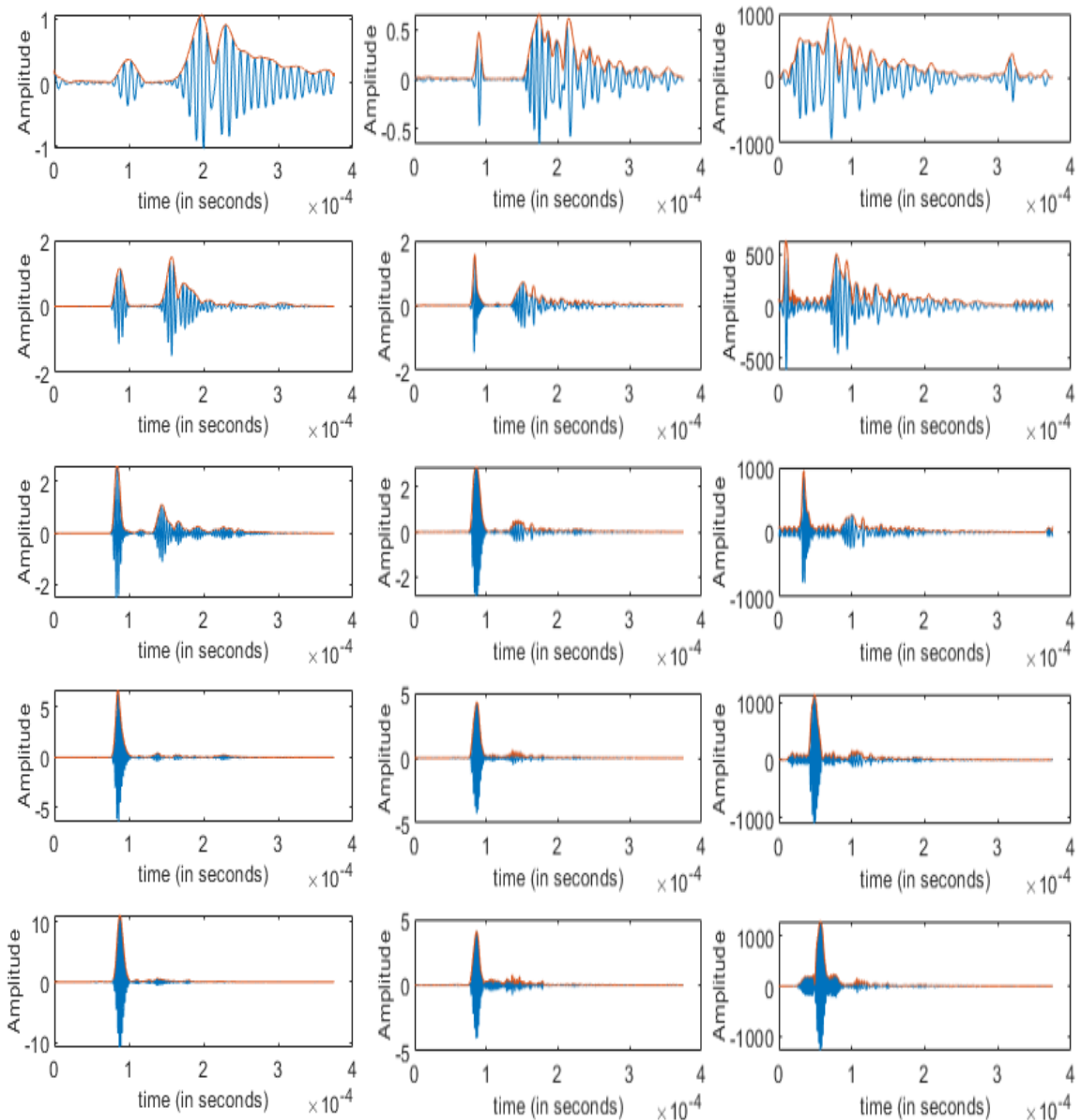


Figure 66: Input signal extracted from a broadband chirp response over a range of frequencies from 100 kHz (top) to 500 kHz (bottom): 5-cycle sine wave (left), Mexican hat (center), and 13-bit Barker code (right).

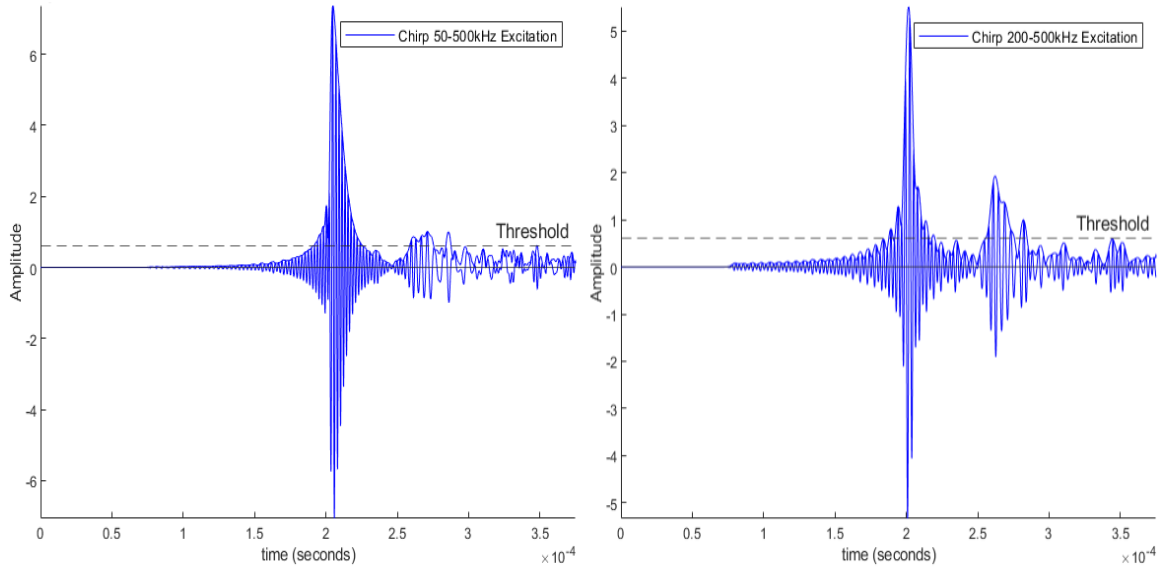


Figure 67: Auto-Correlation of a linear chirp signal from 50 - 500 kHz (Left) and 200 - 500 kHz (Right).

4.3.3 Main Lobe Width Comparison

The signal response resolution is determined by calculating the main lobe width (MLW) for the S_0 , A_0 , and A_0 reflection wave packets at a defined threshold level. The MLW was calculated at frequencies where the A_0 reflection could be distinctly identified, as shown in Section 4.3.2. Table 16 shows the best MLW times and corresponding frequency for each of the five input signals. The S_0 times are determined when the signal is normalized with respect to the S_0 peak, the A_0 times are determined when the signal is normalized with respect to the A_0 peak, and the A_0 reflection times are determined when the signal is normalized with respect to the A_0 reflection peak.

Table 16: The best main lobe width times for S_0 , A_0 , and A_0 reflection and corresponding frequency of the five compared signals.

Input Signal Resolution			
Excitation Signal	Main Lobe Width (10E-5 sec)		
	S_0	A_0	A_0 Reflection
3-Cycle Sine	1.154 (250 kHz)	1.464 (200 kHz)	0.413 (300 kHz)
5-Cycle Sine	1.480 (300 kHz)	1.097 (400 kHz)	0.839 (350 kHz)
Mexican Hat	1.382 (200 kHz)	1.839 (250 kHz)	0.378 (250 kHz)
Barker Code (13-bit)	0.504 (200 kHz)	1.604 (200 kHz)	0.348 (400 kHz)
Chirp Auto-Correlation	2.973 (50 – 500 kHz)	1.645 (200–500 kHz)	0.367 (50 – 500 kHz)

The 13-bit Barker code has the best S_0 resolution (0.504×10^{-5} s) and A_0 reflection resolution (0.348×10^{-5} s), and the 5-cycle sine wave has the best A_0 resolution (1.097×10^{-5} s).

A comparison of each of the five input signals, at their optimal A_0 reflection frequency, as listed in Table 16: 3-cycle sine wave (300 kHz), 5-cycle sine wave (350 kHz), Mexican hat (250 kHz), 13-bit Barker code sine wave (400 kHz), and an auto-correlation of a broadband linear chirp (50-500 kHz), are shown in Figure 68 and Figure 69. The signals were shifted to align with each other for the purpose of comparison. Figure 69 shows the traditional 5-cycle sine wave gives poor resolution of the A_0 delamination reflection and the 13-bit Barker code sine wave gives the best MLW resolution. This is the result of the distinct peak associated with the 13-bit Barker code sine wave; as this distinct peak travels across the delamination defect to produce the A_0 reflection, there is less negative interference between the waves travelling independently along the top and bottom sub-laminates.

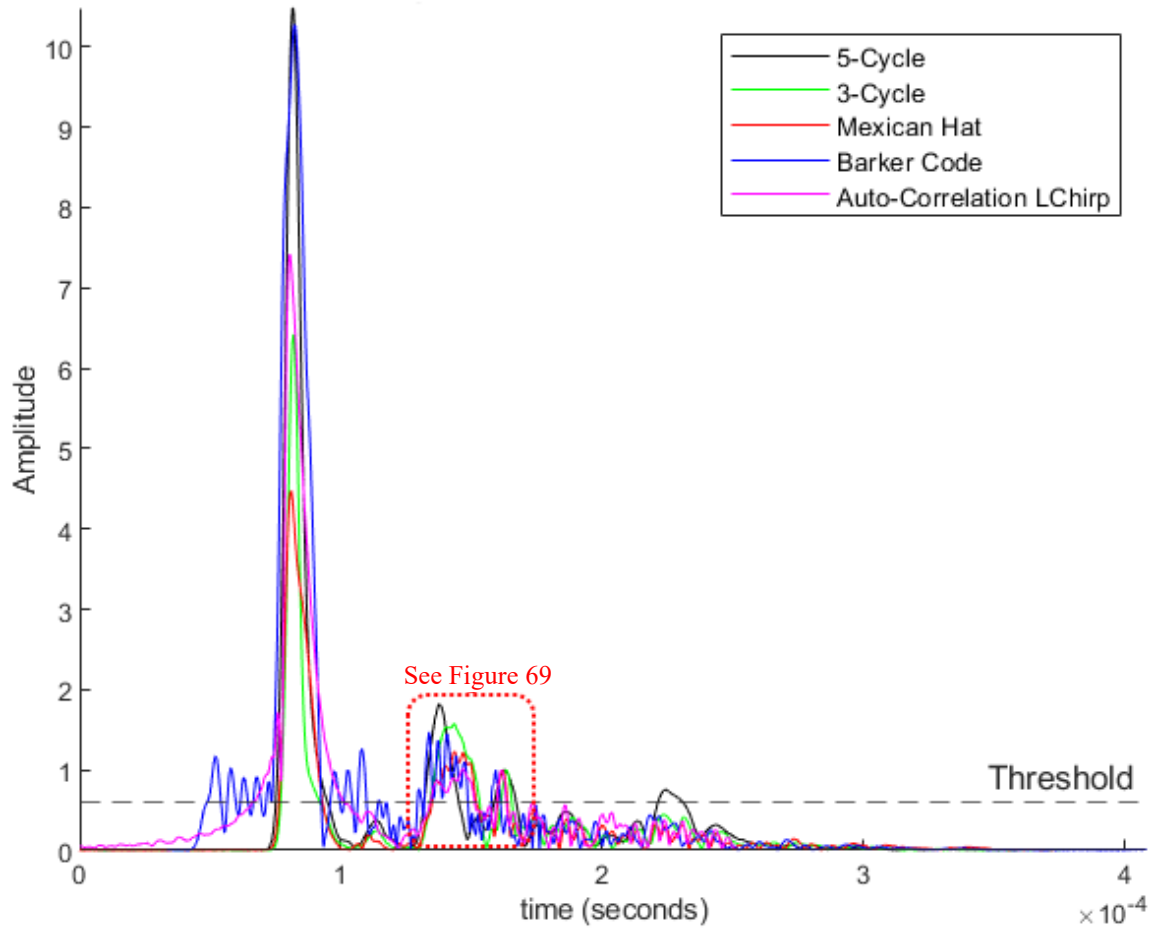


Figure 68: Comparison of five input signals for identification of a delamination (normalized with respect to the A_0 reflection).

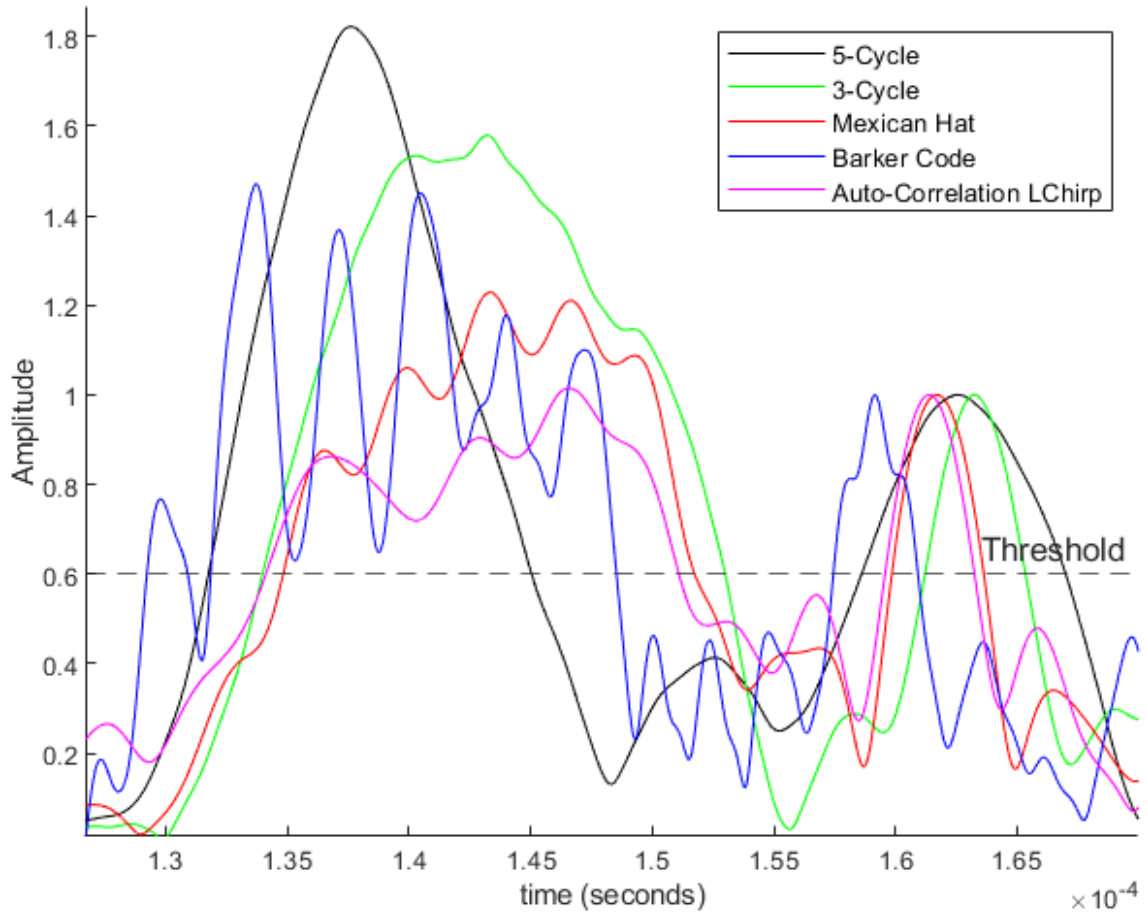


Figure 69: Close-up of Figure 68 to highlight the A_0 and A_0 delamination reflection.

4.3.4 Signal-to-Noise Ratio

The signal-to-noise ratio (SNR) compares the A_0 reflection peak value with the standard deviation of the signal ranging from the start of the A_0 reflection main lobe to the end of the signal, see Table 17. The 13-bit Barker code signal was shown to have the largest SNR value of 7.76, followed by the Mexican Hat (7.48) and the 3-cycle sine wave (7.11).

Table 17: Signal-to-Noise ratio of the A_0 reflection for the five compared signals.

Signal-to-Noise Ratio	
Excitation Signal	SNR (A_0 Reflection)
3-Cycle Sine	7.11 (250 kHz)
5-Cycle Sine	4.99 (300 kHz)
Mexican Hat	7.48 (250 kHz)
Barker Code (13-bit)	7.76 (400 kHz)
Chirp Auto-Correlation	4.08 (200 – 500 kHz)

4.3.5 Effective Frequency Range

The ability for an input signal to effectively identify the delamination damage over a wide range of frequencies is very important for a commercial SHM system. The optimal frequency to detect delamination damage is probably different than the optimal frequency to identify impact damage, a crack, porosity, or various sizes of damage. Therefore, an input signal with the ability to “cast a wide net” increases the probability of damage detection for an SHM system. Based on the results from Section 4.3.3 and Section 4.3.4, the 13-bit Barker code, Mexican hat, and 3-cycle sine wave signals were selected for further examination to determine which is most effective over a broad range of frequencies.

Table 18: A_θ reflection MLW calculated for the 3-cycle sine wave, Mexican hat, and 13-bit Barker Code signals for a range of frequencies.

Input Signal Resolution			
Frequency (kHz)	A_θ Reflection: Main Lobe Width (10E-5 sec)		
	3-Cycle Sine	Mexican Hat	Barker Code
200	0.744	0.431	0.679
250	0.429	0.378	0.461
300	0.413	0.394	0.366
350	0.564	0.417	0.395
400	0.725	0.401	0.348
Average	0.575	0.404	0.450

Table 18 shows the Mexican hat signal has the best MLW resolution at lower frequencies (200 – 250 kHz) and the 13-bit Barker coded sine wave has the best MLW resolution at higher frequencies (300 – 400 kHz). However, the average MLW resolution indicates the Mexican hat is the most robust input signal.

Table 19: A_θ reflection SNR calculated for the 3-cycle sine wave, Mexican hat, and 13-bit Barker code signals for a range of frequencies.

Signal-to-Noise Ratio			
Frequency (kHz)	SNR A_θ Reflection		
	3-Cycle Sine	Mexican Hat	Barker Code
200	6.058	6.993	4.273
250	7.112	7.484	7.122
300	6.822	7.164	7.475
350	5.777	6.700	7.505
400	5.427	6.685	7.764
Average	6.239	7.005	6.828

Similar to Table 18, Table 19 demonstrates the Mexican hat signal has the best SNR average and performs better at lower frequencies; however, the 13-Barker coded sine wave has a larger SNR at higher frequencies.

4.4 Discussion

To identify an effective input excitation for the identification of delamination damage, five signals were compared: 5-cycle sine wave, 3-cycle sine wave, Mexican hat, 13-bit Barker coded sine wave, and an auto-correlated linear chirp. The input signals were excited at a range of frequencies between 50-500 kHz at 50 kHz intervals and the broadband linear chirp signal was excited from 50-500 kHz and 200-500 kHz over 200 μ s. The reflection of the A_0 mode as it passes over the delamination area was used as the damage signature of interest for this study. When the A_0 mode passes over a delamination the initial A_0 wave is both transmitted and reflected from the far edge of the delamination (Figure 63). The reflected A_0 signal travels back across the delamination, reflecting again from the near edge and continuing to travel until it reaches the piezoelectric sensor, which is arranged in a pitch-catch configuration. To determine the most effective signal at identifying a delamination, two measurements were used: resolution of the MLW and SNR of the A_0 reflected signal.

Figure 69 compared the five signals normalized with respect to the A_0 reflection. It was determined that the best MLW resolution was achieved with the 13-bit Barker coded sine wave at 400 kHz (3.48×10^{-6} seconds), followed by the auto-correlated linear chirp from 50-500 kHz (3.67×10^{-6} seconds), and Mexican hat at 250 kHz (3.78×10^{-6} seconds), these results are further presented in Table 16. The traditional 5-cycle sine wave had the

best MLW resolution of the A_0 mode, as shown in Table 16, however, this did not translate to a shorter MLW of the A_0 reflection, but instead the longest MLW time (8.39×10^{-6} seconds). It is also important to note that selecting a 3-cycle sine wave compared to a 5-cycle sine wave reduced the MLW of the A_0 reflection by over half, 4.13×10^{-6} seconds versus 8.39×10^{-6} seconds, respectively.

Additional analysis was performed to identify the SNR of the A_0 reflection signal, as seen in Table 17. The 13-bit Barker code at 400 kHz had the best SNR of 7.76, followed by the Mexican hat at 250 kHz (7.48) and 3-cycle sine wave at 250 kHz (7.11). Although, the 13-bit Barker code had the narrowest MLW and largest SNR, two concerns associated with the 13-bit Barker code, include: 1) large side lobes surrounding the S_0 mode, and 2) poorer performance at low frequencies. The large side lobes surrounding the S_0 mode have the potential to mask reflections or mode conversion resulting when the S_0 mode interacts with delamination damage or other types of damage. At high frequencies the S_0 mode is the dominant mode and at low frequencies the A_0 mode is the dominant mode; therefore, when using the A_0 reflection as a delamination signature it is preferable to be operating at low frequencies. This will become an important consideration if any S_0 mode boundary reflections are introduced.

The results of the MLW and SNR identified the 13-bit Barker coded sine wave, Mexican hat, and 3-cycle sine wave as the best input signals for identifying delamination damage. A further analysis of these three signals was completed to determine which signal was most effective over a broad range of frequencies, 200-400 kHz – frequencies where the A_0 reflection has a distinct wave packet. Table 18 and Table 19 show the Mexican hat has the best average MLW resolution and SNR. A further breakdown identifies the

Mexican hat signal has the best performance at 200 and 250 kHz, while the 13-bit Barker code has the best performance at 300, 350, and 400 kHz. However, as identified above, excitation at high frequency is less desirable because the S_0 mode is dominant.

These results indicated the Mexican hat signal is effective over a range of frequencies, has a high SNR ratio for the A_0 reflection, and has a good MLW resolution for identifying delamination damage. Therefore, the Mexican hat excitation is proposed for identification of delamination damage. The optimal frequency for the Mexican hat signal was 250 kHz. The 13-bit Barker coded sine wave and 3-cycle sine wave also performed well, with optimal excitation frequencies at 400 kHz and 250-300 kHz, respectively.

4.5 Conclusions

This chapter compared five input signals (5-cycle sine wave, 3-cycle sine wave, Mexican hat, 13-bit Barker coded sine wave, and an auto-correlated linear chirp) to determine which is the most effective at identifying delamination damage. A comparison of the A_0 reflection from the delamination, showed:

- 1) MLW resolution was best using the 13-bit Barker coded sine wave (400 kHz), followed by the auto-correlated linear chirp (50-500 kHz) and Mexican hat (250 kHz).
- 2) The SNR was highest for the 13-bit Barker coded sine wave (400 kHz), followed by the Mexican hat (250 kHz) and 3-cycle sine wave (250 kHz).
- 3) The Mexican hat excitation had the best average MLW and SNR over a frequency from 200-400 kHz, demonstrating it was most effective at identifying delamination damage over a broad range of frequencies.

Overall, the Mexican hat excitation is identified as the best input signal for the identification of delamination damage. The simulation results showed the Mexican hat excitation performed the best between 200 – 400 kHz; however, experimental verification is still required to identify the best frequency for manufactured CFRP panels. Further, these results are limited to a specific case (delamination length of 25.4 mm and depth of 25% of the plate thickness) and must be expanded to a general application before the Mexican hat signal can be widely accepted as the most effective signal for delamination identification.

Chapter 5: Delamination Defect Analysis

Delamination damage is one of the most common types of defects found in composites structures. It can be formed in both manufacturing and in-service use. It can occur as a single delamination or multi-surface delaminations resulting from impact damage. Delamination damage poses a danger of occurring or increasing in size undetected, thus compromising the structural integrity of the part. For this reason, delamination damage has been extensively researched as discussed in Chapter 3. As previously mentioned, there are four important considerations for a successful SHM system: 1) recognition, 2) identification, 3) severity, and 4) location. Chapter 3 focused on recognition and identification; therefore, the current chapter focuses on the severity and quantification of delamination damage. Severity will be studied by identifying both the size and through thickness depth of a delamination.

To be able to quantify the severity of a delamination defect using Lamb waves, first, a thorough understanding of the interaction between the Lamb wave and delamination is required. When the Lamb wave contacts the delamination, it travels independently in the top and bottom sub-laminates, reflecting from both the front and back edge of the delamination. Gupta and Rajagopal [89] excited the S_0 mode and discovered the ability to detect a delamination using a reflection coefficient was dependent on the location of the delamination through the thickness. If the delamination was located at the mid-thickness depth, the S_0 was not able to recognize the delamination. Feng *et al.* [61] implemented a 2D FE model of a four ply CFRP plate to identify the behavior of the S_0 and A_0 modes as they interact with a delamination located between the first and second plies. Feng *et al.* [61] discovered that mode conversion occurs as both the S_0 and A_0 mode contact the front

and back edge of the delamination; however, when the S_0 mode contacts the front edge the amplitude of the mode converted A_0 wave is small. When the S_0 mode contacts the back edge of the delamination a larger A_0 mode converted wave is generated. Similarly, when the A_0 mode contacts both the front and back edge of the delamination the amplitude of the mode converted S_0 wave is small. Therefore, Feng *et al.* [61] concluded significant mode conversation only occurs with the S_0 wave, as seen in Figure 70. Further, when the Lamb wave modes travelling independently in the top and bottom laminates arrive at the end of the delamination, superposition will occur. These superimposed waves continue to propagate in the main laminate with the S_0 waves travelling faster and separating from the A_0 modes.

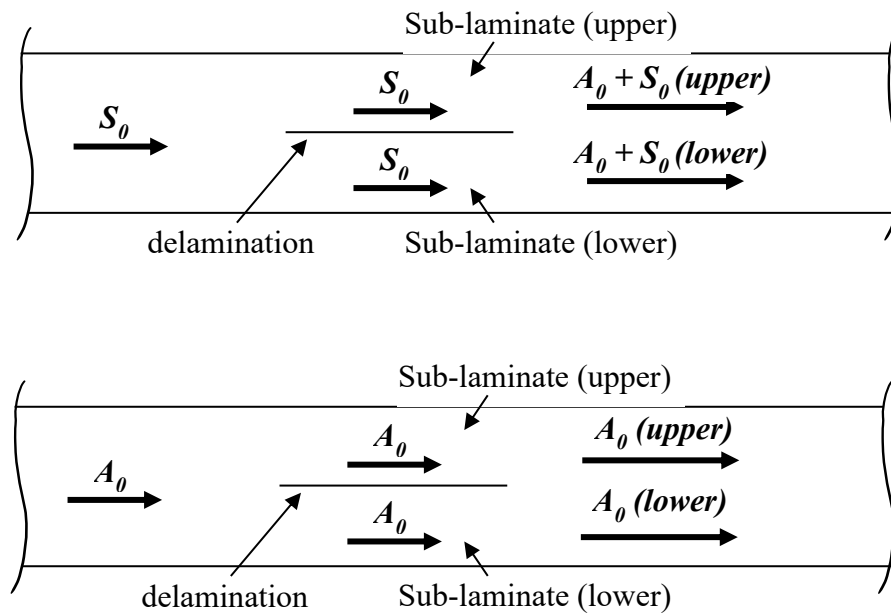


Figure 70: Interaction of S_0 and A_0 modes with a delamination defect.

Ramadas *et al.* [106] provided a detailed description of the A_0 mode conversation for a three ply glass-epoxy laminate with a delamination between the first and second plies. In addition, Ramadas *et al.* [106] described the behaviour of the transmitted waves, reflected (“turning”) waves, and mode converted waves. It was concluded that when using an A_0 excitation signal mode conversion occurs and the resulting forward propagating signal and subsequent reflections can include signals with a mode converted S_0 component. Similarly, Munian *et al.* [108] found that an A_0 excitation signal experienced a S_0 mode conversion when it interacted with asymmetric delamination. Munian *et al.* [108] also noted that when the delamination is located at a mid-thickness location, the waves travelling in the top and bottom sub-laminates remain in phase when they rejoin in the main laminate; therefore, only a weak reflection is created from the back edge of a mid-thickness delamination. Hayashi and Kawashima [107] created a semi-finite element model to study the interaction of Lamb waves with delaminations at different depths, including between plies: 1 – 2, 2 – 3, 3 – 4, and 4 – 5 (mid-thickness). Hayashi and Kawashima [107] concluded reflections are generated at the back edge of the delamination, not the start. These reflections are larger when a phase difference is created by the waves traveling in the top and bottom laminates. Large reflections were identified with delaminations located between plies 1 – 2, 2 – 3, and 3 – 4 with an A_0 incident wave and plies 1 – 2 and 3 – 4 with an S_0 incident wave.

Hu *et al.* [109] studied the S_0 reflected waves to determine the location of a delamination defect. The S_0 reflection was able to recognize a 20 mm and 30 mm delamination but not a 10 mm delamination or delaminations located at the mid-thickness depth when using a pulse-echo configuration with a 100 kHz input signal. Hu *et al.* [109]

noted reflections from the back edge of the delamination defect were larger in amplitude than reflections from the front edge. Hu *et al.* [110] completed additional research studying the A_0 mode and was able to recognize the 10, 20, and 30 mm defects located at both mid-thickness and near-surface. However, Hu *et al.* [110] noted the amplitude of the reflected signals could not be used to quantify the severity of the delamination because the 10 mm delamination produced larger reflections than the 30 mm delamination. It was concluded that the superposition of the waves travelling in the top and bottom laminates when they rejoined in the main laminate was the cause of the amplitude difference.

Ip and Mai [111] used an A_0 excitation signal to determine the location of a delamination based on the arrival time of the initial A_0 wave and subsequent mode converted wave. Using this method, Ip and Mai [111] were able to estimate the damage location within a 4.5% to 8.5% error. Feng *et al.* [112] determined the defect location by analyzing the reflected or scattered waves that occurred from magnets attached to a CFRP plate and proposed this technique would be effective for delamination defects. As part of the analysis, Feng *et al.* [112] subtracted the baseline signal from the damage signal to examine the reflected and mode converted waves. Similarly, Rathod *et al.* [113] subtracted the baseline signal from a signal with mode conversation caused by a delamination to establish a damage index with the potential to classify damage severity.

The above research provides valuable insight into the behavior of Lamb waves with delaminations; however, the focus of this chapter is to determine the severity of damage by quantifying the size and depth of the delamination. Petculescu *et al.* [114] recognized the wave velocity decreases when traveling across the thinner top and bottom laminates, therefore they calculated the delamination size using the time delay of the Lamb wave

compared to a baseline signal. Using this techniques, Petculescu *et al.* [114] determined the size of delaminations with an error ranging from 2.0 % to 76.0%.

Ng and Veidt [115] proposed the amplitude of received signal could be used to determine the size and depth of a delamination defect. However, Ng and Veidt [115] discovered the amplitude of the forward and backward scattering characteristics of a delamination in CFRP was not consistent with either size or depth. Ng [88] extended this research using a 3D finite element model that studied a variety of delamination sizes (4 mm, 6 mm, 8 mm, and 10 mm) at different depths (between plies 1 – 2, 2 – 3, 3 – 4, and 4 – 5). Ng [88] found the amplitude of the transmitted signal was largest for the 4 mm and 10 mm delamination and the delamination located between plies 2 – 3 and 4 – 5. Therefore, this suggests amplitude analysis provides poor insight into defect severity. Murat *et al.* [116] also concluded that amplitude cannot be used to calculate delamination depth, regardless of the fact that there are significant amplitude changes.

Hu *et al.* [117] proposed matching the natural frequency of the delamination sub-laminates with the excitation signal. When these frequencies were matched, the reflection from the delamination was maximized. The natural frequency of the delamination sub-laminates is dependent on the length and depth of the delamination. Therefore, Hu *et al.* [117] proposed that finding the delamination natural frequency would help determine the size and depth of the delamination. Similarly, Munian *et al.* [108] concluded the amplitude of the scattered waves caused by a delamination was dependent on the frequency of the excitation signal and the resonance frequency of the sub-laminates. Feng *et al.* [86] used a chirp excitation with a broadband frequency range to determine the delamination length. Feng *et al.* [86] suggested the size of the delamination was related to the frequency of the

signal perturbed by the delamination; small delaminations perturbed higher frequencies but had no effect on lower frequencies. Therefore, studying which frequency ranges in the broadband signal were disturbed could be used to determine the length of the delamination.

The depth of the delamination is important to know when determining the remaining life of a structure, structural integrity, and necessary repair procedures. Samaitis *et al.* [118] applied multiple excitation frequencies to determine defect depth; the resulting A_0 forward reflection amplitudes were compared to a database of reference amplitude for different delamination depths. Once the delamination depth was determined, this information was used to improve the delamination length calculation. Despite previous research indicating amplitude analysis was not effective at determining delamination depth, the technique Samaitis *et al.* [118] implemented showed accurate FE model results.

Wavefield analysis using a laser Doppler vibrometer has proved to be an effective method for determining delamination size and depth, however, this is not an SHM method. The laser Doppler vibrometer is a large piece of equipment that requires proper setup, alignment, and point-by-point scanning. The wavefield analysis is a very promising NDT method because it is non-contact, but the setup and inspection time prevent it from being classified as a holistic SHM system. Regardless, using the wavefield analysis techniques to identify the delamination depth can provide valuable insight for an SHM inspection technique.

Rogge and Leckey [119] performed a local wavenumber analysis to determine the depth of a delamination. The wavenumber in the delamination sub-laminate is compared to theoretical dispersion curves to determine the depth. The results show that as the depth of the delamination increase so does the error. The error range was 4.2% – 24.1%

depending on the actual delamination depth and excitation frequency. Juarez and Leckey [120] improved the wavenumber analysis by exciting a multi-frequency chirp signal. Juarez and Leckey [120] also found the depth calculation to be fairly accurate for delaminations above the mid-thickness depth; however, delaminations below the mid-thickness depth could not be accurately calculated. The signal processing took 70 minutes on a computer with 6 Intel i7 3.20 GHz processor cores and 24 GB of RAM.

Mesnil *et al.* [121] compared two wavefield analysis techniques using instantaneous and local wavenumbers. The results indicated both methods provided accurate depth calculations for a delamination located two plies beneath the surface; the instantaneous wavenumber analysis calculated the delamination at a depth of 2.52 plies and the local wavenumber analysis calculated the delamination at a depth of 3.08 plies. Tian *et al.* [122] applied a wavenumber analysis to accurately identify a delamination between plies 2 – 3; however, it was noted that additional research is need for more complex delamination shapes and multi-ply delamination damage that are often associated with impact damage. Mei and Giurgiutiu [123] used a wavenumber analysis to identify delaminations in a 24 ply CFRP panel. Two delamination cases were studied: a single delamination located between plies 20 – 21 and a multi-layer delamination located between plies 16 – 17 and 20 – 21. The multi-layer delamination created stronger reflections by trapping more wave energy. However, Mei and Giurgiutiu [123] did not predict the location of each multi-layer delamination location or present associated error values, but demonstrated delamination severity can be identified using a wavenumber analysis.

To successfully determine the length and depth of a delamination defect using an SHM system setup, it is important to recognize that the time of flight (ToF) is dependent

on both the length and depth of the delamination. As the length of the delamination increases, the arrival time of the Lamb wave is delayed. Similarly, as the thickness of the larger sub-laminates decreases, the arrival time of the Lamb wave is delayed. Therefore, the co-dependent relationship between the length and depth of the delamination must be considered to ensure accurate results of each. The length and depth cannot be measured and analyzed independently using sensor arrival times. The following analysis will focus on the reflections from the delamination and the reduced propagation velocity, and associated time delay, as the Lamb waves travels across the delamination in the top and bottom sub-laminates.

This chapter is organized as follows: Section 5.1 provides the theory for the analysis used, Section 5.2, 5.3, and 5.4 present the results for a 25.4 mm delamination at multiple depths using a 2D simulation, 3D simulation, and experimental inspection, respectively, Section 5.5 presents the analysis of 25.4 mm and 50.8 mm delaminations, Section 5.6 discusses the results, and Section 5.7 provides a conclusion.

5.1 Analysis Technique

The discrete wavelet transform (DWT) analysis is implemented to utilize the advantages of the time-frequency domain and the ability to separate the S_0 and A_0 modes to specifically focus on the A_0 mode. The A_0 mode was identified in Chapter 3 to be significantly affected by a delamination defect. The analysis to determine the length and depth of the delamination will focus on the A_0 reflections created by the delamination defect and the ToF delay of the A_0 mode caused by a reduced velocity as it travels across the thinner top and bottom delamination sub-laminates.

This section describes the discrete wavelet transform, multiple level decomposition, and equations used to calculate the delamination length and depth.

5.1.1 Discrete Wavelet Transform (DWT)

The wavelet transform is a convolution of the selected wavelet function, in this case the Daubechies wavelet, with the output signal. Previously, the Continuous Wavelet Transform (CWT) was applied to identify the unique signatures associated with different types of defects (see Chapter 3). The CWT modifies the wavelet dilation and translation in a smooth continuous fashion. The DWT alters the wavelet in discrete steps, which significantly reduces the computational requirements and creates a fast wavelet transform. The DWT is also capable of reconstructing the original signal with the discrete wavelet coefficients when an infinite summation is applied.

The wavelet function is defined as:

$$\psi_{a,b}(t) = \frac{1}{\sqrt{a}} \psi\left(\frac{t-b}{a}\right) \quad (35)$$

where a is the dilation coefficient and b is the translation parameter. However, for the DWT, discrete values of the dilation coefficient and translation parameter are selected as shown below:

$$\psi_{m,n}(t) = \frac{1}{\sqrt{a_0^m}} \psi\left(\frac{t - nb_0 a_0^m}{a_0^m}\right) \quad (36)$$

where m and n are integers; m controls the wavelet dilation and n controls the wavelet translation. The translation parameter, b , is proportional to the dilation coefficient, a , as shown by $nb_0a_0^m$. The discrete wavelet transform is defined by:

$$T_{m,n} = \int_{-\infty}^{\infty} x(t) \frac{1}{a_0^{m/2}} \psi(a_0^{-m}t - nb_0) dt \quad (37)$$

where $T_{m,n}$ are the discrete wavelet coefficients or detail coefficients. For the analysis performed in this chapter, a_0 is equal to 2 and b_0 is equal to 1 - this is referred to as dyadic grid scaling. This creates the following equation for the wavelet transform:

$$T_{m,n} = \int_{-\infty}^{\infty} x(t) \frac{1}{2^{m/2}} \psi(2^{-m}t - n) dt \quad (38)$$

5.1.2 Multiple Level Decomposition

The DWT can decompose the output signal to multiple levels; this provides two primary advantages: 1) analysis of the signal at different discrete frequencies, and 2) downsampling of the output signal to reduce the data storage requirements. To fully outfit an aircraft with an SHM system, thousands or millions of sensors could be required; therefore, a reduction in data storage or transmission is an important consideration. Multiple level decomposition divides the signal into details and approximations. The wavelet details contain the high frequency components and are defined in Equation (38). The wavelet approximations contain the low frequency components, thus smoothing the

original signal (see Equation (41)). The multiple level decomposition is shown in Figure 71; each level of approximations is further divided into approximations and details.

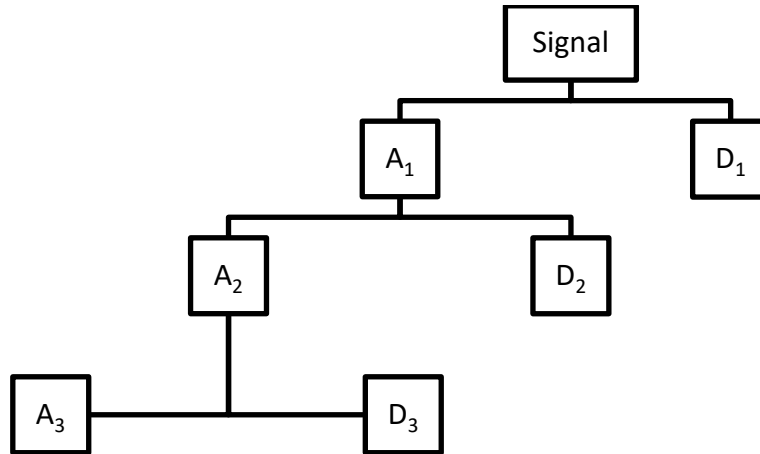


Figure 71: Multiple level decomposition tree (3 levels).

This process can be performed more efficiently using the *fast wavelet transform* decomposition, which applies complementary high-pass and low-pass filters to the original signal; the high-pass filter generates the wavelet details, and the low-pass filter generates the wavelet approximations. If the high-pass and low-pass filters were applied without any additional modifications, each subsequent level of wavelet details and approximations would contain the same number of data points as the original signal, effectively doubling the total number of data points. Therefore, a downsampling step is included so the wavelet details and approximations each contains half the data points of the original signal. Figure 72 shows an example of this procedure, as outlined in the “Matlab Wavelet Toolbox Getting Started Guide” [124].

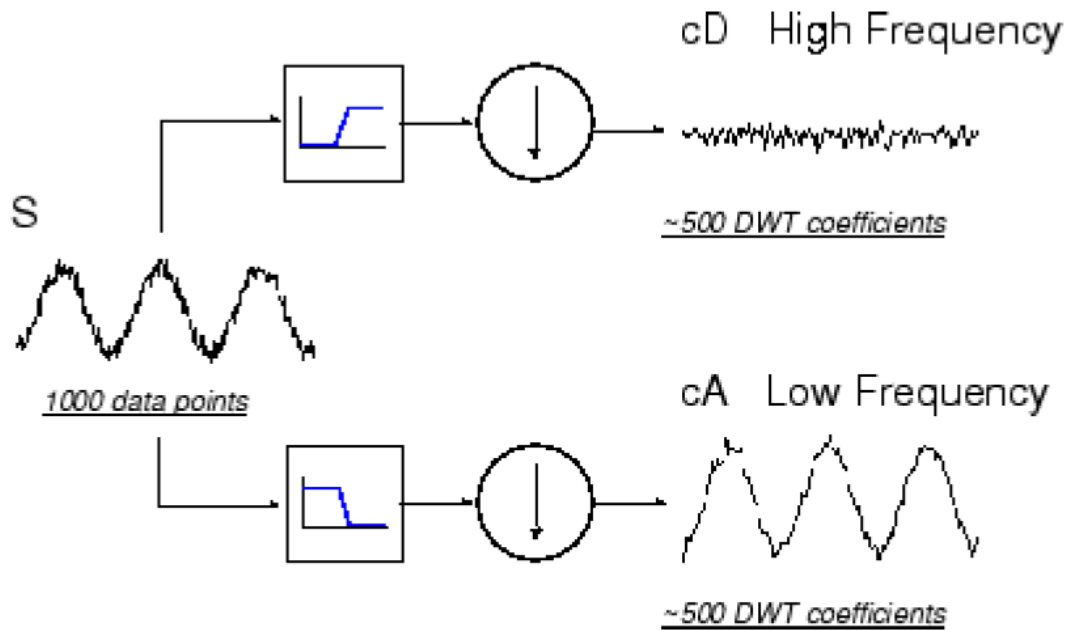


Figure 72: Signal decomposition to generate wavelet details (cD) and approximations (cA) [124].

Similar to the discrete wavelet transform used to generate the detail coefficients (Equation (38)), the wavelet approximations are calculated using a scaling function, as defined below:

$$\phi_{m,n} = \frac{1}{2^{m/2}} \phi(2^{-m}t - n) \quad (39)$$

The scaling function has the property of:

$$\int_{-\infty}^{\infty} \phi_{0,0}(t) dt = 1 \quad (40)$$

The convolution of the above scaling function (Equation (39)) with the signal generates the approximation coefficients as shown below:

$$S_{m,n} = \int_{-\infty}^{\infty} x(t) \frac{1}{2^{m/2}} \phi(2^{-m}t - n) dt \quad (41)$$

This generates discrete approximation coefficients at a given scale index, m . To generate a continuous approximation of the signal, which can be further decomposed, as shown in Figure 71, the following equation is applied:

$$x_m(t) = \sum_{n=-\infty}^{\infty} S_{m,n} \phi_{m,n}(t) \quad (42)$$

5.1.3 Daubechies Wavelets

The selected mother wavelet for the DWT analysis was the Daubechies Wavelet, specifically the db10 wavelet, see Figure 73. The db10 wavelet was selected by trial and error from the available Matlab wavelets. The Daubechies family wavelets are orthonormal wavelets with a finite number of scaling coefficients.

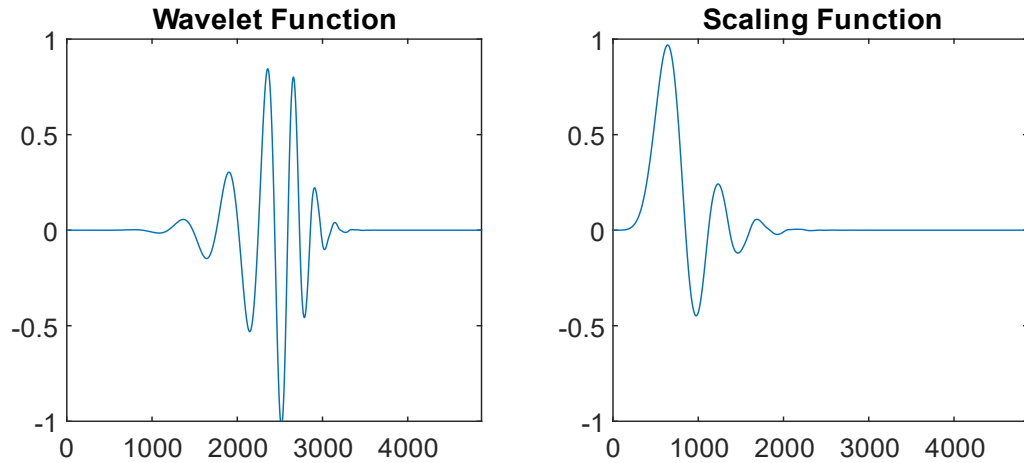


Figure 73: db10 wavelet function and scaling function used to determine the wavelet details and approximations, respectively.

For the db10 wavelet to be used for the DWT multiple level decomposition, first, the wavelet must be associated with the scaling function (Equation (39)) using a scaling equation. The scaling equation describes the dilated and translated wavelet used in the scaling function, see below:

$$\phi(t) = \sum_k c_k \phi(2t - k) \quad (43)$$

where c_k is the scaling coefficient and k is an integer representing the translation along the time axis. The scaling coefficient, c_k , and translation, k , must satisfy the following conditions:

$$\sum_k c_k = 2 \quad (44)$$

And, to ensure an orthogonal system:

$$\sum_k c_k c_{k+2k'} = \begin{cases} 2 & \text{if } k' = 0 \\ 0 & \text{otherwise} \end{cases} \quad (45)$$

Finally, c_k and k must satisfy the following moment condition specific to the Daubechies wavelets:

$$\sum_{k=0}^{N_k-1} (-1)^k c_k k^m = 0 \quad (46)$$

where m is an integer from zero to $N_k/2 - 1$ and N_k is the finite number of scaling coefficients associated with the selected wavelet (e.g., $N_k = 10$ for the db10 wavelet).

These coefficients, c_k and k , are used to generate an associated wavelet equation that are used in the wavelet function (Equation (36)). To ensure the wavelet function and corresponding scaling function are orthogonal, the wavelet equation is reversed with alternating signs, see below:

$$\psi(t) = \sum_k (-1)^k c_{N_k-1-k} \phi(2t - k) \quad (47)$$

Applying the scaling Equation (43) for the db10 wavelet produces the specific scaling function for the db10 wavelet, see below:

$$\begin{aligned}
\phi(t) = & c_0\phi(2t) + c_1\phi(2t - 1) + c_2\phi(2t - 2) + c_3\phi(2t - 3) \\
& + c_4\phi(2t - 4) + c_5\phi(2t - 5) + c_6\phi(2t - 6) \\
& + c_7\phi(2t - 7) + c_8\phi(2t - 8) + c_9\phi(2t - 9)
\end{aligned} \tag{48}$$

Similarly, the wavelet Equation (47) for the db10 wavelet becomes:

$$\begin{aligned}
\psi(t) = & c_9\phi(2t) - c_8(2t - 1) + c_7(2t - 2) - c_6(2t - 3) + c_5(2t - 4) \\
& - c_4(2t - 5) + c_3(2t - 6) - c_2(2t - 7) + c_1(2t - 8) \\
& - c_0(2t - 9)
\end{aligned} \tag{49}$$

Finally, the scaling coefficients, c_0 to c_9 , are solved using the conditions defined in Equations (44), (45), and (46). This results in the scaling coefficient values listed in Table 20. To avoid calculating the scaling coefficients listed in Table 20, they can be looked up in most textbooks [77].

Table 20: Scaling coefficients for the db10 wavelet.

c_0	c_1	c_2	c_3	c_4	c_5	c_6	c_7	c_8	c_9
0.226	0.854	1.024	0.196	-0.343	-0.046	0.110	-0.009	-0.018	0.005

The scaling Equation (48) and wavelet Equation (49) are solved using the scaling coefficients listed in Table 20. Finally, the results of the scaling and wavelet equations are substituted into the scaling function (Equation (39)) and the wavelet function (Equation (36)), and the approximation coefficients and discrete wavelet coefficients are calculated using Equations (41) and (38).

5.1.4 Delamination Length and Depth Calculations

Following the DWT decomposition of the sensor output signal, the length of the delamination is calculated using the following equation:

$$l = v_{A_0} \times \frac{1}{2} (t_{A_0(Ref)} - t_{A_0}) \quad (50)$$

where v_{A_0} is the velocity of the A_0 mode, t_{A_0} is the arrival time of the A_0 mode, and $t_{A_0(Ref)}$ is the arrival time of the delamination reflection. It is important to note that v_{A_0} is the average velocity of the A_0 mode as it travels from the actuator to the sensor, not the velocity across the delamination. The average A_0 mode velocity, v_{A_0} , will be larger than the velocity across the delamination; therefore, this initial length calculation will be increased. However, this is the only available velocity to measure at this stage.

The velocity across the delamination is calculated using the following equation:

$$v_{del} = \frac{l}{\left(t_{A_0} - \left(\frac{d_{sen} - l}{v_{A_0(base)}} \right) \right)} \quad (51)$$

where l is the delamination length calculated in Equation (50), t_{A_0} is the arrival time of the A_0 mode, which is determined using a threshold value, d_{sen} is the distance between the actuator and sensor (0.40 m), and $v_{A_0(base)}$ is the A_0 mode velocity of a baseline signal without a delamination. In a real-world application, this baseline velocity would be determined from the structure before any damage occurs (i.e., before the structure is put in service).

The velocity across the delamination, v_{del} , is then used to improve the delamination length calculation (Equation (50)), then the improve delamination length is used to improve the velocity across the delamination (Equation (51)). This process is repeated until the solutions converge. Finally, the velocity across the delamination, v_{del} , is compared to theoretical dispersion curves to determine the delamination depth.

5.2 2D Analysis of Delamination Length and Depth

A preliminary 2D FE model analysis was performed to determine if the proposed method could determine the length and depth of a delamination defect. This analysis was performed early in this thesis research; therefore, it does not incorporate the Mexican hat input signal proposed in Chapter 4, rather a 100 kHz 5-cycle sine wave as commonly reported in the literature. The 2D FE model is described in Chapter 4 (Section 4.2) and consists of an aluminum 5052 plate with lead zirconate titanate (PZT) piezoelectric sensors bonded to the aluminum plate using a Loctite Ultra™ adhesive layer. The ABAQUS model parameters used for each delamination depth are summarized in Table 21.

Table 21: 2D finite element model parameters for delamination depth.

Model Type	Geometry (m)	Element Size (m)	Element Number	Element Type	Time Step (s)	Force Input
Implicit	1.0 x 0.00206	0.00024	112083	CPE4R	5E-8 (max)	Voltage

The analysis was performed using a pitch-catch arrangement of the actuator and sensor. Multiple simulations were performed consisting of a 25.4 mm long defect located at a depth of: 0.25 mm, 0.50 mm, 0.75 mm, 1.00 mm. Additionally, a baseline simulation

was completed without a defect. The simulations were executed using the implicit finite element method in ABAQUS/Standard.

5.2.1 2D ABAQUS Simulation Results

The 2D simulation results for the sensor voltage using a signal envelope are shown in Figure 74 and Figure 75. Figure 74 confirms the findings from previous research [110] [115] [116] that indicated an amplitude analysis is not a good indicator of delamination length and depth calculations.

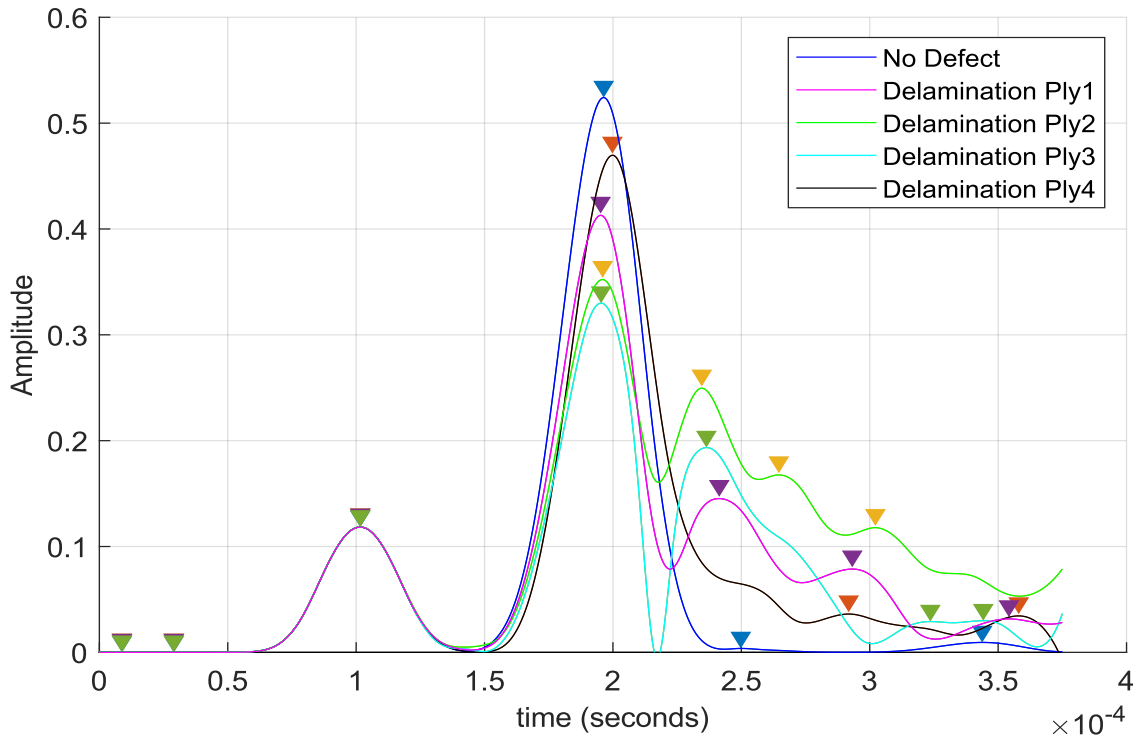


Figure 74: 2D simulation plots for a delamination defect at multiple depths.

A close-up of the A_0 mode arrival time, Figure 75, shows the time of arrival for the A_0 mode is delayed as the depth of the delamination increases (thinner top or bottom sub-laminates). This time delay will be used to calculate the A_0 mode velocity across the

delamination, which will be compared to a theoretical dispersion curve to determine the depth of the delamination.

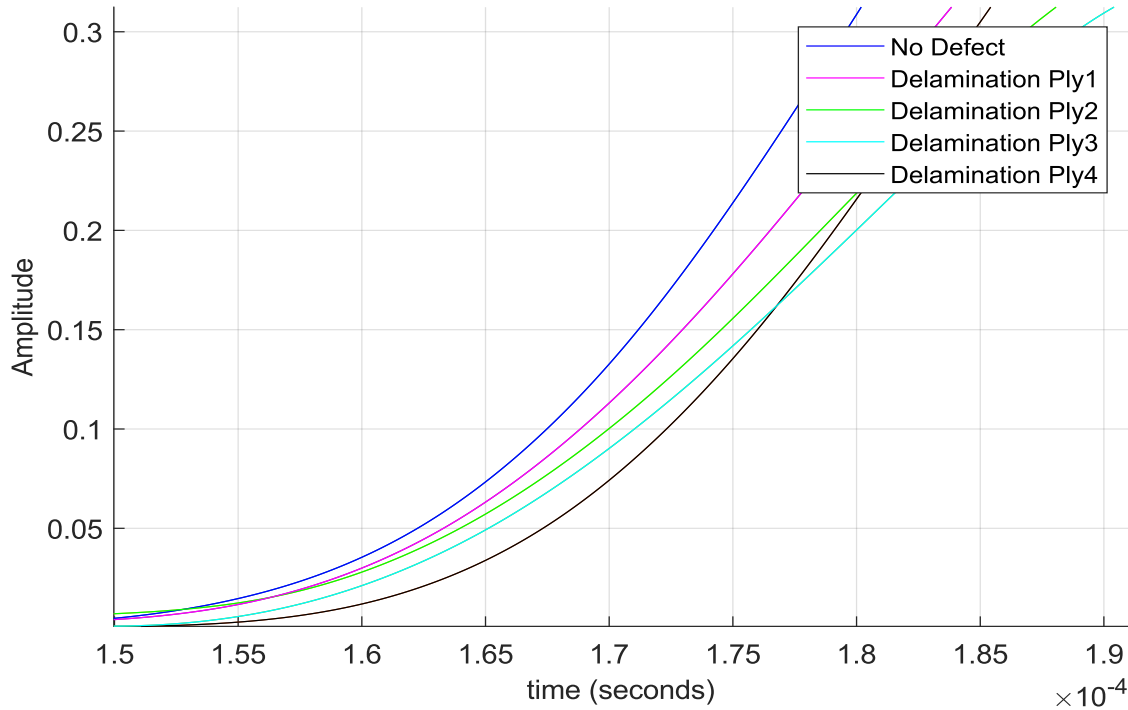


Figure 75: 2D simulation plots for a delamination defect at multiple depths – a close-up of the A_0 arrival time.

5.2.2 2D DWT Analysis

The initial step of the DWT analysis is to perform a multiple level decomposition of the signal to identify which coefficients have the largest amplitude. Large coefficients indicate a frequency range that contains high signal energy. For the 2D aluminum plate, the level 5 decomposition had the largest wavelet coefficients and were selected for further analysis. A comparison of the level 5 approximation coefficients and details coefficients (discrete wavelet coefficients) was performed, and the detail coefficients provided better results for the length and depth calculations. The level 5 detail coefficients for each delamination depth are plotted in Figure 76; the red arrow indicates the A_0 reflection peak.

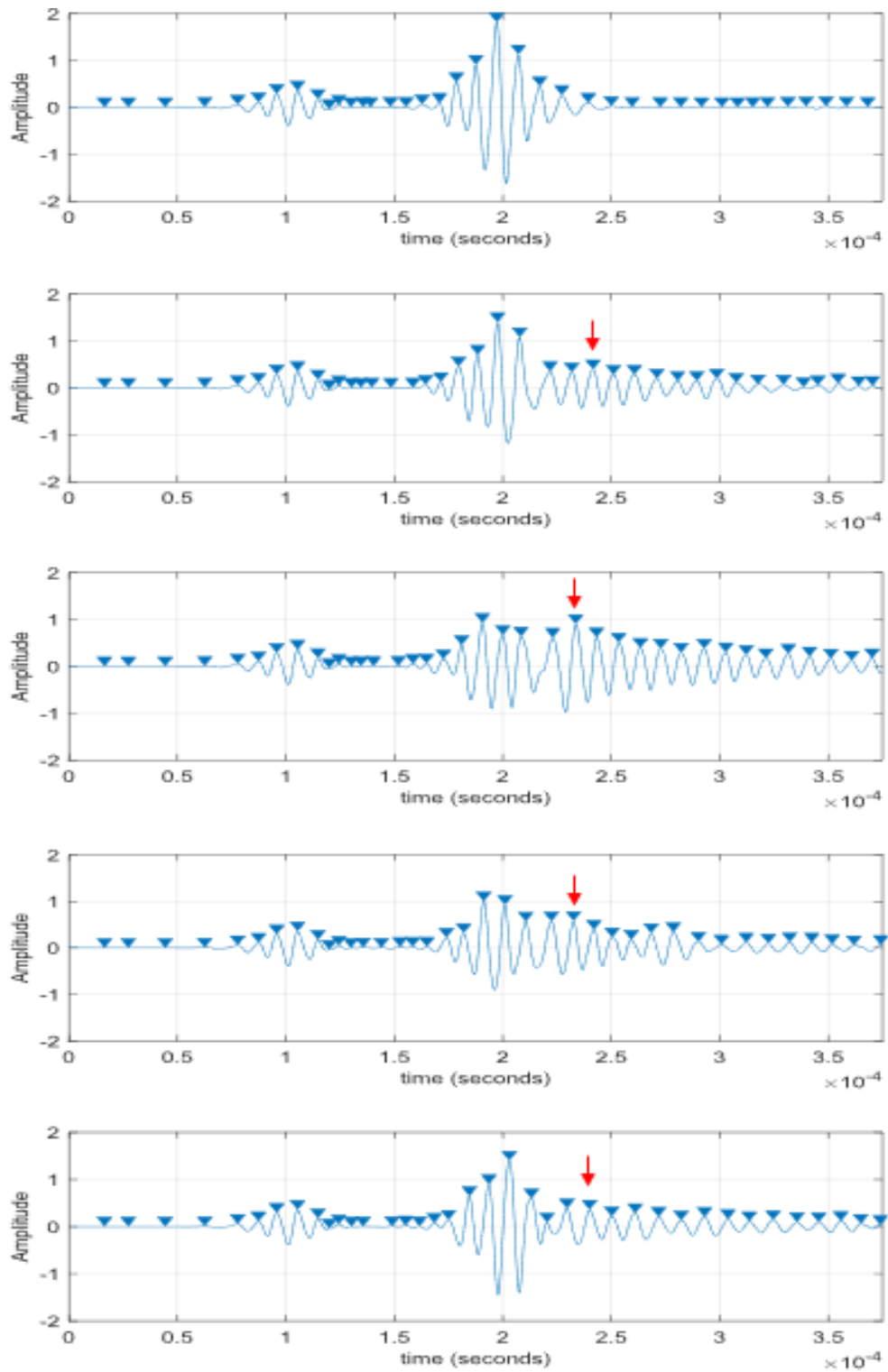


Figure 76: DWT level 5 detail coefficients (2D analysis) for each delamination depth; baseline (top), and ply 1 (second from top) to ply 4 (bottom).

It is important to note that the original ABAQUS sensor signal consisted of 1876 data points, however, the DWT decomposition for the level 5 detail coefficients consisted of only 77 data points.

5.2.3 Theoretical Dispersion Curves

The theoretical dispersion curves can be generated using free online software, see the Dispersion Calculator [125] and LAMSS-COMPOSITES [126]. For the following analysis the Dispersion Calculator [125] was used with the pre-loaded Aluminum 2024 material properties. The theoretical dispersion curve generated for the A_0 mode do not match perfectly with the ABAQUS simulation velocity for the baseline signal. Therefore, the theoretical dispersion curve was shifted to align with the baseline signal velocity for an aluminum panel with thickness of 2.06 mm, see Figure 77.

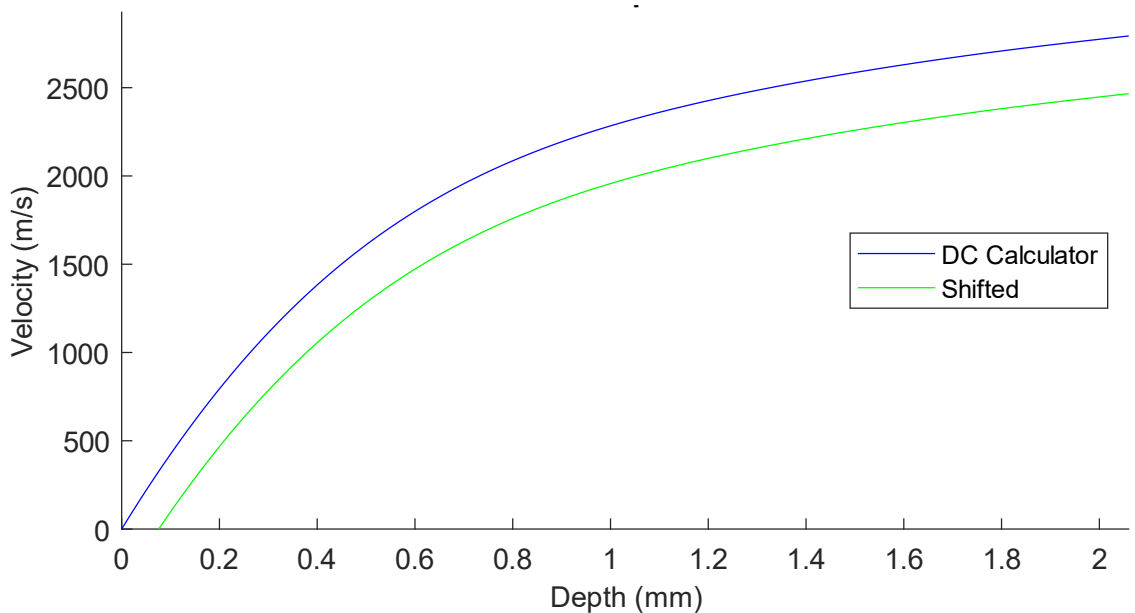


Figure 77: Theoretical dispersion curve for an aluminum plate with thickness of 2.06 mm.

5.2.4 2D Delamination Length and Depth Results

The length and depth of a defect provide important information to quantify a specific defect. Using the DWT level 5 decomposition detail coefficients, Equations (50) and (51) were applied to calculate the delamination length and velocity across the delamination, respectively. The depth of the delamination was then determined by plotting the velocity across the delamination on the shifted theoretical dispersion curve Figure 77. The actual length of the delamination was 25.4 mm at depths of: 1.80 mm, 1.55 mm, 1.29 mm, and 1.03 mm. Table 22 shows the calculated length, depth, and the associated error values for each delamination ply depth equivalent.

Table 22: Calculated length and depth for the 2D ABAQUS simulations.

Ply Depth Equivalent	Length (mm)	Length (% Error)	Depth (mm)	Depth (% Error)
Ply 1 (1.80 mm)	25.5 mm	+ 0.4 %	1.67 mm	- 7.2 %
Ply 2 (1.55 mm)	26.0 mm	+ 2.4 %	0.96 mm	- 38.0 %
Ply 3 (1.29 mm)	24.9 mm	- 2.0 %	0.81 mm	- 37.2 %
Ply 4 (1.03 mm)	20.8 mm	- 18.1 %	0.66 mm	- 35.9 %

The length results in Table 22 show good agreement with the actual delamination length of 25.4 mm. The ply 4 delamination has the highest error value, 18.1 %, but this is consistent with previous findings in the literature that indicate mid-plane defects are difficult to identify and quantify. The error values associated with the depth calculations are large; however, the depth results are consistently decreasing in value corresponding with the ply location (e.g., ply 1 has the largest depth value and ply 4 has the smallest depth value). These preliminary 2D analysis results provide promising results.

5.3 3D Analysis of Delamination Length and Depth

The 3D FE model described in Chapter 3, Section 3.2, was used to determine the length and depth of a delamination. The 3D FE model was created in ABAQUS/Explicit and consisted of an 8 ply CFRP composite panel with a $[0/90/+45/-45]_s$ layup sequence with an overall thickness of 1.6 mm. The FE model parameters are summarized in Table 23. The stiffness reduction method (SRM), Chapter 3, Section 3.2.2.4, was used to reduce edge reflections. The delamination defect, described in Chapter 3, Section 3.2.2.5.1, was 25.4 mm x 25.4 mm with a thickness of 10 μm . Multiple ABAQUS simulation were completed, each with a delamination defect located at different depths (1.4 mm, 1.2 mm, 1.0 mm, and 0.8 mm). The piezoelectric sensors were arranged in a pitch-catch configuration and a Mexican hat excitation signal was used as discussed in Chapter 4. However, the excitation frequency had to be reduced to 90 kHz – this matched the experimental excitation frequency that ensure the A_0 signal amplitude was large enough. The simulations were executed using the explicit method available in ABAQUS and described in Chapter 3, Section 3.2.1.

Table 23: 3D finite element model parameters for delamination depth.

Model Type	Geometry (m)	Element Size (m)	Element Number	Element Type	Time Step (s)	Force Input
Explicit	0.572 x 0.272 x 0.00163	0.0004	8109652	SC8R	5E-8 (max)	Point Force (F1 & F2)

5.3.1 3D ABAQUS Simulation Results

A comparison of the ABAQUS simulations with a delamination defect at different depths is shown in Figure 78. As mentioned in Chapter 3, piezoelectric elements are not available in ABAQUS/Explicit; therefore, the output signal is for the displacement (meters)

of a node located at the center point of the sensor location. The A_0 wave packet associated with the delamination reflection can be easily identified for ply 2 and ply 3 delaminations. However, the delamination reflections associated with ply 1 and ply 4 delaminations are more subtle and require additional signal processing using the DWT analysis. Figure 79 provides a close-up of the A_0 arrival time, both the envelope and wave cycles are shown to display the baseline signal is the first to arrive, followed by the ply 1, ply 2, ply 3, and ply 4 delamination defect signals, respectively. Similar to the 2D analysis, the A_0 time delay will be used to determine the depth of the delamination.

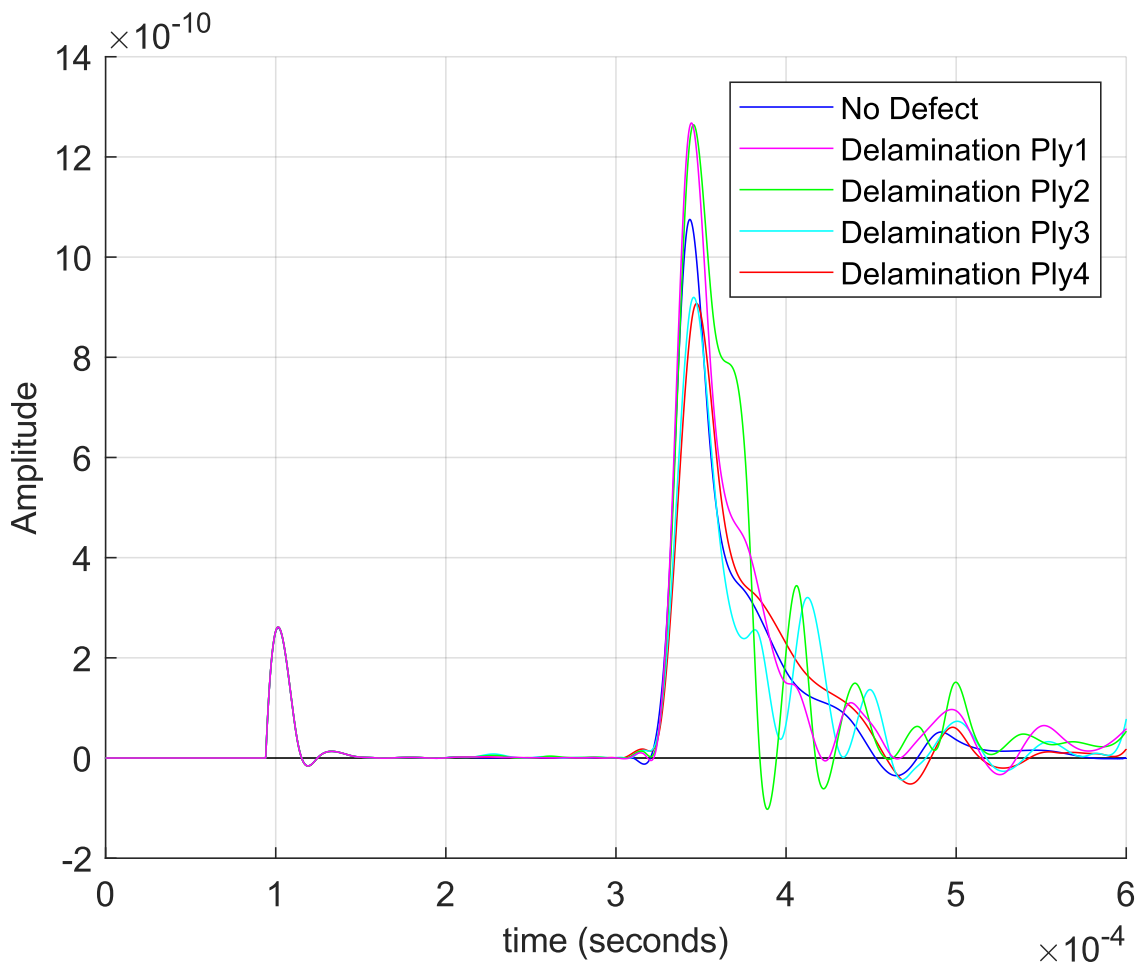


Figure 78: 3D simulation plots for a delamination defect at multiple depths.

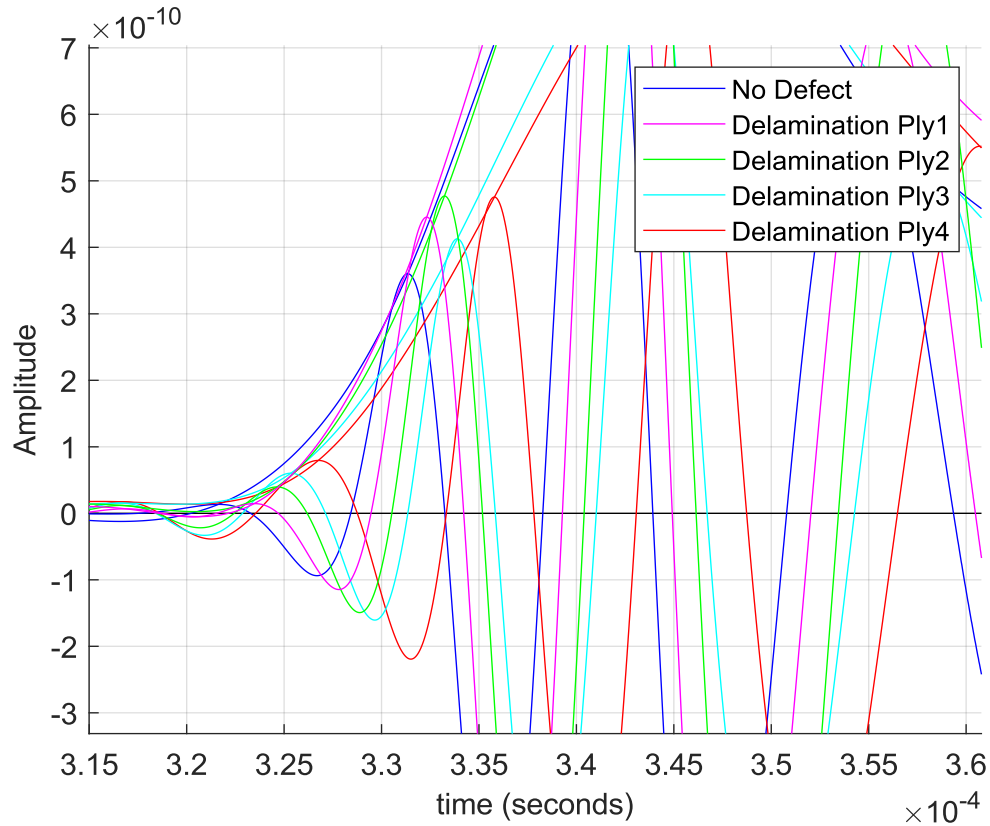


Figure 79: 3D simulation plots for a delamination defect at multiple depths - a close-up of the A_0 arrival times.

5.3.2 3D DWT Analysis

As outlined in Section 5.2.2, the first step of the DWT analysis it to perform a multiple level decomposition to determine which level contains the most signal energy. For the 3D CFRP composite panel, the level 9 decomposition contained the largest wavelet coefficients. Comparing the level 9 approximation coefficients and detail coefficients, both were able to provide accurate results for the delamination length and depth. The delamination reflections were slightly easier to identify when using the detail coefficients; therefore, the level 9 detail coefficients were selected to calculate the delamination length and depth. Figure 80 plots the level 9 detail coefficients for each delamination depth, the arrow indicates the A_0 reflection.

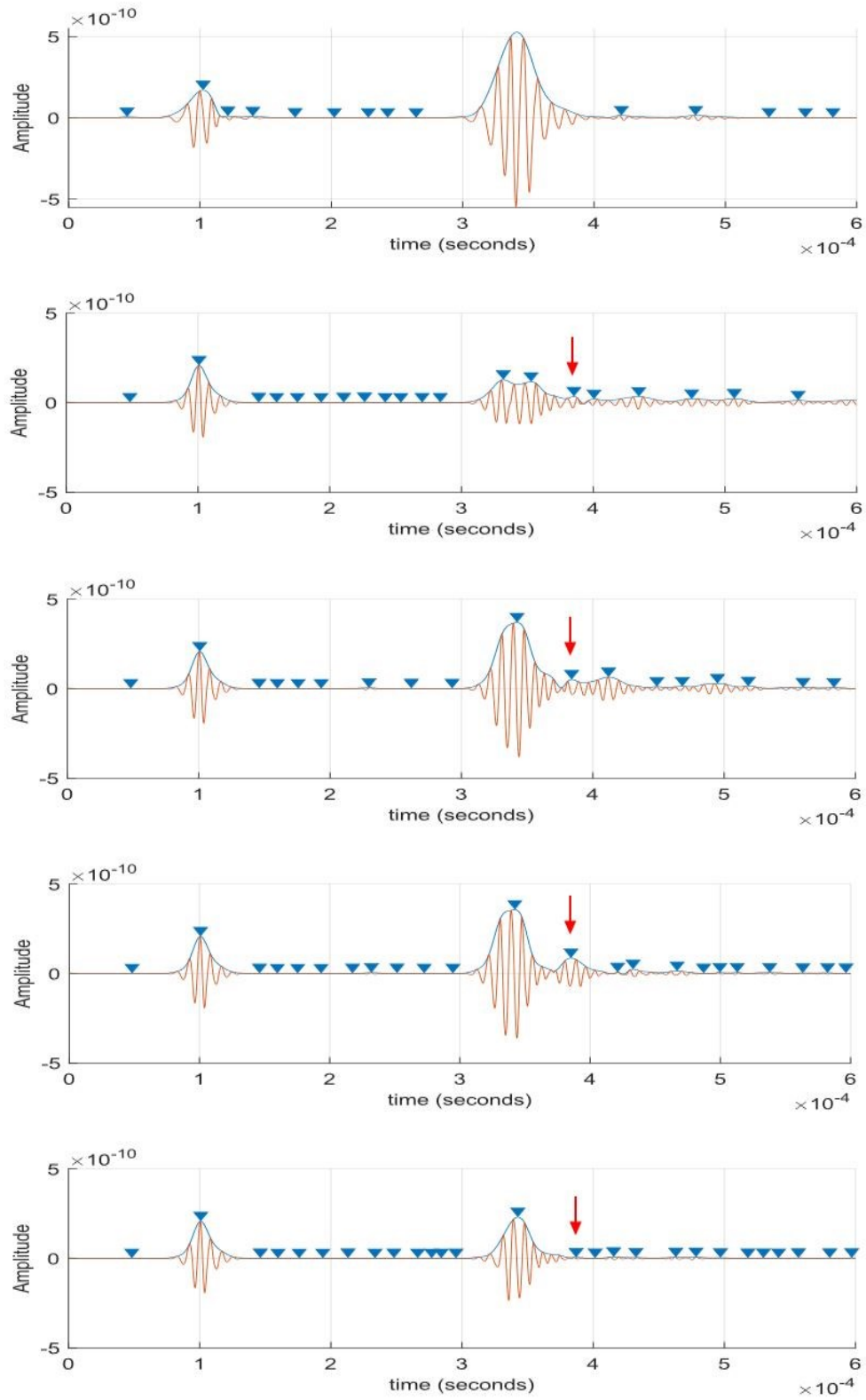


Figure 80: DWT level 9 detail coefficients (3D analysis) for each delamination depth; baseline (top), ply 1 (second from top) to ply 4 (bottom).

Figure 80 shows the ply 4 depth (mid-thickness) has the smallest peak associated with the delamination reflection, but it can be identified and used to determine the delamination length. As reported in the literature, the mid-thickness defect is the most difficult to identify. Additionally, the initial A_0 wave packet associated with the ply 1 delamination has two peaks; this is caused by large thickness discrepancies associated with the top and bottom delamination sub-laminates. The top sub-laminate has 1 ply and the bottom sub-laminate has 7 plies. This causes the A_0 mode to travel faster along the bottom sub-laminate, thus the A_0 mode in the top and bottom sub-laminates spread apart. This lack of definitive peak associated with the A_0 mode will increase the error in the length calculation for the ply 1 depth.

Data storage requirements were highlighted as an important consideration for an SHM system; applying the level 9 DWT analysis reduced the data points from 68094 in the original sensor output signal to 151 data points for the level 9 detail coefficients.

5.3.3 Dispersion Curves

The 2D dispersion curves, described in Section 5.2.3, used a free online software program, Dispersion Calculator [125]. This software program is well suited for isotropic materials with consistent material properties through the thickness. However, CFRP composite materials come in a wide range of material types and properties. Therefore, it was decided to use model-based dispersion curves. Multiple ABAQUS simulations were performed with CFRP panels with different thicknesses, but with the same material properties, layup ply sequence, and simulation parameters as the ABAQUS model with a

delamination. The velocity was measured for each panel thickness and used to generate dispersion curves, see Figure 81.

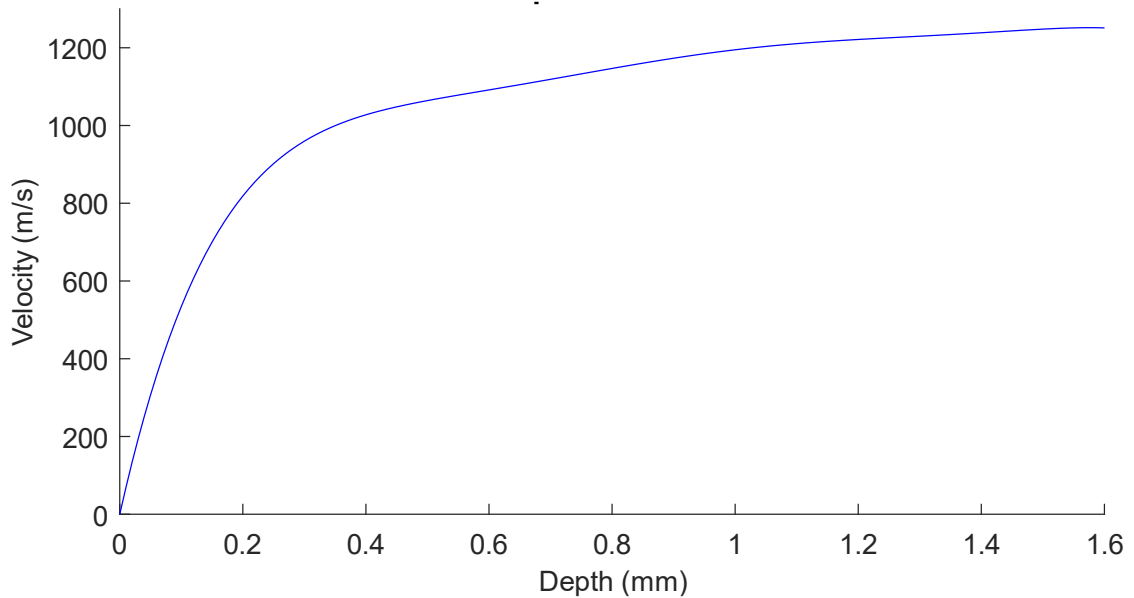


Figure 81: Model based dispersion curve for a CFRP composite plate with a thickness of 1.60 mm.

5.3.4 3D Delamination Length and Depth Results

Applying Equations (50) and (51) to the DWT level 9 detail coefficients, the delamination length and the velocity across the delamination were calculated. The delamination velocity was then compared to the dispersion curve (Figure 81) to determine the depth of the delamination. The length of the delamination modelled in the ABAQUS simulation was 25.4 mm at ply depths of: 1.4 mm, 1.2 mm, 1.0 mm, and 0.8 mm. Table 24 summarizes the calculated length, depth, and error values for each delamination ply depth.

Table 24: Calculated length and depth for the 3D ABAQUS simulations.

Ply Depth Equivalent	Length (mm)	Length (% Error)	Depth (mm)	Depth (% Error)
Ply 1 (1.40 mm)	31.5 mm	+ 24.0 %	1.47 mm	+ 5.0 %
Ply 2 (1.20 mm)	23.4 mm	- 7.9 %	1.00 mm	- 16.7 %
Ply 3 (1.00 mm)	23.9 mm	- 5.9 %	0.90 mm	- 10.0 %
Ply 4 (0.80 mm)	21.6 mm	- 15.0 %	0.34 mm	- 57.5 %

The length results for ply 2 and ply 3, as indicated in Table 24, show good agreement with the actual delamination length used in the ABAQUS simulation. The ply 1 calculated length has a large error value, 24.0 %, which is associated with the lack of definitive peak associated with the A_0 mode (Figure 80) caused by the separation of the A_0 mode as it travels across the top and bottom delamination sub-laminates. The error for the calculated length of the ply 4 depth delamination (mid-thickness) is 15.0%. This is consistent with the 2D findings and confirms previous findings from the literature that found mid-thickness defects to be the most difficult to identify.

The error associated with the depth calculations has been improved from the 2D simulation results. This improvement was the result of the dispersion curves being created from ABAQUS simulations with the exact same material properties and simulation parameters. The dispersion curves need to be accurately matched to the test data for the proposed method to achieve low error values.

5.4 Experimental Results

The experimental setup described in Chapter 3, Section 3.3, was used to verify the ABAQUS simulation results. Two CFRP panels were manufactured using an oven curing process and consisted of 8 plies with a material orientation of $[0/90/+45/-45]_s$. The

delamination defects were embedded between plies 2 – 3 (near surface) and plies 4 – 5 (mid-thickness); equally spaced 200 mm from both the piezoelectric actuator and sensor. The delamination defect was replicated using a piece of Teflon 25.4 x 25.4 mm with a thickness of 10 μm . Three absorbing layers were applied along the part edges to reduce the amplitude of unwanted reflections; these absorbing layers consisted: bagging sealant tape, modelling clay, and a thinner layer of modelling clay, see Chapter 3, Section 3.3.3, for a complete description. A 35 V, 90 kHz Mexican hat excitation signal was used to generate the Lamb wave.

The sensor output signal, as shown Figure 82, was filtered using a Butterworth filter with a bandpass range from 10 kHz to 600 kHz. The plots show the arrival times for the ply 2 delamination is earlier for both the S_0 and A_0 initial wave cycle. The delamination A_0 reflection is visible, as indicated with an arrow, for both the ply 2 and ply 4 delamination defect.

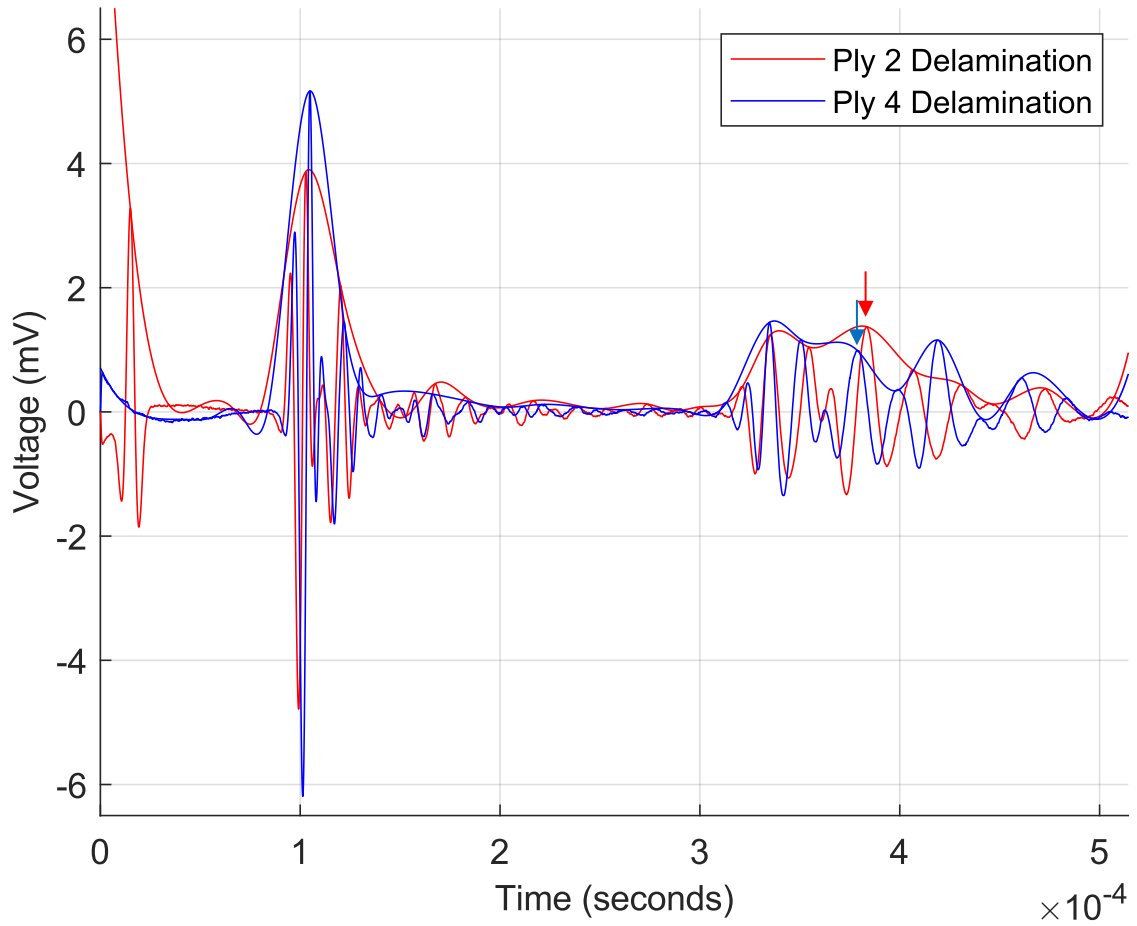


Figure 82: Experimental plots for a ply 2 and ply 4 delamination defect.

5.4.1 Experimental DWT Analysis

An evaluation of the DWT wavelet coefficients at different decomposition level reveals the level 9 detail coefficients had the largest amplitude. A plot of the level 9 detail coefficients for both the near surface (ply 2) and mid-thickness (ply 4) is shown in Figure 83.

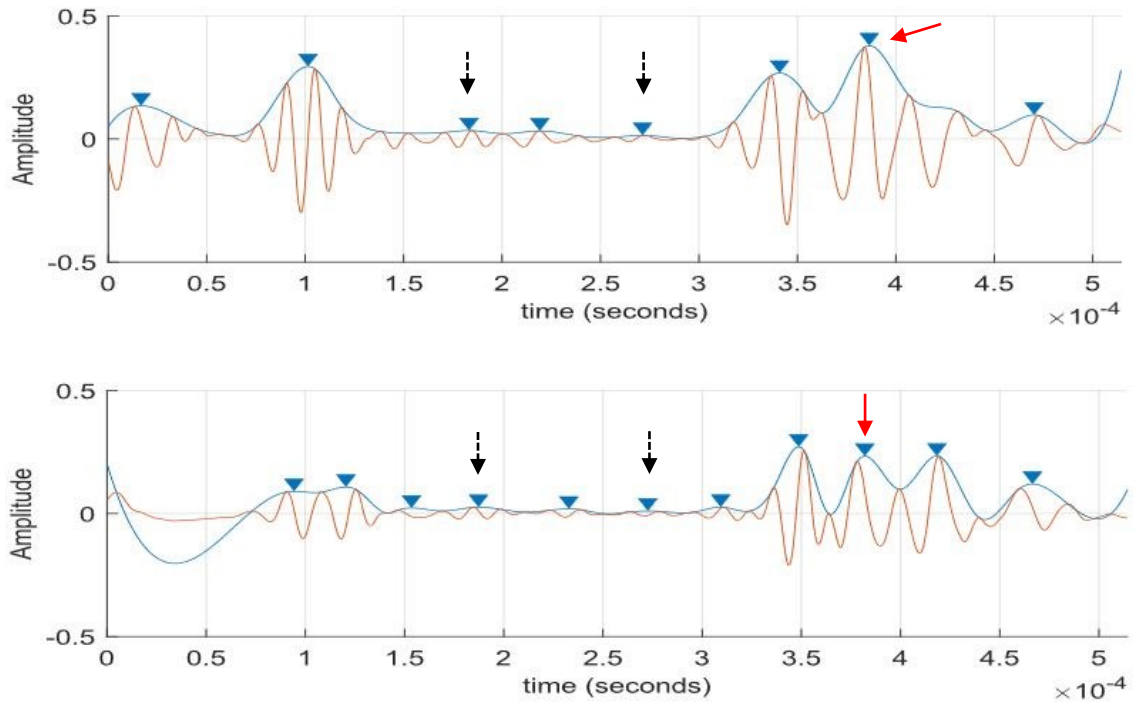


Figure 83: DWT level 9 detail coefficients (experimental analysis) for a ply 2 delamination (top) and a ply 4 delamination (bottom).

Figure 83 shows the A_0 delamination reflection (red arrow) for both the ply 2 and ply 4 delaminations. A baseline signal is not available because the panels were manufactured with an embedded defect. Using a different defect free CFRP panel to generate a baseline signal did not work because of minor differences in the final material properties of the cured panel. To overcome this problem, the baseline velocity was determined from the ToF of an A_0 wave travelling from the sensor location to the edge of the panel and back – a defect free region. In this case, the selected A_0 wave was generated when the S_0 mode contacted the delamination and a mode generated A_0 wave was produced (see Figure 70). This mode generated A_0 wave is shown in Figure 83 with a black dashed arrow. The initial peak is when the mode converted A_0 wave passes the sensor, and the

second peak is when it has reflected off the edge of the part. These peaks were identified using the ABAQUS simulation visualization output. Without the ABAQUS visualization output these peaks would be difficult to identify; therefore, this method would probably not be suitable for real world applications.

The total number of data points in each signal was significantly reduced by applying the DWT decomposition – from 19,785 to 57 data points.

5.4.2 Dispersion Curve

The model-based dispersion curve generated in Section 5.3.3 was used for the experimental panels. However, due to differences between the ABAQUS model and the experimental panels, the dispersion curve was shifted to align with the baseline velocity calculated from the mode converted A_0 wave, see Figure 84.

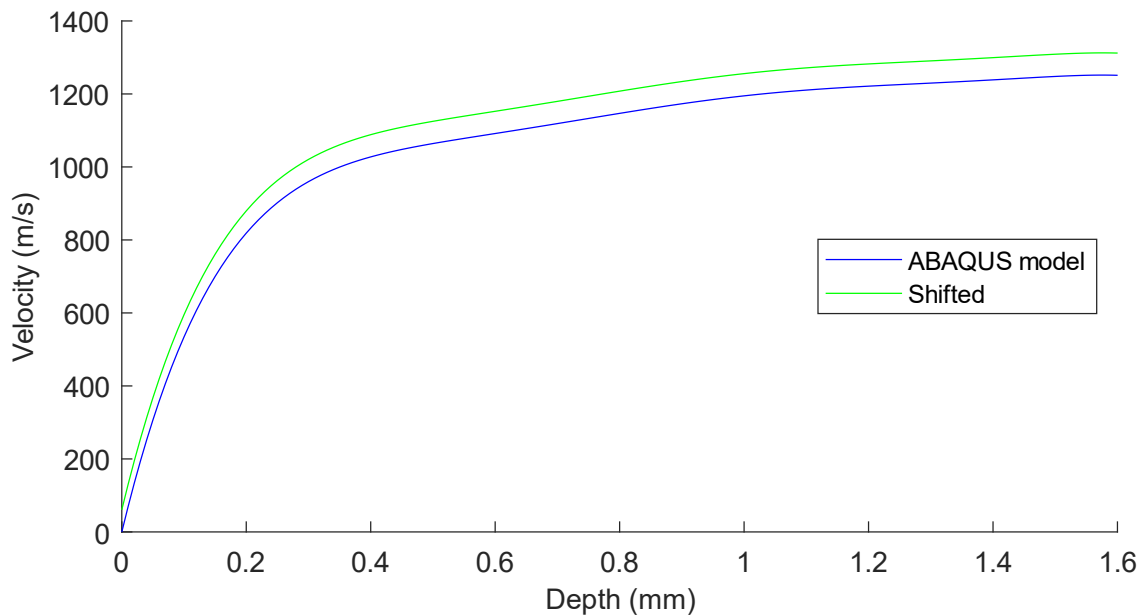


Figure 84: Model based dispersion curve for a CFRP composite plate and a shifted version to match the experimental panel.

5.4.3 Experimental Delamination Length and Depth Results

The delamination length and depth were calculated using the DWT level 9 detail coefficients with Equations (50), (51), and the shifted dispersion curve. The actual size of the delamination was 25.4 x 25.4 mm at a depth of 1.20 mm (ply 2) and 0.80 mm (ply 4). Table 25 shows the results for the experiment panels.

Table 25: Calculated length and depth for experimental panels.

Ply Depth Equivalent	Length (mm)	Length (% Error)	Depth (mm)	Depth (% Error)
Ply 2 (1.20 mm)	29.7 mm	+ 16.9 %	1.17 mm	- 2.5 %
Ply 4 (0.80 mm)	16.0 mm	- 37.0 %	0.77 mm	- 3.8 %

The peaks for the A_0 wave and A_0 reflection wave are clearly visible in Figure 83. However, the calculated length values had larger errors than the 3D ABAQUS simulations. The error values associated with the ply 2 and ply 4 delamination depth were small, 2.5 % and 3.8 %, respectively. The errors associated with the delamination depth are caused by the calculated delamination velocity and mismatch with the model-based dispersion curves. The baseline velocity was calculated with a new method for the experimental panels; this method is not as robust as using a pristine baseline signal from the actual panel before any damage occurs.

5.5 2D Analysis of Delamination Length

A comparison of different delamination lengths was performed to ensure the above method remains valid. This was completed using a 2D ABAQUS simulation with a 25.4 mm and 50.8 mm delamination. The delaminations were located at a depth of 1.54 mm below the surface, equivalent to a ply 2 delamination. The 2D analysis was performed

using the same ABAQUS model described in Chapter 4, Section 4.2, consisting of an aluminum plate and PZT sensors, see Table 26 for the FE model parameters. The actuator-sensor pair were arranged in a pitch-catch configuration using a 90 kHz Mexican hat excitation signal. Plots of the received sensor signals are shown in Figure 85.

Table 26: 2D finite element model parameters for delamination length.

Model Type	Geometry (m)	Element Size (m)	Element Number	Element Type	Time Step (s)	Force Input
Implicit	1.0 x 0.00206	0.00024	120785	CPE4R	1E-7 (max)	Voltage

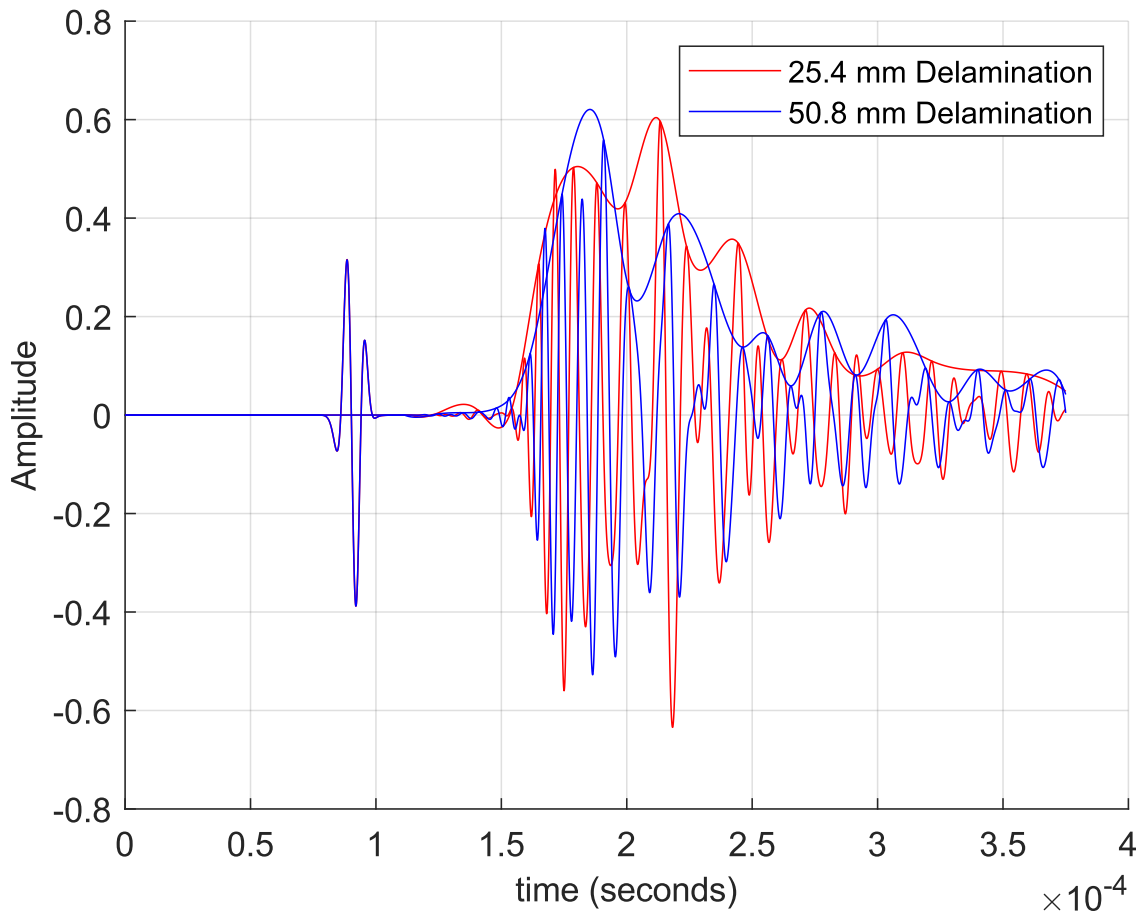


Figure 85: 2D simulation plots for a 25.4 mm and 50.8 mm delamination defect.

The plots in Figure 85 show the S_0 mode is the same for both the 25.4 mm and 50.8 mm delamination defects. Further, the A_0 mode for the 50.8 mm delamination arrives after the A_0 mode for the 25.4 mm delamination, which is expected because the delamination has a slower propagation velocity. The A_0 reflection arrives earlier for the 25.4 mm delamination; however, further analysis is required to identify the A_0 reflection peaks and determine the delamination length.

5.5.1 2D DWT Analysis

A DWT multiple level decomposition revealed the level 6 coefficients had the largest magnitude. A comparison of the approximation and detail coefficients indicated both could be effectively used to identify the A_0 reflection associated with the delamination defect. However, the approximation coefficients provide more distinct A_0 peaks associated with the delamination. A plot of the level 6 approximation coefficients is shown in Figure 86.

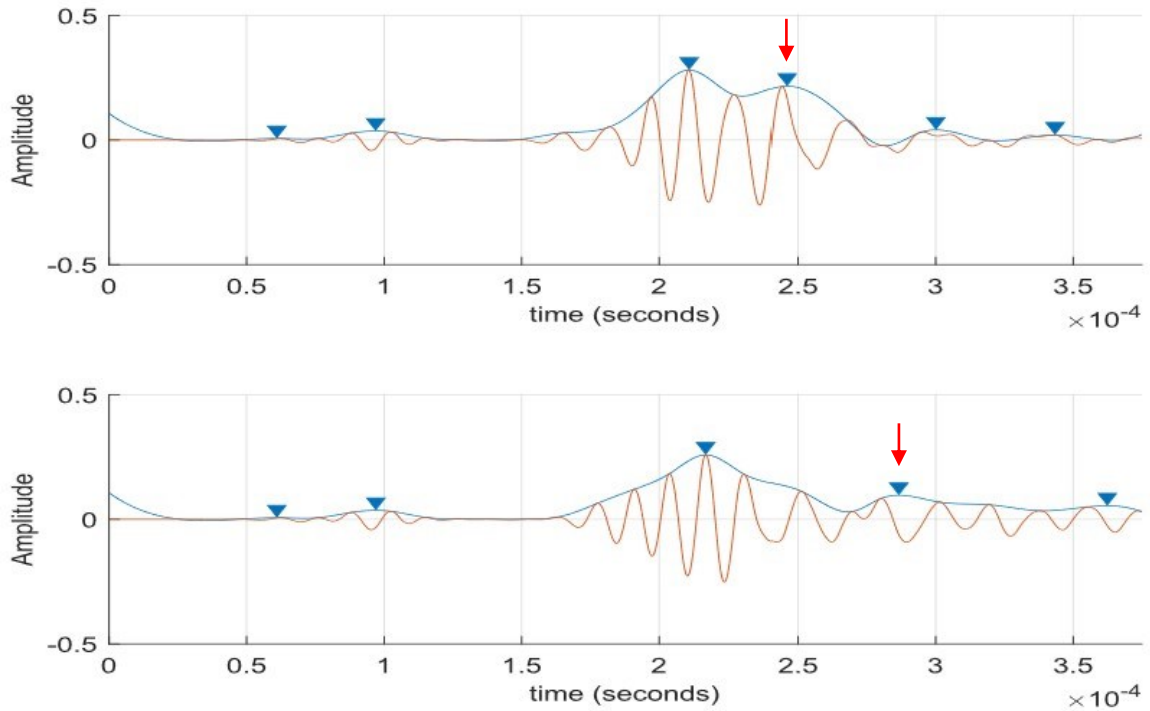


Figure 86: DWT level 5 approximation coefficients for a 2D ABAQUS simulation; 25.4 mm delamination (top) and 50.8 mm delamination (bottom).

Figure 86 shows the A_0 delamination reflection (red arrow); the delay associated with the 50.8 mm delamination can be seen when compared to the 25.4 mm delamination. The initial sensor output signal consisted of 3751 data points, but this was reduced to 77 data points using the level 6 DWT approximation.

5.5.2 Theoretical Dispersion Curve

The theoretical dispersion curve generated for this analysis is shown in Figure 77. The dispersion curve was generated using the free online software Dispersion Calculator [125]. The pre-loaded Aluminum 2024 material properties were used, then the dispersion curve was shifted to match the measured baseline velocity.

5.5.3 2D Delamination Length Results

The results of the DWT level 6 approximation coefficients for the 25.4 mm and 50.8 mm delaminations are shown in Table 27.

Table 27: Calculated length and depth for a 25.4 mm and 50.8 mm delamination defect.

Delamination Length (actual)	Length (mm)	Length (% Error)	Depth (mm)	Depth (% Error)
25.4 mm	22.7 mm	- 10.6 %	1.48 mm	- 3.9 %
50.8 mm	45.3 mm	- 10.8 %	1.61 mm	+ 4.5 %

The calculated length values reported in Table 27 are smaller than the actual length, with error values of 10.6 % and 10.8% for the 25.4 mm and 50.8 mm delamination, respectively. The actual depth of the delamination is 1.54 mm (ply 2 equivalent), but the calculated depth was 1.48 mm and 1.61 mm for the 25.4 m and 50.8 mm delamination, respectively. This indicates a shorter delamination is likely to underestimate the depth and a longer delamination will overestimate the depth. However, the error values of 3.9 % and 4.5 % for the 25.4 mm and 50.8 mm delamination, respectively, were small.

5.6 Discussion

The ability to quantify the severity of a defect or damage in a CFRP structure is an important step in determining the current level of structural integrity, remaining life, and any necessary repairs. When incorporated into an SHM system this allows any new damage or growth of existing damage that occurs between inspection intervals to be recognized before it exceeds dangerous levels. This creates a safer aircraft with the ability to save costs by extending inspection intervals.

Three types of defects were studied in this thesis research: delaminations, foreign objects, and porosity. Delamination damage was selected for further analysis and quantification because of its ability to occur in both manufacturing and in-service operations. To quantify the delamination damage both length and depth were examined. Future research is to consider porosity and foreign objects.

To quantify a delamination defect, an understanding of the interaction of Lamb waves with a delamination defect was gained from previous research. The delamination length and depth were determined from the A_0 reflections generated by the delamination. To correctly calculate the length and depth, it is important to realize that the ToF of the Lamb wave is dependent on both length and depth, see Equations (50) and (51). Therefore, it is not possible to study these independently and obtain correct results, they must be studied together.

A DWT analysis was performed for a delamination at multiple depths using a 2D and 3D ABAQUS simulation and confirmed with experimental testing. An additional analysis was performed with a 2D ABAQUS simulation for delaminations of different lengths. The DWT analysis was performed by completing the following steps:

1. Multiple level decomposition to determine the largest amplitude of the approximation and detail coefficients. The level with the largest coefficients was used for the analysis.
2. The arrival time of the A_0 mode and A_0 reflection was determined and used to calculate the length using the A_0 velocity.
3. The velocity across the delamination is determined using the length calculated in step 2.

4. The delamination velocity calculated in step 3 is used to improve the length calculation. Steps 2 and 3 are repeated until the solution converges.
5. The delamination velocity is compared to theoretical or model-based dispersion curves to determine the depth.

The 2D ABAQUS analysis provided promising results for the length calculation and the correct depth sequence (Table 22). However, the mid-thickness delamination had large length and depth error values, 18.1% and 35.9%, respectively. This is consistent with previous research that indicated mid-thickness defects are the most difficult to identify. Additionally, the error values associated with the depth calculation were large – exceeding 35 % for the ply 2, ply 3, and ply 4 delaminations.

The 3D ABAQUS analysis reduced the error values associated with the depth calculation – with the exception of the ply 4 mid-thickness delamination (Table 24). The improved depth calculations were the result of the model-based dispersion curve that was created using the same 3D ABAQUS model with different thicknesses, while maintaining the correct ply stacking sequence $[0/90/+45/-45]_s$. For example, a single ply simulation was completed with a 0° orientation, a two-ply simulation was complete with a $[0/90]$ ply sequence – this was completed for all 8 ply thicknesses. The large depth error associated with the ply 4 delamination, 57.5%, is caused by the disproportionately large time delay of the A_0 mode, as seen in Figure 79. This arrival time reduces the calculated delamination velocity (Equation (51)), which is then compared to the dispersion curve to determine the depth – a reduce delamination velocity results in a smaller depth prediction.

The 3D ABAQUS analysis resulted in a 24.0 % error for the ply 1 length calculation. This high error is the result of the superposition of the A_0 wave travelling

across the top and bottom sub-laminate. For a ply 1 delamination, there is a significant difference in the thickness of the top laminate (1 ply) and bottom laminate (7 plies). This allows the two waves to separate in time before rejoining at the end of the delamination. This separation results in two distinct peaks for the A_0 mode, as shown in Figure 80 (ply 1 plot). If there was not superposition the actual A_0 peak would fall someplace between the two peaks shown, thus reducing the calculated length.

The experimental results clearly display the A_0 mode and A_0 reflection associated with the delamination defect for both ply 2 and ply 4. However, the errors associated with the length calculation for the ply 2 and ply 4 delamination were 16.9 % and 37.0%, respectively. The ply 4 A_0 reflection peak arrives earlier than anticipated, this could be caused by a partial superposition of the A_0 mode and A_0 reflection. This partial superposition could cause the A_0 reflection peak to shift earlier in time. As mentioned in Section 5.4.1, a new method to determine the A_0 baseline velocity had to be implemented because a pristine signal was not available since these panels were manufactured with an embedded defect. The baseline signal velocity was calculated from the ToF of a mode converted A_0 wave as it passed the sensor, reflected off the part edge, and return to the sensor. This region was a pristine region and provide a good baseline signal, as shown by the depth results. However, this method is not recommended for real world applications because the amplitude associate with the selected mode converted A_0 wave was small and could be difficult to properly identify with additional noise.

Finally, the 2D analysis of different length defects, 25.4 mm and 50.8 mm, provided promising results with length error values of 10.6 % and 10.8%, respectively, and depth

error values of 3.9 % and 4.5 %, respectively. In future research, these results will be confirmed with experimental results and the minimum detectable length will be identified.

5.7 Conclusions

This chapter quantified the size of a delamination defect by calculating the length and depth. The analysis was performed with 2D ABAQUS simulations, 3D ABAQUS simulations, and experimental results. A multiple level DWT decomposition demonstrated:

1. A_0 reflections from the delamination defect could be identified for all cases.
2. The depth sequence for all delaminations was correctly identified.
3. The length ratio of the 25.4 mm and 50.8 mm delamination was correctly found to be 2.0. The calculated lengths were 22.7 mm and 45.3 mm.
4. The DWT decomposition greatly reduces data storage requirements (e.g., 3D ABAQUS data compression from 68094 to 151 data points).

Overall, some error values were large, but from a practical SHM perspective the results will provide valuable information to ensure a delamination is properly identified. The calculated length and depth values will help determine if further NDT inspection by a technician is required. In future, this will allow the transition from fixed inspection intervals (i.e., find it - fix it) to a health monitoring process that is condition based (i.e., find it - monitor it - fix it when needed).

Chapter 6: Discussion

As aircraft fleets are aging and new designs are emerging, an important capability to ensure a safe aircraft is the continuous health monitoring of structural components. This can be achieved with a holistic approach to SHM that continuously monitors a CFRP structure from the curing process through to end of life. Although much research is required to achieve this goal, the present thesis research takes a step in that direction.

The research objectives were outlined in Chapter 1 and shown below. These objectives focus on moving towards a holistic approach to SHM by including the manufacturing of CFRP structures and manufacturing defects.

1. Design a manufacturing process that incorporates piezoelectric sensors into the CFRP structure during the curing process.
2. Identifying unique features associated with three types of manufacturing defects: delaminations, porosity, and foreign objects.
3. Quantifying the severity of a defect by determining the length and depth of a delamination defect. This will also include identifying the optimal excitation signal to interrogate defects.

This chapter provides an overview of the research completed for this dissertation as it relates to the above research objectives.

6.1 Manufacturing of CFRP Structures

Encompassing the manufacturing process, including curing the CFRP structure, as part of the SHM systems provides a complete understanding of the health of the structures including any manufacturing defects. In the future, this type of holistic approach could

eliminate the need for traditional NDT inspections and improve the quality of the structure by customizing the curing process based on feedback from the *in-situ* cure monitoring.

A novel manufacturing method capable of co-curing piezoelectric sensors to CFRP structures was introduced in Chapter 2. The proposed method ensured proper alignment and location of the sensors by modifying the layup tool to securely hold the sensors in place. *In-situ* cure monitoring was possible by installing spring pins through the layup tool with electrical connections on the backside of the tooling. The spring pins made temporary contact with the piezoelectric sensors during the curing process. The result was a CRFP structure with piezoelectric sensors incorporated without limiting future manufacturing process steps (e.g., trimming, inspection, assembly, and finishing).

Experimental testing compared the waveform shape, signal amplitude, and Lamb wave velocity of the co-cured sensors with traditionally bonded sensors. The results showed good agreement between the waveform shape, Lamb wave velocity, and the A_0 mode amplitude; however, the amplitude for S_0 mode was larger for the bonded sensors, particularly for frequencies above 100 kHz. The discrepancies were the result of minor imperfections that occurred during the curing process and were revealed using NDT. Small imperfections are often experienced with changes to the layup and curing process; therefore, with minor improvements and additional experiments it is believe these can be eliminated. Overall, the advantages of the novel approach to co-cure sensors to the CFRP structures are promising and advance the research relating to an SHM system on actual aircraft structures.

6.2 Identification of Multiple Defect Types

The ability to identify and classify different defect types is an important feature of an SHM systems. Each defect type has unique requirements and corrective actions that must be taken. The maximum allowable size, repair procedure, corrective and preventative actions are specific to the type of defect. For example, the corrective and preventative action is different for an embedded foreign object than porosity; the allowable size and concentration of porosity is different than a delamination.

In Chapter 3, numerical and experimental results were used to identify three different types of defects (delamination, porosity, and foreign object) and the unique signal features associated with them. Applying the continuous wavelet transform, a time-frequency domain analysis was able to separate the S_0 and A_0 modes for a more detailed analysis. This allowed the identification of unique features associated with each defect type: delamination – large A_0 reflection amplitude, early A_0 wave cycle, and a A_0 frequency range between 41 – 55 kHz; foreign object – amplitude of the A_0 reflection larger than A_0 mode amplitude, and a narrow A_0 reflection frequency range between 43 – 54 kHz; and Porosity – large S_0 reflection and a large A_0 reflection frequency range between 35 – 63 kHz.

The defect types considered in this research occur during the manufacturing process. This maintains the research objective of developing a holistic SHM system that can extend the existing in-service research to encompasses the full life cycle of the CFRP structure.

6.3 Defect Severity

The severity of a defect has a direct impact on safety; therefore, it is important for an SHM system to be able to quantify the size of a defect. Delaminations are a common type of defect found in both the manufacturing and in-service stages. Further, delamination defects tend to increase in size under cyclic loading, compromising the structure integrity of the CFRP structure. The final objective for this research is to quantify the severity of a delamination defect by calculating the length and depth.

The research presented in Chapters 4 and 5 provides the ability to calculate the length and depth of a delamination defect. First, Chapter 4 studies five excitation signals and determine the Mexican hat signal provides the best combination of resolution, signal-to-noise ratio, and effective frequency range. These measurements are important to accurately size a defect; therefore, the Mexican hat signal was used to quantify the delamination defect as shown in Chapter 5.

Chapter 5 presented the time-frequency domain analysis using a discrete wavelet transform. The relationship between the length and depth calculations was highlighted, showing each affects the arrival time of the A_0 mode. This co-dependent relationship requires the length and depth to be studied together – it is not possible to calculate just the length or just the depth. The numerical and experimental results had large error values for the length calculation, ranging from 0.4 % to 37.0%. The largest error values were associated with a mid-thickness delamination; this was consistent with other research studies that were unable, or had difficulties, recognizing mid-thickness delaminations. The depth calculations also resulted in large error values, ranging from 2.5 % to 57.5 %. Similar to the length calculation, the largest error values were associated with the mid-thickness

delamination. Despite the large error values, the results did correctly identify the depth sequence.

6.4 Summary

The research objectives, as outlined in Chapter 1, were successfully achieved. This provides an important contribution to the existing body of knowledge and a promising step towards a holistic SHM system capable of monitoring a structure thorough its entire life cycle. With further development, this has the potential to eliminate the need for NDT inspections and transition the aircraft industry from schedule-based maintenance to condition-based maintenance. This would greatly improve the safety of aircraft and potentially reduce the operational costs.

Chapter 7: Conclusions and Statement of Contributions

This research investigated the recognition, identification, and severity of defects in CFRP composite panels using ultrasonic Lamb waves. This required the design of a novel manufacturing method to co-cure piezoelectric sensors to CFRP panels. The investigation was performed on three defect types: delamination, porosity, and foreign objects using both numerical and experimental methods. Conclusions were included at the end of each chapter but are summarized below for clarity.

7.1 Manufacturing Process to Integrate Sensors (Chapter 2)

Implementing a novel method to co-cure piezoelectric sensor with a CFRP panel demonstrated the following benefits:

- Precise and repeatable location of sensors. This is important when interpreting results from multiple structures.
- Capability of *in-situ* cure monitoring by using temporary electrical connections to the piezoelectric sensor. Temporary connections are important features that overcomes issues associated with wire management during subsequent manufacturing processes (e.g., trimming, inspection, assembly, and finishing).
- Reduction in the number of manufacturing steps by eliminating secondary bonding of sensors.

A comparison of Lamb wave propagation for the co-cured and bonded piezoelectric sensors showed:

- Similar waveform shape with minor differences experienced for the S_0 and A_0 reflections when the excitation signal was above 75 kHz.

- No change in the Lamb wave propagation velocity for the S_0 and A_0 mode.
- Similar signal amplitude for the A_0 mode.
- Larger S_0 signal amplitude for the bonded sensor, especially above 100 kHz.

7.2 Defect Identification (Chapter 3)

Implementing the continuous wavelet transform to perform a time-frequency analysis on different types of defects using numerical and experimental results showed:

- Unique signal features associated with delamination, porosity, and foreign object defects.
- The ability to identify each defect type based on the unique signal features.

7.3 Input Signal Comparison (Chapter 4)

The comparison of five input signals was performed to determine the best signal to identify delamination damage. The five signals included: 5-cycle sine wave, 3-cycle sine wave, Mexican hat, 13-bit Barker coded sine wave, and an auto-correlated linear chirp. Chapter 3 found the A_0 reflection was the main feature generated by a delamination defect; therefore, the A_0 reflection was compared for each of the five signals, this showed:

- The best results for the main lobe width (MLW) resolution were determined in the following order: 13-bit Barker coded sine wave, auto-correlated linear chirp, Mexican hat, 3-cycle sine wave, and 5-cycle sine wave.
- The best results for the signal-to-noise ratio (SNR) were determined in the following order: 13-bit Barker coded sine wave, Mexican hat, 3-cycle sine wave, 5-cycle sine wave, and auto-correlated linear chirp.

- The Mexican hat signal had the best average MLW and SNR over a range of frequencies and performed better at lower frequencies.

Based on the findings, the Mexican hat signal was recommended to determine the severity of delamination defects.

7.4 Delamination Defect Analysis (Chapter 5)

The severity of a delamination defect was determined by calculating the length and depth. A multiple level discrete wavelet transform (DWT) decomposition was applied to numerical and experimental results, and determined:

- The depth sequence for all delamination defects was correctly identified (e.g., the ply 1 defect was deeper than the ply 2 defect, the ply 2 defect was deeper than the ply 3 defect, etc.).
- The comparison of two delamination with different lengths correctly identified the length ratio.
- The multiple level discrete wavelet transform decomposition greatly reduced data storage requirements. The data reduction ranged from 24 – 450 times, depending on the original signal length and the level of decomposition.

The error values for the length and depth were large, especially for the mid-thickness delamination (experimental length error – 37.0 % and 3D ABAQUS depth error - 57.5%). However, all delamination defects were identified. The proposed method to determine the severity of a delamination defect still provides valuable information; however, as a first step, this information would need to be confirmed with NDT inspections.

7.5 Statement of Research Contributions

The objective of this dissertation research was the development of a holistic SHM system using Lamb waves to monitor CFRP structures. Several important contributions were made in the pursuit of this objective, including:

1. The development of a unique manufacturing method to co-cure piezoelectric sensors on CFRP structures. This is very significant from a practical perspective. To transition SHM research from an academic setting to a viable industry technique, the focus must include a “design for manufacturing” approach. The proposed co-curing manufacturing technique allows for *in-situ* cure monitoring and manufacturing inspections. This has the potential to improve the efficiency of manufacturing CFRP structures by improving the curing process and eliminating both the NDT inspection and a specify step to bond the sensors to the structure. Additionally, this co-curing technique does not hamper other manufacturing process, including trimming, inspection, finishing, and assembly.
2. The identification of different types of defects, including: delamination, porosity, and foreign objects. This extends previous research that focused on in-service defect types to defects found during the manufacturing process. Currently, there is very limited research on the interaction of Lamb waves with porosity and foreign objects. This extends the capability of an SHM system to monitor the full life cycle of the CFRP structure.
3. The comparison of five different excitation signals for the purpose of defect identification. Previous research had focused on optimizing the input signal for

the purpose of increasing propagation distance and reducing dispersion. However, the primary goal of an SHM system is to recognize defects; therefore, an input signal capable of improving the ability to recognize and quantify defects is important. It was determined that a Mexican hat input signal is most effective at identifying delamination defects.

4. Quantifying the severity of a delamination defect by calculating the length and depth using piezoelectric sensors in a pitch-catch configuration. This was completed using a multiple level DWT decomposition, which revealed two important research contributions. First, the utilization of time-of-flight data from the A_0 mode and A_0 reflection – this establishes a simple method to calculate the length and depth of a delamination defect. Second, and very important, the ability to reduce the amount of data storage or transmission using the DWT decomposition. This demonstrated the ability to reduce the data 450 times, while still maintaining the important signal features to recognize and quantify a delamination defect. Installing an SHM system on an aircraft could require thousands or millions of sensors; therefore, data compression is a critical consideration.

Overall, maintaining a focus on the practical applications of an SHM systems provided an important contribution in narrowing the gap between theoretical research and real-world application.

7.6 Future Recommendations

Although important steps and significant contributions were made towards the development of a holistic SHM system, many gaps and research opportunities still exist.

Recommendations for future research include:

1. Analysis of complex CFRP structures with different geometries, thicknesses, and bonded components (e.g., stiffeners). The present thesis research focused on flat panels. Before an SHM system can be applied to an aircraft it must be demonstrated on similar structures.
2. Study the effects of environmental factors and different loading conditions. This would include the effects of temperature, humidity, and cyclic loads. The proposed research focused on a system that could provide active ground-based monitoring when environmental and loading conditions are controlled. However, the ultimate goal of an SHM systems is to provide in-flight monitoring.
3. Extend the current research to additional advance composite materials and manufacturing processes. For example, glass and aramid fibers or resin infusion, resin transfer moulding, and autoclave curing. Aircraft structures are composed of many different types of materials, manufactured with different processes – an SHM system should be capable of accommodating most types of aircraft structures.
4. Study and incorporate *in-situ* cure monitoring as part of the SHM system. The proposed co-curing manufacturing method has the capability for *in-situ* cure monitoring; however, preliminary research failed because cure temperatures

were above the maximum operating temperature of the connection wires. *In-situ* cure monitoring has the ability to improve the quality of components and improve the curing efficiency; this is achieved by avoiding under or over cured components.

5. Quantify the severity of other defect types; this should include porosity and foreign object defects, but also in-service damage such as impact damage, matrix cracking, and fibre breakage.
6. Determine the defect location. Four important considerations for an SHM systems were identified to include: 1) recognition, 2) identification, 3) severity, and 4) location. This research addressed the first three items, however, the ability to locate a defect has been left to future research. The ability to locate a defect is important for efficient maintenance and to determine the effect on the structural integrity.
7. Recognize defects that are not located on a direct path from the actuator to sensor. For the current research, defects were centered between the actuator and sensor; however, actual defects may occur anywhere on the structure. Therefore, it is important to determine the effects of defect position relative to the actuator-sensor pair. The ABAQUS simulation provide promising insight by showing the Lamb wave reflections propagate outwards in a circular pattern away from the defect location.
8. Determine the probability of detection for each defect type. This will require manufacturing additional CFRP panels to perform a statistical analysis.

The current research has made significant steps towards a holistic SHM system; however, additional research is required. Pursuing the above recommendations will continue to advance the technology readiness level of SHM with the potential to make aircraft safer while reducing operating costs – an exciting field to research.

References

- [1] Boeing, “<http://www.boeing.com/commercial/787/#/design-highlights/visionary-design/composites/advanced-composite-use/>,” *Website*, 2015. .
- [2] Airbus,
“<http://www.airbus.com/aircraftfamilies/passengeraircraft/a350xwbfamily/technology-and-innovation/>,” *Website*, 2015.
<http://www.airbus.com/aircraftfamilies/passengeraircraft/a350xwbfamily/technology-and-innovation/> (accessed Aug. 20, 2015).
- [3] P. K. Mallick, “Fiber-Reinforced Composites: Materials, Manufacturing, and Design,” in *Fiber-Reinforced Composites*, 3rd ed., CRC Press, 2007.
- [4] Unknown_Author, *Composite Materials Handbook, Volume 3: United States Department of Defense Handbook*. United States Department of Defense, 1997.
- [5] Author_Unknown, “Aviation Accident Report – Loss of Rudder in Flight – Air Transat, Airbus A310-308, C-GPAT,” 2007.
- [6] Author_Unknown, “In-Flight Separation of Vertical Stabilizer American Airlines Flight 587 Airbus Industrie A300-605R,” *Natl. Transp. Saf. Board, Aircr. Accid. Rep. NTSB_AAR-04-04*, 2001.
- [7] S. R. Hall and T. J. Conquest, “The total data integrity initiative - structural health monitoring, the next generation,” 1999.
- [8] M. Bowkett and K. Thanapalan, “Comparative analysis of failure detection methods of composites materials’ systems,” *Syst. Sci. Control Eng.*, vol. 5, no. 1, pp. 168–177, 2017, doi: 10.1080/21642583.2017.1311240.
- [9] R. Di Sante, “Fibre optic sensors for structural health monitoring of aircraft

- composite structures: Recent advances and applications,” *Sensors*, vol. 15, no. 8, pp. 18666–18713, 2015.
- [10] V. Giurgiutiu, *Structural health monitoring of aerospace composites*. 2016.
- [11] A. Pegoretti, *Structural health monitoring: Current state and future trends*. 2019.
- [12] S. Konstantopoulos, “Monitoring the production of FRP composites: A review of in-line sensing methods,” *Express Polym. Lett.*, vol. 8, no. 11, pp. 823–840, 2014, doi: 10.3144/expresspolymlett.2014.84.
- [13] A. Maslouhi, “Fatigue crack growth monitoring in aluminum using acoustic emission and acousto-ultrasonic methods,” *Struct. Control Heal. Monit.*, pp. 790-806., 2011.
- [14] Y. Pappas and V. Kostopoulos, “Toughness characterization and acoustic emission monitoring of a 2D carbon/carbon composite,” *Eng. Fract. Mech.*, vol. 68, no. 14, pp. 1557–1573, 2001.
- [15] D. Roach, “Real time crack detection using mountable comparative vacuum monitoring sensors,” *Smart Struct. Syst.*, vol. 5, no. 4, pp. 317–328, 2009.
- [16] F. Eialdi and K. H. Okulu, “An Overview for Structural Health Monitoring of Composites in Aerospace Applications,” in *RAST 2005. Proceedings of 2nd International Conference on Recent Advances in Space Technologies*, 2005, pp. 309–314.
- [17] M. D. Rogge and C. A. C. Leckey, “Characterization of impact damage in composite laminates using guided wavefield imaging and local wavenumber domain analysis,” *Ultrasonics*, vol. 53, no. 7, pp. 1217–1226, 2013, doi: 10.1016/j.ultras.2012.12.015.

- [18] T. B. Hudson, T. H. Hou, B. W. Grimsley, and F. G. Yuan, “Imaging of local porosity/voids using a fully non-contact air-coupled transducer and laser Doppler vibrometer system,” *Struct. Heal. Monit.*, vol. 16, no. 2, pp. 164–173, 2017, doi: 10.1177/1475921716668843.
- [19] R. Jenal, W. Staszewski, A. Klepka, and T. Uhl, “Structural damage detection using laser vibrometers,” 2010.
- [20] Z. Su and L. Ye, *Ch2-Fundamentals and Analysis of Lamb Waves*, vol. 48. Berlin: Springer, 2009.
- [21] S. Pant, “Lamb Wave Propagation and Material Characterization of Metallic and Composite Aerospace Structures for Improved Structural Health Monitoring (SHM),” Carleton University, 2014.
- [22] S. Pant, J. Laliberte, M. Martinez, B. Rocha, and D. Ancrum, “Effects of composite lamina properties on fundamental Lamb wave mode dispersion characteristics,” *Compos. Struct.*, vol. 124, pp. 236–252, 2015, doi: 10.1016/j.compstruct.2015.01.017.
- [23] S. Pant, J. Laliberte, M. Martinez, and B. Rocha, “Derivation and experimental validation of Lamb wave equations for an n-layered anisotropic composite laminate,” *Compos. Struct.*, vol. 111, no. 1, pp. 566–579, 2014, doi: 10.1016/j.compstruct.2014.01.034.
- [24] S. Pant, J. Laliberte, M. Martinez, and B. Rocha, “In-situ characterization of isotropic and transversely isotropic elastic properties using ultrasonic wave velocities,” *Mater. Perform. Charact.*, vol. 5, no. 1, pp. 164–188, 2016, doi: 10.1520/MPC20150021.

- [25] P. D. Wilcox, M. J. S. Lowe, and P. Cawley, "Mode and Transducer Selection for Long Range Lamb Wave Inspection," vol. 12, no. August 2001, pp. 553–565, 2002, doi: 10.1106/N9PB-Y62E-P0Y2-50QF.
- [26] K. Maslov and T. Kundu, "Selection of Lamb modes for detecting internal defects in composite laminates.pdf." 1997.
- [27] J. L. Rose, a. Pilarski, and J. J. Ditri, "An Approach to Guided Wave Mode Selection for Inspection of Laminated Plate," *J. Reinf. Plast. Compos.*, vol. 12, no. 5, pp. 536–544, 1993, doi: 10.1177/073168449301200504.
- [28] Z. Su, L. Ye, and Y. Lu, "Guided Lamb waves for identification of damage in composite structures: A review," *J. Sound Vib.*, vol. 295, pp. 753–780, 2006, doi: 10.1016/j.jsv.2006.01.020.
- [29] H. Sohn and S. J. Lee, "Lamb wave tuning curve calibration for surface-bonded piezoelectric transducers," *Smart Mater. Struct.*, vol. 19, no. 1, p. 015007, 2009, doi: 10.1088/0964-1726/19/1/015007.
- [30] Z. Su and L. Ye, "Selective generation of Lamb wave modes and their propagation characteristics in defective composite laminates.pdf," *Proc. Inst. Mech. Eng. Part L. J. Mater. Des. Appl.*, vol. 218, pp. 95–110, 2004.
- [31] S. Grondel, C. Paget, C. Delebarre, J. Assaad, and K. Levin, "Design of optimal configuration for generating A0 Lamb mode in a composite plate using piezoceramic transducers," *J. Acoust. Soc. Am.*, vol. 112, no. 1, pp. 84–90, 2002, doi: 10.1121/1.1481062.
- [32] Y. J. Yan and L. H. Yam, "Mechanical interaction issues in piezoelectric composite structures," *Compos. Struct.*, vol. 59, pp. 61–65, 2003, doi:

10.1016/S0263-8223(02)00229-5.

- [33] S. Masmoudi, A. El Mahi, and R. El Guerjouma, “Mechanical behaviour and health monitoring by acoustic emission of sandwich composite integrated by piezoelectric implant,” *Compos. Part B Eng.*, vol. 67, pp. 76–83, 2014, doi: 10.1016/j.compositesb.2014.05.032.
- [34] M. Lin and F.-K. Chang, “The manufacture of composite structures with a built-in network of piezoceramics,” *Compos. Sci. Technol.*, vol. 62, pp. 919–939, Jun. 2002, doi: 10.1016/S0266-3538(02)00007-6.
- [35] S. Mall, “Integrity of graphite / epoxy laminate embedded with piezoelectric sensor / actuator under monotonic and fatigue loads,” *Smart Mater. Struct.*, vol. 11, pp. 527–533, 2002.
- [36] M. Arellano, L. Crouzeix, F. Collombet, B. Douchin, and Y. H. Grunevald, “Mechanical characterization of an alternative technique to embed sensors in composite structures: The monitoring patch,” *Appl. Compos. Mater.*, vol. 19, pp. 379–391, 2012, doi: 10.1007/s10443-011-9198-7.
- [37] S. Masmoudi, A. El Mahi, and S. Turki, “Fatigue behaviour and structural health monitoring by acoustic emission of E-glass/epoxy laminates with piezoelectric implant,” *Appl. Acoust.*, vol. 108, pp. 50–58, 2015, doi: 10.1016/j.apacoust.2015.10.024.
- [38] J. Chilles, A. Croxford, and I. P. Bond, “Design, application, and validation of embedded ultrasonic sensors within composite structures,” in *SPIE - Structural Health Monitoring and Inspection of Advanced Materials*, 2015, vol. 9437, p. 12 pp., doi: 10.1117/12.2083944.

- [39] Y. Xiao, W. Qiao, H. Fukuda, and H. Hatta, "The effect of embedded devices on structural integrity of composite laminates," *Compos. Struct.*, vol. 153, pp. 21–29, 2016, doi: 10.1016/j.compstruct.2016.06.007.
- [40] F. Ghezzi, Y. Huang, and S. Nemat-Nasser, "Onset of Resin Micro-Cracks in Unidirectional Glass Fiber Laminates with Integrated SHM Sensors: Experimental Results," *Struct. Heal. Monit.*, vol. 8, no. 6, pp. 477–491, 2009, doi: 10.1177/1475921709340976.
- [41] M. Javdanitehran, R. Hoffmann, J. Groh, M. Vossiek, and G. Ziegmann, "Effect of embedded printed circuit board (PCB) sensors on the mechanical behavior of glass fiber-reinforced polymer (GFRP) structures," *Smart Mater. Struct.*, vol. 25, p. 11 pp., 2016, doi: 10.1088/0964-1726/25/6/065016.
- [42] D. J. Warkentin, E. F. Crawley, and S. D. Senturia, "Feasibility of Embedded Electronics for Intelligent Structures," *J. Intell. Mater. Syst. Struct.*, vol. 3, no. July, pp. 462–482, 1992.
- [43] K. P. Duffy, B. A. Lerch, N. G. Wilmoth, N. Kray, and G. Gemeinhardt, "Mechanical and vibration testing of carbon fiber composite material with embedded piezoelectric sensors," *Proc. SPIE - Int. Soc. Opt. Eng.*, vol. 8341, pp. 1–14, 2012, doi: 10.1117/12.916769.
- [44] X. P. Qing, S. J. Beard, A. Kumar, T. K. Ooi, and F.-K. Chang, "Built-in Sensor Network for Structural Health Monitoring of Composite Structure," *J. Intell. Mater. Syst. Struct.*, vol. 18, pp. 39–49, 2007, doi: 10.1177/1045389X06064353.
- [45] J. S. Chilles, A. Croxford, and I. P. Bond, "Design of an embedded sensor, for improved structural performance," *Smart Mater. Struct.*, vol. 24, p. 10pp, 2015,

doi: 10.1088/0964-1726/24/11/115014.

- [46] M. N. Ghasemi-Nejhad, R. Russ, and S. Pourjalali, “Manufacturing and testing of active composite panels with embedded piezoelectric sensors and actuators,” *J. Intell. Mater. Syst. Struct.*, vol. 16, pp. 319–333, 2005, doi: 10.1177/1045389X05050103.
- [47] D. R. Shukla and A. J. Vizzini, “Interlacing for improved performance of laminates with embedded devices,” *Smart Mater. Struct.*, vol. 5, pp. 225–229, 1996.
- [48] P. C. GmbH, “No Title.” <https://www.piceramic.com/en/products/piezoceramic-components/disks-rods-and-cylinders/> (accessed Sep. 10, 2021).
- [49] S. Mustapha and L. Ye, “Bonding Piezoelectric Wafers for Application in Structural Health Monitoring—Adhesive Selection,” *Res. Nondestruct. Eval.*, vol. 26, pp. 23–42, 2015, doi: 10.1080/09349847.2014.934575.
- [50] C. Rosania, C. Larrosa, and F. Chang, “Design of intelligent composites with life-cycle health management capabilities.pdf,” in *Proceedings of the SPIE - The International Society for Optical Engineering: Health Monitoring of Structural and Biological Systems*, 2015, p. Vol 9438, 11 pages.
- [51] S. Pavlopoulou, C. Soutis, and W. Staszewski, “Cure monitoring through time-frequency analysis of guided ultrasonic waves,” *Plast. Rubber Compos.*, vol. 41, pp. 180–186, 2012.
- [52] K. Mizukami, T. Ikeda, and K. Ogi, “Measurement of velocity and attenuation of ultrasonic guided wave for real-time estimation of cure-dependent anisotropic viscoelastic properties of carbon fiber-reinforced plastics,” *Ultrasonics*, vol. 99,

- no. February, p. 105952, 2019, doi: 10.1016/j.ultras.2019.105952.
- [53] T. B. Hudson and F. G. Yuan, “Automated in-process cure monitoring of composite laminates using a guided wave-based system with high-temperature piezoelectric transducers,” *J. Nondestruct. Eval. Diagnostics Progn. Eng. Syst.*, vol. 1, no. 2, pp. 1–8, 2018, doi: 10.1115/1.4039230.
- [54] T. B. Hudson, N. Auwajjan, and F. G. Yuan, “Guided wave-based system for real-time cure monitoring of composites using piezoelectric discs and phase-shifted fiber Bragg gratings,” *J. Compos. Mater.*, vol. 53, no. 7, pp. 969–979, 2019, doi: 10.1177/0021998318793512.
- [55] L. Su, Z., and Ye, *Identification of Damage Using Lamb Waves from Fundamentals to Applications*, Lecture No. Berlin: Springer, 2009.
- [56] V. Giurgiutiu, *Structural Health Monitoring with Piezoelectric Wafer Active Sensors*. Boston: Elsevier/Academic, 2008.
- [57] Y. Bar-Cohen and D. E. Chimenti, “Detection of porosity in composite laminates by leaky lamb waves,” in *Int Committee on Nondestructive Testing*, 1985, pp. 1661–1668.
- [58] T. B. Hudson, T. H. Hou, B. W. Grimsley, and F. G. Yuan, “Detection of CFRP composite manufacturing defects using a guided wave approach,” in *International SAMPE technical conference*, 2015, p. 16 pages.
- [59] F. C. Campbell, *Structural Composite Materials*. Materials Park, Ohio: ASM International, 2010.
- [60] S. S. Kessler, S. M. Spearing, and C. Soutis, “Damage detection in composite materials using Lamb wave methods,” *Smart Mater. Struct.*, vol. 11, pp. 269–278,

2002, doi: 10.1088/0964-1726/11/2/310.

- [61] B. Feng, A. L. Ribeiro, and H. G. Ramos, “Interaction of Lamb waves with the edges of a delamination in CFRP composites and a reference-free localization method for delamination,” *Measurement*, vol. 122, pp. 424–431, 2018, doi: 10.1016/j.measurement.2017.10.016.
- [62] Y. Liu, M. Yekani Fard, S. B. Kim, A. Chattopadhyay, and D. Doyle, “Damage detection in composite structures using Lamb wave analysis and time-frequency approach,” *Proc. SPIE - Sensors Smart Struct. Technol. Civil, Mech. Aerosp. Syst.*, vol. 7981, no. April 2011, p. 16 pages, 2011, doi: 10.1117/12.880664.
- [63] M. Carboni, A. Gianneo, and M. Giglio, “A Lamb waves based statistical approach to structural health monitoring of carbon fibre reinforced polymer composites,” *Ultrasonics*, no. In press, 2015, doi: 10.1016/j.ultras.2015.02.011.
- [64] E. A. Birt, “Damage detection in carbon-fibre composites using ultrasonic Lamb waves,” *Insight*, vol. 40, no. 5, pp. 335–339, 1998, Accessed: May 14, 2015. [Online]. Available: <http://cat.inist.fr/?aModele=afficheN>.
- [65] P. Kudela and W. Ostachowicz, “A Multilayer Delaminated Composite Beam and Plate Elements: Reflections of Lamb Waves at Delamination,” *Mech. Adv. Mater. Struct.*, vol. 16, no. 3, pp. 174–187, 2009, doi: 10.1080/15376490902746749.
- [66] Z. Ma and L. Yu, “Ultrasonic Lamb wave inspection of composite defects,” *Proc. SPIE - Int. Soc. Opt. Eng.*, vol. 11381, no. April, p. 7 pages, 2020, doi: 10.1117/12.2558188.
- [67] H. Mei, M. F. Haider, R. James, and V. Giurgiutiu, “Pure S0 and SH0 detections of various damage types in aerospace composites,” *Compos. Part B Eng.*, vol. 189,

- no. 107906, pp. 1–18, 2020, doi: 10.1016/j.compositesb.2020.107906.
- [68] I. Dafydd and Z. Sharif Khodaei, “Analysis of barely visible impact damage severity with ultrasonic guided Lamb waves,” *Struct. Heal. Monit.*, vol. 19, no. 4, pp. 1104–1122, 2020, doi: 10.1177/1475921719878850.
- [69] C. M. Yeum, H. Sohn, J. B. Ihn, and H. J. Lim, “Instantaneous delamination detection in a composite plate using a dual piezoelectric transducer network,” *Compos. Struct.*, vol. 94, no. 12, pp. 3490–3499, 2012, doi: 10.1016/j.compstruct.2012.06.003.
- [70] M. J. Santos, J. B. Santos, a. M. Amaro, and M. a. Neto, “Low velocity impact damage evaluation in fiber glass composite plates using PZT sensors,” *Compos. Part B Eng.*, vol. 55, pp. 269–276, 2013, doi: 10.1016/j.compositesb.2013.06.036.
- [71] P. Guy, Y. Jayet, and L. Goujon, “Guided waves interaction with complex delaminations. Application to damage detection in composite structures.,” *NDE Heal. Monit. Diagnostics*, vol. 5047, pp. 25–33, 2003, doi: 10.1117/12.483926.
- [72] X. Liu, B. Wang, F. Ai, D. Wei, and L. Bo, “Evaluation of matrix cracking in composite laminates based on anomaly indices,” *Int. J. Fatigue*, vol. 140, no. July, 2020, doi: 10.1016/j.ijfatigue.2020.105841.
- [73] H. Jia, H. Liu, Z. Zhang, F. Dai, Y. Liu, and J. Leng, “A baseline-free approach of locating defect based on mode conversion and the reciprocity principle of Lamb waves,” *Ultrasonics*, vol. 102, no. February 2019, p. 106063, 2020, doi: 10.1016/j.ultras.2020.106063.
- [74] Z. Su and L. Ye, “Lamb Wave Propagation-based Damage Identification for Quasi-isotropic CF/EP Composite Laminates Using Artificial Neural Algorithm:

- Part I - Methodology and Database Development,” *J. Intell. Mater. Syst. Struct.*, vol. 16, no. February, pp. 97–111, 2005, doi: 10.1177/1045389X05047599.
- [75] J. Liu, W. Wang, and F. Golnaraghi, “An extended wavelet spectrum for bearing fault diagnostics,” *IEEE Trans. Instrum. Meas.*, vol. 57, no. 12, pp. 2801–2812, 2008, doi: 10.1109/TIM.2008.927211.
- [76] R. A. Esmael and F. Taheri, “Delamination detection in laminated composite beams using the empirical mode decomposition energy damage index,” *Compos. Struct.*, vol. 94, no. 5, pp. 1515–1523, 2012, doi: 10.1016/j.compstruct.2011.12.029.
- [77] P. S. Addison, *The illustrated wavelet transform handbook: Introductory theory and applications in science, engineering, medicine and finance*. Bristol, UK: Institute of Physics Publishing, 2002.
- [78] C. A. C. Leckey, K. R. Wheeler, V. N. Hafiychuk, H. Hafiychuk, and D. A. Timuçin, “Simulation of guided-wave ultrasound propagation in composite laminates: Benchmark comparisons of numerical codes and experiment,” *Ultrasonics*, vol. 84, pp. 187–200, 2018, doi: 10.1016/j.ultras.2017.11.002.
- [79] *ABAQUS Documentation*. .
- [80] F. Moser, L. J. Jacobs, and J. Qu, “Modeling elastic wave propagation in waveguides with the finite element method,” *NDT E Int.*, vol. 32, no. 4, pp. 225–234, 1999, doi: 10.1016/S0963-8695(98)00045-0.
- [81] D. N. Alleyne and P. Cawley, “The Interaction of Lamb Waves with Defects,” *IEEE Trans. Ultrason. Ferroelectr. Freq. Control*, vol. 39, no. 3, pp. 381–397, 1992, doi: 10.1063/1.1570251.

- [82] M. Gresil, V. Giurgiutiu, Y. Shen, and B. Poddar, "Guidelines for Using the Finite Element Method for Modeling Guided Lamb Wave Propagation in SHM Processes," in *6th European Workshop on Structural Health Monitoring*, 2014, pp. 1–8.
- [83] P. Rajagopal, M. Drozd, E. A. Skelton, M. J. S. Lowe, and R. V Craster, "On the use of absorbing layers to simulate the propagation of elastic waves in unbounded isotropic media using commercially available Finite Element packages," *NDT E Int.*, vol. 51, pp. 30–40, 2012, doi: 10.1016/j.ndteint.2012.04.001.
- [84] G. Lui and Quek, "A non-reflecting boundary for analyzing wave propagation using the finite element method," *Finite Elem. Anal. Des.*, vol. 39, no. 5–6, pp. 403–417, 2003.
- [85] J. R. Pettit, A. Walker, P. Cawley, and M. J. S. Lowe, "A Stiffness Reduction Method for efficient absorption of waves at boundaries for use in commercial Finite Element codes," *Ultrasonics*, vol. 54, no. 7, pp. 1868–1879, 2014, doi: 10.1016/j.ultras.2013.11.013.
- [86] B. Feng, A. L. Ribeiro, and H. G. Ramos, "A new method to detect delamination in composites using chirp-excited Lamb wave and wavelet analysis," *NDT E Int.*, vol. 100, pp. 64–73, 2018, doi: 10.1016/j.ndteint.2018.08.004.
- [87] Y. Okabe, K. Fujibayashi, M. Shimazaki, H. Soejima, and T. Ogisu, "Delamination detection in composite laminates using dispersion change based on mode conversion of Lamb waves," *Smart Mater. Struct.*, vol. 19, no. 11, 2010, doi: 10.1088/0964-1726/19/11/115013.
- [88] C. Ng, "3D Finite Element Modeling of Absorbing Regions for Guided Wave

- Scattering Problems in Composite Materials,” *GSTF Int. J. Eng. Technol.*, vol. 2, no. 1, pp. 244–249, 2013, doi: 10.5176/2251-3701.
- [89] S. Gupta and P. Rajagopal, “Effect of ply orientation and through-thickness position of delamination on the reflection of fundamental symmetric S0 Lamb mode in GFRP composite plate structures,” *Ultrasonics*, vol. 90, no. June, pp. 109–119, 2018, doi: 10.1016/j.ultras.2018.06.007.
- [90] N. Guo and P. Cawley, “The interaction of Lamb waves with delaminations in composite laminates,” *J. Acoust. Soc. Am.*, vol. 94, no. 4, pp. 2240–2246, 1993, doi: 10.1121/1.407495.
- [91] F. C. Campbell, A. R. Mallow, and C. E. Browning, “Porosity in carbon fiber composites an overview of causes,” *J. Adv. Mater.*, vol. 26, no. 4, pp. 18–33, 1995.
- [92] M. F. Haider, B. Poddar, and V. Giurgiutiu, “Experimental validation of an analytical method to predict lamb wave scattering from a discontinuity,” *Smart Mater. Struct.*, vol. 28, no. 1, p. 15012, 2019, doi: 10.1088/1361-665X/aae910.
- [93] D. N. Alleyne and P. Cawley, “Optimization of lamb wave inspection techniques,” *NDT E Int.*, vol. 25, no. 1, pp. 11–22, 1992, doi: 10.1016/0963-8695(92)90003-Y.
- [94] P. Wilcox, M. Lowe, and P. Cawley, “The effect of dispersion on long-range inspection using ultrasonic guided waves,” *NDT E Int.*, vol. 34, no. 1, pp. 1–9, 2001, doi: 10.1016/S0963-8695(00)00024-4.
- [95] P. D. Wilcox, M. J. S. Lowe, and P. Cawley, “Mode and transducer selection for long range lamb wave inspection,” *J. Intell. Mater. Syst. Struct.*, vol. 12, no. 8, pp. 553–565, 2002, doi: 10.1106/N9PB-Y62E-P0Y2-50QF.
- [96] J. Lin, J. Hua, L. Zeng, and Z. Luo, “Excitation Waveform Design for Lamb Wave

- Pulse Compression,” *IEEE Trans. Ultrason. Ferroelectr. Freq. Control*, vol. 63, no. 1, pp. 165–177, 2016, doi: 10.1109/TUFFC.2015.2496292.
- [97] J. Hua, L. Zeng, J. Lin, and L. Huang, “Excitation series design and pulse compression synthesis for high resolution Lamb wave inspection,” *Struct. Heal. Monit.*, vol. 00, pp. 1–15, 2018, doi: 10.1177/1475921718801996.
- [98] S. Malo, S. Fateri, M. Livadas, C. Mares, and T. Gan, “Wave Mode Discrimination of Coded Ultrasonic Guided Waves Using Two-Dimensional Compressed Pulse Analysis,” *IEEE Trans. Ultrason. Ferroelectr. Freq. Control*, vol. 64, no. 7, pp. 1092–1101, 2017.
- [99] Z. Zhou *et al.*, “Application of wavelet filtering and Barker-coded pulse compression hybrid method to air-coupled ultrasonic testing,” *Nondestruct. Test. Eval.*, vol. 29, no. 4, pp. 297–314, 2014, doi: 10.1080/10589759.2014.941840.
- [100] N. Quaegebeur, P. Masson, P. Micheau, and N. Mrad, “Broadband Generation of Ultrasonic Guided Waves Using Piezoceramics and Sub-Band Decomposition,” *IEEE Trans. Ultrason. Ferroelectr. Freq. Control*, vol. 59, no. 5, pp. 928–938, 2012, doi: 10.1109/TUFFC.2012.2277.
- [101] J. E. Michaels, S. J. Lee, A. J. Croxford, and P. D. Wilcox, “Chirp excitation of ultrasonic guided waves,” *Ultrasonics*, vol. 53, no. 2013, pp. 265–270, 2013, doi: 10.1016/j.ultras.2012.06.010.
- [102] J. E. Michaels, S. J. Lee, J. S. Hall, and T. E. Michaels, “Multi-mode and multi-frequency guided wave imaging via chirp excitations,” *SPIE Heal. Monit. Struct. Biol. Syst. 2011*, vol. 7984, no. 798401, p. 11 pages, 2011, doi: 10.1117/12.880963.

- [103] I. Dafydd and Z. S. Khodaei, "Damage severity assessment in composite structures using ultrasonic guided waves with chirp excitation," *SPIE - Smart Struct. Mater.*, vol. 10598, p. 11 pages, 2018, doi: 10.1117/12.2299647.
- [104] Z. Liu, Y. Xu, C. He, and B. Wu, "Lamb Waves Inspection by Using Chirp Signal and Mode Purification," in *Engineering Asset Management - Systems, Professional Practices and Certification*, T. P, M. J, W. K, L. R, and K. C, Eds. Springer, Cham, 2015, pp. 137–147.
- [105] F. A. A. United States, *Metallic Materials Properties Development and Standardization (MMPDS) Handbook*, MMPDS-13. Washington, D.C.: Battelle Memorial Institute, 2018.
- [106] C. Ramadas, K. Balasubramaniam, M. Joshi, and C. V. Krishnamurthy, "Interaction of guided Lamb waves with an asymmetrically located delamination in a laminated composite plate," *Smart Mater. Struct.*, vol. 19, p. 11 pages, 2010, doi: 10.1088/0964-1726/19/6/065009.
- [107] T. Hayashi and K. Kawashima, "Multiple reflections of Lamb waves at a delamination," *Ultrasonics*, vol. 40, pp. 193–197, 2002.
- [108] R. Kumar Munian, D. Roy Mahapatra, and S. Gopalakrishnan, "Lamb Wave Interaction with Composite Delamination," *Compos. Struct.*, vol. 206, no. August, pp. 484–498, 2018, doi: 10.1016/j.compstruct.2018.08.072.
- [109] N. Hu, T. Shimomukai, C. Yan, and H. Fukunaga, "Identification of delamination position in cross-ply laminated composite beams using S₀ Lamb mode," *Compos. Sci. Technol.*, vol. 68, no. 6, pp. 1548–1554, 2008, doi: 10.1016/j.compscitech.2007.10.015.

- [110] N. Hu *et al.*, “Locating delamination in composite laminated beams using the A0 Lamb mode,” *Mech. Adv. Mater. Struct.*, vol. 19, no. 6, pp. 431–440, 2012, doi: 10.1080/15376494.2010.528156.
- [111] K.-H. Ip and Y.-W. Mai, “Delamination detection in smart composite beams using Lamb waves,” *Smart Mater. Struct.*, vol. 13, no. 3, pp. 544–551, 2004, doi: 10.1088/0964-1726/13/3/013.
- [112] B. Feng, D. J. Pasadas, A. L. Ribeiro, and H. G. Ramos, “Locating Defects in Anisotropic CFRP Plates Using ToF-Based Probability Matrix and Neural Networks,” *IEEE Trans. Instrum. Meas.*, vol. 68, no. 5, pp. 1252–1260, 2019.
- [113] V. T. Rathod, S. Mukherjee, L. Udpa, and Y. Deng, “Extracting Mode Converted Guided Wave Response due to Delamination using Embedded Thin Film Sensors,” *IEEE Int. Conf. Progn. Heal. Manag.*, pp. 1–8, 2020.
- [114] G. Petculescu, S. Krishnaswamy, and J. D. Achenbach, “Group delay measurements using modally selective Lamb wave transducers for detection and sizing of delaminations in composites,” *Smart Mater. Struct.*, vol. 17, no. 1, pp. 1–10, 2008, doi: 10.1088/0964-1726/17/01/015007.
- [115] C. Ng and M. Veidt, “Scattering of the fundamental anti-symmetric Lamb wave at delaminations in composite laminates,” *J. Acoust. Soc. Am.*, vol. 129, no. 3, pp. 1288–1296, 2011, doi: 10.1121/1.3533741.
- [116] B. I. S. Murat, P. Khalili, and P. Fromme, “Scattering of guided waves at delaminations in composite plates,” *J. Acoust. Soc. Am.*, vol. 139, no. 6, pp. 3044–3052, 2016, doi: 10.1121/1.4953016.
- [117] N. Hu, Y. Liu, Y. Li, X. Peng, and B. Yan, “Optimal excitation frequency of lamb

- waves for delamination detection in CFRP laminates,” *J. Compos. Mater.*, vol. 44, no. 13, pp. 1643–1663, 2010, doi: 10.1177/0021998309353965.
- [118] V. Samaitis, L. Mazeika, and R. Rekuviene, “Assessment of the Length and Depth of Delamination-Type Defects Using Ultrasonic Guided Waves,” *Appl. Sci.*, vol. 10, no. 5236, pp. 1–19, 2020.
- [119] M. D. Rogge and C. A. C. Leckey, “Characterization of impact damage in composite laminates using guided wavefield imaging and local wavenumber domain analysis,” *Ultrasonics*, vol. 53, no. 7, pp. 1217–1226, 2013, doi: 10.1016/j.ultras.2012.12.015.
- [120] P. D. Juarez and C. A. C. Leckey, “Multi-frequency local wavenumber analysis and ply correlation of delamination damage,” *Ultrasonics*, vol. 62, pp. 56–65, 2015, doi: 10.1016/j.ultras.2015.05.001.
- [121] O. Mesnil, C. A. C. Leckey, and M. Ruzzene, “Instantaneous and local wavenumber estimations for damage quantification in composites,” *Struct. Heal. Monit.*, vol. 14, no. 3, pp. 193–204, 2015, doi: 10.1177/1475921714560073.
- [122] Z. Tian, L. Yu, and C. Leckey, “Delamination detection and quantification on laminated composite structures with Lamb waves and wavenumber analysis,” *J. Intell. Mater. Syst. Struct.*, vol. 26, no. 13, pp. 1723–1738, 2015, doi: 10.1177/1045389X14557506.
- [123] H. Mei and V. Giurgiutiu, “Characterization of multilayer delaminations in composites using wavenumber analysis : numerical and experimental studies,” *Struct. Heal. Monit.*, vol. 20, no. 3, pp. 1004–1029, 2021, doi: 10.1177/1475921720939616.

- [124] M. Misiti, Y. Misiti, G. Oppenheim, and J.-M. Poggi, *Matlab wavelet toolbox: Getting started guide*, R2018b ed. Natick, MA: The MathWorks, Inc., 2018.
- [125] A. Huber, “Dispersion Calculator.” Center for Lightweight Production Technology Institute of Structures and Design, German Aerospace Center, Augsburg, Germany, 2018, [Online]. Available:
https://www.dlr.de/zlp/en/desktopdefault.aspx/tabid-14332/24874%7B/_%7Dread-61142/%7B/24874_read-61142/.
- [126] “LAMSS-COMPOSITES.” Laboratory for Active Materials and Smart Structures, University of South Carolina, South Carolina, [Online]. Available:
<http://www.me.sc.edu/research/lamss/html/software.html>.